

NORTHWESTERN UNIVERSITY

Exploratory Synthesis and Characterization of Heavy Metal Halide Semiconductors:

Unveiling New Properties and Structures

A DISSERTATION

SUBMITTED TO THE GRADUATE SCHOOL
IN PARTIAL FUFILLMENT OF THE REQUIREMENTS

for the degree

DOCTOR OF PHILOSOPHY

Field of Chemistry

By

Grant C. B. Alexander

EVANSTON, ILLINOIS

March 2020

All Rights Reserved

ABSTRACT

Exploratory Synthesis and Characterization of Heavy Metal Halide Semiconductors: Unveiling
New Properties and Structures

Grant C. B. Alexander

The development of heavy metal semiconductors is a growing field of interest for their application in photovoltaics, light emission, and radiation detection. This is due to their robust ability to convert incident photons of visible wavelength and high energy into charge current while remaining stable, optimizable, and readily synthesizable. As the field continues to expand there must also be expansion into new phases and chemistry that drive for the development of new technologies. Beginning from the heavy metal halide binaries, MI_n ($M = \text{Pb, Bi}; n = 2,3$), and the ternary compounds inspired by the perovskites, $AM'X_3$ ($A = \text{Cs, Rb}; M' = \text{Ge, Sn, Pb}; X = \text{Cl, Br, I}$), an effort is made to modify their compositions to unveil new structures and properties by optical, structural, computational, and electrical analysis. From mixtures of 2D PbI_2 and BiI_3 , the material $(\text{PbI}_2)_{1-x}(\text{BiI}_3)_x$ was synthesized, characterized and discovered to have remarkable conductance switching properties due to nanoscale phase separation and integration. $(\text{PbI}_2)_{1-x}(\text{BiI}_3)_x$ also displays unconventional, controllable optical properties where mid-gap states can promote below band gap absorption due to clustering of Bi within vacancy deficient phase boundaries. The modification of these binary mixtures with the addition of Cu^{1+} to results in the quaternary CuMBi_6 ($M = \text{Sn, Cd, Pb}$) phases synthesized and found to adopt defect abundant 3D structures promoting Cu ion conduction. Investigation of the substitution of Au for A-site cation in AMX_3 yields black $\text{Au}^{3+}\text{Pb}_2\text{I}_7$ where the low band gap is induced by Au-I ligand charge transfer. Overall, this

dissertation exemplifies the use of exploratory synthesis for the discovery of new materials and their resulting properties.

Acknowledgements

I would like to thank everyone that has been a vital part of the completion of this thesis and for my success in during my time in the program.

My advisor, Prof. Mercuri G. Kanatzidis, has been instrumental in my development and understanding of chemistry from a fundamental perspective. I admire his drive to continually be curious about new compounds, structures and properties. He has helped me learn how to narrow down the infinite number of experiments I could conduct, but also encouraged me to dive deeper into the unknown to uncover some phenomenally complex and beautiful systems.

My thanks go out to all my collaborators in the Department of Physics and Astronomy at Northwetsern. Prof. Venkat Chandrasekhar and his students Patrick W. Krantz and Dr. Samuel K. Davis were instrumental in unveiling and understanding the new electrical properties described within this dissertation. Additonal thanks goes to Dr. Giancarlo Trimarchi for his work on the Density Functional Theory Calculaitons that lead aided in our understanding of the structural and optoelectronic relationships in our 2D materials.

My thanks go out to my collaborators in the Department of Materials Science and Engineering at Northwetsern, Prof. Vinayak P. Dravid and his postdoctoral reserachers Dr. Hee Joon Jung and Dr. Yaobin Xu. Thier characterization of materials by various Transmission Electron Microscopy techniques made it possible to accurately describe the a majority of the material in this thesis from a structural perspective.

For their aid in developing an understanding of the electronic nature of the AuPb_2I_7 system I would like to thank Dr. Douglas Fabini and Prof. Ram Sheshadiri in the Department of Chemistry

at the University of California Santa Barbra. The resultant theoretical calculations were a strong contribution to our publication and added significant scientific value.

To my other collaborators Dr. Constantinos Stoumpous, Dr. Ido Hadar, Dr. Yihui He, Dr. Kyle McCall, and Shiqiang Hao, I would like to thank you for your scientific and intellectual support both within and beyond the scope of the experiments and results within this thesis.

Thank you to Katelyn, who has been through this entire graduate program and thesis writing with me. This journey has been one of growth, struggle, and success and I would not have been able to achieve what I have without your support. You always continue to inspire me.

Few people have been as incredibly influential as Elizabeth Fischer and Amy Abe. From my time at Lake Forest and through my time at Northwestern they have been incredible sources of support and guidance. Always willing to listen and advise, you have made a direct impact on my success and growth both as a person and as an academic.

My thanks also go out to Jason Cody and the Lake Forest College Chemistry Dept, who taught me how to conduct research during my first undergraduate position. My love of exploratory synthesis and crystallography was made during my time at Lake Forest.

Thank you to my parents, Char and Dave, and my sister, Katherine, for being supportive through this graduate degree program and beyond.

To all my lab mates, thank you. This experience would not have been what it was without your input both academic and beyond.

Dedicated to

Rev. R. James Bos (1925 – 2018)

Genevieve P. Bos (1926 – 2019)

Table of Contents

Abstract.....	3
Acknowledgement.....	5
Table of Contents.....	8
List of Figures and Tables.....	14

Chapter 1

An Introduction and Motivation to the Synthesis of Semiconducting Heavy Metal Halides

1.1. An Introduction to Semiconductors for Radiation Detection.....	40
1.2. Design Principles of Optoelectronic Semiconductors for Radiation Detection.....	45
1.2.1. Design with Regard Density and Composition.....	46
1.2.2. Design with Regard to the Band Gap, E_g	47
1.2.3. Design with Regard to Resistivity, ρ	48
1.2.4. Design with Regard to Mobility-Lifetime Product, $\mu\tau$	48
1.3. Structure and Properties of Semiconducting Heavy Metal Halides.....	49
1.3.1. Justification for Halide-Based Room Temperature Semiconductor Detectors.....	49
1.3.2. The Binary Heavy Metal Halides.....	51
1.3.3. Ternary Heavy Metal Halide Semiconductors.....	57

1.3.4. The Structure and Properties of Halide Perovskites.....	59
1.3.5. Lower Dimensionality Derivatives of the Perovskites.....	64
1.4. Thesis Goal: Exploratory Approach to Greater Materials Discovery.....	65
1.5. Thesis Outline.....	66

Chapter 2

Controllable Nonclassical Conductance Switching in Nanoscale Phase Separated $(\text{PbI}_2)_{1-x}(\text{BiI}_3)_x$
Layered Crystals

2.1. Abstract.....	68
2.2. Introduction.....	79
2.3. Materials and Methods.....	71
2.3.1. Synthesis of $(\text{PbI}_2)_{1-x}(\text{BiI}_3)_x$	71
2.3.2. Thermal Analysis.....	72
2.3.3. Structural Characterization.....	72
2.3.3.1. Powder X-ray diffraction.....	72
2.3.3.2. Single Crystal X-ray Diffraction.....	73
2.3.4. Room Temperature Electrical Property Measurements.....	73
2.3.5. Time Resolved Charge Collection Measurements.....	74
2.3.6. Variable Temperature Electrical Property Measurements.....	74
2.3.7. TEM/STEM microscope condition and sample preparation.....	75
2.4. Results and Discussion.....	76
2.4.1. Material Preparation.....	76
2.4.2. Conductance Switching Behavior.....	79

	10
2.4.2.1. Room Temperature IV.....	79
2.4.2.2. Time Dependent Decay Measurements.....	83
2.4.2.3. Temperature Dependent Electrical Characterization.....	85
2.4.2.4. Stoichiometric Dependence of the Conductance Switching.....	88
2.4.2.5. Stability of the Conductance Switching Effect.....	89
2.4.3. Structural Analysis.....	94
2.4.3.1. Single Crystal Analysis.....	94
2.4.3.2. Transmission Electron Microscopy, Unveiling the True Nature of (PbI ₂) _{0.5} (BiI ₃) _{0.5}	102
2.5. Conclusion.....	119

Chapter 3

Unconventional Below Band Gap Absorption in Nanoscale Phase Separated (PbI₂)_{1-x}(BiI₃)_x

3.1. Abstract.....	120
3.2. Introduction.....	121
3.3. Materials and Methods.....	123
3.3.1. Synthesis of Wide Gap (PbI ₂) _{1-x} (BiI ₃) _x	123
3.3.2. Synthesis of Narrow Gap (PbI ₂) _{1-x} (BiI ₃) _x	123
3.3.3. Conversion of Wide Gap (PbI ₂) _{0.5} (BiI ₃) _{0.5} to Narrow Gap (PbI ₂) _{0.5} (BiI ₃) _{0.5}	124
3.3.4. Solid State UV-Vis Spectroscopy.....	124
3.3.5. Powder X-ray Diffraction.....	124
3.3.6. Thermal Analysis.....	124
3.3.7. TEM/STEM Microscope Conditions and Sample Preparation.....	125

	11
3.3.8. DFT Method and Calculations.....	126
3.4. Results and Discussion.....	126
3.4.1. Synthetic Approach to Narrow and Wide Gap Samples.....	126
3.4.2. The Origin of Narrow Gap Behavior.....	132
3.5. Conclusion	142

Chapter 4

Rudorffite-like, Vacancy Dependent, Copper Conducting Quaternary CuMBiI_6 ($M = \text{Cd}, \text{Pb}$)
Phases

4.1. Abstract.....	143
4.2. Introduction.....	144
4.3. Materials and Methods.....	147
4.3.1. Bulk Synthesis of CuPbBiI_6 (1).....	147
4.3.2. Bulk Synthesis of CuCdBiI_6 (2).....	148
4.3.3. Spark Plasma Sintering (SPS).....	149
4.3.4. Structural Characterization.....	149
4.3.4.1. Powder X-ray Diffraction.....	149
4.3.4.2. Single Crystal X-ray Diffraction.....	150
4.3.4.3. In Situ Powder X-ray Diffraction at 11-BM.....	150
4.3.5. Thermal Analysis.....	150
4.3.6. Scanning Electron Microscopy.....	151
4.3.7. Solid State UV-Vis Spectroscopy.....	151
4.3.8. Electronic Property Measurements.....	151

4.4. Results and Discussion.....	152
4.4.1. Synthesis and Thermal Behavior.....	152
4.4.2. Single Crystal X-ray Diffraction Analysis of CuPbBiI ₆ (1).....	156
4.4.3. Single Crystal X-ray Diffraction Analysis of CuCdBiI ₆ (2).....	164
4.4.4. Probing the limits of Cu addition to (MI ₂) _{0.5} (BiI ₃) _{0.5} Layers.....	175
4.4.5. High Temperature In Situ Powder Diffraction of CuPbBiI ₆ (1).....	178
4.4.6. High Temperature In Situ Powder Diffraction of CuCdBiI ₆ (2).....	181
4.4.7. Optical properties of CuPbBiI ₆ (1) and CuCdBiI ₆ (2).....	186
4.4.8. Electronic Transport Measurements.....	188
4.5. Conclusion	196

Chapter 5

AuPb₂I₇: A Narrow Bandgap Au³⁺ Iodide Semiconductor

5.1. Abstract.....	197
5.2. Introduction.....	198
5.3. Experimental Details.....	200
5.3.1. Synthesis and Isolation.....	200
5.3.2. Single Crystal X-Ray Diffraction.....	201
5.3.3. Powder X-ray diffraction.....	201
5.3.4. Scanning Electron Microscopy.....	201
5.3.5. Solid State UV-Vis Spectroscopy.....	202
5.3.6. Density Functional Theory (DFT) Calculations.....	202
5.4. Results and Discussion.....	203

	13
5.4.1. Synthesis and Isolation.....	203
5.4.2. Crystal Structure Description.....	209
5.4.3. Optical Absorption and Electronic Structure.....	219
5.5. Conclusion	224
Concluding Remarks.....	225
References.....	226
Curriculum Vitae.....	242

List of Figures and Tables

Chapter 1

- Figure 1.** Comparison of the spectral response from a ^{133}Ba source as produced by a range of commercially available spectrometers. CsI(Tl) (1.27 cm \varnothing \times 3.05 cm), NaI(Tl) (5.08 cm \varnothing \times 5.08 cm), LaBr₃ (3.81 cm \varnothing \times 3.81 cm), CZT (0.5 \times 0.5 \times 0.5 cm³), and HPGe (6.5 cm \varnothing \times 5 cm) are shown to highlight the differences in resolution between different sensor materials. Adapted from Reference 5.....41
- Figure 2.** The basic schematic of a metal vs. a semiconductor vs. an insulator. Semiconductors have a moderate gap between conduction and valence bands that gives rise to photon absorption given that the particle is energetic enough. As band gap increases materials become more resistive and acts as an insulator.....42
- Figure 3.** A schematic representation of a semiconductor photodetector detector. Charge collection occurs when an incident photon of sufficient energy impacts the material exciting electrons and thereby creating electron hole pairs for collection.....43
- Figure 4.** The comparison of a perfect semiconductor compared to a realistic semiconductor. Trapping, defects and impurities can reduce the overall number of charge carrier yielding poorly performing material. Adapted from Reference 5.....44
- Figure 5.** Regions of the Periodic table highlighted in red. These regions are those that semiconductor detectors are typically developed from.....47

Figure 6. The Zinc-Blende (sphalerite) crystal structure of CZT. The high symmetry and its relation to the similar wurtzite structure promote the formation of structural and compositional defects in CZT crystals.....50

Figure 7. The unit cell of α -HgI₂ displaying the tetrahedral coordination of Hg and bridging coordination of I. The result is the 2D van der Waals material.....51

Figure 8. A ball and stick model of the unit cell of PbI₂. The Pb atoms are octahedrally coordinated to I, which displays a trigonal prismatic coordination between adjacent Pb atoms. The result is again 2D layered a van der Waals material that does not contain implicit metal site vacancies.....53

Figure 9. A ball and stick representation of the BiI₃ unit cell. Like PbI₂, Bi atoms are all octahedral coordination to I, however I displays both trigonal prismatic coordination to Bi and bridging coordination due to the ordered vacancies. BiI₃ is a 2D van der Waals material.....54

Figure 10. Supercells of a) PbI₂ and b) BiI₃ demonstrating their similar CdI₂-type structure and the necessary vacancies that give rise to the supercell BiI₃.....54

Figure 11. A ball and stick representation of the unit cell of InI. The alternating ordered packing of InI yields 5 coordinate geometry for both elements. As shown, InI is a 2D van der Waals material... ..56

Figure 12. The simple 3D CsCl-type unit cell of TlBr. Both Tl and Br are 8 coordinate.....56

Figure 13. A ball and stick representation of the unit cell of Tl₄CdI₆. Tl₄HgI₆ displays analogous behavior. [MI₆]⁴⁻ octahedra are charge balanced by large TI⁺ counterions leading to a 0D structure.

- Figure 14.** A ball and stick representation of the unit cell of TlSn_2I_5 . The layers of $[\text{Sn}_2\text{I}_5]^-$ are charge balanced Tl located between them leading to a 2D structure.....58
- Figure 15.** Polyhedral representation of the structure of the 3D halide perovskites as adapted from Reference 70. Metal halide octahedra are corner sharing in all directions that lead to 12 coordinate cation A sites. This results in a 3D structure.....59
- Figure 16.** A representation of the unit cell of the double perovskite $\text{Cs}_2\text{AgBiBr}_6$. Alternating Ag^+ and Bi^{3+} occupancy on the metal sites leads to charge compensation to form the perovskite structure.....63
- Figure 17.** The ball and stick representation of the structures of 0D $\text{Cs}_3\text{Bi}_2\text{I}_9$ (a,d), 2D $\text{Cs}_3\text{Sb}_2\text{I}_9$ (b,e) and 2D $\text{Rb}_3\text{Sb}_2\text{I}_9$ (c,f). $\text{Rb}_3\text{Bi}_2\text{I}_9$ displays an analogous structure to $\text{Rb}_3\text{Sb}_2\text{I}_9$. Adapted from Reference 101.....65

Chapter 2

- Figure 18.** a) The structure of a PbI_2 layer. b) The structure of a BiI_3 layer possessing ordered vacancies. c,d) A model of $(\text{PbI}_2)_{0.5}(\text{BiI}_3)_{0.5}$ randomly generated with a mixture of the two lattice types as represented by polyhedral and ball and stick models.....70
- Table 1.** Furnace Profiles for $(\text{PbI}_2)_x(\text{BiI}_3)_x$ Preparations.....72
- Figure 19.** A representative ingot of $(\text{PbI}_2)_{0.5}(\text{BiI}_3)_{0.5}$ after the molten mixture is slowly cooled. Large crystalline regions can be cleaved from these samples for charge transport measurements..77

Figure 20. Powder diffraction patterns of $(\text{PbI}_2)_{0.5}(\text{BiI}_3)_{0.5}$ samples demonstrating well defined interplanar $00l$ Bragg peaks as well as diffuse scattering in both samples.....77

Figure 21. DTA of $(\text{PbI}_2)_{0.5}(\text{BiI}_3)_{0.5}$ noting that when the binaries are combined the resultant mixture has an apparent melting point of 381 C, nearly 25 C both parent compounds. The overlapping peaks in the exothermic curve demonstrate the that mixture is congruently melting. It was from these thermal analysis data we designed the standardized cooling regime for all future samples of mixed stoichiometry.....78

Figure 22. A representative I-V curve for a sample of $(\text{PbI}_2)_{1-x}(\text{BiI}_3)_x$ sample after the memristor-like behavior has been engendered in the sample, note the on and off regions as designated by the arrows.....79

Figure 23. First and second sweeps of the unbiased $(\text{PbI}_2)_{0.5}(\text{BiI}_3)_{0.5}$ sample from Figures 30 - 34, 2.4.2.4. On the first sweep the conductance switching peak is not observed as the sample is being biased for the first time. An explanation of this behavior is given in the section on the Mechanism of the Conductance Switching Action.....80

Figure 24. Relaxation behavior of $(\text{PbI}_2)_{0.5}(\text{BiI}_3)_{0.5}$ where the sample was held at -100 V for two min followed by a direct swap to the given applied positive bias. Current was measured as a function of time to observe charge extracted from the material and was observed to be on the second scale.....83

Figure 25. a) Plot of the voltage and maximum current from the relaxation curves seen in Figure 24 as a function of peak time, with a representative exponential fit. b) The corresponding current vs voltage plot a demonstrating the highly correlated nature of peak characteristics.....84

- Figure 26.** Temperature dependent I-V curves of $(\text{PbI}_2)_{0.5}(\text{BiI}_3)_{0.5}$ beginning at 78 K to 260 K demonstrating the thermally dependent behavior of the conductance switching behavior beginning around 225 K.....85
- Figure 27.** Current from a sample held at 40 V constant bias and allowed to warm up. This range informed the investigation of further temperature dependent IV sweeps.....86
- Figure 28.** Arrhenius relation for temperature dependent charge transport, obtained by integrating over the forward and backward currents sweep direction of each of the IV curves.....87
- Figure 29.** I-V curves samples of multiple compositions of $(\text{PbI}_2)_{1-x}(\text{BiI}_3)_x$ ($x = 0.2, 0.4, 0.5, 0.6$) demonstrating a compositional dependence on the degree of memristor-like behavior.....88
- Figure 30.** Demonstration of bake in fatigue, which decays both the turn-on transport peak and the leakage current as a function of number of cycles swept.....90
- Figure 31.** Demonstration of initial current fatigue due to a bake-in of iodine into low energy states on the edge of phase boundaries.....90
- Figure 32.** Initial increase in current caused by the formation of preferred conduction channels and the return to fatigue behavior.....92
- Figure 33.** Demonstration of two successive runs of ~130 cycles from +50 V to – 50V on a sample of $(\text{PbI}_2)_{0.5}(\text{BiI}_3)_{0.5}$. As successive runs cycles are completed the maximum current degrades due to sample fatigue, but after a recovery time the initial cycle current increased, demonstrating competing effects in the transport behavior.....92

- Figure 34.** A closer look at the later cycles show the return to fatigue behavior for runs on the same sample. There are remaining structural effects in the current that result in more net charge transfer in the positive bias for the first run that is suppressed in the second, but peak conduction magnitude and total cycle charge transfer otherwise remain the same.....93
- Table 2.** Crystal data and structure refinement for $\text{Pb}_{0.40}\text{Bi}_{0.40}\text{I}_2$ at 293 K.....95
- Table 3.** Atomic coordinates ($\times 10^4$) and equivalent isotropic displacement parameters ($\text{\AA}^2 \times 10^3$) for $\text{Pb}_{0.40}\text{Bi}_{0.40}\text{I}_2$ at 293 K with estimated standard deviations in parentheses.....96
- Table 4.** Anisotropic displacement parameters ($\text{\AA}^2 \times 10^3$) for $\text{Pb}_{0.40}\text{Bi}_{0.40}\text{I}_2$ at 293 K with estimated standard deviations in parentheses.....96
- Figure 35.** A projection of the single crystal refinement model of $(\text{PbI}_2)_{0.5}(\text{BiI}_3)_{0.5}$, which appears as $\text{Pb}_{0.4}\text{Bi}_{0.4}\text{I}_2$ by x-ray diffraction along the [010] direction. Metal sites are represented by the partial occupancy of Bi, Pb, and vacancies.....97
- Figure 36.** A projection of the single crystal refinement model of $(\text{PbI}_2)_{0.5}(\text{BiI}_3)_{0.5}$, which appears as $\text{Pb}_{0.4}\text{Bi}_{0.4}\text{I}_2$ by x-ray diffraction along the [100] direction. Metal sites are represented by the partial occupancy of Bi, Pb, and vacancies. This is the most commonly seen pattern in the TEM imaging.....98
- Figure 37.** Electron Images of the single crystal used for structural refinement.....99
- Table 5.** EDS Data Summary for crystal pictured in Figure 20. Due to the high operating voltage and current of the SEM (25 KeV, 90 μA) some iodine loss is observed; however, the metal ratio is conserved at 1:1 as expected.....99

Figure 38. Comparison of a representative plot of PXRD data from $(\text{PbI}_2)_{0.5}(\text{BiI}_3)_{0.5}$ to the theoretical pattern generated using the representative CIF file. As the major $00l$ peaks were well matched we initially suspected massive vacancy disorder as the reason for the diffuse diffraction, rather than the phase separation and strain caused by phase boundary formation.....100

Figure 39. Projections of reciprocal space from single crystal diffraction data taken from the above experiment. a) Observation of diffraction patterns down the $[001]$ axis that show that there are unindexable peaks between the most intense reflections. Vectors could be partially fit for a $1/3$ modulation vector, however, there also appeared a $1/2$ vector that could not be co-indexed. b) Projection of reciprocal space taken from the $[010]$ direction demonstrating similar results of greater order that could not be indexed as in a).....101

Figure 40. BFTEM image (defocus $\Delta f = +100$ nm) of a sample of $(\text{PbI}_2)_{0.5}(\text{BiI}_3)_{0.5}$ displaying the “brick wall” patterning where bright phases are Pb-rich while dark regions are Bi-rich.....102

Figure 41. HRTEM and (002) -filtered IFFT of 2D layers of $(\text{PbI}_2)_{0.5}(\text{BiI}_3)_{0.5}$ displaying variance in layer spacing and defects on the 10 nm scale which contribute to the diffuse scattering. b) Locally magnified HRTEM images from image a) showing perfect vertical alignment of 2D stacking (left) and stacking faults with bottom iodine misalignment (middle) and both top/bottom iodine misalignment (right).....103

Figure 42. HAADF of phase boundaries exhibiting dislocation cores and extra half planes (green symbol) because of lattice mismatch that leads to the undercoordinated iodine atoms that are liberated by under bias to induce the unique I-V behavior.....105

- Figure 43.** HAADF and ABF of $(\text{PbI}_2)_{0.5}(\text{BiI}_3)_{0.5}$ on [100] zone showing dislocation cores (green symbols) and Iodine misalignment by Iodine layer shift (yellow arrows for shift direction). Please note that brick phase boundary is located at left side of this image area.....105
- Figure 44.** STEM-EDS map of $(\text{PbI}_2)_{0.5}(\text{BiI}_3)_{0.5}$ showing HAADF and corresponding Bi, Pb and I. Please note that Pb and I show same trend and dark regions (less-dense) in HAADF are matched to deficiency of Pb and I.....106
- Figure 45.** HAADF of $(\text{PbI}_2)_{0.8}(\text{BiI}_3)_{0.2}$ along the [100] zone showing single-crystallinity over a relatively large area confirmed by (002)-filtered IFFT as inset.....107
- Figure 46.** HAADF and ABF of $(\text{PbI}_2)_{0.8}(\text{BiI}_3)_{0.2}$ on [100] zone exhibiting perfect 2D atomic configuration.....108
- Figure 47.** HAADF with overlay of corresponding 2D stacking of Pb-Bi layer sandwiched by two iodine layers. The sandwich structure is chemically verified by STEM-EDS line profile in Figure 48.....109
- Figure 48.** a) HAADF of $(\text{PbI}_2)_{0.8}(\text{BiI}_3)_{0.2}$ with STEM-EDS line profile (yellow dotted arrow). b) Line profile of EDS count of Pb M, Bi M and I L. c) Overall EDS signal analysis showing weight and atomic percentage of Pb, Bi and I. Please note that EDS line profile confirms Pb-Bi layers are sandwiched by two top/bottom Iodine layers.....109
- Figure 49.** a) Electron diffraction of $(\text{PbI}_2)_{0.8}(\text{BiI}_3)_{0.2}$ presenting representative rectangular array (blue, yellow lines) of reflections on [100] zone with horizontally mirrored superlattice spots (green arrows). b) Simulated diffraction of $\text{Pb}_{0.4}\text{Bi}_{0.4}\text{I}_2$ along the [100] zone matching to a).....110

Figure 50. HAADF of $(\text{PbI}_2)_{0.8}(\text{BiI}_3)_{0.2}$ where PbI_2 is the dominant binary, showing a significant decrease in phase boundaries because of the scarcity of small BiI_3 -rich regions (dark).....110

Figure 51. a) Both $(\text{PbI}_2)_{0.5}(\text{BiI}_3)_{0.5}$ and $(\text{PbI}_2)_{0.2}(\text{BiI}_3)_{0.8}$ present representative rectangular array (blue, yellow lines) of reflections on [100] zone with horizontally mirrored superlattice spots (green arrows). Note that $(\text{PbI}_2)_{0.5}(\text{BiI}_3)_{0.5}$ and $(\text{PbI}_2)_{0.2}(\text{BiI}_3)_{0.8}$ shows double peak splits because of the two-phase separation (see inset box). Strong and split superlattice array at magnified view (a right side) and the disappearance of (001) type spots. b) Simulated diffraction overlay of PbI_2 on [1-10] zone and horizontally mirrored BiI_3 on [010] and [0-10] elaborated on in Figure 35....111

Figure 52. a) Simulated cross-sectional diffraction overlay of PbI_2 of [1-10] zone and BiI_3 of horizontally mirrored [010] and [0-10] zones. Note that diffractions are color-coded as blue, black and red and representative out-of-plane (①) and in-plane (②) in rectangular pattern (blue) are summarized at bottom. b) Experimental $(\text{PbI}_2)_{0.5}(\text{BiI}_3)_{0.5}$ of [100] zone showing similar rectangular pattern (yellow) and mirrored superlattice array (green). Note that double splits of same diffraction spots are observed readily and representative out-of-plane (①) and in-plane (②) in rectangular pattern (yellow) are summarized at bottom.....112

Figure 53. HAADF of $(\text{PbI}_2)_{0.2}(\text{BiI}_3)_{0.8}$ where BiI_3 is dominant leading to greater number and area of phase boundaries because of the greater number of big large BiI_3 -rich regions.....113

Figure 54. a) Simulated plane-view diffraction overlay of both PbI_2 and BiI_3 on [001] zone. Note that diffraction overly is color-coded as blue, and red for PbI_2 and BiI_3 respectively and shows hexagonal array with peak double splits. b) Experimental plane-view of $(\text{PbI}_2)_{0.5}(\text{BiI}_3)_{0.5}$ on [001] zone showing hexagonal array and double split of same spots. c) TEM image of thin

$(\text{PbI}_2)_{0.5}(\text{BiI}_3)_{0.5}$ film prepared by Scotch tape peeling/transfer method. Please note contrast and brightness were modified to distinguish clear double split of reflections in b).....114

Figure 55. a) Step 1: Schematic representation of a sample of $(\text{PbI}_2)_{1-x}(\text{BiI}_3)_x$ with applied contacts that is previously unbiased. Unliberated, undercoordinated iodide atoms (depicted as colored circles) are resting at the phase boundaries between Pb and Bi rich phases. b) Step 2: Bias is applied across the crystal parallel to the c-axis, which leads to the movement and drift of iodine atoms as shown in (c). c) Step 3: As bias is applied across the crystal the undercoordinated iodine atoms bound to metals are liberated to iodide ions, creating positive vacancies near metal sites at the phase boundary, engendering the states that are required for memristor-like behavior, but not displaying the “turn on” current yet. (see Figure 23) Step 4: As current flows through the material the leakage current increases with voltage and electrons are trapped at vacancies locally charge balancing the material. As bias is decreased the current decreases towards (e), where no bias is applied but locally trapped electrons remain. e) Step 5: The unbiased state of the $(\text{PbI}_2)_{1-x}(\text{BiI}_3)_x$ sample where iodide atoms remain in and or near their drift position and electrons remain trapped near the engendered vacancies. f) Step 6: The sample of $(\text{PbI}_2)_{1-x}(\text{BiI}_3)_x$ is biased in the opposite direction leading to the charge extraction observed shown in (g). g) Step 7: When the critical bias is achieved the iodide atoms move the opposite direction leading to electrons previously bound to the vacancies tunneling though from one “brick” to another through the material observed as charge extraction peak. h) Step 8: As the new vacancies are filled by electrons the charge extraction current is complete, leading the low resistive state that is dominated by the leakage current, analogous to the state shown in (d). i) Step 9: As the I-V sweep returns to 0 V the iodide atoms and the vacancies with bound electrons remain as in f, but charged in the opposite direction. If

positive bias was swept at this time the current peak would be observed instead of steps 2 and 3, analogous to Step 7 in (g). j) Representation of the steps of the memristor-like behavior indicated on the prototypical “butterfly” I-V plot as noted by step number. Note that Steps 1, 2, and 3 will never occur again in the material as they are formative steps.....117

Chapter 3

Figure 56. a) Representative supercell of PbI_2 observed along the c-axis (top) to display the a-b plane and along b (bottom) to display the 2D stacking of the van der Waals material. b) Representative supercell of BiI_3 , displayed along c-axis (top) to display the a-b plane. There are ordered vacancies that are required of the material to account for Bi being trivalent rather than divalent. The bottom diagram displays the stacking of BiI_3 sheets in a single unit cell. Due to the ordered vacancies the a and b axes in BiI_3 are doubled relative to BiI_3 and c is tripled. c) Our approximation of a mixture of PbI_2 and BiI_3 leading to a possible coulombic frustration. As shown the top projection along a theoretical c-axis displaying the a-b plane assumes a random distribution of vacancies, Pb and Bi. The bottom figure assumes that the material remains a layered van der Waals material.

Figure 57. UV-Vis absorbance of the wide and narrow gap states of $(\text{PbI}_2)_{0.5}(\text{BiI}_3)_{0.5}$. Wide gap samples derive from quickly cooled melts of Pb, Bi and I_2 where the narrow gap behavior arises from slow cooling.....127

Table 6. Furnace Profiles for $(\text{PbI}_2)_x(\text{BiI}_3)_x$ Preparations.....127

Figure 58. Wide and narrow gap powder diffraction patterns indicating that between wide and narrow gaps the sharp basal 00 l reflections persist whereas the other reflections have become very diffuse.....128

Figure 59. DTA demonstrates that the mixture $(\text{PbI}_2)_{0.5}(\text{BiI}_3)_{0.5}$ melts congruently at 381 C and crystallizes congruently at 371 C, below that of the parent binary mixtures.....129

Figure 60. A wide gap sample of $(\text{PbI}_2)_{0.5}(\text{BiI}_3)_{0.5}$ was re-melted at 500 C and cooled for 24 hours, the resultant material was converted to narrow gap.....130

Figure 61. Wide gap material annealed at 160 C for 24 hours. No change in band gap was observed.....131

Figure 62. Compositional variation across multiple samples of $(\text{PbI}_2)_{1-x}(\text{BiI}_3)_x$ indicating that even at $x = 0.2$ the band gap is converted to that of BiI_3 and the low energy absorption is maximized at $x = 0.4$132

Figure 63. a, b) High angle annular dark field (HAADF) and annular bright field (ABF) images of wide gap $(\text{PbI}_2)_{0.5}(\text{BiI}_3)_{0.5}$ along the [100] zone. The dark regions in the HAADF image correlate to Bi-rich regions where the overall Z is less than that of the bright Pb-rich regions due to 2/3 of the metal atom density. This is reversed in the ABF image. The hallmark of these samples is distinct boundaries between Pb and Bi rich regions, indicative of our phase boundaries that give rise to conductance switching behavior in Chapter two. c, d) HAADF and ABF images of a narrow gap sample of $(\text{PbI}_2)_{0.5}(\text{BiI}_3)_{0.5}$, where dark regions in c again correlate to Bi-rich regions and the lighter correlate to Pb-rich regions. Here the clear phase boundaries that we observe in the wide

gap samples are far more diffuse, indicating far more mixing between the Bi and Pb rich phases.....134

Figure 64. Configurations 1 through 5 of randomly generated supercells of $(\text{PbI}_2)_{0.5}(\text{BiI}_3)_{0.5}$. Configurations were built via random number generation made with the assumption that no vacancies were adjacent in a supercell model of the bilayer $\text{Pb}_{0.4}\text{Bi}_{0.4}\text{I}_2$ model described in Chapter two. Note that for configuration 3 the bandgap is the smallest at 0.74 eV, whereas for configuration the bandgap is the widest at 1.61 eV.135

Figure 65. The top layer of configuration 3 as defined in the manuscript. Each vacancy was defined 1 – 8 and the nearest metal atoms were tabulated in Table 7. Every vacancy was defined in such a way for every configuration.136

Figure 66. The bottom layer of configuration 3 as defined in the manuscript. Each vacancy was defined 1 – 8 and the nearest neighbors were tabulated in Table 7.....136

Table 7. Tabulated Results of the Vacancy Assessment for Configurations 1 – 5. (V = Vacancy).....137

Table 8. Configurations 1 through 5 of $(\text{PbI}_2)_{0.5}(\text{BiI}_3)_{0.5}$ listed in decreasing bandgap with the average number of Bi and Pb neighbors to each vacancy calculated between each layer. Energy per formula unit (f.u. = $\text{Pb}_{0.4}\text{Bi}_{0.4}\text{I}_2$) is calculated from each supercell of 32 formula units.....139

Figure 67. The band gap of Configurations 1 – 5 plotted as a function of Average Bi Neighbors per vacancy and Calculated Energy per formula unit. As the number of Bi neighbors increases at the vacancies the band gap increases and the eV/f.u. decreases.....139

Figure 68. Expansion and Comparison of the DOS of the five supercell configurations. From top to bottom the band gap decreases from the 1.61 eV to 0.74 eV in the order defined in Table 8. Note the expansion of the Bi and I p states that leads to the decrease in the apparent band gap.....140

Figure 69. a) A well-defined phase boundary model built to probe the difference between it and the randomly generated configurations. b) The resulting calculated DOS from the model defined in a with a resultant gap of 1.43 eV. No significant broadening of the Bi and I p bands are observed.....141

Chapter 4

Figure 70. a) The prototypical hexagonal 3D structure of the ruderfite AgBiI_4 which consists of layers of Ag, Bi, Δ and Bi, Δ . The results is highly defect riddled crystal structure. b) A representation of the monoclinic structure of AbBiI_4 which demonstrates alternative ordering of Ag, Bi, and Δ that leads to monoclinic symmetry. c) The highly symmetric cubic crystal structure of AgBiI_4 which arises from equal ordering of Ag, Bi, and Δ on all sites.....145

Figure 71. PXRD patterns of quenched and slow cooled samples of **1**. Note the similar, but less intense level of diffuse diffraction that was observed for the $(\text{PbI}_2)_{0.5}(\text{BiI}_3)_{0.5}$ system in chapters two and three.....153

Figure 72. PXRD patterns of quenched and slow cooled samples of **2**.....153

- Figure 73.** Differential thermal analysis of **1** showing congruent melting and crystallization at 369 C and 362 C respectively. The small peak at 220 C in the first heating cycle does not reoccur in the second cycle, indicating a possible phase transition or incomplete reaction.....154
- Figure 74.** Differential thermal analysis of **2** showing congruent melting and crystallization at 352 C and 356 C respectively. The additional peaks at 264 C and 276 indicate the possibility of a high temperature phase.....154
- Figure 75.** Differential thermal analysis of the precursor $(\text{CdI}_2)_{0.5}(\text{BiI}_3)_{0.5}$ to CuCdBiI_6 demonstrating melting of crystallization points of 375 C and 386 C respectively. The small endothermic peak in the first heating cycle can be attributed to polytype transitions in CdI₂-type van der Waals materials.....155
- Table 9.** Crystal data and structure refinement for CuPbBiI_6 at 293 K.....157
- Table 10.** Atomic coordinates (x104) and equivalent isotropic displacement parameters ($\text{\AA}^2 \times 10^3$) for CuPbBiI_6 at 293 K with estimated standard deviations in parentheses.....158
- Table 11.** Anisotropic displacement parameters ($\text{\AA}^2 \times 10^3$) for CuPbBiI_6 at 293 K with estimated standard deviations in parentheses.....158
- Figure 77.** The rudorffite-like unit cell of **1** where Cu sites and Pb, Bi, and Δ sites occupy one layer dominated by edge sharing octahedra. Diffuse Cu disorder leads to the generation of the second layer as better shown in Figure 78. The metal site contains 2/3 metal and 1/3 vacancies and metal composition is set to equal amounts of Pb and Bi. Anisotropic parameters are shown for the heavy metal site and I.....159

Figure 78. The rudorffite-like unit cell of **1** where Cu sites and Pb, Bi, and Δ sites occupy one layer and diffuse Cu disorder leads to the generation of the second layer. There the coordination polyhedra have been added to the Cu atoms to further explore the rudorffite behavior.....160

Figure 79. SEM image of the surface of a sample of **1**. Multiple spectra have been averaged to find a composition of $\text{Cu}_{1.13}\text{Pb}_{1.07}\text{BiI}_{5.99}$. Given the inherent error in EDS signal this agrees well with our crystallographic model.....161

Table 12. SEM-EDS Results for **1**. Some variance is seen across the material.....161

Figure 80. The octahedral coordination of the Pb, Bi, Δ site which generates the heavy metal containing layers in **1**.....163

Figure 81. The three different copper sites that are found within the structure of **1**. Note that Cu1 sits near the edge of the heavy metal layer, Cu2 sits on a distorted site between the two layers, and Cu3 is found between the layers.....163

Figure 82. Left: the coordination environment of Cu1, which sits on a tetrahedral site between the two heavy metal layers. Bond distances to the four iodine atoms are given next to the respective atom. Middle: The coordination environment of Cu2, which resides within a distorted octahedral site. The bond distances are given as the maximum and minimum values for a given distorted Cu octahedron. Right: The tetrahedral coordination of Cu3 within the rudorffite-like heavy metal layer. Due to the density of Δ on the metal site, some copper can be found in these sites.....165

Figure 83. Comparison of the calculated pattern of **1** with experimental and to the Ag_3BiI_6 rudorffite. The additional peaks can be attributed to PbI_2 and BiI_3 -type layers as no other traces of the binary are apparent. The theoretical patterns of **1** and Ag_3BiI_6 agree well..... 165

Table 13. Crystal data and structure refinement for $\text{Cu}_{0.67}\text{Bi}_{0.67}\text{Cd}_{0.67}\text{I}_4$ at 293 K.....	166
Table 14. Atomic coordinates ($\times 10^4$) and equivalent isotropic displacement parameters ($\text{\AA}^2 \times 10^3$) for $\text{Cu}_{0.67}\text{Bi}_{0.67}\text{Cd}_{0.67}\text{I}_4$ at 293 K with estimated standard deviations in parentheses.....	167
Table 15. Anisotropic displacement parameters ($\text{\AA}^2 \times 10^3$) for $\text{Cu}_{0.67}\text{Bi}_{0.67}\text{Cd}_{0.67}\text{I}_4$ at 293 K with estimated standard deviations in parentheses.....	167
Figure 84. A [110] projection of the unit cell of 2 demonstrating the 3D nature of the defect-spinel as corner sharing heavy metal octahedra generate channels for Cu coordination. Anisotropic thermal parameters are shown for the heavy metal site and I, while Cu remains isotropic. The larger isotropic parameters on the Cu atoms reflect greater occupancy, where tetrahedral copper is more likely to fall channel tetrahedral sites rather than within the heavy metal lakes akin to Cu3 in 1 ...168	
Figure 85. A [110] projection of the unit cell of 2 demonstrating the 3D nature of the defect-spinel as corner sharing heavy metal octahedra generate channels for Cu coordination as shown in Figure 84, however the addition of the CuI_4 polyhedra demonstrates that opposed to the AgBiI_4 defect spinel, the inclusion of tetrahedral copper generates far more space filling sites that would otherwise be empty.....	169
Figure 86. SEM image of the surface of a sample of 2 . Multiple spectra have been averaged to find a composition of $\text{Cu}_{1.13}\text{Pb}_{0.94}\text{Bi}_{5.99}$. Given the inherent error in EDS signal this agrees well with our crystallographic model.....	170
Table 16. SEM-EDS Results for 2 . Some variance is seen across the material.....	170

Figure 87. The octahedral coordination of the Cd, Bi, and Δ site which generates the 3D edge sharing $(\text{Cd/Bi}/\Delta)\text{I}_6$ octahedra network in **2**.....172

Figure 88. The three different copper sites that are found within the structure of **2**. Note that Cu1 sits between four possible $(\text{Cd/Bi}/\Delta)\text{I}_6$ octahedra, whereas Cu2 sits in a tetrahedral channel site, and Cu3 sits between $(\text{Cd/Bi}/\Delta)\text{I}_6$ octahedra akin to Cu3 in **1**.....172

Figure 89. Right: The coordination environment of Cu1, which is found between four edge sharing $(\text{Cd/Bi}/\Delta)\text{I}_6$ octahedra. Despite this, the occupancy of this site is still refined to have 14.9% occupancy. Middle: The coordination environment of Cu2 which resides in a tetrahedral site in the channels of the defect-spinel with 16.9% occupancy. Right: The Cu3 sites which reside between two $(\text{Cd/Bi}/\Delta)\text{I}_6$ octahedra within the 3D structure and features the lowest occupancy of 5.9%. It features the only tetrahedral distortion with Cu pushed from the shared edge of the octahedra....173

Figure 90. Comparison of the calculated pattern of **2** with experimental and to the AgBiI_4 ruderffite. The theoretical patterns of **2** and AgBiI_4 agree well.....174

Figure 91. Powder diffraction patterns of $\text{Cu}_{1-x}\text{PbBiI}_{6-x}$ compositions. By $x = 0.2$ the 3D phase is the dominant phase in the powder diffraction pattern and by $x = 0.3$ there is no observation of the 2D parent mixtures. Note that $x = 0.4$ is missing as the ampoule broke during quenching.....175

Figure 92. Powder diffraction patterns of $\text{Cu}_{1-x}\text{CdBiI}_{6-x}$ compositions. Only at $x = 0.6$ does the 3D defect spinel phase become apparently phase pure. Note that the $x = 0.2$ sample is missing due the ampoule breaking during the quenching process.....176

Figure 93. In Situ powder diffraction of **1**, where upon heating the binaries react by 299 C to yield the 3D rudorffite phase. Upon cooling crystallization is observed near 326 C which yields a well ordered rudorffite phase at high temperature. Further cooling promotes disorder below 201 C...177

Figure 94. Comparison of the PXRD pattern on cooling for **1**. As noted, upon cooling between 267 C and 223 C the rudorffite phase is observed demonstrated in Figure 95 . Cooling below 201 C demonstrates the ability of the mixed Pb/Bi systems to induce disorder with the clear reflections corresponding to basal $00l$ peaks similar to the $(\text{PbI}_2)_{1-x}(\text{BiI}_3)_x$ system in chapter two.....178

Figure 95. Fitted PXRD profile for the 223 C cooling of **1**. The fitted pattern agrees well with the experimental with regard to the predicted peak locations for the trigonal $R-3m$ unit cell. Peak shapes were irregular due to particle sizes and relatively low intensities due to heavy absorbing elements. The excluded regions did not contain useful data for profile matching only the reflection from the Kapton windows of the apparatus.....179

Figure 96. In Situ powder diffraction of **2**, where upon heating the binaries react by 241 C to yield the defect-spinel phase. An CuI and $\text{Cu}_{1-x}\text{CdBiI}_{6-x}$ high temperature phases begin to appear near 298 C. Upon cooling, crystallization of the defect-spinel begins at 244 C. Further cooling promotes disorder below 198 C from multiple phase compositions arising from Cu inhomogeneity.....180

Figure 97. Comparison of the calculated PXRD pattern of **2** to the formation of **2** observed at 241 C. Additionally, the pattern of the combined hexagonal phase and cubic sphalerite CuI phase mixture at 273 C upon cooling demonstrate no low angle reflections.....181

Figure 98. Fitted PXRD profile for the 273 C cooling of **2**. The fitted pattern agrees well with the experimental with regard to the predicted peak locations for the both the cubic sphalerite CuI

(Phase #2) and the hexagonal $\text{CuHg}_{0.5}\text{I}_2$ -type phase (Phase #1) . The excluded regions did not contain useful data for profile matching only the reflection from the Kapton windows of the apparatus.....182

Figure 99. The $P6_3/mmc$ Unit cell of $\text{CuHg}_{0.5}\text{I}_2$ which reflects the same symmetry and analogous unit cell parameters as the high temperature hexagonal phase. The metal sites have no more than 30% occupancy between the Cu and Hg. For $\text{Cu}_{1-x}\text{CdBiI}_6$ the metal sites would have Cu, Cd, and Bi occupancy.....183

Figure 100. Fitted PXRD profile for the 241 C cooling of **2**. Due to Cu inhomogeneity in the sample two very similar cubic defect-spinel phases need to be accounted for, giving similar lattice parameters of $a = 12.565 \text{ \AA}$ or 12.349 \AA . The excluded regions did not contain useful data for profile matching only the reflection from the Kapton windows of the apparatus.....184

Figure 101. The optical absorbance of quenched samples of **1** and **2**. Both materials display band gaps like those seen in chapter three where the mixture of the $(\text{MI}_2)_{0.5}(\text{BiI}_3)_{0.5}$ ($M = \text{Cd}, \text{Pb}$) leads to low energy absorption. The addition of Cu does not make a significant effect on the band gap, indicating the BiI_3 -type absorption and clustering is still in effect in these quaternary materials..185

Figure 102. Comparison of pre and post-SPS samples of **1** compared to the constituent binaries and the calculated powder diffraction pattern from single crystal refinement.....188

Figure 103. Comparison of pre and post-SPS samples of **2** compared to the constituent binaries and the calculated powder diffraction pattern from single crystal refinement.....188

Figure 104. Polished post-SPS samples of **1** and **2**. Contacts were applied to the faces of the pellets on both sides.....190

- Figure 105.** PXRD patterns of samples of **1** and **2** that were annealed for 24 hours at 200 C. After annealing both samples had degraded with additional binary peaks observed in both. Annealed samples were not used in transport measurements.....190
- Figure 106.** Successive sweeps of ± 25 V on a sample of **1**. Successive sweeps demonstrate that the OFF, ON, and DISCHARGE cycle are dependent on the number of bias applications.....191
- Figure 107.** Successive sweeps of ± 20 V on a sample of **1**. Successive sweep show that for a given sample the intrinsic conductivity varies. Sweep 1 resulted hitting the maximum current for the electrometer. Successive sweeps were conducted and current was within measurable limits.....191
- Figure 108.** Representative I-V sweep of samples of **2**. Similar increasing current is observed over subsequent sweeps with the magnitude of the current peak dependent on the contact site for the given side of a device as demonstrated in Figure 107.....192
- Figure 109.** Single point measurement of **1** under constant 1 V bias for hour. The material hit the conductivity limit of the instrument within the first 20 minutes.....193
- Figure 110.** Single point measurement of **2** under constant 1 V bias for 20 minutes. The material hit the conductivity limit of the instrument within the first 7 minutes.....193
- Figure 111.** Evidence of Cu buildup for **1** at the carbon contact site after long term single point measurements bias measurements.....194
- Figure 112.** Evidence of Cu buildup for **2** at the carbon contact site after long term single point measurements bias measurements.....194

Chapter 5

Figure 113. a) The structure of KAu_3I_4 where $[\text{AuI}_4]^-$ units extend down $[010]$ charge balanced by K^+ , a direct analog of LiAuI_4 as drawn from reference 16. b) The perovskite-like structure of $\text{Cs}_2\text{Au}^{\text{I}^+}\text{Au}^{\text{3}^+}\text{I}_6$ where alternating $[\text{AuI}_2]^-$ and $[\text{AuI}_4]^-$ form pseudo-octahedra around charge balancing Cs cations, as drawn from reference 15. $\text{Rb}_2\text{Au}^{\text{I}^+}\text{Au}^{\text{3}^+}\text{I}_6$ forms the same structure...198

Figure 114. SEM image of the regions chosen to gather EDS data from AuPb_2I_7 . Due to growth on the surface of PbI_2 , often the penetration depth of the electron beam will be greater than the thickness of the crystal resulting in overrepresented Pb and I atomic %.....203

Table 17. SEM-EDS Spectra Results of AuPb_2I_7 as assessed from the regions in Figure 114 in Atomic %.....203

Table 18. Average Values and Standard Deviation of SEM-EDS Results from Table S1.....204

Figure 115. SEM Images of single crystals of AuPb_2I_7 growing on the surface of recrystallized PbI_2 . Crystals tend to grow near edges where nucleation begins to occur.....205

Figure 116. A typical powder diffraction pattern for the reaction mixture of AuPb_2I_7 . Au and PbI_2 are clearly represented in the pattern, but peaks of the calculated pattern from single crystal data confirms the presence of the title compound.....205

Figure 117. Powder diffraction from the vapor transport mixture shows little evidence of the title compound despite having the most observed by electron microscopy. Due to transport of unreacted PbI_2 away from the melt the mixture that remained in the hot end of the tube was far more gold rich as further described in Figure 118.....206

Figure 118. Vapor Transport tube after the transport experiment shows the transported PbI_2 on the right side of the image. The black solid on the left hand side is the remaining AuPb_2I_7 grown on PbI_2 , with a dominant amount of metallic gold. This was in the hot zone.....207

Figure 119. a) A larger forest of needles found after vapor transport. These crystals still grow as layers on top of PbI_2 substrate. b) Au metal expelling from needles of AuPb_2I_7 one month after preparation.....207

Table 19. Crystal data and structure refinement for AuPb_2I_7 at 100 and 298 K.....209

Table 20. Atomic coordinates ($\times 10^4$) and equivalent isotropic displacement parameters ($\text{\AA}^2 \times 10^3$) for AuPb_2I_7 at 298 K with estimated standard deviations in parentheses.....210

Table 21. Anisotropic displacement parameters ($\text{\AA}^2 \times 10^3$) for AuPb_2I_7 at 298 K with estimated standard deviations in parentheses.....210

Table 22. Selected Bond lengths [\AA] and Bond angles [$^\circ$] for AuPb_2I_7 Pb_2 at 298 K with estimated standard deviations in parentheses.....211

Table 23. Atomic coordinates ($\times 10^4$) and equivalent isotropic displacement parameters ($\text{\AA}^2 \times 10^3$) for AuPb_2I_7 at 100 K with estimated standard deviations in parentheses.....212

Table 24. Anisotropic displacement parameters ($\text{\AA}^2 \times 10^3$) for AuPb_2I_7 at 100 K with estimated standard deviations in parentheses.....212

Table 25. Selected Bond lengths [\AA] for AuPb_2I_7 Pb_2 at 298 K and 100 K with estimated standard deviations in parentheses.....213

Figure 120. Left) A projection of along [100] of the pseudo-layers in a 3 x 3 x 3 supercell of AuPb₂I₇. $1/\infty[\text{Pb}_2\text{I}_2]^{2+}$ can be seen propagating down [100] and bridged by Au³⁺. Middle) A projection down [010] further demonstrates the pseudo-layered nature of the system. Right) The projection down [001] which shows the corrugated nature of the pseudo-layers.....214

Figure 121. Stick and ball model of the structure of AuPb₂I₇ viewed down the three different crystallographic directions. In the view down the [001] direction the Au are totally eclipsed....215

Figure 122. Au³⁺ center in a square planar site of I atoms with bond lengths of 2.6330(9) and 2.6344(9) Å.....217

Figure 123. a) The distorted hendecahedron that Pb forms when fully coordinated to neighboring I atoms. b) Atoms labels and bond distances for the Pb hendecahedron in the same relative representation as given in a. c) The greater packing of the Pb polyhedra that extend form the pseudo-layers that are bridged by Au³⁺ with a representation of the $1/\infty[\text{Pb}_2\text{I}_2]^{2+}$ backbone in the same orientation. d) The square planar orientation of I bridging the $1/\infty[\text{Pb}_2\text{I}_2]^{2+}$ units to facilitate coordination down [010].....218

Figure 124. Unit cells of AuPb₂I₇ at 298 K and 100 K with the low temperature cell superimposed in red. Due to the change in Au – I bond lengths at low temperature and the general decrease of Pb – I bond distances the I₄ – I₄ distance decreases and becomes the c axis of the low temperature unit cell.....219

Figure 125. The optical absorbance of a mixture of AuPb₂I₇ with some contaminant PbI₂ that can be observed at 2.3 eV. The band gap for the title compound was determined to be 1.17 eV and a direct function of the [AuI₄]⁻ unit in the structure.....220

Figure 126. Electronic band structure and density of states (DOS) for AuPb₂I₇ from density functional theory, calculated using the generalized gradient approximation (GGA–PBE, with spin-orbit coupling). Orbital projections indicate the bandgap is dominated by filled I *p* states and empty Au *d* states (consistent with the square planar environment for Au³⁺), while the empty Pb *p* orbitals lie higher in energy.....221

Figure 127. Electronic band structure and density of states (DOS) for AuPb₂I₇ from density functional theory, calculated using the generalized gradient approximation (GGA–PBE). The band structure is shown with and without the inclusion of spin-orbit coupling (SOC), which most strongly affects states with Pb character.....223

Chapter 1

An Introduction and Motivation to the Synthesis of Semiconducting Heavy Metal Halides

1.1. An Introduction to Semiconductors for Radiation Detection

In 1876 British scientist William Grylls Adams found that when selenium was exposed to light that it generated electricity, thereby discovering the first material demonstrating photovoltaic properties.¹ Now nearly 150 years later it is well understood that for many applications the capture and conversion of light into electronic signals is essential. It drives the development of new technologies that have given rise to the modern era, most visibility the development of solar panels for the generation of renewable energy. Beyond solar applications, semiconductors can be applied more precisely than to gather broad spectrum light from the sun. Optoelectronic semiconductors have been developed to detect photons from the infrared to the ultraviolet, advancing the application and development of UV-Vis and IR spectroscopy. However, we can go beyond that range of wavelength and energy to one much greater, hard radiation. The development of semiconductor materials for x-ray and γ -ray radiation detection is not only an important leap for the scientific community, but also has widespread application for benefit of the greater public including implementation in medical imaging, national security, among others.^{2, 3} The aim is not only to detect the presence of an incident high energy photon, but resolve the energy of the photon as well which is far more complex.

Before an elaboration on the merits of semiconductor detectors it is important to make a clear distinction for why they are more desirable than already extant technology. Of the prevailing spectroscopic radiation detectors that are on the market the majority are scintillators, such as NaI:Tl. Scintillators use the absorption of an incident high energy photon to excite the material and further emit lower energy photons which can then be measured by another photodetector and converted into signal.⁴ The coupling of the scintillation to the photodetector unfortunately reduces

the spectroscopic ability of scintillation based detectors. When compared to the leading commercial semiconductors such as $\text{Cd}_{1-x}\text{Zn}_x\text{Te}$ (CZT) and high purity germanium (HPGe) the difference is clear (Figure 1).⁵ Both of these materials will be discussed further along in the chapter.

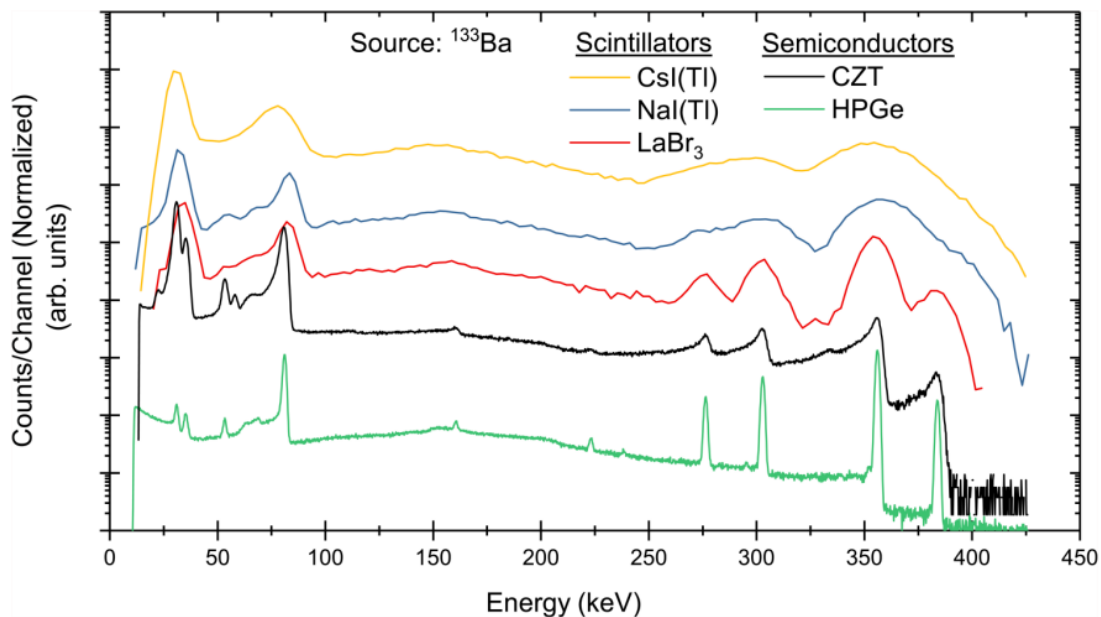


Figure 1. Comparison of the spectral response from a ^{133}Ba source as produced by a range of commercially available spectrometers. CsI(Tl) NaI(Tl), LaBr₃, CZT, and HPGe are shown to highlight the differences in resolution between different sensor materials. Adapted from Reference 5

The fundamental property of the in the application of optoelectronic semiconductors for radiation detection is photovoltaic effect. This allows for a direct method of charge collection. For a given semiconductor the gap between the valence band and the conduction band can be defined the band gap, E_g (Figure 2). Photons with $E > E_g$ are able to be absorbed by the material and

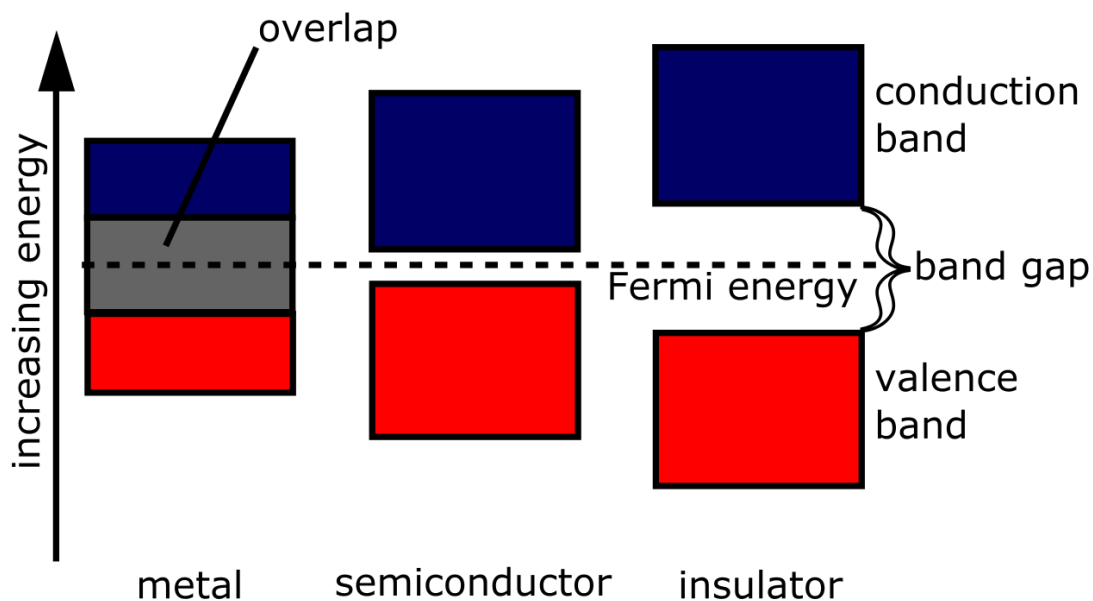


Figure 2. The basic schematic of a metal vs. a semiconductor vs. an insulator. Semiconductors have a moderate gap between conduction and valence bands that gives rise to photon absorption given that the particle is energetic enough. As band gap increases materials become more resistive and acts as an insulator. The Fermi energy is the highest occupied state electrons could be found at if energy levels were available.

promote electrons from the valence band into the conduction band creating electron hole pairs. Akin to this, incident hard radiation photons are also able to generate electrons and holes when they are absorbed (Figure 3). Under applied bias these electrons and holes can be collected and current is generated. The magnitude of the generated current is proportional to the energy of the incident photon that causes the electronic excitement.

However, this current is limited by the fundamental electronic properties of a given material. For charge to be measured the electrons and holes generated must be able to move in order to be collected. This effect is governed the mobility-lifetime product for given charge carriers

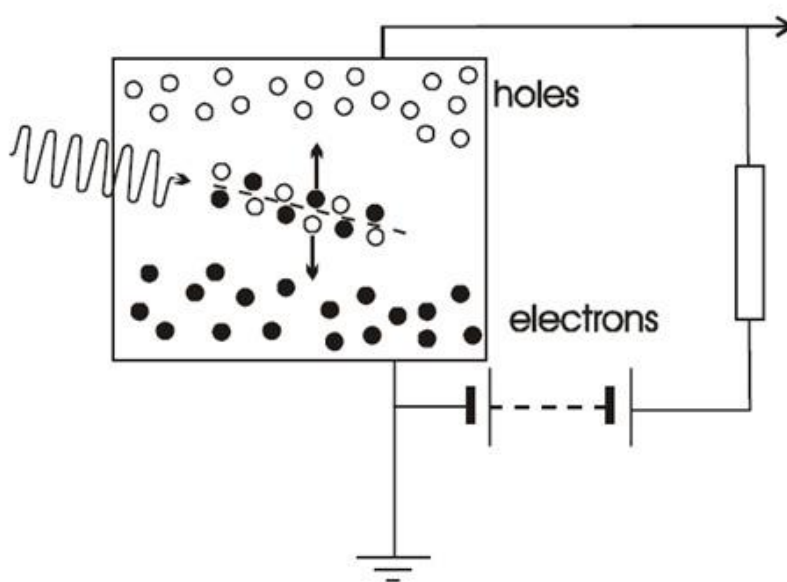


Figure 3. A schematic representation of a semiconductor photodetector detector. Charge collection occurs when an incident photon of sufficient energy impacts the material exciting electrons and thereby creating electron hole pairs for collection.

in semiconductors, $\mu\tau$. The μ term defines the relative mobility of a charge carrier as defined by cm^2V^{-1}) whereas τ reflects the lifetime of the charge carrier in s. This results in the mobility-lifetime product demonstrating the ability for a given semiconductor to successfully transport charge carriers. If the value of $\mu\tau$ is found to be low for a given semiconductor, then the resultant charge carriers do not sufficiently move in a material to be used for applications. While in a perfect

world $\mu\tau$ would be the only limiting factor in a material, there are additional important factors that affect charge carrier mobility.

In a perfect material the only governing factor for charge conduction would be the implicit structure and bonding that gives rise to the solid. Unfortunately, that is not how materials form and crystallize. For a given synthesized semiconductor there are range of implicit barriers that charge carriers must overcome in order to be collected. First, once electrons and holes are generated within a semiconductor they can recombine by to reduce the amount of charge carriers. This can be due to structural defects, compositional defects, and impurities (Figure 4).⁵ Additionally, electrons and holes may become trapped in mid gap energy states in the band gap and can no longer move within the lattice, thereby no longer be able to play a role in conduction. For a given material this would reflect in the experimental value of $\mu\tau$ being below that of what is expected based on a perfect pure crystal.

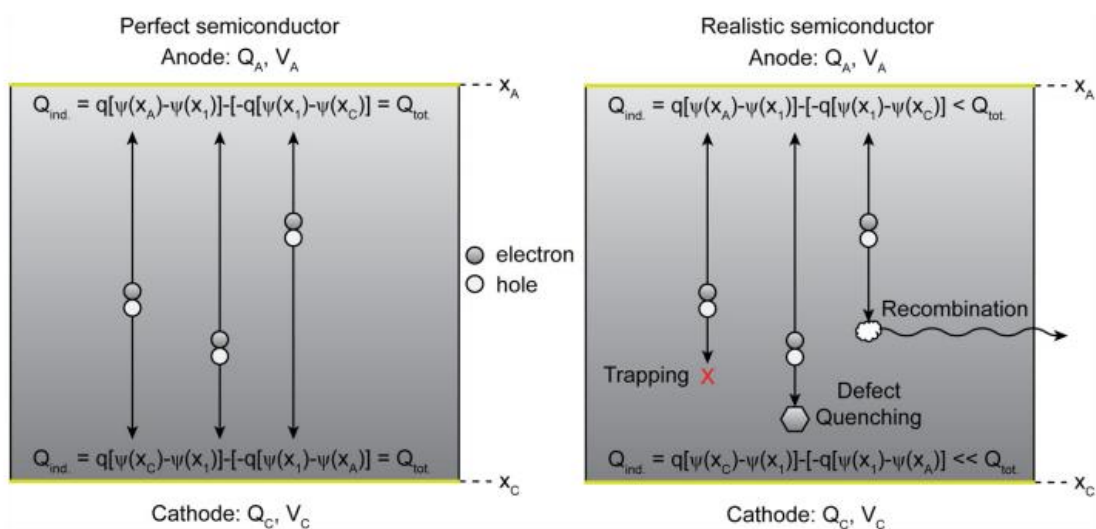


Figure 4. The comparison of a perfect semiconductor compared to a realistic semiconductor. Trapping, defects and impurities can reduce the overall number of charge carrier yielding poorly performing material. Adapted from Reference 5.

In summary, semiconductors are a ripe area for implementation in radiation detection relative to their more commercially distributed scintillators. They can directly convert incoming incident radiation into charge carriers, and already demonstrate their successes with the aforementioned CZT and HPGGe. That being clear, not every synthesized semiconductor is applicable to radiation detection nor is a given high purity element. Despite the success of CZT and HPGGe (which have their own implicit difficulties), the field of semiconductor radiation detection is constantly evolving as new materials are being developed and optimized. The goal is a cheap, durable, readily synthesizable material that can spectrally resolve hard radiation at room temperature. This development is governed by strict list of requirements implicit to semiconductor radiation detectors that go beyond the photovoltaic effect.

1.2. Principles of Optoelectronic Semiconductor Design for Radiation Detection

When conceptualizing a possible semiconductor that would be applicable for radiation detection there are certain conditions that the material must possess for room temperature applications.^{5,6} In this exploratory investigation of new materials for semiconductor detectors, the following inherent conditions were considered during experimental development.

1. High density, ρ
2. High Average Atomic Number, Z
3. The Band Gap, E_g , must be between 1.6 – 3.0 eV
4. High Resistance to applied Bias, Resistivity ρ
5. High mobility-lifetime product, $\mu\tau$

1.2.1. Design with Regard Density and Composition

For a semiconductor detector to function well, incident high energy photons must be captured by the material for electrons to be excited. To optimize this, semiconductors that are being developed usually target compositions that retain high densities and higher average values of Z . This is due to the stopping power, the absorption efficiency of hard radiation, scaling with higher density and Z for a material. For lighter, less dense materials the length of the detector needs to be longer for sufficient absorption to occur, which is particularly true in the case of HPGc ($\rho = 5.32 \text{ g/cm}^3$ and $z = 32$) where detectors need to be on the orders of tens of centimeters thick in order to adequately absorb incident high energy photons. Conversely, example materials CZT and HgI₂ which have densities of 5.86 and 6.30 g/cm^3 respectively have effective Z values of ~ 50 and 55.3 require far less detector length to achieve spectroscopic resolution.⁶ Due to this, heavier elements which high Z values are most often considered for room temperature radiation detectors. Additionally, the elements selected for a possible detector material need to be selected to be either d^0 or d^{10} such that no additional $d-d$ absorption events can occur separate from a photovoltaic effect. Within these constraints, the metals, chalcogenides, and halides most often selected for semiconductor detectors as highlighted in Figure 5 in red.

Group Period	1	2	3	4	5	6	7	8	9	10	11	12	13	14	15	16	17	18
1	1 H																	2 He
2	3 Li	4 Be											5 B	6 C	7 N	8 O	9 F	10 Ne
3	11 Na	12 Mg											13 Al	14 Si	15 P	16 S	17 Cl	18 Ar
4	19 K	20 Ca	21 Sc	22 Ti	23 V	24 Cr	25 Mn	26 Fe	27 Co	28 Ni	29 Cu	30 Zn	31 Ga	32 Ge	33 As	34 Se	35 Br	36 Kr
5	37 Rb	38 Sr	39 Y	40 Zr	41 Nb	42 Mo	43 Tc	44 Ru	45 Rh	46 Pd	47 Ag	48 Cd	49 In	50 Sn	51 Sb	52 Te	53 I	54 Xe
6	55 Cs	56 Ba	57 La *	72 Hf	73 Ta	74 W	75 Re	76 Os	77 Ir	78 Pt	79 Au	80 Hg	81 Tl	82 Pb	83 Bi	84 Po	85 At	86 Rn
7	87 Fr	88 Ra	89 Ac *	104 Rf	105 Db	106 Sg	107 Bh	108 Hs	109 Mt	110 Ds	111 Rg	112 Cn	113 Nh	114 Fl	115 Mc	116 Lv	117 Ts	118 Og

Figure 5. Regions of the Periodic table highlighted in red. These regions are those that semiconductor detectors typically developed from.

1.2.2. Design with Regard to the Band Gap, Eg

As noted above, materials that considered useful for room temperature radiation must have a bandgap between the range of 1.6 – 3.0 eV. This usually puts detector materials in the range of optically observable band gaps as a gap of 1.6 eV induces a black color in a solid. As we increase this value the observed color ranges from black, to red, orange, yellow, and finally colorless above 3.0 eV. At room temperature, thermal energy in addition to light is able to promote electrons within a given material. This additional current leads to a loss of spectroscopic ability, however, if the band gap is sufficiently large thermal conduction is mitigated and the material more applicable for use. While HPCGe has been discussed as a state-of-the-art detector solution, its major downside is the band gap of 0.67 eV which engenders too much thermally stimulated current at room temperature. Due to this, HPCGe detectors are require cryogenic cooling to mitigate this inherently small bandgap and this undermines their ability to be used as readily portable detector systems.

When considering what compositions to explore, it is critical to assess what the resultant band gap might be from other similar reported systems in the literature.

1.2.3. Design with Regard to Resistivity, ρ

The relative resistance of a semiconductor detector also needs to be high such that when bias is applied across the material the resultant leakage current is low. This is necessary as the generated charge carriers from an incident high energy photon can generate a significant amount of current relative to the baseline conduction at high bias. A resistivity value of at least 10^8 ohm-cm is generally regarded as the baseline resistance for an applicable material for radiation detection. For example, CZT detectors generally have resistivity values of 10^9 - 10^{10} ohm-cm.⁵ While this is an important factor in material development, it generally is found post synthesis and is highly dependent on composition, defects, and impurities. Values of similar semiconductor systems are referenced when conceptualizing a new avenue of investigation because this value is

1.2.4. Design with Regard to Mobility-Lifetime Product, $\mu\tau$

As noted in section 1.1, the mobility-lifetime product is a significant factor in the operation of any semiconductor detector. However, akin to the value of resistivity, this property is inherent to the material and is measured post-synthesis while also being affected composition, defects, and impurities. While $\mu\tau$ is important for optimization, development, and application of a material, in terms of the design and synthesis of new semiconductor materials it serves as a driving motivation rather than a targetable result.

1.3. Structure and Properties of Semiconducting Heavy Metal Halides

1.3.1. Justification for Halide-Based Room Temperature Semiconductor Detectors

Due the requirements of high Z , the chalcogenides and halides are often used as counter ions for the heavy metals that engender the high effective Z values. This is clear in CZT, where the heaviest possible chalcogenide Te has been used. However, as much as CZT has been implemented and commercialized it suffers from several implicit inefficiencies and cost-raising issues. The structural nature of CdTe which has a predisposition to structural defects such as secondary phase precipitation of tellurium, variable composition with the addition Zn, dislocations, twins, and grain boundaries.^{5, 7-9} These issues stem from the highly symmetric nature of the 3D zinc blende (sphalerite) crystal structure (Figure 6) which is only contains two distinct tetrahedral crystallographic sites for Cd, Zn, and Te. While the presence of these implicit defects has been mitigated over time, this still requires CZT to be grown in large ingots so defect-poor regions to be harvested for secondary processing and application which further increase cost.¹⁰ Further, the use of tellurium as the basis of the semiconductor increases the cost of the material dramatically considering its low overall natural occurrence.¹¹

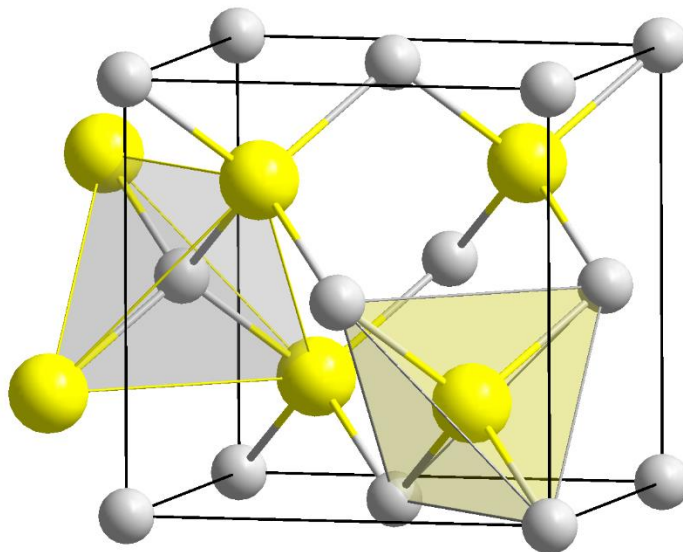


Figure 6. The Zinc-Blende (sphalerite) crystal structure of CZT. The high symmetry and its relation to the similar wurtzite structure promote the formation of structural and compositional defects in CZT crystals.

Due to the overall costs associated with CZT, semiconductors based on the halides have been of recurring interest due to their diverse structural chemistry, appropriate densities, Z values, moderate band gaps, applicable resistivity, and high values of $\mu\tau$ as discussed further in sections **1.3.1 – 1.3.4**.¹² Further, halide semiconductors have already been demonstrated their ability to act as spectroscopic hard radiation detectors.⁵ The development of these known systems and the search for new phases demonstrates a continued effort towards greater material understanding and discovery. In the following sections the structures, properties, benefits and deficits of a selection of promising halide semiconductors will be discussed. This is to provide a foundation for which to understand the exploratory nature of the research and results contained within this dissertation.

1.3.2. The Binary Heavy Metal Halides

The simplest heavy metal halides respective to their composition are the binary halides which have been well studied. In particular, the 2D iodides α -HgI₂^{2, 13-15}, PbI₂^{16, 17}, BiI₃¹⁸⁻²⁰, InI^{21, 22} have been investigated for more than twenty years. One exception to this is the bromide containing 3D TlBr which has also been well characterized.^{23, 24}

α -HgI₂ is a 2D semiconductor that displays a band gap of 2.15 eV, a resistivity perpendicular to the 2D layers on the order of 10¹³ ohm-cm, and a value of $\mu\tau$ for electrons of 3 x 10⁻⁴ cm²/V.² The structure consists of layers of corner sharing HgI₄ tetrahedra which give rise to the polymeric structure of tetragonal $P4_2/nmc$ α -HgI₂ (Figure 7) which yields a high density of 6.36 g/cm³.²⁵

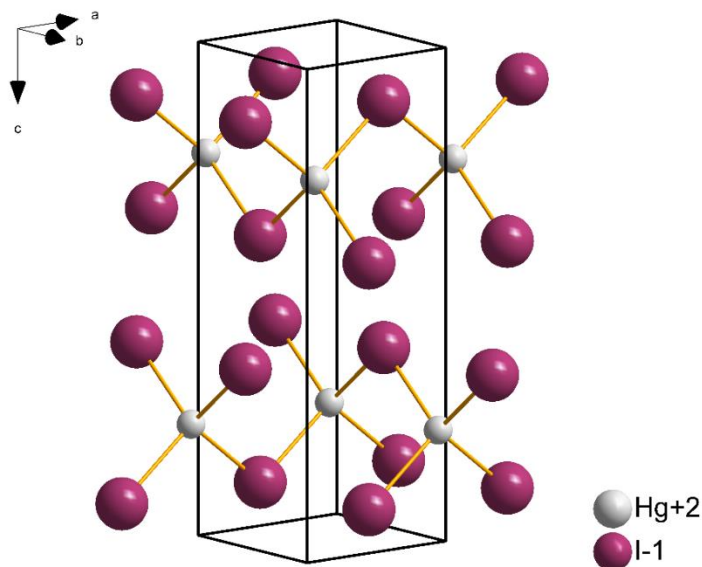


Figure 7. A ball and stick model of a unit cell of α -HgI₂ displaying the tetrahedral coordination of Hg and linear bridging coordination of I. The result is the 2D layered van der Waals material.

Further observed is the that two layers contained within the unit cell give rise to a 2D van der Waals material. Preparation of single crystals of α -HgI₂ is not as trivial as slow cooling from a melt. HgI₂ undergoes a destructive phase transition at 127 C from the orthorhombic β phase to the desirable α phase which has required a number of vapor²⁶⁻²⁸ and solution^{15, 29, 30} phase transport methods to be implemented. While HgI₂ has been praised as a possible room temperature detector, due to the nature of the van der Waals connectivity between layers it suffers from poor mechanical stability and crystal growth defects that reduce its the overall viability.^{15, 31} Despite this HgI₂ has been able to display spectroscopic response to hard radiation and is still being developed.^{5, 32, 33}

While the synthesis of HgI₂ must account for the phase transition, the closest neighbor PbI₂ does not. 2D layered PbI₂ displays a band gap of 2.32 eV with resistivity on the order of 10¹³ ohm-cm perpendicular to the layers and a higher average Z value than HgI₂. However, measured values of $\mu\tau$ are an order of magnitude less than that of HgI₂ at 1 x 10⁻⁵ cm²V⁻¹.⁵ As shown in Figure 8, PbI₂ also adopts a CdI₂-type 2D van der Waals structure in a trigonal *P-3m1* space group with corner edge sharing PbI₆ octahedral units leading to density of 6.16 g/cm³.³⁴ PbI₂ single crystals can be prepared by several methods including solution,³⁵ vapor³⁶ solid state techniques³⁷⁻³⁹ and do not undergo phase transition after crystallization at 403 C.³² As PbI₂ is also a van der Waals material this results in material instability similar to HgI₂. This manifests in a reduction the mechanical properties of the material and an increase in the possibility of defects related to crystallization.³² While the development of PbI₂ has slowed it still has still been able to display spectroscopic response to hard radiation.⁴⁰

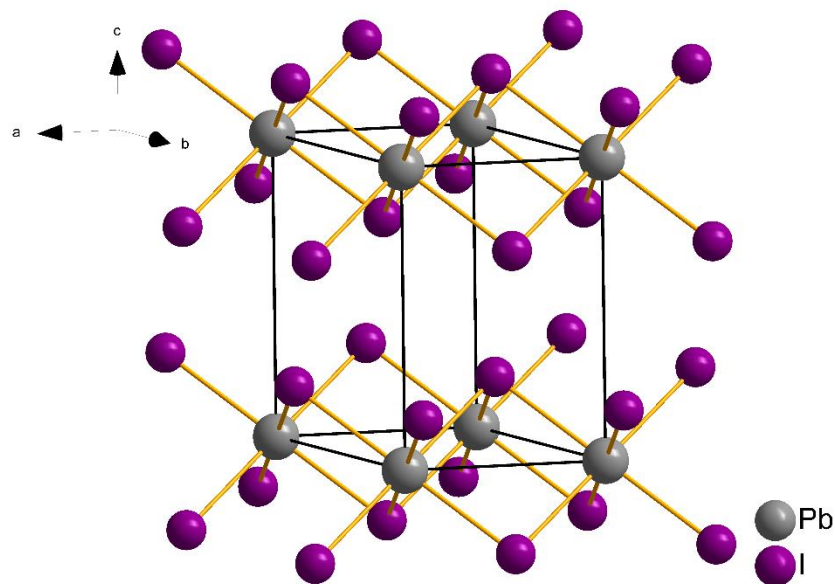


Figure 8. A ball and stick model of the unit cell of PbI_2 . The Pb atoms are octahedrally coordinated to I, which displays a trigonal prismatic coordination between adjacent Pb atoms. The result is again 2D layered a van der Waals material that does not contain implicit metal site vacancies.

Related to the 2D CdI_2 -type structure of PbI_2 , BiI_3 is another binary heavy metal semiconductor that has been of interest for semiconductor detection. BiI_3 has a band gap below that of HgI_2 and PbI_2 of 1.7 eV (though reports vary) and displays resistivity values perpendicular to the layers of up to 10^{11} ohm-cm.^{5, 19, 32, 41}. Like HgI_2 , the value of $\mu\tau$ is on the order of 1×10^{-4} cm^2V^{-1} for electrons which is promising as HgI_2 has been able to show spectroscopic responses.⁵ BiI_3 crystallizes in a hexagonal $R\bar{3}h$ space group in a vacancy moderated CdI_2 -type supercell (Figure 9).⁴² This transformation occurs when moving from divalent Pb to trivalent Bi due to the additional single charge inducing 1/3 of the metal sites with ordered vacancies to compensate (Figure 10). This is also reflected in a decrease in the density of the material at 5.78 g/cm^3 .

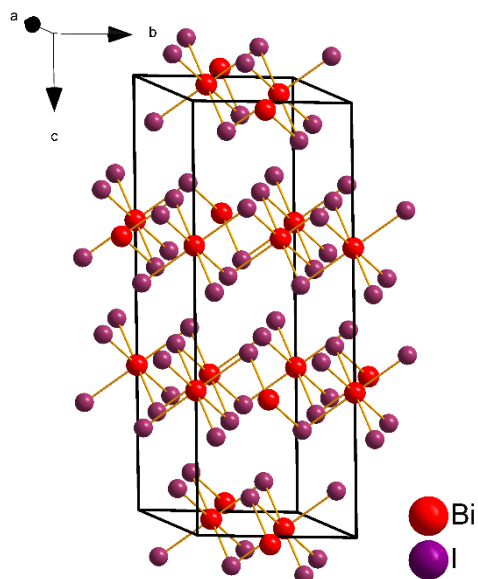


Figure 9. A ball and stick representation of the BiI_3 unit cell. Like PbI_2 , Bi atoms are all octahedral coordination to I, however I displays both trigonal prismatic coordination to Bi and bridging coordination due to the ordered vacancies. BiI_3 is a 2D van der Waals material.

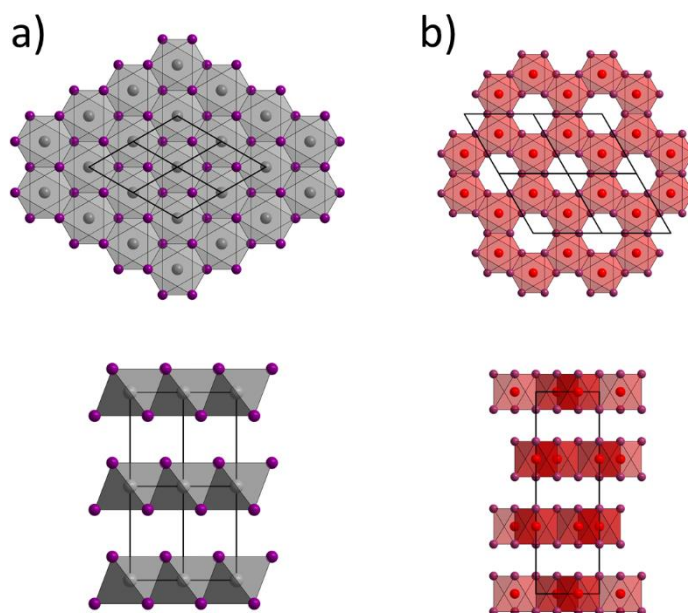


Figure 10. Supercells of a) PbI_2 and b) BiI_3 demonstrating their similar CdI_2 -type structure and the necessary vacancies that give rise to the supercell BiI_3 .

Preparations of single crystal BiI_3 are completed by vapor transport⁴³ or solid state^{19, 20} crystal growth methods which have led to spectroscopic response.⁴⁴ Like the other 2D van der Waals materials, BiI_3 also suffers from structural defects during crystallization which have to be mitigated to improve material performance. Currently superheating of the melt has been found to reduce a number of structural issues related to crystallization.⁴⁵

Beyond the multivalent metals, monovalent InI and TlBr have also been investigated for possible applications. InI has a band gap of 2.0 eV with Z nearly identical to CZT and displays resistivity values of up to 10^{11} ohm-cm.⁵ Reported values for $\mu\tau$ of electrons on the order of $7 \times 10^{-5} \text{ cm}^2\text{V}^{-1}$ indicating a need for is ongoing optimization.^{21, 22, 46} InI crystallizes in another 2D layered structure type that is analogous to the orthorhombic $Cmcm$ unit cell of TlI (Figure 11), with a density of 5.39 g/cm^3 .⁴⁷ In the previously discussed binaries corner and edge sharing polyhedral connectivity gave rise to the 2D structure. In the case of InI In and I both display 5 coordinate geometry that arises from the alternating ordered packing of InI in the material and not from well-defined polyhedra. Despite the 2D nature of InI, ingots can be mechanically processed without significant damage to the material which is promising if the optoelectronic properties can be optimized.

Of the heavy metal binaries discussed only one, TlBr, displays a 3D crystal structure. TlBr has a band gap of 2.68 eV with resistivity on the order of 10^{10} ohm-cm and reported $\mu\tau$ for electrons of $3 \times 10^{-3} \text{ cm}^2\text{V}^{-1}$.⁵ Of the discussed binaries TlBr also the lowest average Z value due to Br, at 58.5. The crystal structure of TlBr is analogous to CsCl as shown in Figure 12 with a density of 7.56 g/cm^3 .⁴⁸ While TlBr displays three dimensional connectivity without the formation of van der Waals layers, the material is soft and defects can be engendered during processing which requires

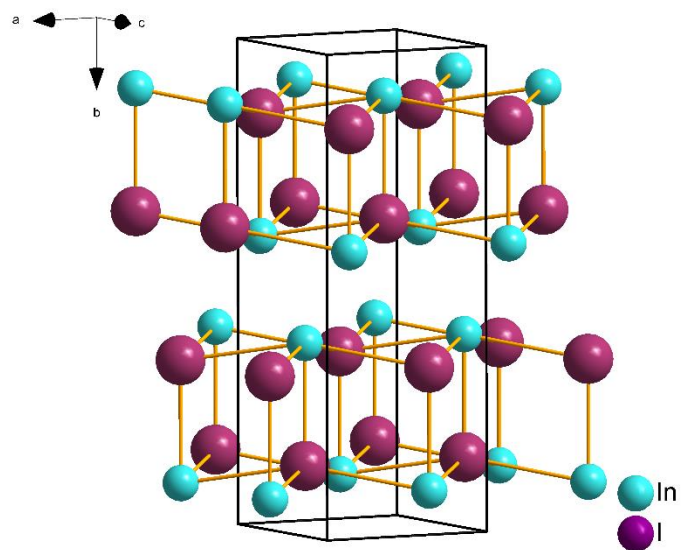


Figure 11. A ball and stick representation of the unit cell of InI. The alternating ordered packing of InI yields 5 coordinate geometry for both elements. As shown, InI is a 2D van der Waals material.

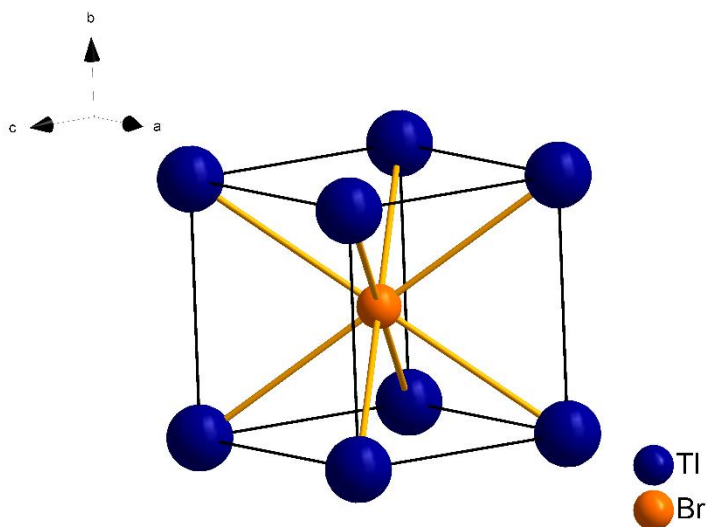


Figure 12. The simple 3D CsCl-type unit cell of TlBr. Both Tl and Br are 8 coordinate.

greater care when preparing samples.³² Fortunately this has not hindered the spectroscopic response of TlBr to hard radiation and continued optimization of the material.^{49, 50} However due to the inherent ionic conductivity and polarization in TlBr, detector performance degrades over time leading to cooling and contact engineering being implemented to mitigate these effects.^{32, 41}

The heavy metal halide binaries demonstrate that for the simpler compounds the favorable properties that promote detector performance, such as high density, Z , resistivity, and moderate band gaps, are undercut by the structures and mechanical properties of the material. While this hurdle can be overcome with improvements to synthesis and processing, the binary heavy metal halides still lack structural diversity and greater bonding due to their simplicity. While adding additional complexity does not directly imply better implicit properties, the development of ternary heavy metal halide semiconductors demonstrates their significant value.

1.3.3. Ternary Heavy Metal Halide Semiconductors

Ternary heavy metal halide semiconductors can be separated into two classes. One is the development of new semiconductors that are inspired by the perovskite crystal structure and its derivatives (which is discussed heavily in **1.3.4**). The other is those that are not. For the non-perovskite-based materials there are very few with only halides as the anion. These include Tl_4CdI_6 ^{51, 52} and Tl_4HgI_6 ^{53, 54} and TlSn_2I_5 ⁵⁵ whose structures are displayed in Figures 13 and 14. Both the 0D Tl_4CdI_6 and Tl_4HgI_6 compounds crystallize in the tetragonal unit cell where $[\text{MI}_6]^{4-}$ octahedra are charge balanced by large Tl^+ counterions leading to no interconnectivity between the bonding metals through the present halides. Their respective densities are 6.87 g/cm^3 and 7.15 g/cm^3 for the Cd and Hg analogs. For TlSn_2I_5 the structure is also tetragonal and displays layers of $[\text{Sn}_2\text{I}_5]^-$ charge balanced Tl located between them. Sn is seven coordinate and is connected between

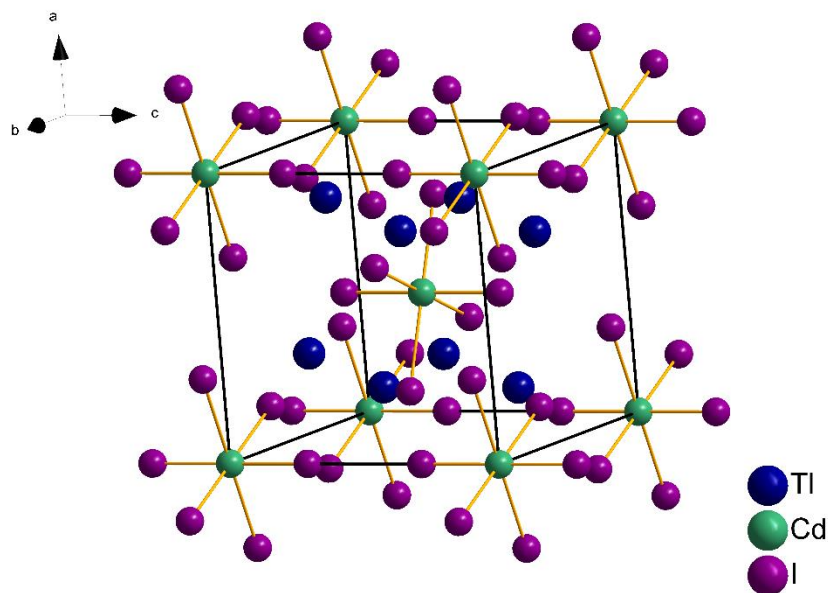


Figure 13. A ball and stick representation of the unit cell of Tl_4CdI_6 . Tl_4HgI_6 displays an analogous structure. $[\text{MI}_6]^{4-}$ octahedra are charge balanced by large Tl^+ counterions leading to a 0D structure.

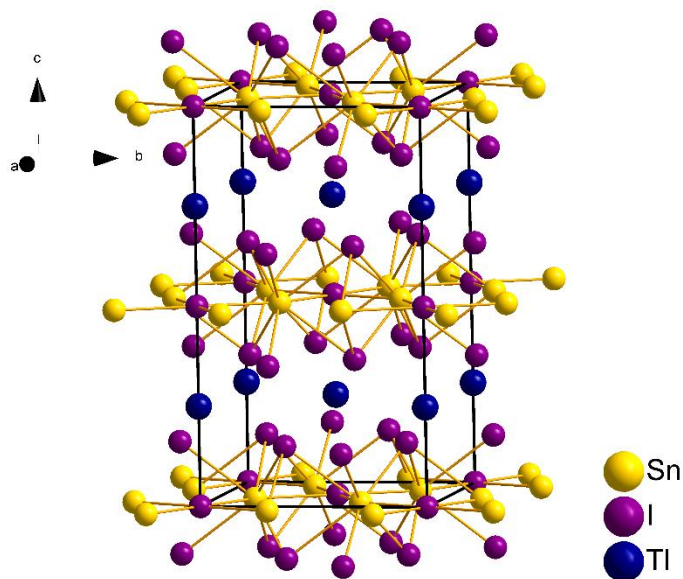


Figure 14. A ball and stick representation of the unit cell of TlSn_2I_5 . The layers of $[\text{Sn}_2\text{I}_5]^-$ are charge balanced Tl^+ located between them leading to a 2D structure.

square planar iodine atoms and distorted trigonal prismatic bridging iodine atoms. Despite the use of Sn the resultant density of 6.05 g/cm^3 is still significant due to Tl.

Of these three purely halide semiconductors they display band gaps of 2.14 eV, 2.15 eV, and 2.8 eV for TlSn_2I_5 , Tl_4HgI_6 , and Tl_4CdI_6 respectively. Their values of resistivity are all in the range of $10^{10-11} \text{ ohm-cm}$ with $\mu\tau$ of electrons on the scale of $10^{-3-4} \text{ cm}^2\text{V}^{-1}$, the best being for TlSn_2I_5 . While having the most favorable $\mu\tau$, TlSn_2I_5 does not display spectroscopic response to hard radiation while both Tl_4HgI_6 , and Tl_4CdI_6 do. Of these materials only the Cd and Sn based materials remain under recent development.⁵

While not under the scope of this dissertation, the promising chalcogenide based detector materials should be mentioned as they are important to the development in this field. These materials contain both chalcogenide and halide anions and conform well to the design parameters as outlined in section 1.2. Successful examples of these materials are the mercury chalcogenides $\text{Hg}_3\text{Q}_2\text{X}_2$ (Q = S, Se, Te; X = Cl, Br, I),⁵⁶⁻⁵⁸ thallium chalcogenides TlQI (Q = S, Se),^{59, 60} SbSeI ,⁶¹ and $\text{Cu}_2\text{I}_2\text{Se}_6$.⁶² These materials display a wealth of new structural chemistry over a range of dimensionalities. The use of the chalcogenide in addition to the halide adds an additional parameter for material design, further allowing material tuning.

1.3.4. The Structure and Properties of Halide Perovskites

The AMX_3 perovskites have been a very promising class of ternary heavy metal halide semiconductors and have been on the forefront of development for photovoltaic applications.^{63, 64} They have also been of interest for application in radiation detection due to their ability to engender all the properties laid out in 1.2, and have already been shown to be able detect and resolve incident

hard radiation.⁶⁵⁻⁶⁸ These recent developments have driven the halide perovskites to the forefront of material research and offer inspiration to investigate not only the pure perovskite structures, but their derivatives as well.

The 3D perovskite crystal structure was first discovered in 1926 for ternary oxide CaTiO_3 and is shown in Figure 15.^{69, 70} The oxide perovskites were designated ABO_3 where B was a tetravalent transition metal and A a divalent alkaline earth metal. For the halides, we can generalize to AMX_3 where A is a monovalent alkali earth metal or organic cation, M a divalent main group metal, and X a corresponding halide. The structure consists of corner sharing MX_6 octahedra forming voids at which the 12 coordinate A site cation balances the charge. Of the AMX_3

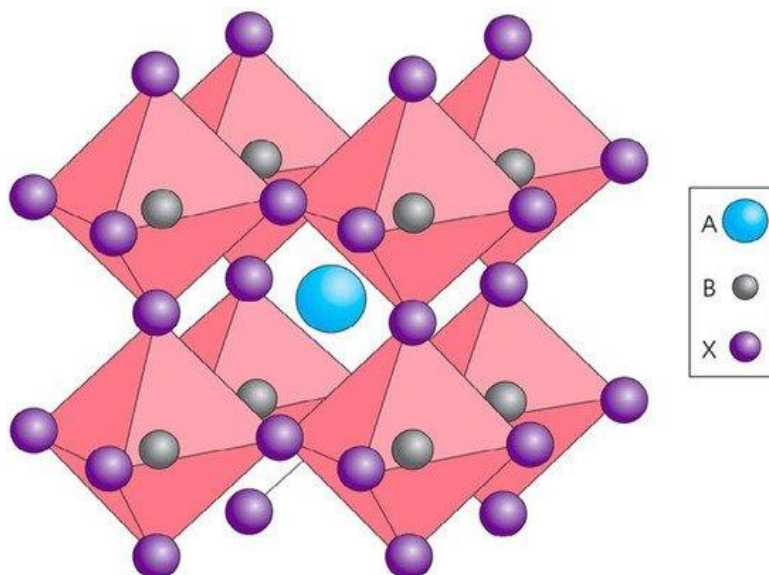


Figure 15. Polyhedral representation of the structure of the 3D halide perovskites as adapted from Reference 70. Metal halide octahedra are corner sharing in all directions that lead to 12 coordinate cation A sites. This results in a 3D structure.

compounds that are 3D a tolerance factor has been determined that predicts the viability of the formation of given the radii of the given A, M and X components.^{71, 72} As of this time, the most common components in both 3D hybrid organic and inorganic halide perovskites are A = Cs, methylammonium (MA, CH₃NH₃⁺), formamidinium (FA, HC(NH₂)₂⁺); M = Ge, Sn, Pb; X = Cl, Br, I. As discussed in section 1.2, sufficient Z and density is important for material application in semiconductor detection. As a result, the focus on the 3D perovskites has been towards MAPbI₃, FAPbI₃, and CsPbBr₃ and their derivatives.

MAPbI₃ and FAPbI₃ have both been identified as promising candidates for applications in semiconductor detection applications due to their applicable bandgaps and high values of $\mu\tau$. Both materials display band gaps between 1.4-1.5 eV to mitigate some thermally stimulated dark current.⁷³ This band gap has been shown to be highly tunable by anion composition.^{74, 75} Additionally, the higher density and Z engendered by Pb and I increases the stopping power and decreases the required crystal size, with densities for both cations approximately 4 g/cm³. Most importantly, the favorable electronic properties and defect tolerance of the iodide halide perovskites lead to high mobilities for generated carrier and long lifetimes.⁷⁶⁻⁷⁸ This combination leads to values of $\mu\tau$ for electrons on the order of 10⁻² cm²V⁻¹ which is higher than that of other applicable materials.⁵ As a result both MAPbI₃^{67, 79} and FAPbI₃^{80, 81} have been shown to be able to detect or spectrally resolve gamma ray energy photons. This is despite the lower resistivity values of each material, 10⁸-10⁹ ohm-cm and 10⁶-10⁹ ohm-cm for MAPbI₃ and FAPbI₃ respectively.⁵ Crystals of detector quality can also be easily grown from a number of different methods,⁸² most advantageously inverse temperature crystallization.^{66, 80} Unfortunately, despite the positive

qualities of the hybrid-organic lead iodides for radiation detection they suffer from stability issues⁸³ and the environmental factors of developing semiconductor devices based on toxic lead.⁸⁴

CsPbBr₃, while not containing the heaviest of the halides iodine, has been demonstrated to be a robust semiconductor detector for hard radiation detection.^{79, 85} However, this is mitigated by the use of Cs instead of the organic cation which aids in the retainment of high Z. The density of 4.84 g/cm³ for CsPbBr₃ is lower than that of the 2D heavy metals and non-perovskite ternary materials, but benefits from the purely inorganic character of the material. The inclusion of an inorganic cation further increases the relative resistivity to 10⁹-10¹¹ ohm-cm allowing for greater bias application, which is further aided by the 2.25 eV band gap to reduce thermal noise.⁵ As with the hybrid perovskites this is also tunable.⁸⁶ The resultant optimized CsPbBr₃ material has a $\mu\tau$ value on the order of 10⁻³ cm²V⁻¹. CsPbBr₃ benefits from the defect tolerance⁸⁷ and carrier lifetimes⁷⁹ as the other hybrid inorganic-organic lead halides. A further advantage is that the hybrid inorganic-organic lead halides suffer from stability issues due to the organic cations,^{73, 88} while CsPbBr₃ does not.^{79, 89, 90} It should be noted that the iodide CsPbI₃, does not exist in the perovskite structure at room temperature and instead undergoes a destructive phase transition which undercuts the viability of the compound.⁷³

A more recent development on the 3D halide perovskites has been the synthesis and study of the quaternary double perovskites, A₂M'M''X₆ where A = alkali metal; M' = an octahedral monovalent metal; M'' = an octahedral trivalent metal; X= Cl, Br I.^{91, 92} These perovskite materials aim to replace lead with non-toxic elements, the noble metals, antimony and bismuth, by inducing charge stability though alternating monovalent and trivalent cations. This removes the need for pure divalent Pb.

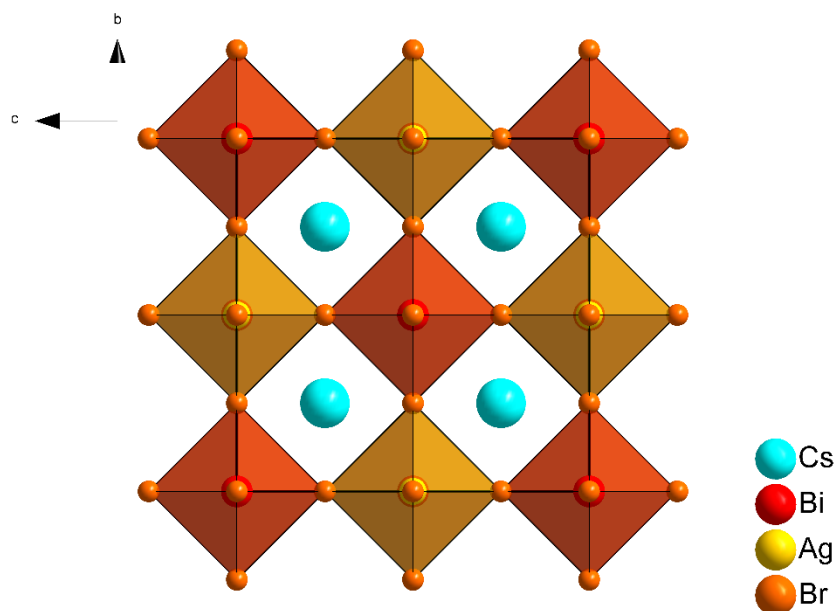


Figure 16. A representation of the unit cell of the double perovskite $\text{Cs}_2\text{AgBiBr}_6$.⁹³ Alternating Ag^+ and Bi^{3+} occupancy on the metal sites leads to charge compensation to form the perovskite structure.

As of this moment, $\text{Cs}_2\text{AgBiBr}_6$ has been the most readily synthesized double perovskite (Figure 16) with alternating AgBr_6 and BiBr_6 octahedra charge balanced by Cs^+ .⁹³ While the material has not been shown to be spectroscopically developed for radiation detection, it has been shown to engender similar defect tolerance and carrier lifetimes to that of the lead based perovskites.^{94, 95} While these materials do not specifically fit within the category of ternary semiconducting halides, they are a developing feature of perovskite chemistry that needs to be accounted for. These materials serve as additional starting points in the development of perovskite and non-perovskite exploratory chemistry.

1.3.5 Lower Dimensionality Derivatives of the Perovskites

Beyond the AMX_3 perovskites there exist related structural families that have been shown to be of interest as for their structural, electronic, and compositional features. The dominant feature in these materials is that the divalent lead cation has been substituted for either a trivalent cation, which induces a reduction in the dimensionality of the material and the $A_3M_2X_9$ composition and reduces its relative environmental toxicity. These materials can be thought of as the defect perovskites where the additional charge on the M atom induces a compensating vacancy. This can be written as $A_3M_2V^*X_9$ where V^* is the induced vacancy.⁹⁶ At this time many $A_3M_2X_9$ compositions both hybrid organic-inorganic and fully inorganic have been investigated for solar cell applications.⁹⁷⁻¹⁰⁰ Of these materials, $A_3M_2I_9$ (A= Rb, Cs; M = Sb, Bi) have been evaluated for hard radiation detection.¹⁰¹

With implicitly high Z values from Cs and I, and the use of Sb and Bi in the $A_3M_2I_9$ (A= Rb, Cs; M = Sb, Bi) compounds have applicably high densities and stopping power.¹⁰¹ Their structures range from 2D to 0D due the size of the cation and metal ion. As shown in Figure 17a,d, $Cs_3Bi_2I_9$ develops a 0D molecular structure that contains $[Bi_2I_9]^{2-}$ units are charge balanced by Cs cations. Contrary to this $Cs_3Sb_2I_9$ develops a 2D structure that persists in the a-b plane as induced by 1/3 of the metal sites becoming vacant due to the trivalent metal. As a result, the perovskite structure is dimensionally reduced. $Cs_3Sb_2I_9$ is well ordered (Figure 17b,e), as opposed to both $Rb_3Sb_2I_9$ and $Rb_3Bi_2I_9$, where structure an analogous 2D system but the Rb disorder and irregular coordination between MI_6 octahedra yield greater disorder and reduced symmetry (Figure 17d,f). Unfortunately these materials all have values of $\mu\tau$ on the order of 10^{-5} to 10^{-6} cm^2V^{-1} which limits their viability for further development. However such skepticism at their future applicability can

should be taken lightly as materials such as CsPbBr_3 and MAPbI_3 were originally thought to be unsatisfactory at early in development as well.

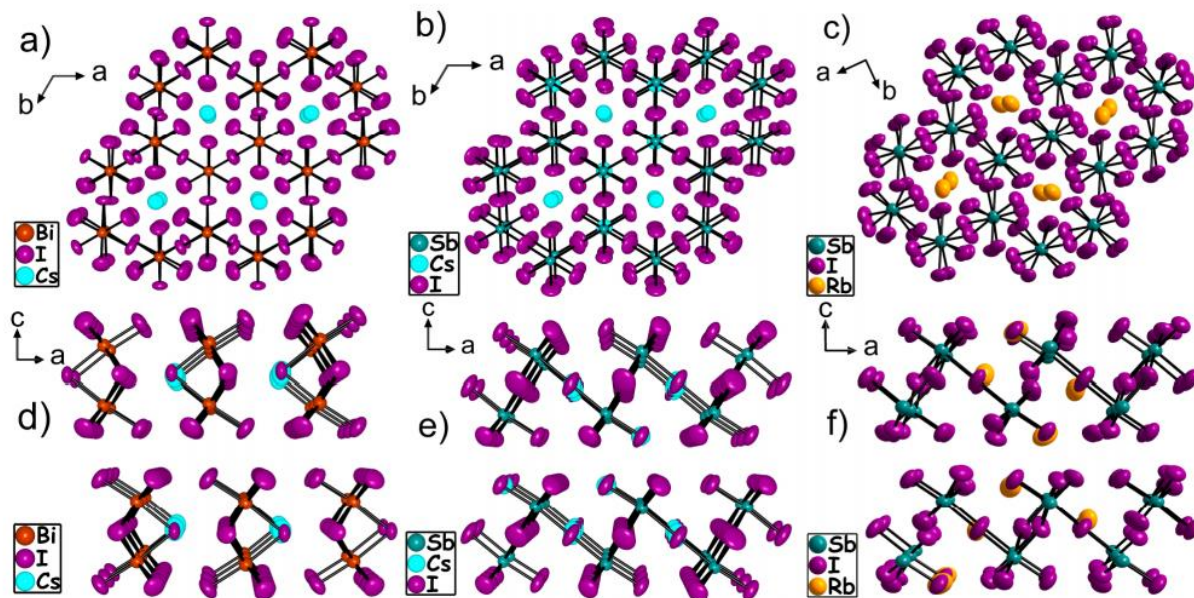


Figure 17. The ball and stick representation of the structures of 0D $\text{Cs}_3\text{Bi}_2\text{I}_9$ (a,d), 2D $\text{Cs}_3\text{Sb}_2\text{I}_9$ (b,e) and 2D $\text{Rb}_3\text{Sb}_2\text{I}_9$ (c,f). $\text{Rb}_3\text{Bi}_2\text{I}_9$ displays an analogous structure to $\text{Rb}_3\text{Sb}_2\text{I}_9$. Adapted from Reference 101.

1.4. Thesis Goal: Exploratory Approach to Greater Materials Discovery

The goal of dissertation is to demonstrate the value of exploratory chemistry using the foundations laid out in sections 1.2 with the understanding of heavy metal halide semiconductors as discussed in section 1.3 to discover new compounds under the design principles for semiconductor radiation detection. This focuses on the exploration of the structural features of the 2D and 3D halide semiconductors, their mixtures, and substitution on given metal sites for new materials and new property discovery.

1.5. Thesis Outline

The content of this dissertation is broken up into seven chapters. Chapter One introduces the concepts of semiconductors, their application in radiation detection, design principles, and a discussion of developed and developing radiation semiconductor materials.

Chapter Two demonstrates the unconventional conductance switching properties of mixtures of the well-known radiation semiconductors PbI_2 and BiI_3 . Initially synthesized in an attempt to mitigate the van der Waals nature of the two materials $(\text{PbI}_2)_{1-x}(\text{BiI}_3)_x$ demonstrates nanoscale phase separation and phase integration that leads to novel memory-like electronic effects. This chapter describes the exhaustive structural and electronic characterization of the material to understand the origins of the transport behavior in $(\text{PbI}_2)_{1-x}(\text{BiI}_3)_x$.

Chapter Three expands on the discussion of $(\text{PbI}_2)_{1-x}(\text{BiI}_3)_x$ mixtures to examine the unconventional, nonlinear optical properties observed. These properties, separate from those described in chapter two, arise from phase integration between Pb and Bi rich phases which promotes low energy absorption. This hypothesis is supported by DFT and subsequent structural analysis.

Chapter Four demonstrates an effort to add additional order into mixtures of MI_2 ($\text{M} = \text{Cd}, \text{Pb}$) and BiI_3 with the addition of CuI . This study was inspired by the examination of the ternary $\text{A}_3\text{M}_2\text{X}_9$ compounds, the double perovskites, as well as the lack of many Cu containing quaternary heavy metal halides. The results show that for the CuMBiI_6 ($\text{M} = \text{Cd}, \text{Pb}$) the Cd compound readily forms a 3D defect-spinel type structure and the Pb forms a phase akin to the Ag – Bi – I system. Both of these compounds display nonlinear Cu ion conductivity when under bias.

Chapter five elaborates on our attempt to substitute Au onto the A site in APbI_3 compounds. We instead find that Au^{1+} disproportionates in situ leading to self-reduction and the formation of the remarkable 3D triclinic $\text{Au}^{3+}\text{Pb}_2\text{I}_7$ compound. This new material forms only on the surface of recrystallized PbI_2 and displays that the a square planar $[\text{AuI}_4]^{1-}$ subunit dominates the band gap acting as a chromophore.

Overall, this dissertation demonstrates that that from an exploratory perspective there can be greater developments in known systems by mixture or stoichiometric substitution. Here the results uncover completely new properties beyond application for semiconductor detectors (despite the preliminary results in chapter six). Beyond this, we can hypothesize that inspiration from this targeted, yet fundamental approach to exploratory synthesis can serve broader applicability in fields beyond that of heavy metal semiconductor synthesis.

Chapter 2

Controllable Nonclassical Conductance Switching in Nanoscale Phase Separated $(\text{PbI}_2)_{1-x}(\text{BiI}_3)_x$ Layered Crystals

2.1. Abstract

Lead and bismuth halides are impacting a variety of photovoltaic, light emission and radiation detection applications. Here we report the 2D materials $(\text{PbI}_2)_{1-x}(\text{BiI}_3)_x$, exhibit a nonlinear dependence in structural and charge transport properties beyond those anticipated from the combination of PbI_2 and BiI_3 binaries. The layered $(\text{PbI}_2)_{1-x}(\text{BiI}_3)_x$ crystals demonstrate both phase integration and phase boundary separation which lead to new electronic properties. Phase integration yields a deceptive structural features while phase boundary formation leads to a new type of robust and reproducible conductance switching behavior. We observe this conductance switching behavior as large peaks in current during current-voltage (I-V) measurements when the voltage is swept between ± 100 V along the stacking c axis of the 2D material. We use temperature and time dependent electrical measurements to show that the behavior is attributed to ionic transport perpendicular to the layers. High resolution transmission electron microscopy (HRTEM) reveals that the true structure of $(\text{PbI}_2)_{1-x}(\text{BiI}_3)_x$ is not a single phase but rather a “brick wall” of two phases, one Pb-rich and one Bi-rich. These brick-in-a-way like features are 10s nm to a side and we posit that the ion transport of iodide at the interfaces of these regions is responsible for the conductance switching action we observe.

Portions of this chapter will appear in the upcoming publication:

G. C. B. Alexander, H. J. Jung, P. W. Krantz, [§]G. Trimarchi, K. M. McCall, S. Davis, Y. Xu, B. W. Wessels, V. P. Dravid, V. Chandrasekhar, M. G. Kanatzidis. “Controllable Nonclassical Conductance Switching in Nanoscale Phase Separated $(\text{PbI}_2)_{1-x}(\text{BiI}_3)_x$ Layered Crystals ” (In preparation)

2.2. Introduction

Perovskite halide semiconductors have sparked a growing interest in understanding their structural chemistry, optoelectronic properties, and potential uses in various electronic devices including hard and soft radiation detection.^{63, 79, 85, 97, 101, 102} Ion migration is now a well-documented and characteristic feature of most perovskite halides that derives from the highly dynamic and disordered nature of the structures at room temperature.¹⁰³⁻¹⁰⁵ The mobile ions are generally the halides and are responsible for a number of phenomena such as hysteretic behavior in solar cells^{106, 107}, light induced lattice expansion^{108, 109}, environmental instability^{110, 111}, light induced phase separation in mixed I/Br systems and others.^{112, 113} The parent compounds of these perovskites are the binary 2D PbI_2 ($E_g = 2.3$ eV) and BiI_3 ($E_g = 1.7$ eV) which are also photoluminescent and photoconductive semiconductors have been exhaustively characterized for optoelectronic device applications properties^{6, 19, 114, 115}. PbI_2 crystallizes in the CdI_2 structure type with layers of fully edge-sharing octahedral PbI_6 units whereas BiI_3 displays an analogous structure with additional ordered vacancies to compensate for Bi being trivalent (Figures 18a and 18b). These materials exhibit more rigid and less dynamic lattices with negligible ion migration. We hypothesized that the combination of these two binaries to obtain a solid solution of $(\text{PbI}_2)_{1-x}(\text{BiI}_3)_x$ could give new structural features and the creation of coulombic frustration in the distribution of Pb^{2+} and Bi^{3+} ions because of the inability of the system to produce ordered vacancies a (Figure 18c,d).

The very few reported investigations of the $(\text{PbI}_2)_{1-x}(\text{BiI}_3)_x$ have studied X-ray diffraction, optical absorption properties and Nuclear Quadrupole Resonance spectroscopy of powder samples.¹¹⁶⁻¹¹⁸ Here we report that the $(\text{PbI}_2)_{1-x}(\text{BiI}_3)_x$ compositions exhibit unprecedented

conductance switching properties. Specifically, the I-V plots measured perpendicular to the layers show that as the material is biased it “remembers” which bias direction it was under. When exposed

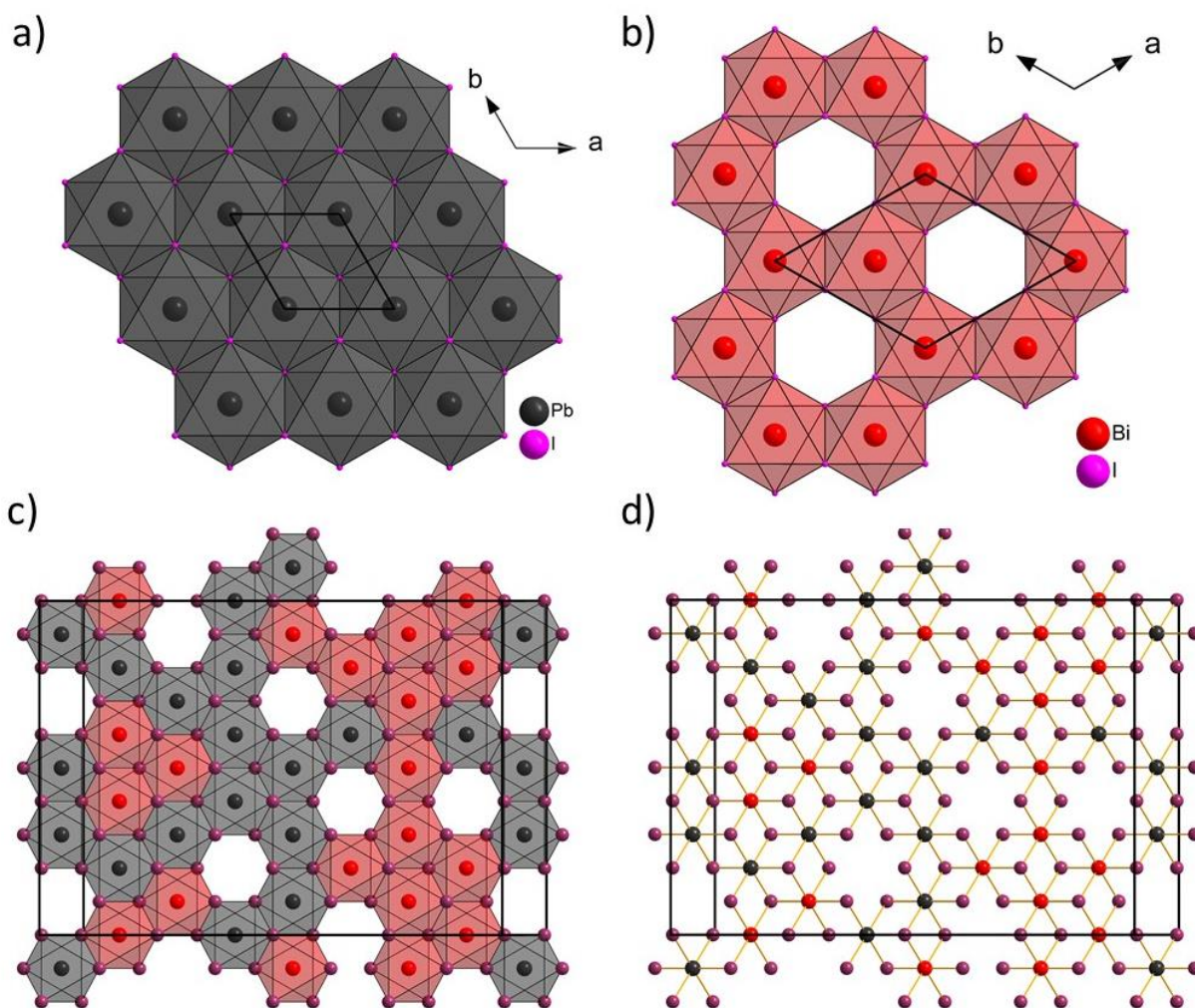


Figure 18. a) The structure of a PbI₂ layer. b) The structure of a BiI₃ layer possessing ordered vacancies. c,d) A model of (PbI₂)_{0.5}(BiI₃)_{0.5} randomly generated with a mixture of the two lattice types as represented by polyhedral and ball and stick models

to the opposite bias, we observe a significant reduction in the material's resistance that we attribute to movement of stored charge. In this sense, we reveal that $(\text{PbI}_2)_{1-x}(\text{BiI}_3)_x$ has “memory”. Beginning from synthesis we demonstrate a multi-faceted characterization approach to determining the true nature of $(\text{PbI}_2)_{1-x}(\text{BiI}_3)_x$ which is critical in understanding the ion induced charge transport and the structural properties. We find that the peculiar nanoscale separation of phases found in the 2D crystals is predominantly responsible for these properties and we propose an ion migration mechanism for the origin of the conductance switching behavior.

2.3. Materials and Methods

2.3.1. Synthesis of $(\text{PbI}_2)_{1-x}(\text{BiI}_3)_x$

Pb and Bi (99.999% American Elements) were combined with I_2 (99.99% Sigma Aldrich or Alfa Aesar) in stoichiometric ratios at the 4 mmol to 20 mmol scale of metals and sealed in 1 mm walled fused silica ampoules at or below 3×10^{-3} mbar. Due to the thickness of the tubes and the relatively large amount of molecular iodine being employed a ramp rate of 10 C / hr was used to heat samples to 500 C. Samples were held at 500 C for 10 hours and then cooled to RT at variable rates described in Table 1. Yield is 95 – 100 % based on Bi.

It should be noted that working with I_2 under solid state conditions leads to the possibility of tubes bursting due to the pressure of vaporous iodine in the tube becoming too great. For this reason, heating profiles have been designed such that slow heating yields reaction of iodine with the present metals before pressure builds.

Table 1. Furnace Profiles for $(\text{PbI}_2)_x(\text{BiI}_3)_x$ Preparations

Run Type	Start T (C)	Target T (C)	Ramp Rate (C/Hr)	Hold Time (Hr)	Ramp to (C)	Rate (C/Hr)	Ramp To (C)	Rate (C/Hr)	Ramp To (C)	Rate (C/Hr)
Initial	RT	500	10	10	30	47	N/A	N/A	N/A	N/A
Slow Cool	RT	500	10	10	300	2	30	27	N/A	N/A
Standardized	RT	500	10	10	400	50	300	1	30	27

2.3.2. Thermal Analysis

Thermal properties were determined by differential thermal analysis (DTA) conducted on a Netzsch STA 449 F3 Jupiter simultaneous thermal analysis (STA) instrument. Cleaved crystals of $(\text{PbI}_2)_{0.5}(\text{BiI}_3)_{0.5}$ were ground into a fine powder which was then loaded (approximately 50 ug) into silica ampoules and flame sealed at or below 3×10^{-3} mbar. The sample was heated to 475 °C at a rate of 10 °C/min. Heating and cooling runs were repeated to observe if the thermal behavior was replicable.

2.3.3. Structural Characterization

2.3.3.1. Powder X-ray diffraction

Samples $\text{Pb}_{0.4}\text{Bi}_{0.4}\text{I}_2$ were examined by powder diffraction using a Rigaku Miniflex power X-ray diffractometer with Ni-filtered Cu $K\alpha$ radiation operating at 30 kV and 15 mA. Scans were performed with a resolution of 0.02° and a scan rate of $10^\circ/\text{min}$. Simulated powder patterns of $(\text{PbI}_2)_{0.5}(\text{BiI}_3)_{0.5}$ were calculated using the refined room-temperature crystal structure CIF with MERCURY, part of the CSD software suite.¹¹⁹

2.3.3.2. Single Crystal X-ray Diffraction

Data collection for $(\text{PbI}_2)_{0.5}(\text{BiI}_3)_{0.5}$ was performed on a STOE IPDS II diffractometer using Mo $K\alpha$ radiation ($\lambda = 0.71073 \text{ \AA}$) operating at 50 kV and 40 mA at 293 K. Crystals were isolated from the reaction ingot and fixed to glass fibers using super glue. Data collection was performed as 1° scans in ω at from 0 to 180° an optimized ϕ angle. Integration and numerical absorption corrections were performed on each structure using X-AREA, X-RED, and X-SHAPE.¹²⁰ The structure solved by the direct method and refined on F^2 using the SHELX14 program suite.¹²¹

2.3.4. Room Temperature Electrical Property Measurements

All measurements were conducted with a Keithley 230 programmable voltage source which was externally monitored in real time by a HP 34401A multimeter. The current was measured from the same two terminal contacts by first passing the signal through an Ithico 1211 current preamplifier with a sensitivity of 10^{-7} a discrimination of 10^{-8} and a rise time of 1 second, then collecting with another HP 34401A multimeter. The signals were passed via GPIB to a computer which averaged each data point on half second intervals. The entire setup was consistent through each of the measurement types with additional channels added as needed. Leads themselves were connected to the sample with graphite paste and copper wires which were connected to the low temperature probe with silver paste. Total resistance of the external measurement setup was ~ 120 ohms, compared to the 10^7 ohms of the sample so its contribution was excluded from analysis.

The sweeps themselves were conducted via computer control with a defined sweep rate of 2400V / hr starting at zero bias. This sweep rate was selected for data clarity and was consistent across all reported measurements unless otherwise noted. For the normal I-V sweeps the sample

was swept from 0 to 100 V, immediately swept down to -100 V, then immediately swept back to 0V at which point it was allowed to dwell for some time to try and eliminate hysteretic effects. All measurements were collected with multiple runs of this sweep pattern and were checked against inverted order, with sweeps from 0 to -100 V to 100 V to 0. The direction of the sweep did not seem to matter, but fatigue was a major contributor to sample response, so measurements were always conducted with the same sequence to facilitate comparison. Data was plotted and saved in real time in the measurement program and data analysis and presentation were completed afterward using the open source QTIPlot followed by Origin 8 Pro.

2.3.5. Time Resolved Charge Collection Measurements

Relaxation measurements provide insight into the activation conditions of the large turn on current. The sample was measured on the same low temperature probe as previously described with current and voltage being measured through HP multimeters and collected in real time by a computer. For these experiments the sample was subjected to a large bias of -100V and allowed to saturate over the course of 10 min before being quickly swept to some secondary bias. The current was then monitored over time at this new bias.

2.3.6. Variable Temperature Electrical Property Measurements

Temperature Dependent I-V sweeps were completed with the same setup listed above, but in a bath of liquid nitrogen. The low temperature probe was lowered into a Dewar filled with liquid nitrogen and allowed to reach thermal equilibrium as measured by a silicon diode configured to measure down to 1.5 K and recorded with a HP 34401A multimeter. Temperature was then controlled by a resistive heater powered by a Keithley 230 programmable voltage source and a

Keepco amplifier. The sample was kept in vacuum during this time, but had the same electrical connections and contacts.

The voltage sweep described above was applied in the same pattern across multiple runs to verify results and heating hysteresis. Measurements were taken initially with steps of 10 K up from nitrogen equilibrium temperatures of 78 K. Detailed measurements were taken in steps of 5 K around the region of activation as is reported below in the Results section. After each set of low temperature runs there was also a room temperature sweep measured to ensure no damage or change to the sample.

2.3.7. TEM/STEM microscope condition and sample preparation

A Cs-corrected JEOL ARM200CF transmission electron microscope equipped with a cold field emission gun was used for STEM imaging. The microscope was operated at 200kV acceleration voltage in STEM mode. Micrographs were acquired at electron probe sizes of 8C or 9C (JEOL defined) which are measured to be 1.28 Å and 1.2 Å respectively, and a pixel dwell time of 10~15 μ s with 2048x2048 pixel² area. Utilized emission current of 8~13 μ A results in probe current range of 10~20 pA. A 40- μ m aperture was used resulting in a beam convergence semi-angle of $\alpha=27.5$ mrad. The semi-angle measuring active area to collect the ADF signal (i.e., the inner and outer radius) is 90-370 mrad. The electron dose introduced per image varied in around 1,000 ~2,000 $e/\text{\AA}^2$ depending on magnification. Micrograph was taken under spherical aberration (C3) of 0.5~1 μ m results in measured phase of 27~28 mrad. ABF images are obtained with a BF aperture of 3 mm with center beam stop producing semi-collection angle ranges in 10-23 mrad. TEM Imaging conducted done with JEOL GrandARM (or ARM300CF) TEM with a Gatan® Oneview CCD detector of large viewing area (4k x 4k pixels²) that allowed rapid

acquisition (0.1~0.2 s) with automatic drift correction. HRTEM was taken with large beam spread to limit total dose below $10 \text{ e } \text{Å}^{-2}$ in order to reduce irradiation effect. Cross-section TEM samples which reveal 2D layer stacking on [100] zone of $(\text{PbI}_2)_{1-x}(\text{BiI}_3)_x$ were prepared using FEI Helios NanoLab 600 DualBeam FIB/SEM at 30 kV Ga ion beam and the sample surface is fine-cleaned at final stage using low acceleration of 2 kV beam. Plane-view TEM samples of [001] zone were prepared and transferred on holey carbon TEM grid (Ted Pella®) by scotch-tape method (numerous detachment/peeling process using thermal tape which can release final thin 2D film above 80~100 °C).

2.4. Results and Discussion

2.4.1. Material Preparation

Samples of $(\text{PbI}_2)_{1-x}(\text{BiI}_3)_x$ were synthesized from the elemental components, Pb, Bi, and I_2 in sealed silica ampoules heated in a computer controlled furnace and is detailed above. All ingots of $(\text{PbI}_2)_{1-x}(\text{BiI}_3)_x$ were black upon removal irrespective of composition and they cleave easily to thin flakes consistent with the 2D nature of these materials (Figure 19). Initial syntheses using the elements yielded material that was relatively brittle and did not have well-formed crystals when observed by PXRD and SCXRD. The powder X-ray diffraction (PXRD) patterns of the samples (Figure 20) show peaks consistent with a layered structure namely $00l$ basal reflections but do not match the patterns of either binary PbI_2 or BiI_3 . Instead, they exhibit broad non basal hkl reflections along with very diffuse scattering indicative of disorder. Attempts to decrease the level of disorder by cooling ingots more slowly through the crystallization point of $(\text{PbI}_2)_{0.5}(\text{BiI}_3)_{0.5}$ at 371 C determined by DTA (Figure 21) did not result in less diffuse X-ray scattering. We now understand that this is due the amount of vacancy disorder and phase boundary formation in the



Figure 19. A representative ingot of $(\text{PbI}_2)_{0.5}(\text{BiI}_3)_{0.5}$ after the molten mixture is slowly cooled. Large crystalline regions can be cleaved from these samples for charge transport measurements.

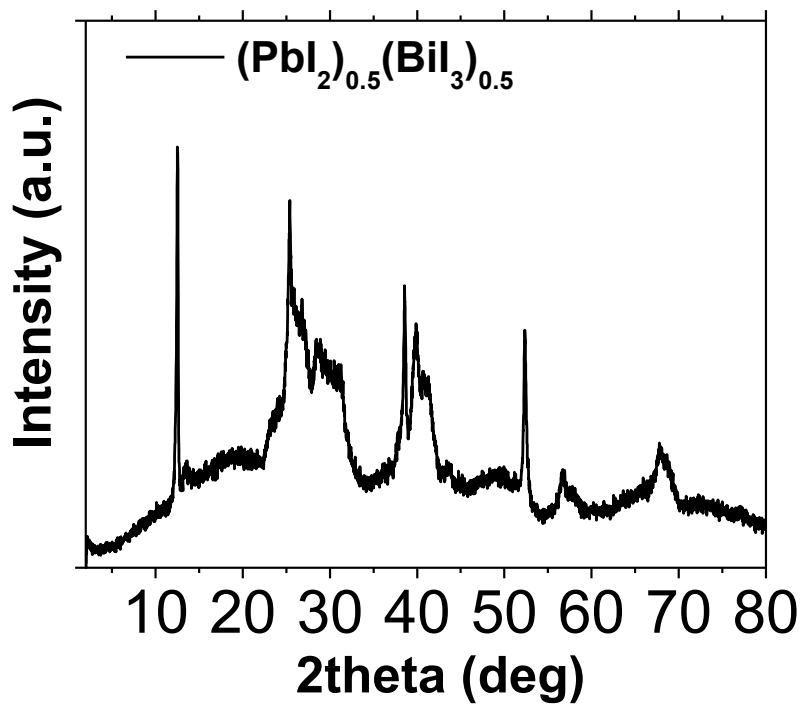


Figure 20. Powder diffraction patterns of $(\text{PbI}_2)_{0.5}(\text{BiI}_3)_{0.5}$ samples demonstrating well defined interplanar $00l$ Bragg peaks as well as diffuse scattering in both samples.

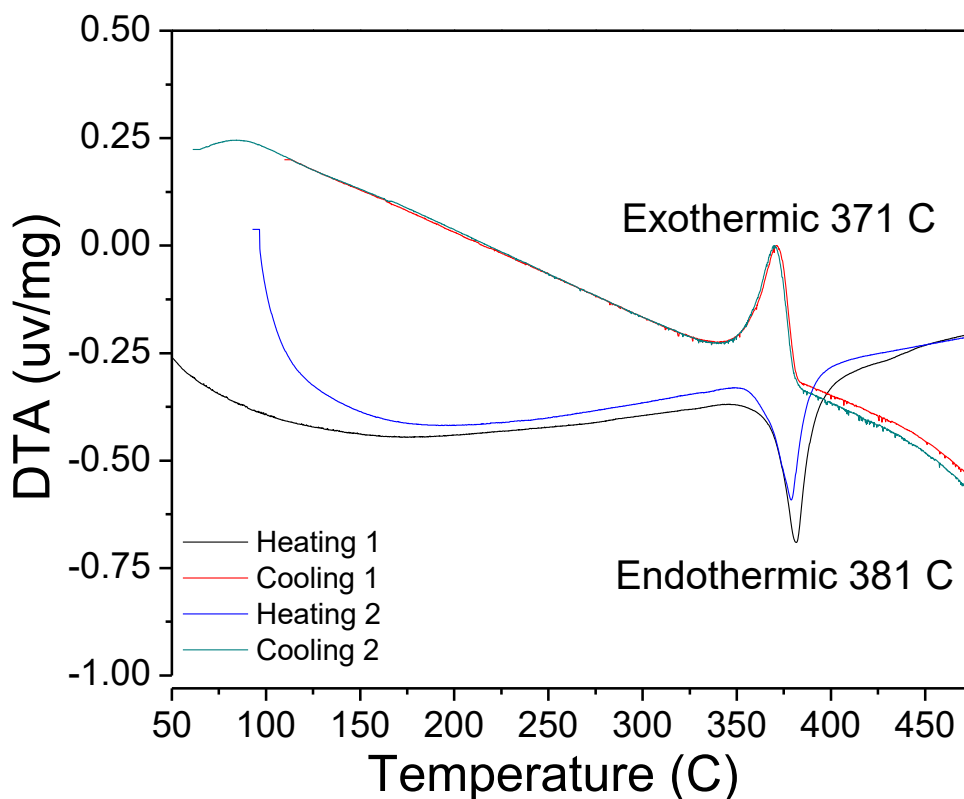


Figure 21. DTA of $(\text{PbI}_2)_{0.5}(\text{BiI}_3)_{0.5}$ noting that when the binaries are combined the resultant mixture has an apparent melting point of 381 C, nearly 25 C both parent compounds. The overlapping peaks in the exothermic curve demonstrate that the mixture is congruently melting. It was from these thermal analysis data we designed the standardized cooling regime for all future samples of mixed stoichiometry.

material discussed in section 2.4.3. Additionally, no strictly ordered phases were observed, contrary to Dmitriev et al's predictions. Even with the implementation of slow cooling the interaction of the vacancy-based BiI_3 lattice with that of the PbI_2 lattice does not favor ordering but locks in disorder. Despite this disorder, the samples are structurally robust and can be readily cleaved to yield large crystal flakes several millimeters in the planar direction and hundreds of microns thick.

2.4.2. Conductance Switching Behavior

2.4.2.1. Room Temperature IV

The hallmark feature of $(\text{PbI}_2)_{1-x}(\text{BiI}_3)_x$ compositions is an unprecedented conductance switching behavior that is not apparent in either parent binary, Figure 22 This behavior is only observed when an applied electrical field is applied perpendicular to the planar direction, parallel to the c axis of the material. On the initial application of a positive voltage bias the current does not show an activation peak, only the leakage current (Figure 23). The next voltage sweep between ± 100 V traces the nonlinear, hysteretic current-voltage (I-V) curve shown in the figure. The distinguishing

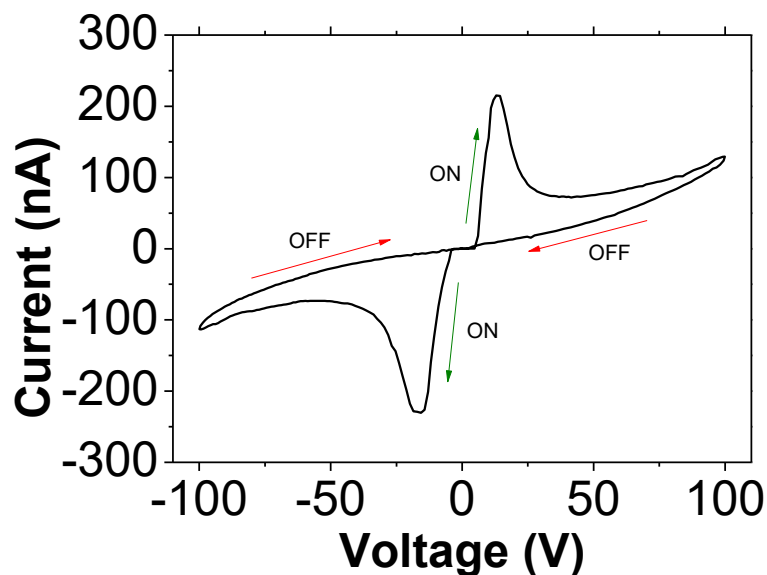


Figure 22. A representative I-V curve for a sample of $(\text{PbI}_2)_{1-x}(\text{BiI}_3)_x$ sample after the memristor-like behavior has been engendered in the sample, note the on and off regions as designated by the arrows.

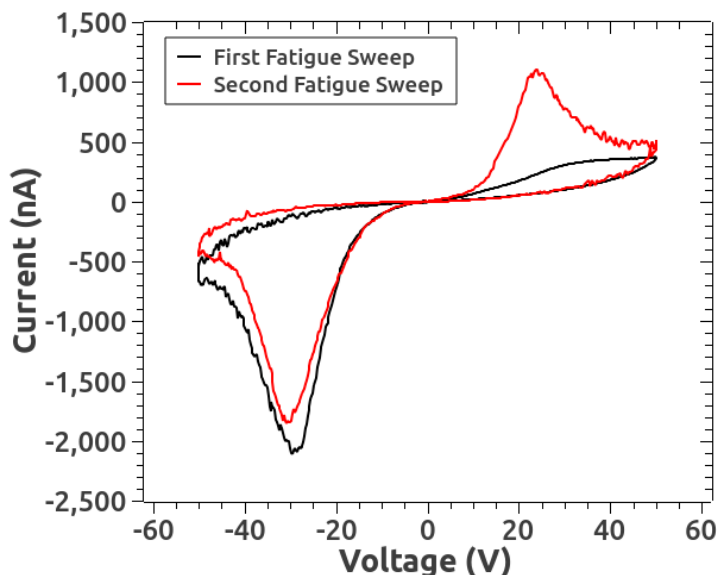


Figure 23. First and second sweeps of the unbiased $(\text{PbI}_2)_{0.5}(\text{BiI}_3)_{0.5}$ sample from Figures 30 - 34, 2.4.2.4. On the first sweep the conductance switching peak is not observed as the sample is being biased for the first time. An explanation of this behavior is given in the section on the Mechanism of the Conductance Switching Action.

feature of this I-V characteristic is a sharp sudden increase in current a few volts after the voltage switches sign. The magnitude of this current increase depends on the voltage range and sweep rate. No current peak is observed when the voltage is swept down to $V=0$ from ± 100 V. In subsequent voltage sweeps between ± 100 V, the magnitude of the current peaks progressively reduces, saturating at about 5-10% of its initial value, and the position of the peaks moves closer to $V=0$, but the overall nonlinear hysteretic characteristic is preserved, discussed further on in this chapter in section 2.4.2.4. This behavior is reproducible and consistent between samples and is insensitive to light. In contrast, when bias was applied parallel to the crystal planes across the surface of the

sample, we observed the standard ohmic behavior typical of a resistor with no “butterfly” behavior in the resulting I-V sweeps.

To better characterize these “butterfly” I-V plots, we broke them into two parts, the background current that we call the “off” region and the activated current we call the “on” region. The “off” region is the highly resistive background behavior made of leakage current with asymptotic conductivity that scales with applied voltage. The “on” current we associate with ionic transport in the material perpendicular to the crystal plates. This contribution is long-lived, with duration on the order of tens of seconds, which is significantly slower than normal electronic relaxation times. For a given sample thickness and sweep rate, the maximum of the current peak associated with this “turn on” behavior occurs at a fixed voltage.

The magnitude of the peak, and the ratio between it and the asymptotic current magnitude, are highly susceptible to hysteretic effects, the most extreme of which is the complete suppression of the turn-on peak for sequential voltage sweeps with the same polarity. Many of the effects are extrinsic, highly hysteretic, and incredibly long lasting. To account for these effects, multiple runs were completed for each test and representative current voltage curves were constructed by averaging several individual runs. The location, magnitude, and asymptotic behaviors of the two major current contributions were the same across each of the selected runs. This simplifying step helps to clarify the interesting behaviors and their relationship to the investigated experimental parameters. Despite these effects, for a given sample thickness at a constant temperature the peak current value associated with this turn on behavior seen in the I-V plots occurred at a fixed voltage. Moreover, the location and magnitude of the peaks were predictable, an effect which can be seen in the peak time and magnitude in the relaxation data shown discussed in **2.4.2.2**.

Another variable accounted for in I-V sweeps was the bias sweep rate. Changing the sweep rate of the bias changed the shape and location of the transport peak, so to account for this a fixed sweep rate of 2400V/hr was chosen arbitrarily based on trial and error. Unless otherwise noted all measurements were conducted with this standard voltage sweep rate. Although conductance switching like behaviors have been reported in several types of materials, this particular sequence of events in the “on” and “off” switching action, to our knowledge, has not been reported.

The two-part conductance switching transport action is consistent for a given sample and sweep rate but is subject to fatigue effects over repeated trials. To account for this, sequential tests were conducted with low bias dwell time to help relax the behavior of the sample. Tests run without this dwell time show a clear annealing behavior that decreased the asymptotic conductivity, which was later explored in multi-cycle fatigue testing discussed in section **2.4.2.5**. For tests run with dwell time, the asymptotic current was remarkably consistent, and resulted in a well-defined return curve for the “off” current when returning to zero bias. However, the magnitude of the peak, and the ratio between it and the leakage current were highly susceptible to hysteretic effects, the most extreme of which is the complete suppression of the turn-on peak for sequential voltage sweeps with the same polarity, 100 V to 0 V and back to 100 V for example. This effect persists over long periods of time and can be trained by conditioning the sample with saturation bias. Additionally, the “on” and “off” current could be tuned with sweep rate or sample thickness. These plots also look very similar to behavior displayed by unipolar resistive switching, a subset of memristor properties that have been well documented.

2.4.2.2. Time dependent Decay Measurement

As we examined the shape of the I-V plots, we found that when the voltage was held at the peak position the current decayed over time (e.g. the 5 V trace in Figure 24). To investigate this, we conducted relaxation measurements to decouple the effect of the current sweep from the “turn on” behavior. The sample was saturated in reverse bias at -100 V, then stepped to a positive constant voltage in the range of 0-15 V and allowed to relax (Figure 24). This was repeated in integer voltage steps to generate a set of voltage dependent relaxation curves. One interesting characteristic of this plot is that both the time and magnitude of the maximum current peak follow

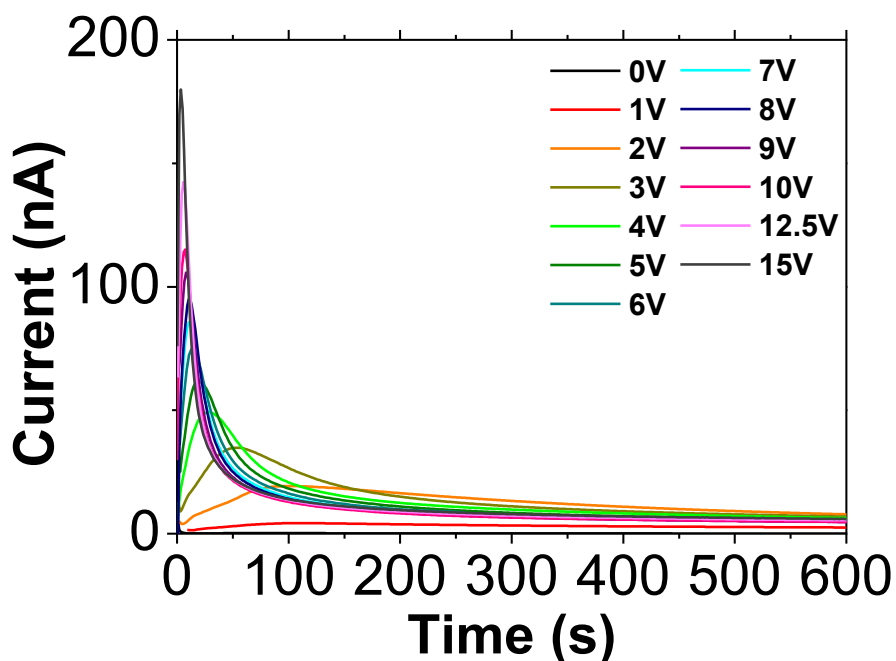


Figure 24. Relaxation behavior of $(\text{PbI}_2)_{0.5}(\text{BiI}_3)_{0.5}$ where the sample was held at -100 V for two min followed by a direct swap to the given applied positive bias. Current was measured as a function of time to observe charge extracted from the material and was observed to be on the second scale.

a well-defined pattern as a function of setpoint voltage (Figure 25,b). The total charge transported at a specific voltage in Figure 24 can be obtained by integrating the current over the full measurement time. As shown in Figure 25a the maximum current shows a sharp increase with voltage up until approximately 3 V, consistent with the threshold turn-on voltage seen in Figure 22, then shows a gradual increase associated with the background leakage current of the device. The long decay times on the scale of seconds point to a transport mechanism that is ionic rather than electronic in nature. Since the current decays on constant bias in $(\text{PbI}_2)_{1-x}(\text{BiI}_3)_x$, it cannot be classified as a classical conductance switching which would retain the low and high resistive states until otherwise reset. In Figure 25b we can observe that the magnitude of the maximum current peak is linearly correlated with the set voltage within the 0 – 15 V range.

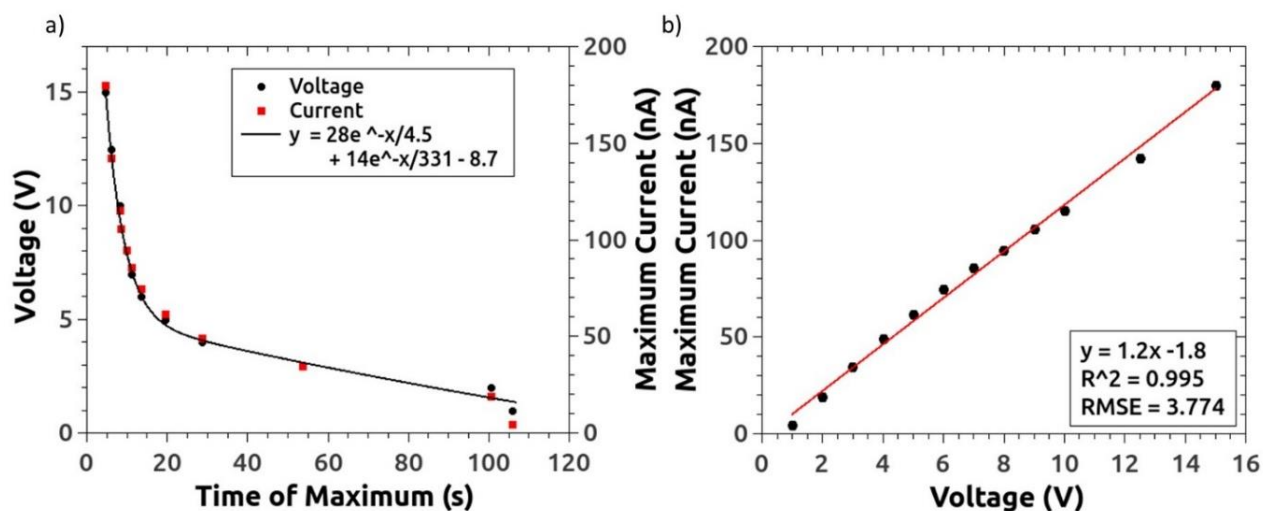


Figure 25. a) Plot of the voltage and maximum current from the relaxation curves seen in Figure 24 as a function of peak time, with a representative exponential fit. b) The corresponding current vs voltage plot demonstrating the highly correlated nature of peak characteristics.

2.4.2.3. Temperature Dependent Electrical Characterization

To determine if there was a thermal barrier to our proposed ionic motion we conducted low temperature I-V sweeps as shown in Figure 26. When cooled to liquid nitrogen temperatures the resistance of the $(\text{PbI}_2)_{0.5}(\text{BiI}_3)_{0.5}$ samples increased dramatically as the thermally activated leakage current was quenched. The measurements were repeated at 5K intervals around the expected activation temperature of 225 K as described in Figure 27. As demonstrated in Figure 26 the same two major contributions to the current can be seen in the higher temperature sweeps and are more subtly present down to the activation temperature of 220K. As temperature is increased from 225 K to 260 K a broad peak is observed farther out in the plot which proceeds to move towards lower voltages with increasing temperature.

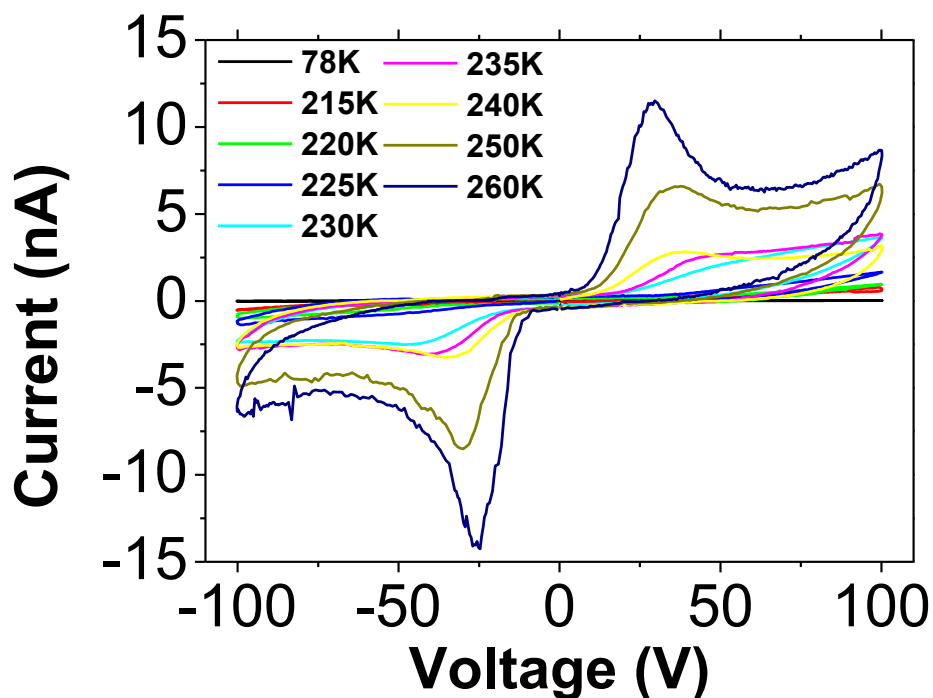


Figure 26. Temperature dependent I-V curves of $(\text{PbI}_2)_{0.5}(\text{BiI}_3)_{0.5}$ beginning at 78 K to 260 K demonstrating the thermally dependent behavior of the conductance switching behavior beginning around 225 K.

Initial characterization of the temperature dependence showed complete suppression of the turn on peak at liquid nitrogen temperature. The only component of the current appears as leakage current with a characterization resistance on the order of 10^{12} ohms. Gradual increase of the temperature allowed for improvement in the magnitude of the leakage current but offered no hint of the major transport peak up to 200 K. Instead, a sample was biased at 40 V and allowed to cool up slowly from nitrogen temperatures. The result of the measurement can be seen in Figure 27 and indicated a saturation temperature of about 225 K for the major component of the conduction peak.

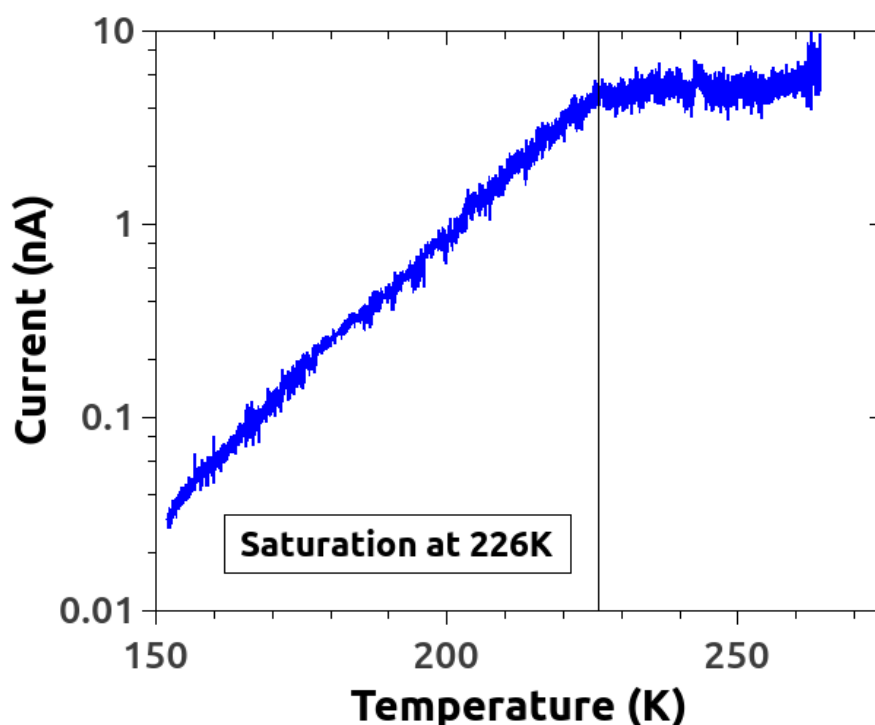


Figure 27. Current from a sample held at 40 V constant bias and allowed to warm up. This range informed the investigation of further temperature dependent IV sweeps.

We then used this as a basis for detailed temperature dependent I-V sweeps with steps of 5K from 215 K to 240 K, and steps of 10K up to 260 K. Results from these sweeps are reported as already discussed in Figure 26. It should be noted that the room temperature sweep was omitted from this plot due to a full order of magnitude difference in the current peak. Here we observe that the magnitude of the peak increases with temperature as more conduction is allowed. Additionally, the voltage position of the peak shifts lower as more temperature is increased, further showing bias dependence that we observed in section 2.4.2.2.

Calculation of the total charge transported in each of the sweeps allowed for a rough estimate of the activation energy by means of an Arrhenius Plot which can be found in Figure 28. The resulting fit was insufficient to definitively qualify the transport mechanism but did give an activation energy of ~ 38 kJ/mol. (0.39eV) This does not take into account the leakage current contribution, only the charge transported in the ionic “turn on” peak, estimated by integrating the area swept out in the I-V plot between the “on” part of the curve and the “off” part of the curve (Figure 5).

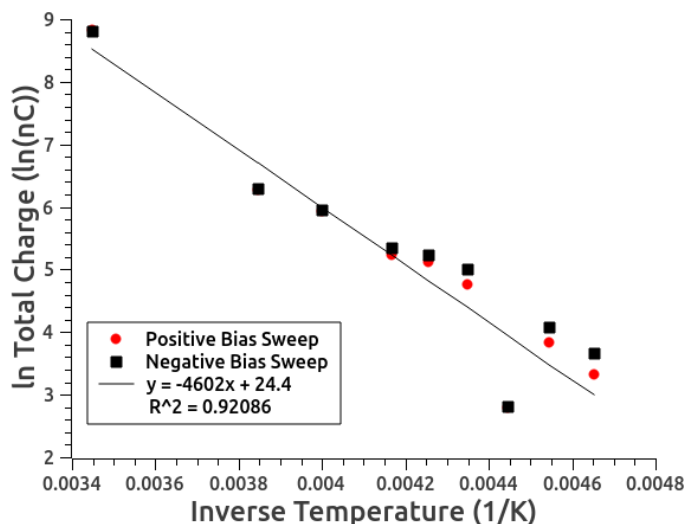


Figure 28. Arrhenius relation for temperature dependent charge transport, obtained by integrating over the forward and backward currents sweep direction of each of the IV curves.

2.4.2.4. Stoichiometric Dependence of the Conductance Switching

The strong temperature dependence of electrical transport in $(\text{PbI}_2)_{1-x}(\text{BiI}_3)_x$ is indicative of ionic transport within the material and is likely responsible for the I-V behavior. We sought to further investigate the I-V behavior stoichiometric $(\text{PbI}_2)_{1-x}(\text{BiI}_3)_x$ samples where x ranges from $x = 0.2$ to $x = 0.8$. The I-V curves of these samples, Figure 29, demonstrate that there is a direct dependence of the magnitude of the current extracted on the composition that is examined. The $x = 0.2$ samples which are PbI_2 dominant exhibit almost no conductance switching like behavior within the standard bias range, but as the composition reaches $x = 0.4$ the conductance switching behavior is apparent at higher voltage than the $x = 0.5$ sample, indicating increasing Bi concentration reduces the energy needed to induce the ionic transport. However, as we move to x

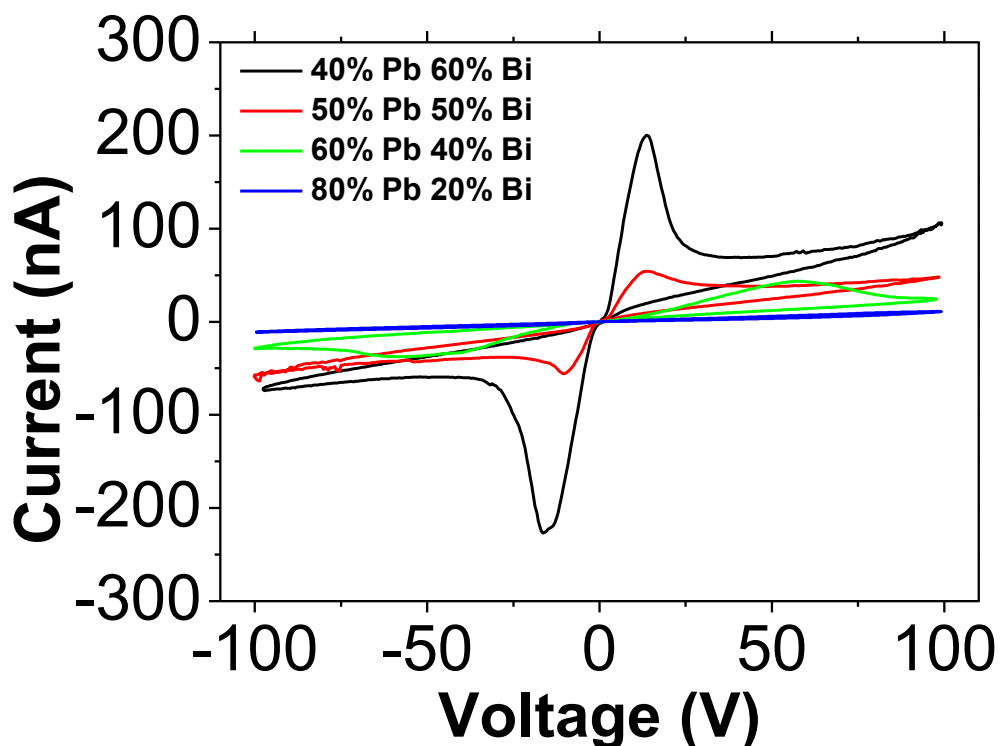


Figure 29. I-V curves samples of multiple compositions of $(\text{PbI}_2)_{1-x}(\text{BiI}_3)_x$ ($x = 0.2, 0.4, 0.5, 0.6$) demonstrating a compositional dependence on the degree of memristor-like behavior.

= 0.6 and BiI_3 becomes dominant we observe a much larger current extraction at nearly the same voltage as the $x = 0.5$ samples, indicating that moving towards Bi rich phases increases the conductivity within both the “on” and “off” regions. We can attribute the off-region conductivity change to the decrease in electrical resistivity as the lower bandgap BiI_3 becomes the bulk and is intrinsically less resistive. For $x = 0.8$ samples that are most BiI_3 rich, crystals were so electrically conductive that could not be characterized in our bias range, immediately shorting and hitting the maximum detected current for the instrumentation with visible damage on the sample. It is likely that the 80% Pb sample still shows “turn on” behavior, but the threshold voltage is outside of the measured range.

2.4.2.5. Stability of the Conductance Switching Effect

The switching behavior described so far shows significant stability despite hysteresis and fatigue. The samples were subjected to a range of conditions including prolonged bias, asymmetric charging, and repeated cycling to well over 100 cycles. Samples showed current peaks of about 10% of the initial transport reached after a small number of cycles, as seen in Figures 30 and 31. Repeated measurements on the same sample showed reproducible behavior after an increase in peak current for initial cycles discussed further below. This suggests a development of preferred conduction channels in the material which compete with an annealing effect where charge carriers are locked into low energy configurations and are no longer able to contribute to the current transport.

The stability of the electronic behavior is of critical importance for potential applications, and studies of fatigue behaviors allowed insight into the transport mechanisms of the material. A

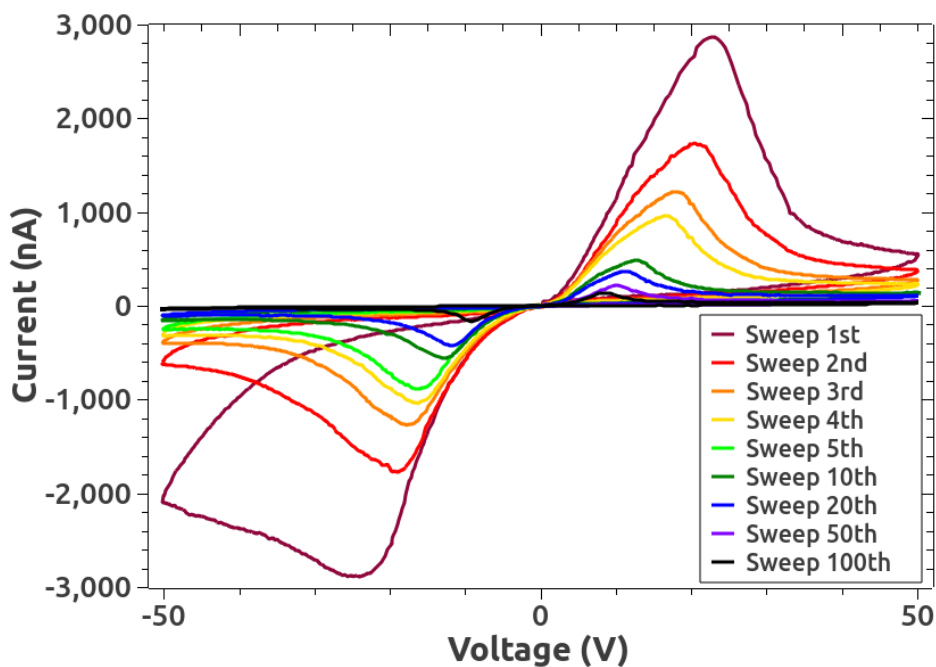


Figure 30. Demonstration of bake in fatigue, which decays both the turn-on transport peak and the leakage current as a function of number of cycles swept.

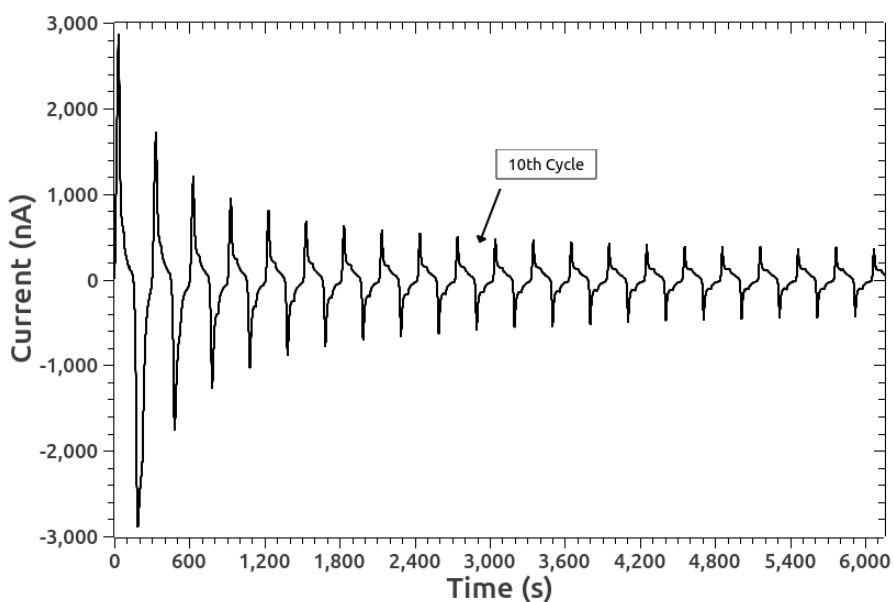


Figure 31. Demonstration of initial current fatigue due to a bake-in of iodine into low energy states on the edge of phase boundaries.

large part of the hysteresis mentioned above can be explained by two competing effects in the ionic transport and is seen in repeated cycle testing of the samples.

The first is a fatigue of the transport current which we attribute to a bake-in of iodine ions into low energy states at the edges of grain boundaries discussed extensively in section **2.4.3**. This results in both a reduction of the ionic transport peak and a gradual reduction in the leakage current because of an effective increase in the fully coordinated tunnel length between grain boundaries. The magnitude of the transport peak decreases as much as 90% over a hundred cycles but reaches a relatively stable behavior after as few as 10 cycles.

The second effect is more subtle, and only manifests after a neutral bias recovery time is allowed for the sample. The initial transport current for cycles run on the same sample after a completed fatigue cycle test is significantly higher than was seen in the initial test. This increase in the initial transport current can be attributed to the creation of preferred transport channels in the material, similar to electrical breakdown channels in other systems. The effect is short lived, as the sample return to their long-cycle amplitudes and behavior within a few (~10) cycles. A demonstration of this effect can be seen in Figure 32. Figure 33 and Figure 34 below demonstrate the combination of these two effects, with the initial increase in current for the second run followed by a return to the high cycle behavior. Figure 34 additionally shows a closeup of the high-cycle fatigue behavior for two subsequent fatigue runs on the same sample.

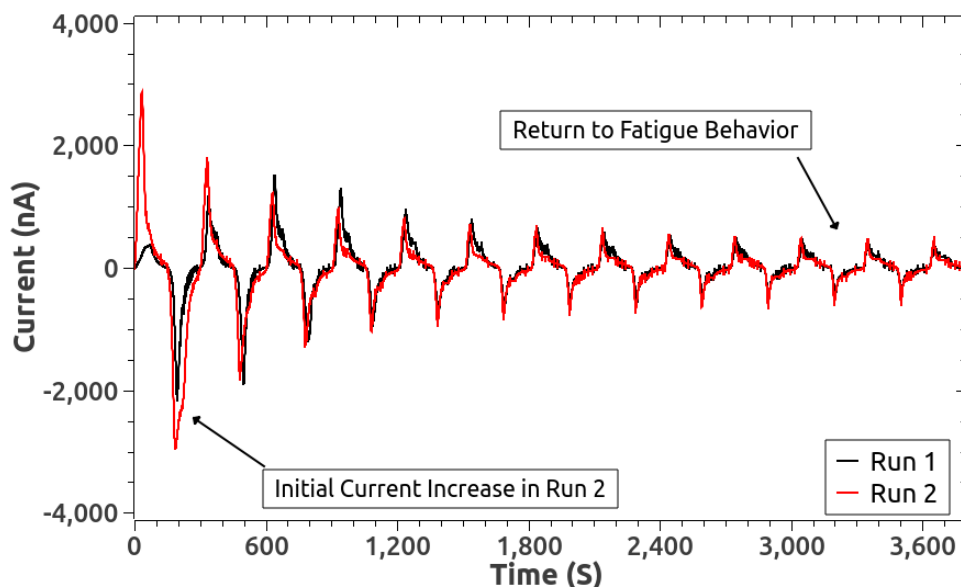


Figure 32. Initial increase in current caused by the formation of preferred conduction channels and the return to fatigue behavior.

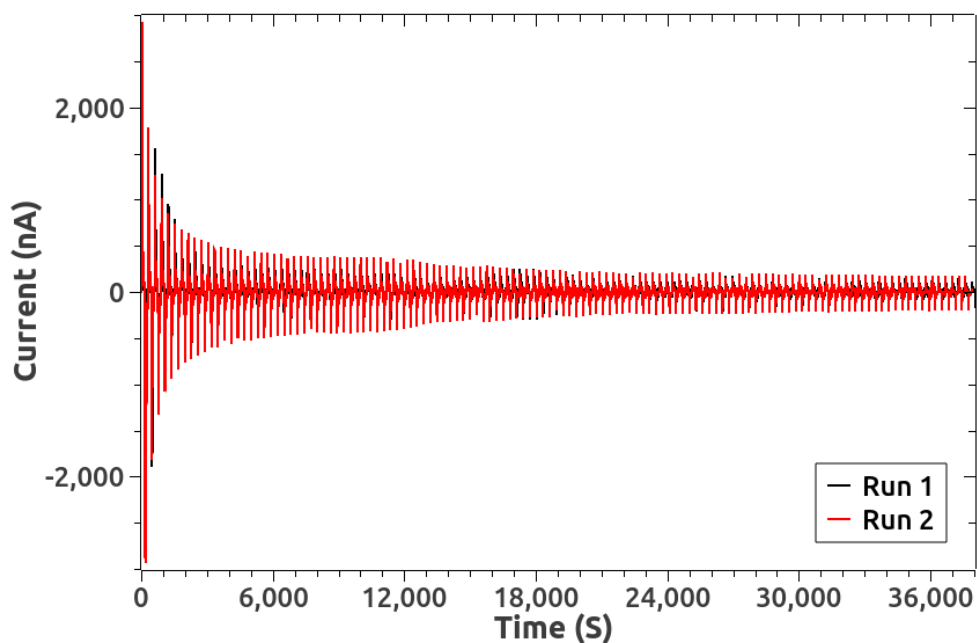


Figure 33. Demonstration of two successive runs of ~ 130 cycles from $+50$ V to -50 V on a sample of $(\text{PbI}_2)_{0.5}(\text{BiI}_3)_{0.5}$. As successive runs cycles are completed the maximum current degrades due to sample fatigue, but after a recovery time the initial cycle current increased, demonstrating competing effects in the transport behavior.

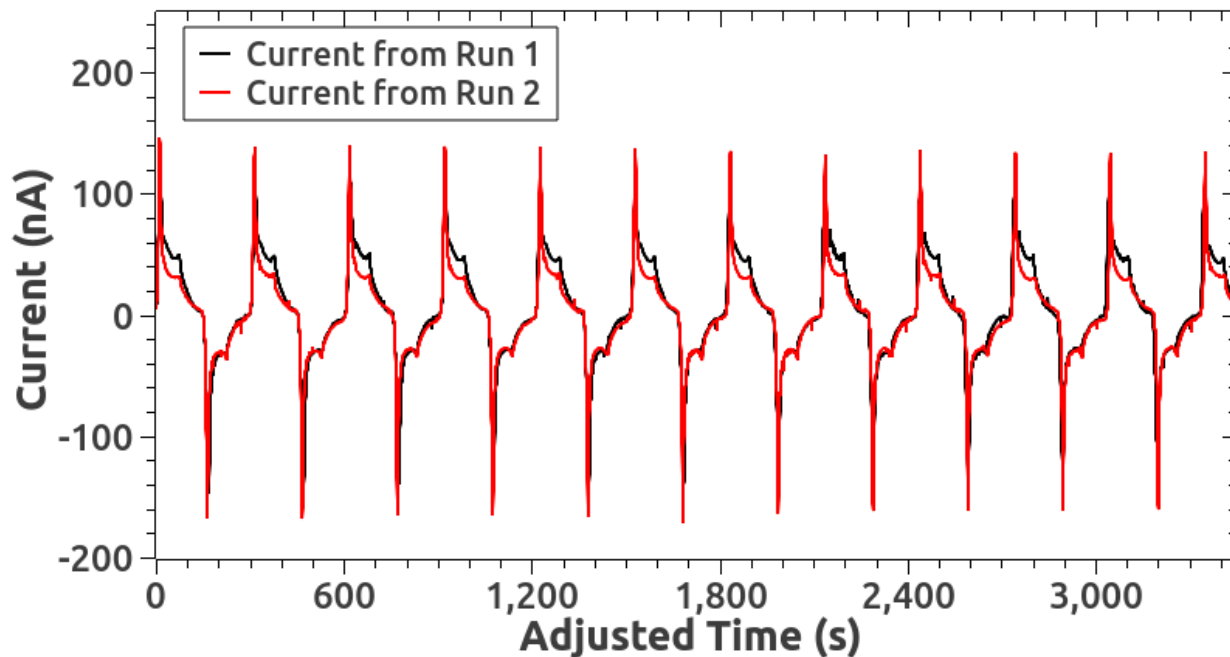


Figure 34. A closer look at the later cycles show the return to fatigue behavior for runs on the same sample. There are remaining structural effects in the current that result in more net charge transfer in the positive bias for the first run that is suppressed in the second, but peak conduction magnitude and total cycle charge transfer otherwise remain the same.

There is significant work to be done to account for other variations in the fatigue behavior of these samples, including to describe the non-monotonic nature of the maximum current peak decay as seen in Figure 24. These behaviors were not investigated as of yet, but it is important to note their reproducibility over several tests on multiple different samples.

2.4.3. Structural Analysis

From the X-ray powder diffraction results, which indicate both sharp Bragg reflections and diffuse scattering, we can conclude that these 2D materials have disorder on several scales from the atomic to the nanoscale. This implies an inability of these compositions to form long range ordered lattices with uniform composition, consistent with our original hypothesis. It points to the presence of inhomogeneities on the atomic scale related to the Bi/Pb atom distribution in the layers leading to nanoscale segregation into Pb-rich and Bi-rich domains in the layers. In order to probe these phenomena we used both single crystal X-ray diffraction (which ignores diffuse scattering and probes the average structure over mm scales) and high resolution transmission electron microscopy (probing the local structure over nm scales).

2.4.3.1. Single Crystal Analysis

From ingots of $(\text{PbI}_2)_{0.5}(\text{BiI}_3)_{0.5}$ we selected crystals of sufficient size for single crystal X-ray diffraction (SCXRD) expecting to observe the diffuse scattering that was apparent in the PXRD patterns. Instead we were met with well-ordered single crystal data from which we extracted a two-layer structural model that did not demonstrate the diffuse scattering; a monoclinic cell in which each layer had variable occupancy of the metal sites with fully occupied iodine atoms. What we observed as $\text{Pb}_{0.4}\text{Bi}_{0.4}\text{I}_2$ crystallizes in the monoclinic space group $C2/m$ with lattice parameters and refinement details given in Table 2. Further thermal parameters and atomic coordinates are given in Tables 3 and 4.

Table 2. Crystal data and structure refinement for $\text{Pb}_{0.40}\text{Bi}_{0.40}\text{I}_2$ at 293 K.

Empirical formula	$\text{Pb}_{0.40}\text{Bi}_{0.40}\text{I}_2$
Formula weight	420.27
Temperature	293(2) K
Wavelength	0.71073 Å
Crystal system	Monoclinic
Space group	$C2/m$
Unit cell dimensions	$a = 7.6770(15)$ Å, $\alpha = 90^\circ$ $b = 4.4282(9)$ Å, $\beta = 100.51(3)^\circ$ $c = 14.102(3)$ Å, $\gamma = 90^\circ$
Volume	471.37(17) Å ³
Z	4
Density (calculated)	5.922 g/cm ³
Absorption coefficient	42.209 mm ⁻¹
F(000)	688
Crystal size	0.2 x 0.4 x 0.05 mm ³
θ range for data collection	2.938 to 34.827°
Index ranges	$-12 \leq h \leq 12$, $-7 \leq k \leq 7$, $-22 \leq l \leq 21$
Reflections collected	3338
Independent reflections	1127 [$R_{\text{int}} = 0.0640$]
Completeness to $\theta = 25.242^\circ$	99.6%
Refinement method	Full-matrix least-squares on F^2
Data / restraints / parameters	1127 / 0 / 22
Goodness-of-fit	1.262
Final R indices [$I > 2\sigma(I)$]	$R_{\text{obs}} = 0.0639$, $wR_{\text{obs}} = 0.1645$
R indices [all data]	$R_{\text{all}} = 0.0970$, $wR_{\text{all}} = 0.1802$
Extinction coefficient	0.0162(15)
Largest diff. peak and hole	2.312 and -3.102 e ⁻ Å ⁻³

$R = \sum ||F_o| - |F_c|| / \sum |F_o|$, $wR = (\sum [w(|F_o|^2 - |F_c|^2)^2] / \sum [w(|F_o|^4)])^{1/2}$ and $w = 1 / [\sigma^2(F_o^2) + (0.0809P)^2 + 0.8188P]$
where $P = (F_o^2 + 2F_c^2) / 3$

Table 3. Atomic coordinates ($\times 10^4$) and equivalent isotropic displacement parameters ($\text{\AA}^2 \times 10^3$) for $\text{Pb}_{0.40}\text{Bi}_{0.40}\text{I}_2$ at 293 K with estimated standard deviations in parentheses.

Label	x	y	z	Occupancy	U_{eq}^*
Pb(01)	5000	10000	5000	0.4205	54(1)
Bi(01)	5000	10000	5000	0.4205	54(1)
Pb(02)	0	0	0	0.3795	50(1)
Bi(02)	0	0	0	0.3795	50(1)
I(003)	6225(2)	5000	3676(1)	1	47(1)
I(004)	2103(2)	5000	1316(1)	1	50(1)

* U_{eq} is defined as one third of the trace of the orthogonalized U_{ij} tensor.

Table 4. Anisotropic displacement parameters ($\text{\AA}^2 \times 10^3$) for $\text{Pb}_{0.40}\text{Bi}_{0.40}\text{I}_2$ at 293 K with estimated standard deviations in parentheses.

Label	U_{11}	U_{22}	U_{33}	U_{12}	U_{13}	U_{23}
Pb(01)	54(1)	57(1)	49(1)	0	8(1)	0
Bi(01)	54(1)	57(1)	49(1)	0	8(1)	0
Pb(02)	52(1)	55(1)	43(1)	0	7(1)	0
Bi(02)	52(1)	55(1)	43(1)	0	7(1)	0
I(003)	51(1)	53(1)	38(1)	0	6(1)	0
I(004)	56(1)	58(1)	36(1)	0	6(1)	0

The anisotropic displacement factor exponent takes the form: $-2\pi^2[h^2a^{*2}U_{11} + \dots + 2hka^*b^*U_{12}]$.

The structure consists of two CdI_2 type layers, but due to the mixing of the $P-3m1$ space group of PbI_2 and $R-3h$ of BiI_3 the ordered vacancies of BiI_3 are introduced into the matrix randomly (Figures 35 and 36). As evidenced in the refinement, iodine is a fully occupied position, but the metal sites between layers exhibit some variance in total occupancy (Table 5).

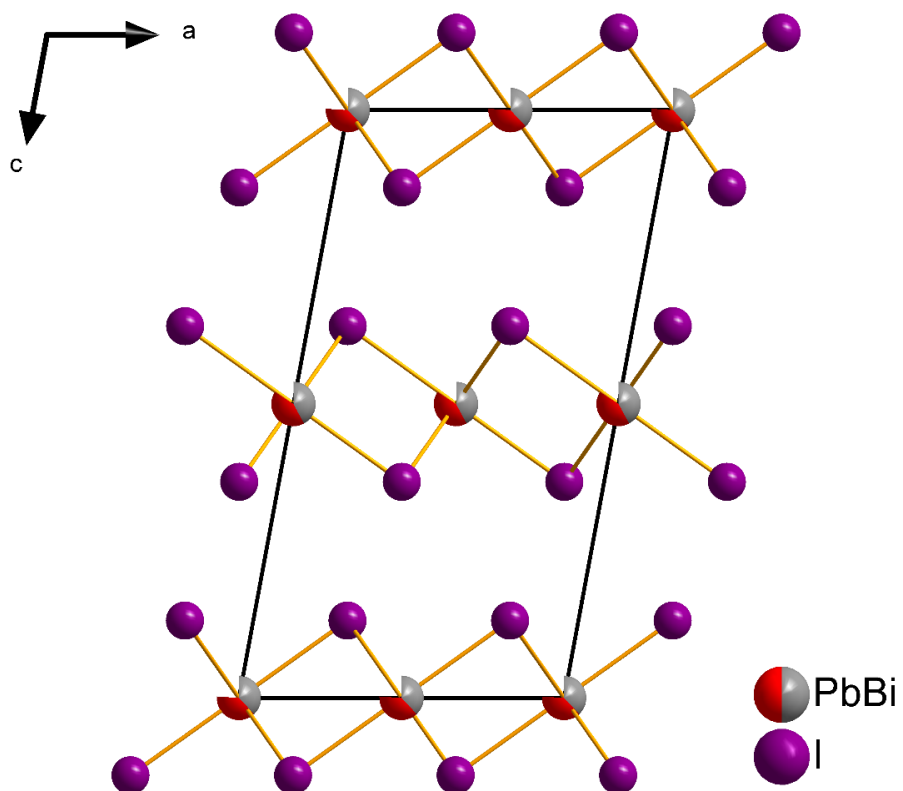


Figure 35. A projection of the single crystal refinement model of $(\text{PbI}_2)_{0.5}(\text{BiI}_3)_{0.5}$, which appears as $\text{Pb}_{0.4}\text{Bi}_{0.4}\text{I}_2$ by x-ray diffraction along the $[010]$ direction. Metal sites are represented by the partial occupancy of Bi, Pb, and vacancies.

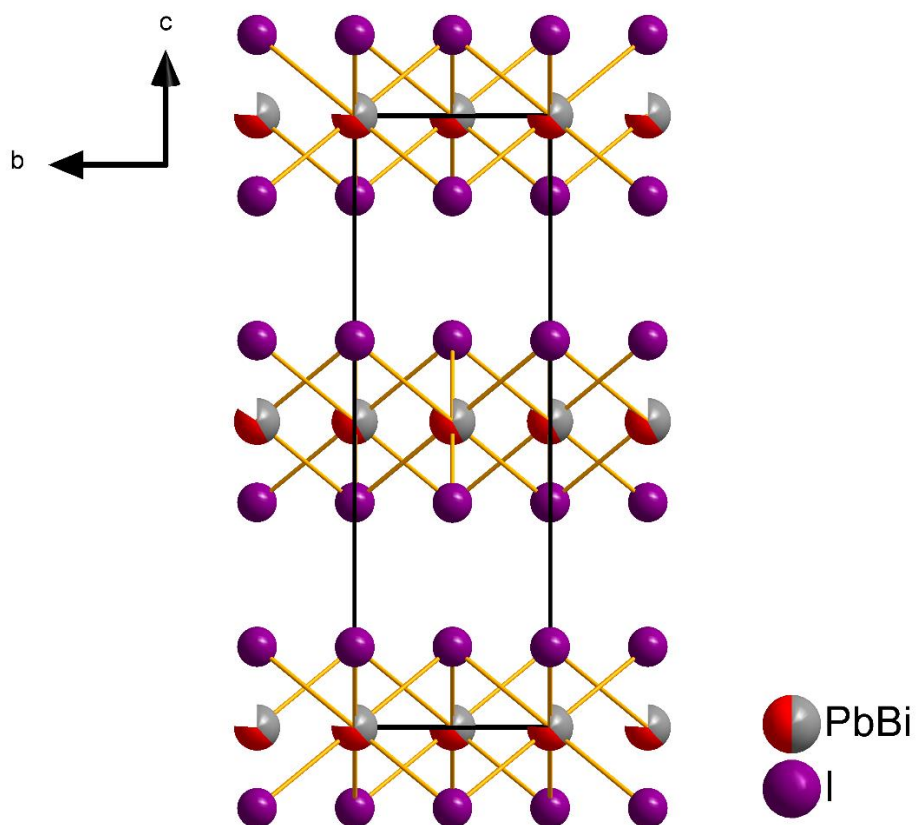


Figure 36. A projection of the single crystal refinement model of $(\text{PbI}_2)_{0.5}(\text{BiI}_3)_{0.5}$, which appears as $\text{Pb}_{0.4}\text{Bi}_{0.4}\text{I}_2$ by x-ray diffraction along the $[100]$ direction. Metal sites are represented by the partial occupancy of Bi, Pb, and vacancies. This is the most commonly seen pattern in the TEM imaging.

In this model the top layer was found to have approximately 84% occupancy on the metal site whereas the bottom layer was 76% occupied. This added up to the nominal composition of $\text{Pb}_{0.4}\text{Bi}_{0.4}\text{I}_2$, consistent with our energy dispersive spectroscopy (EDS) results shown in Figure 37 and Table 6. However, this experiment was limited due Pb and Bi being neighbors on the periodic table and having the same electron configuration when in their respective divalent and trivalent

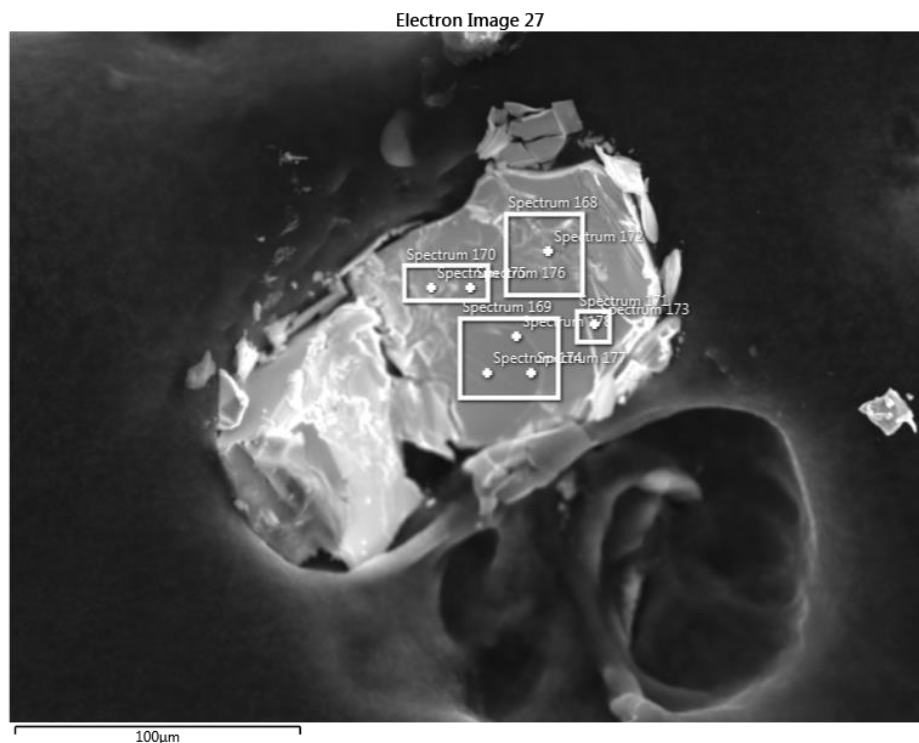


Figure 37. Electron Images of the single crystal used for structural refinement.

Table 5. EDS Data Summary for crystal pictured in Figure 20. Due to the high operating voltage and current of the SEM (25 KeV, 90 uA) some iodine loss is observed; however, the metal ratio is conserved at 1:1 as expected.

Result Type	Atomic %		
	I	Pb	Bi
Statistics			
Max	62.88	33.6	35.18
Min	31.22	19.04	18.08
Average	55.71	22.12	22.17
Standard Deviation	8.56	3.98	4.59
Ratio	2.51	1.00	1.00

states and we could not directly refine differences in each metal's occupancy on the same site. Regardless of this shortfall, the model did inform our overall understanding that the average apparent structure by SCXRD was a bilayer model between the monolayer unit cell of PbI_2 and the three trilayer unit cell of BiI_3 , but included a significant amount of vacancy disorder (8%) between the two layers indicating one was PbI_2 -like (84%) and BiI_3 -like (74%) yielding the compositions $\text{Pb}_{0.38}\text{Bi}_{0.38}\text{I}_2$ and $\text{Pb}_{0.42}\text{Bi}_{0.42}\text{I}_2$. Unfortunately, while the cell fit well with the hypothesis of metal occupancy disorder leading to the diffuse scattering in the PXRD patterns as evidenced by comparison to calculated patterns from the model in Figure 38, the single crystal

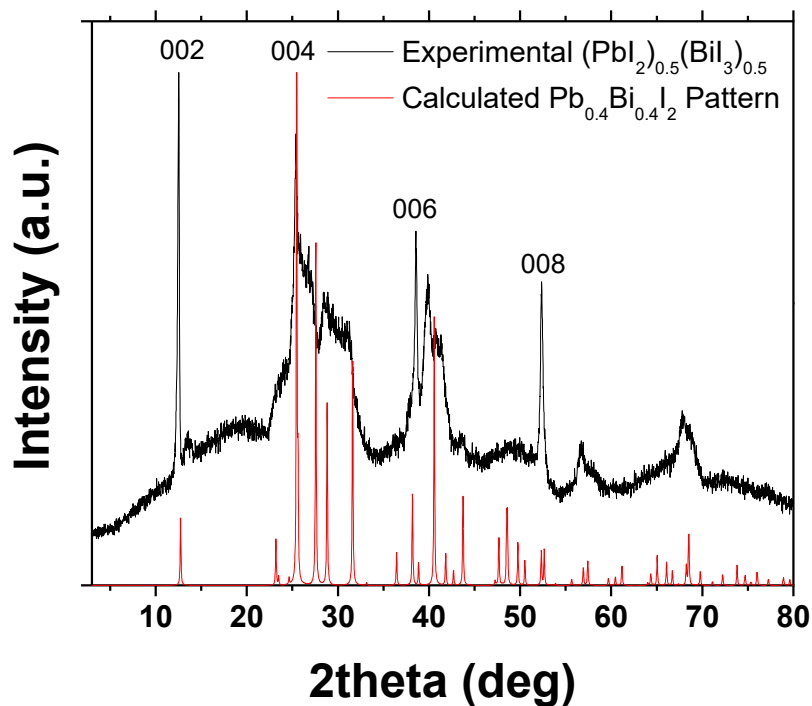


Figure 38. Comparison of a representative plot of PXRD data from $(\text{PbI}_2)_{0.5}(\text{BiI}_3)_{0.5}$ to the theoretical pattern generated using the representative CIF file. As the major $00l$ peaks were well matched we initially suspected massive vacancy disorder as the reason for the diffuse diffraction, rather than the phase separation and strain caused by phase boundary formation.

data also included a fraction of additional peaks that alluded to a larger supercell with modulation q -vectors shown in Figure 39. These additional hints at greater order were unable to be indexed in any meaningful way. This hint at a greater order that was left unresolved by our usual X-ray technique indicated that we needed to turn to additional experiments that could better resolve our conflicting single crystal and powder diffraction experiments. Until TEM was implemented this was thought to be modulation, however, the resultant TEM analysis in the following section 2.4.4. explains that due to lattice mismatch and off stoichiometry “bricks” this average diffraction pattern is found that is a superimposition of two phases.

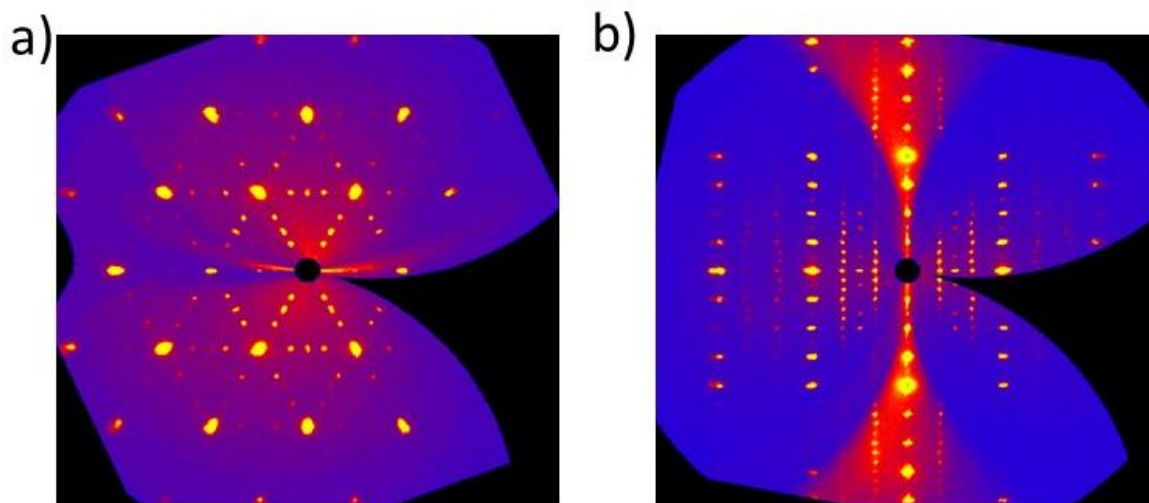


Figure 39. Projections of reciprocal space from single crystal diffraction data taken from the above experiment. a) Observation of diffraction patterns down the [001] axis that show that there are unindexable peaks between the most intense reflections. Vectors could be partially fit for a $1/3$ modulation vector, however, there also appeared a $1/2$ vector that could not be co-indexed. b) Projection of reciprocal space taken from the [010] direction demonstrating similar results of greater order that could not be indexed as in a).

2.4.3.2. Transmission Electron Microscopy, Unveiling the True Nature of $(\text{PbI}_2)_{0.5}(\text{BiI}_3)_{0.5}$

Despite the excellent structure refinement we achieved with this crystal, PbBiI_5 is only one structural description in the $(\text{PbI}_2)_{0.5}(\text{BiI}_3)_{0.5}$ composition and presents a long-range averaged structure which if taken at face value can lead to a misunderstanding of the real nature of these materials. Below we present a more representative view of the structure of these systems, which derives from HRTEM and HRSTEM, and reveals clear nanoscale segregation as the dominant feature in these samples that aid in our explanation for the origin of the conductance switching behavior.

HRTEM images of specimens across the $(\text{PbI}_2)_{1-x}(\text{BiI}_3)_x$ formulation reveal an extensive nanoscale phase separation. From cross-section samples cut parallel to the layers using focused ion beam (FIB), we found that all showed a “brick wall” like patterning shown in Figure 40. The

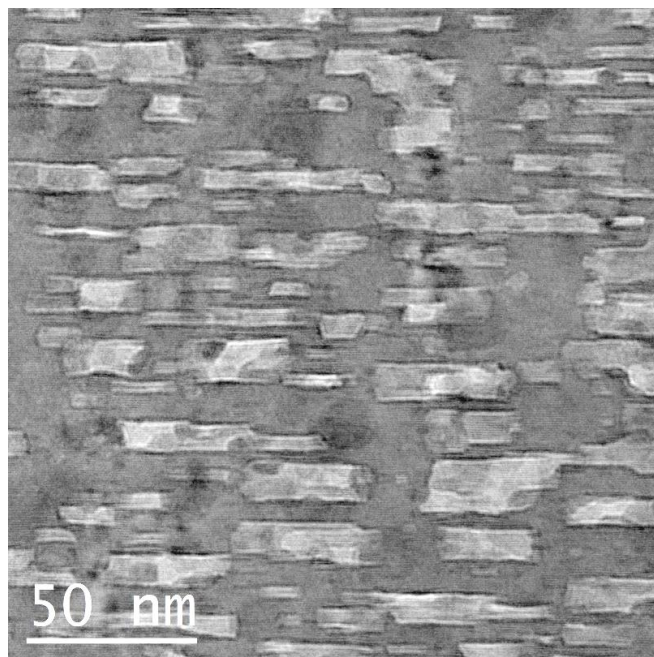


Figure 40. BFTEM image (defocus $\Delta f = +100$ nm) of a sample of $(\text{PbI}_2)_{0.5}(\text{BiI}_3)_{0.5}$ displaying the “brick wall” patterning where bright phases are Pb-rich while dark regions are Bi-rich.

edge-on view of $(\text{PbI}_2)_{0.5}(\text{BiI}_3)_{0.5}$ in Figure 40 shows clear brick pattern from bright field TEM (BFTEM), which is over-defocused ($\Delta f = +100$ nm) to enhance the boundary of crystallites in the matrix by Fresnel fringe formation.¹²² Plus, HRTEM at focus ($\Delta f = 0$ nm) using Gatan® One-view camera (4k x 4k pixels²) in Figure 24a (left) captures lattice fringes over a large area so that we

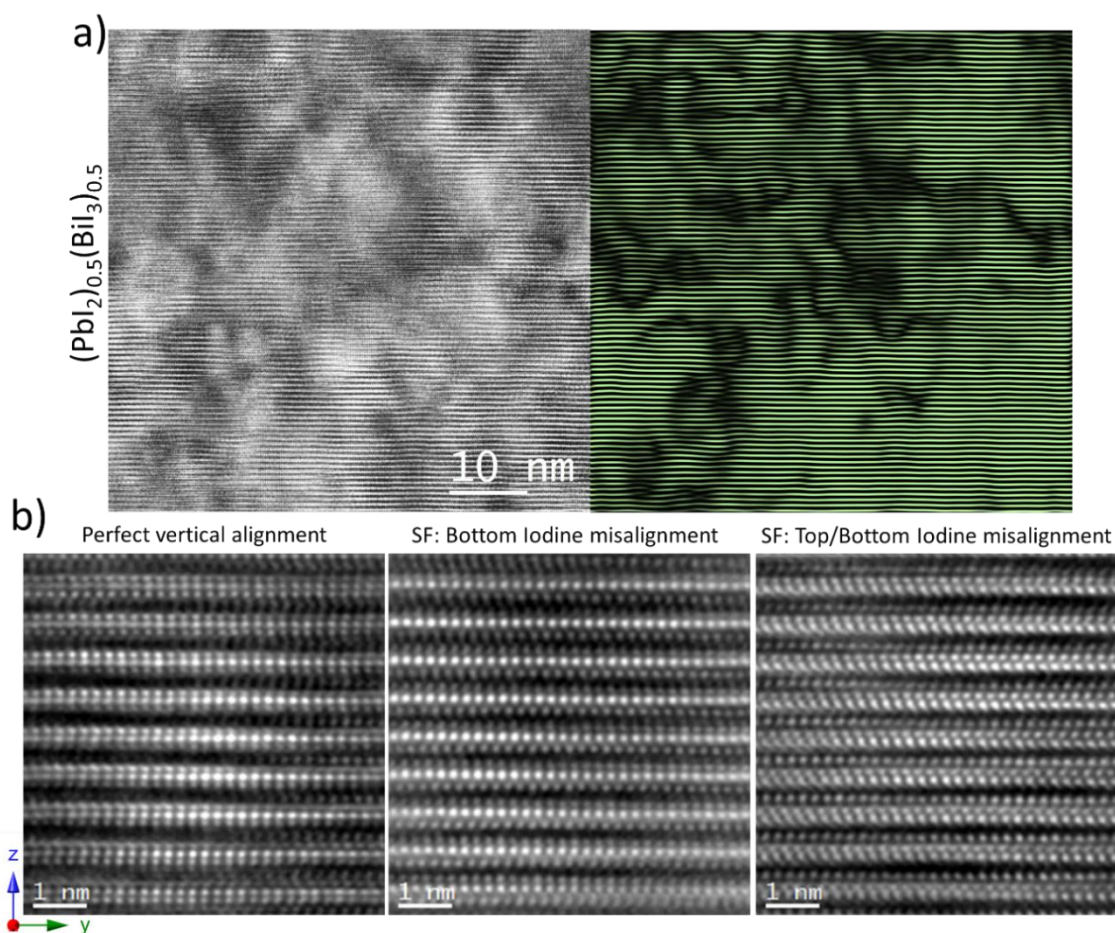


Figure 41. HRTEM and (002)-filtered IFFT of 2D layers of $(\text{PbI}_2)_{0.5}(\text{BiI}_3)_{0.5}$ displaying variance in layer spacing and defects on the 10 nm scale which contribute to the diffuse scattering. b) Locally magnified HRTEM images from image a) showing perfect vertical alignment of 2D stacking (left) and stacking faults with bottom iodine misalignment (middle) and both top/bottom iodine misalignment (right).

can analyze detailed dislocations of (002) planes originating from “brick” boundaries. Also note that Fresnel fringe contrast is near invisible at focus ($\Delta f=0$ nm).²⁷ A (002)-filtered inverse-fast-fourier-transform (IFFT) image, which filters (002) planes from the HRTEM, displays significant stacking faults, dislocation cores and slight variability in spacing between the layers. This becomes apparent as dark contrast as can be seen in Figure 41a (right). Also, locally magnified HRTEM shows stacking faults by iodine layer shift shown in Figure 41b. The dislocations, stacking faults or deformations stem from the brick phase boundaries as proved by high angle annular dark field (HAADF) STEM at the atomic scale in Figures 42 and 43. The Z contrast of HAADF, which is

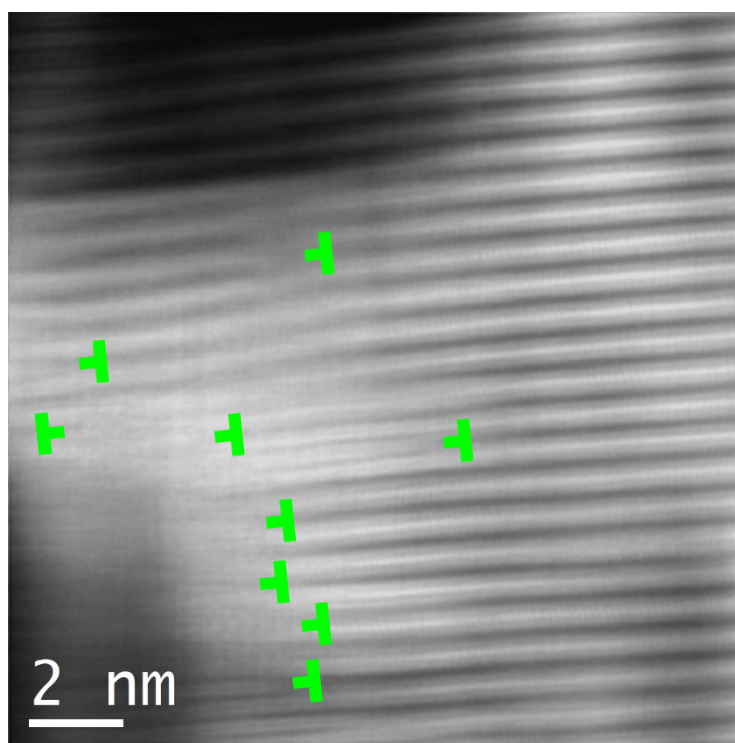


Figure 42. HAADF of phase boundaries exhibiting dislocation cores and extra half planes (green symbol) because of lattice mismatch that leads to the undercoordinated iodine atoms that are liberated by under bias to induce the unique I-V behavior.

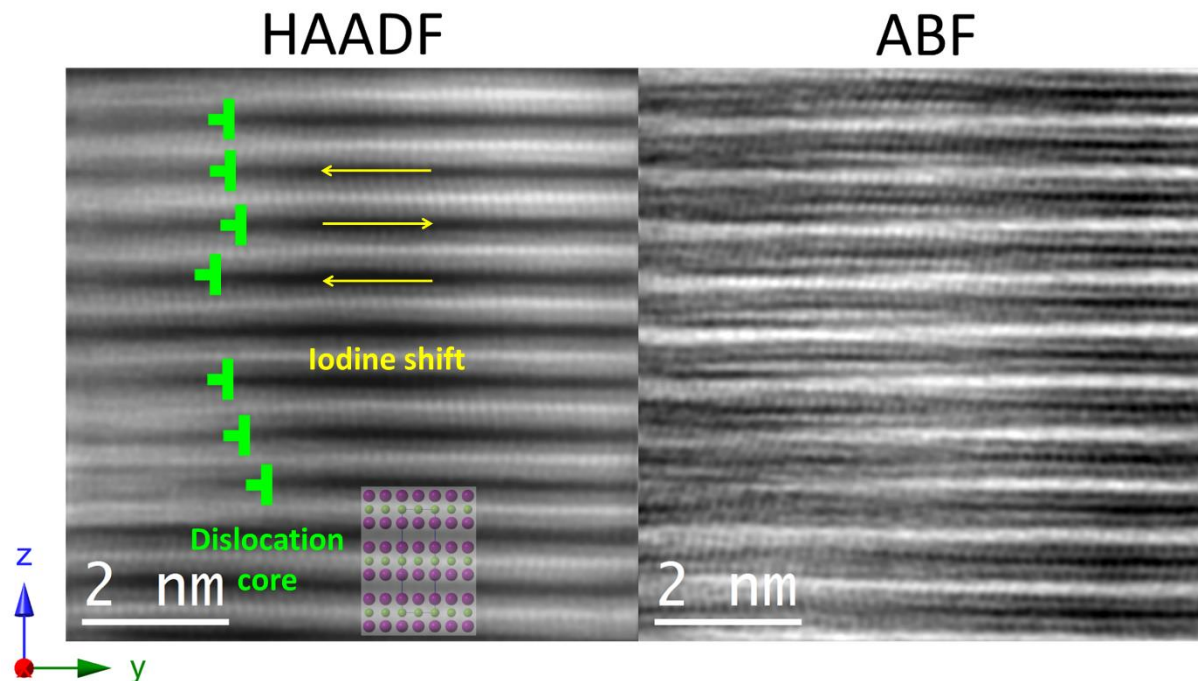


Figure 43. HAADF and ABF of $(\text{PbI}_2)_{0.5}(\text{BiI}_3)_{0.5}$ on $[100]$ zone showing dislocation cores (green symbols) and Iodine misalignment by Iodine layer shift (yellow arrows for shift direction). Please note that brick phase boundary is located at left side of this image area.

sensitive to the average atomic number (Z),²⁷ demonstrates that this material has a significant phase separation between Pb, I-rich (brighter) and Pb, I-poor (darker) regions indicating variability in Bi distribution. This was also confirmed by STEM-energy dispersive spectroscopy (EDS) map in Figure 44. Most importantly, extra half planes related to dislocation cores (green symbols in Figure 42,43) form readily at the periphery of phase boundaries between the Pb rich bright and Bi dark phases.

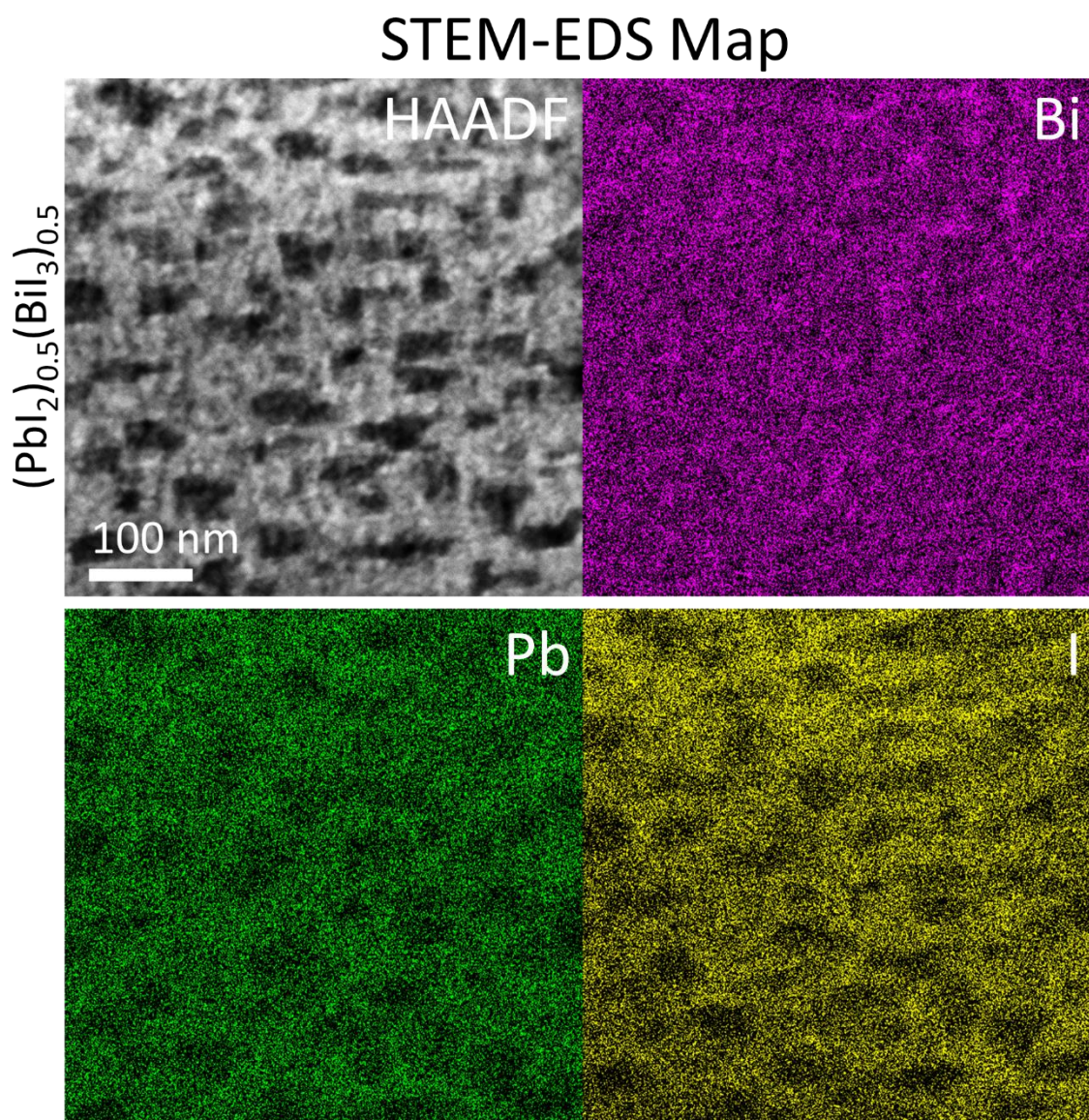


Figure 44. STEM-EDS map of $(\text{PbI}_2)_{0.5}(\text{BiI}_3)_{0.5}$ showing HAADF and corresponding Bi, Pb and I. Please note that Pb and I show same trend and dark regions (less-dense) in HAADF are matched to deficiency of Pb and I.

Interestingly, HAADF of $(\text{PbI}_2)_{0.8}(\text{BiI}_3)_{0.2}$ taken on [100] zone (Figure 45) shows a nearly single crystalline structure with no defect or deformation in larger area than that of $(\text{PbI}_2)_{0.5}(\text{BiI}_3)_{0.5}$ in Figure 25. (002)-filtered IFFT (inset in Figure 45) confirms perfect stacking of (002) planes without deformation. HAADF and annular bright field (ABF) in Figure 46 clearly proves the

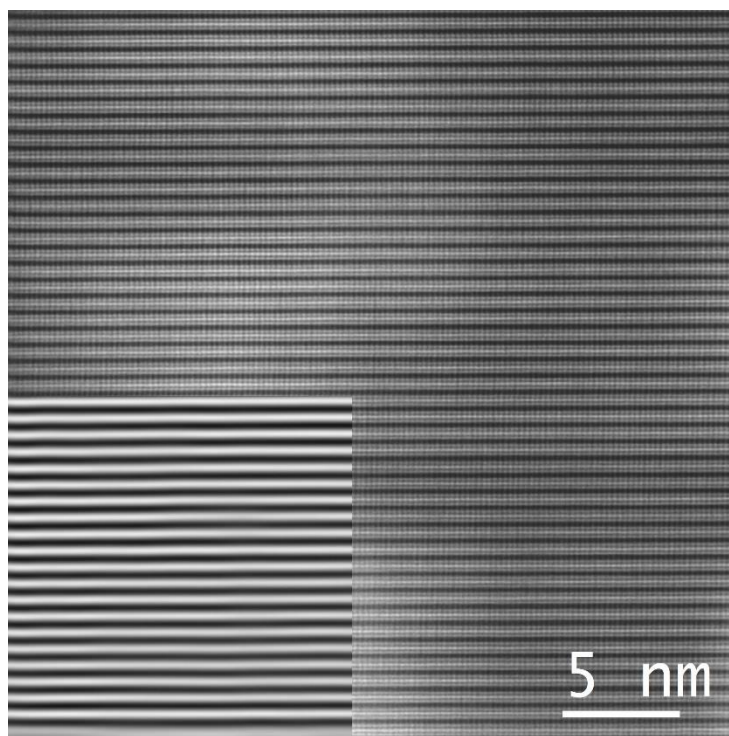


Figure 45. HAADF of $(\text{PbI}_2)_{0.8}(\text{BiI}_3)_{0.2}$ along the [100] zone showing single-crystallinity over a relatively large area confirmed by (002)-filtered IFFT as inset.

perfect 2D stacking as indicated by overlay of $\text{Pb}_{0.4}\text{Bi}_{0.4}\text{I}_2$ SCXRD structural model on [100] zone. The magnified HAADF image in Figure 47 exhibits Pb-Bi layers sandwiched by two iodine layers and the measured b and $c/2$ are 4.4 Å and 7.1 Å in $(\text{PbI}_2)_{0.8}(\text{BiI}_3)_{0.2}$, while those in $(\text{PbI}_2)_{0.5}(\text{BiI}_3)_{0.5}$

determined from XRD are 4.428 Å and 7.051 Å, in good agreement. The structure of Pb-Bi layer sandwiched by two iodine layers is confirmed by the atomic EDS line profile, Figure 48.

The Electron diffraction (ED) pattern of $(\text{PbI}_2)_{0.8}(\text{BiI}_3)_{0.2}$ in Figure 49a matches the simulated ED pattern of $(\text{PbI}_2)_{0.5}(\text{BiI}_3)_{0.5}$ in Figure 49b. However, we also observe very weak superlattice spots indicating another phase with extremely low concentration. The large area HAADF image of $(\text{PbI}_2)_{0.8}(\text{BiI}_3)_{0.2}$ in Figure 50, contains a very low density of small dark bricks.

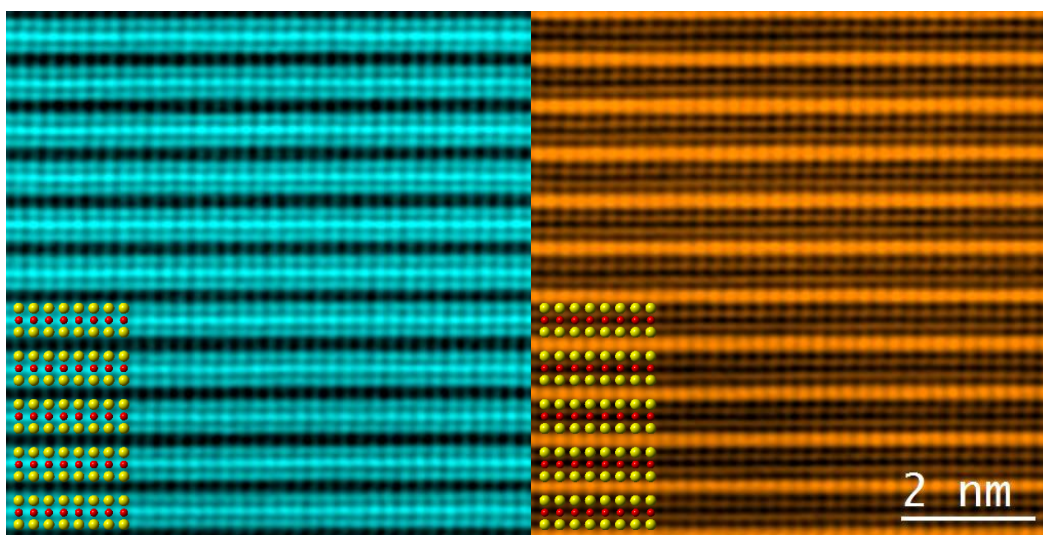


Figure 46. HAADF and ABF of $(\text{PbI}_2)_{0.8}(\text{BiI}_3)_{0.2}$ on [100] zone exhibiting perfect 2D atomic configuration.

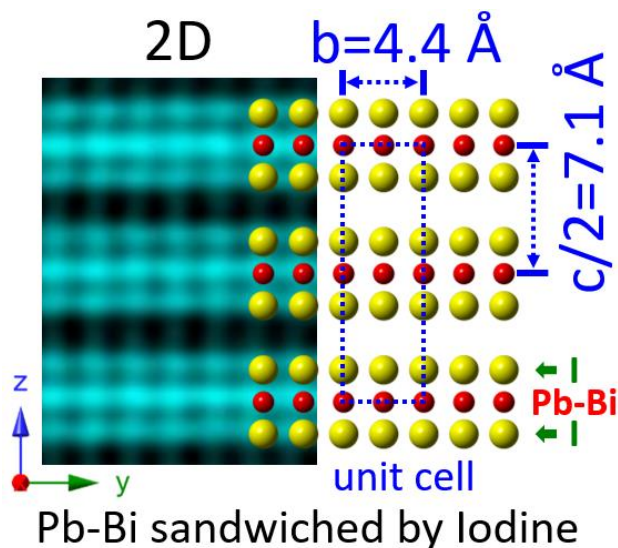


Figure 47. HAADF with overlay of corresponding 2D stacking of Pb-Bi layer sandwiched by two iodine layers. The sandwich structure is chemically verified by STEM-EDS line profile in Figure 48.

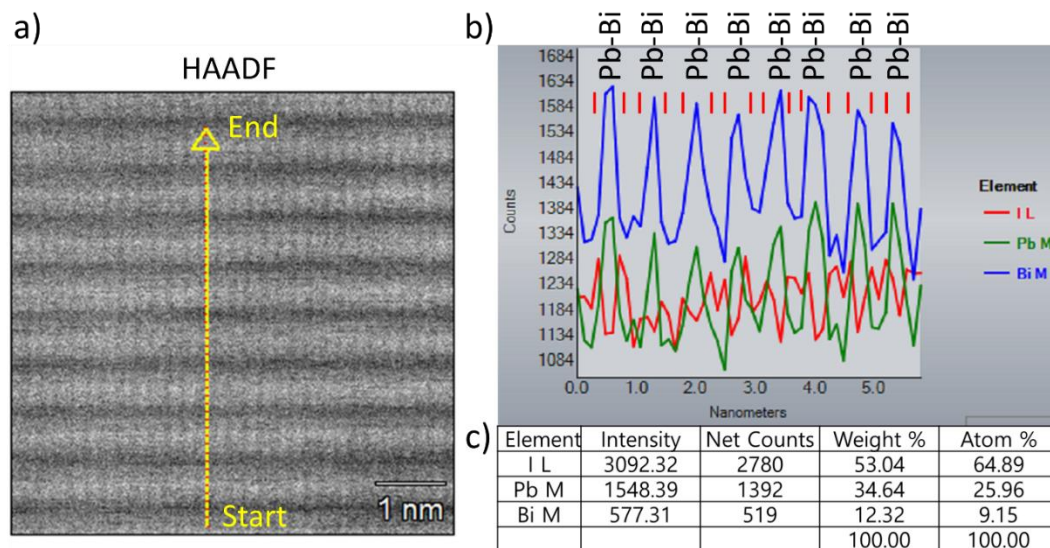


Figure 48. a) HAADF of $(\text{PbI}_2)_{0.8}(\text{BiI}_3)_{0.2}$ with STEM-EDS line profile (yellow dotted arrow). b) Line profile of EDS count of Pb M, Bi M and I L. c) Overall EDS signal analysis showing weight and atomic percentage of Pb, Bi and I. Please note that EDS line profile confirms Pb-Bi layers are sandwiched by two top/bottom Iodine layers.

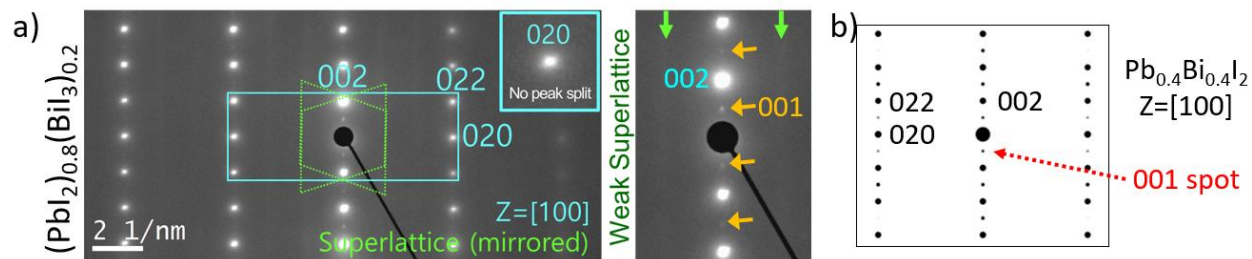


Figure 49. a) Electron diffraction of $(\text{PbI}_2)_{0.8}(\text{BiI}_3)_{0.2}$ presenting representative rectangular array (blue, yellow lines) of reflections on $[100]$ zone with horizontally mirrored superlattice spots (green arrows). b) Simulated diffraction of $\text{Pb}_{0.4}\text{Bi}_{0.4}\text{I}_2$ along the $[100]$ zone matching to a).

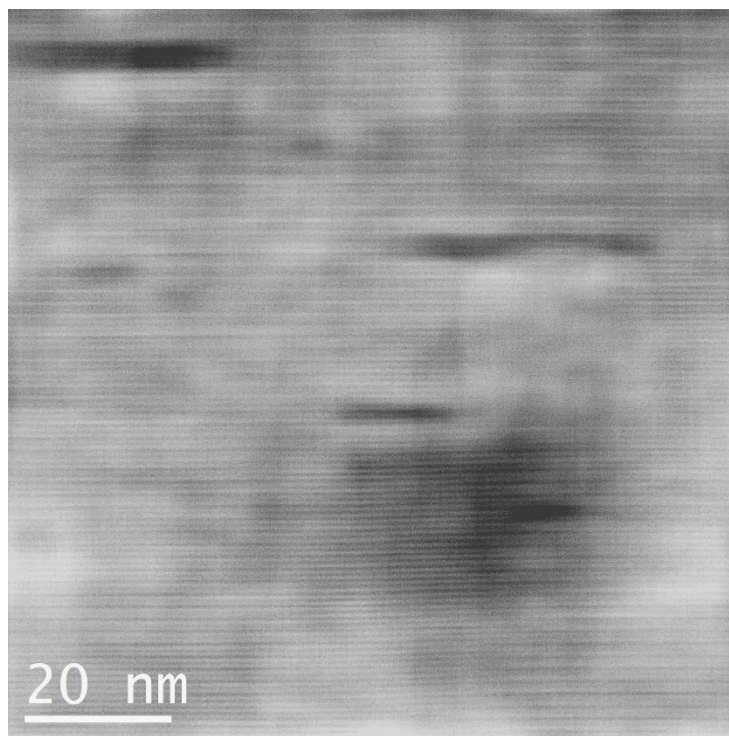


Figure 50. HAADF of $(\text{PbI}_2)_{0.8}(\text{BiI}_3)_{0.2}$ where PbI_2 is the dominant binary, showing a significant decrease in phase boundaries because of the scarcity of small BiI_3 -rich regions (dark).

Interestingly, the ED patterns of both $(\text{PbI}_2)_{0.5}(\text{BiI}_3)_{0.5}$ and $(\text{PbI}_2)_{0.2}(\text{BiI}_3)_{0.8}$ in Figure 51a display streaking of reflections which are related to the phase separation. When the contrast/brightness of this ED pattern is reduced, double diffraction spots of two phases are clearly separated as shown in the yellow box inset of Figure 51a while the blue box inset of Figure 49Sa shows only one. Additionally, we observe very strong superlattice reflections only when there is an increased density of Pb and I poor “bricks” in as seen in Figures 40 and 53 but not Figure 46. These superlattice spots which are slightly double-split in Figure 51a means they stem from two different phases. Reflections diffuse or broaden in both strongly lateral and slightly vertical directions implying certain degree of stoichiometric freedom. A structural clue is obtained from the overlay of simulated ED of PbI_2 ($Z=[1-10]$) and horizontally mirrored BiI_3 ($Z=[010]$ and $[0\bar{1}0]$) in Figure 34b.

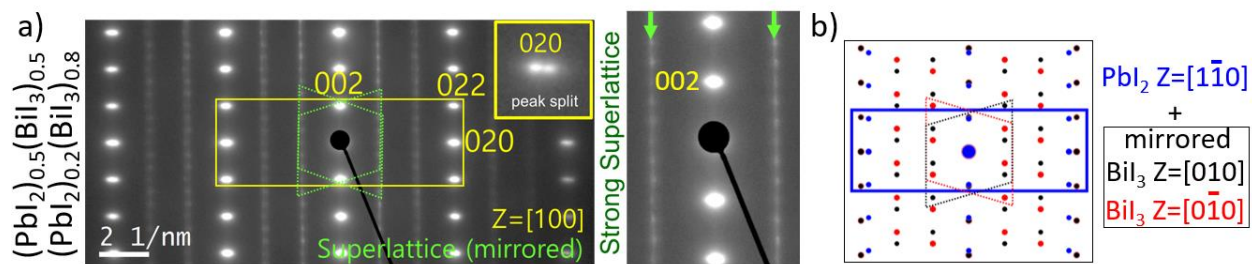


Figure 51. a) Both $(\text{PbI}_2)_{0.5}(\text{BiI}_3)_{0.5}$ and $(\text{PbI}_2)_{0.2}(\text{BiI}_3)_{0.8}$ present representative rectangular array (blue, yellow lines) of reflections on $[100]$ zone with horizontally mirrored superlattice spots (green arrows). Note that $(\text{PbI}_2)_{0.5}(\text{BiI}_3)_{0.5}$ and $(\text{PbI}_2)_{0.2}(\text{BiI}_3)_{0.8}$ shows double peak splits because of the two-phase separation (see inset box). Strong and split superlattice array at magnified view (a right side) and the disappearance of (001) type spots. b) Simulated diffraction overlay of PbI_2 on $[1-10]$ zone and horizontally mirrored BiI_3 on $[010]$ and $[0-10]$ elaborated on in Figure 35

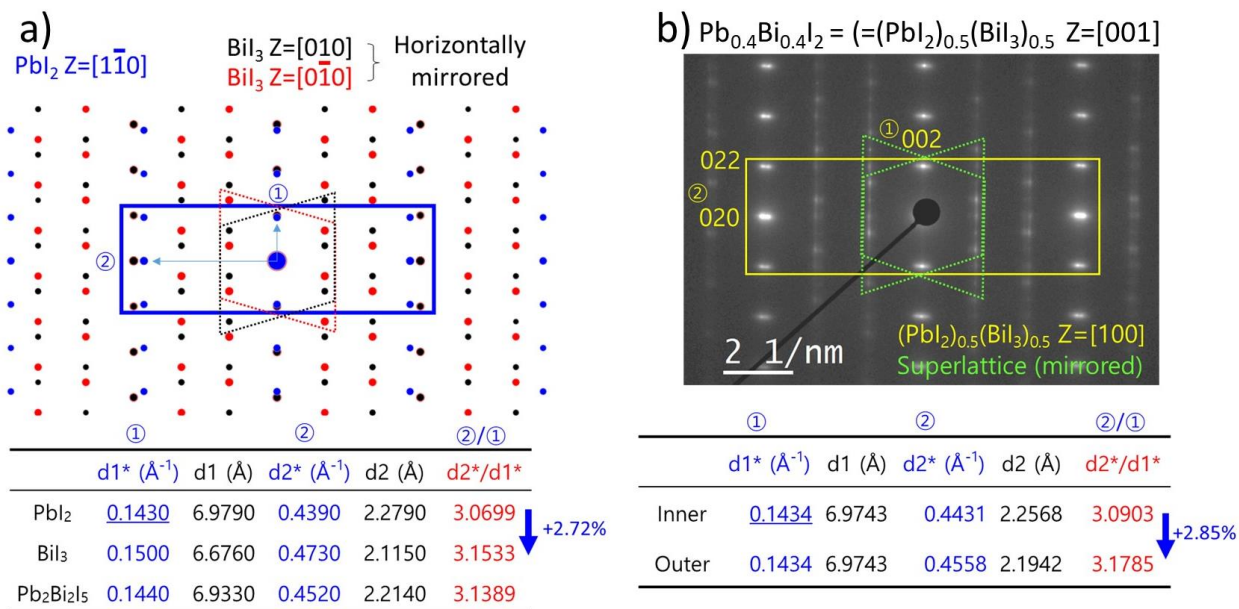


Figure 52. a) Simulated cross-sectional diffraction overlay of PbI_2 of $[1-10]$ zone and BiI_3 of horizontally mirrored $[010]$ and $[0-10]$ zones. Note that diffractions are color-coded as blue, black and red and representative out-of-plane (①) and in-plane (②) in rectangular pattern (blue) are summarized at bottom. b) Experimental $(\text{PbI}_2)_{0.5}(\text{BiI}_3)_{0.5}$ of $[100]$ zone showing similar rectangular pattern (yellow) and mirrored superlattice array (green). Note that double splits of same diffraction spots are observed readily and representative out-of-plane (①) and in-plane (②) in rectangular pattern (yellow) are summarized at bottom.

Considering the measured interplanar distance of each phase (Figure 52a) and the fact that only BiI_3 is related to the superlattice spots, both phases are of the $(\text{PbI}_2)_{1-x}(\text{BiI}_3)_x$ type but have different x values.

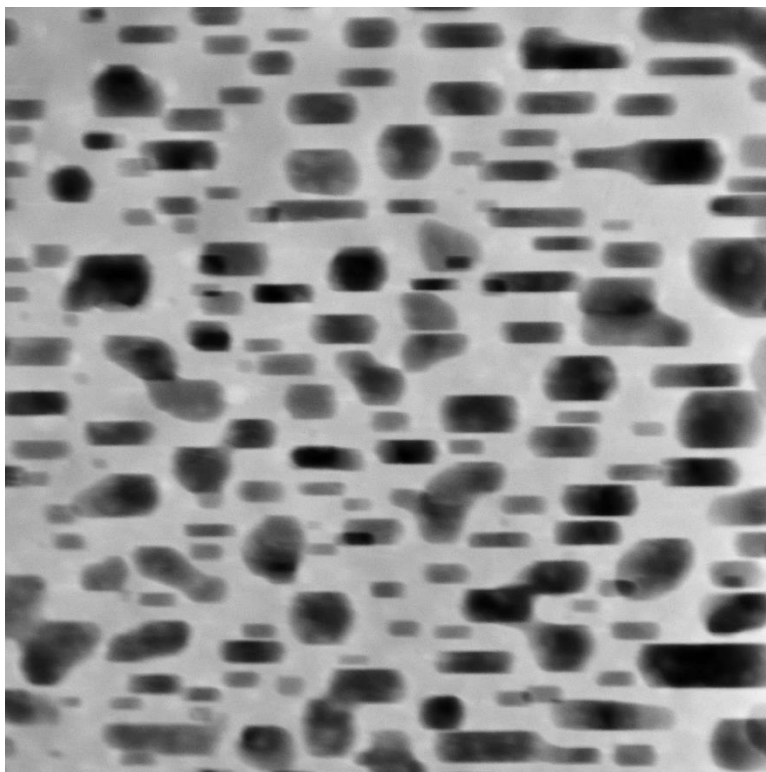


Figure 53. HAADF of $(\text{PbI}_2)_{0.2}(\text{BiI}_3)_{0.8}$ where BiI_3 is dominant leading to greater number and area of phase boundaries because of the greater number of big large BiI_3 -rich regions.

The experimental ED patterns show only lateral diffraction spot split and no split in vertical spots signifying that there is lattice parameter variation of two phases in the in-plane directions only, not in the out-of-plane direction. This is verified by the plane-view ED along the $[001]$ zone from thin 2D samples prepared by the scotch tape method (Figure 54). The measured interplanar spacings of (002) and (020) from Figures 51 and 52 are 6.97 \AA and 2.26 for one phase and 6.97 \AA and 2.19 \AA for the other. Thus, the resultant ED patterns are a result of a mixture of the diffraction patterns of a PbI_2 -rich $(\text{PbI}_2)_{1-x}(\text{BiI}_3)_x$ composition and BiI_3 -rich $(\text{PbI}_2)_{1-x}(\text{BiI}_3)_x$ composition because one phase has similar lattice parameters to PbI_2 and the other to BiI_3 . Since the in-plane

lattice parameter of each phase varies (as confirmed by the diffuse or elongated lateral peaks), it is reasonable that the Pb/Bi ratio in both phases also varies. Note that the elongation of the peaks along the $[00l]$ direction is due to lattice strain introduced by the in-plane lattice mismatch and variable out-of-plane (002) layer spacing as observed in Figures 24, 25, and 26.

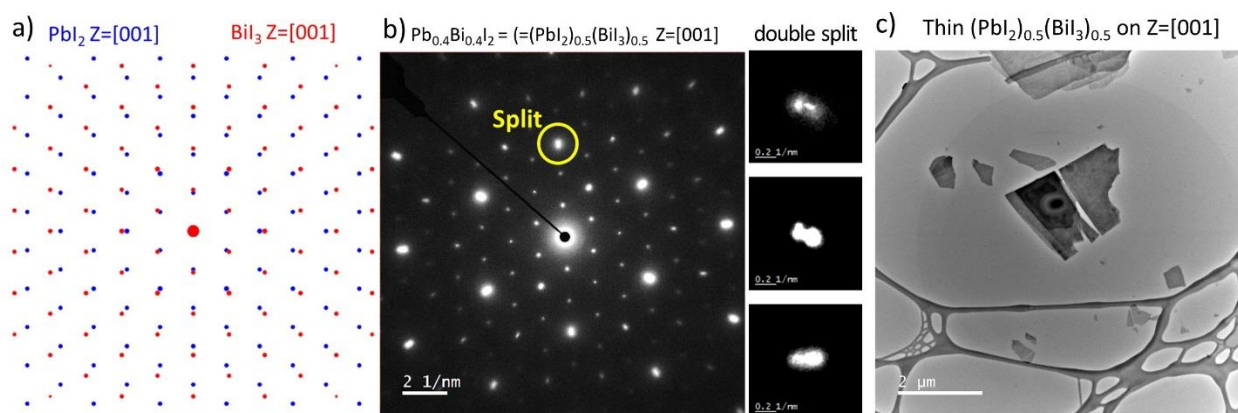


Figure 54. a) Simulated plane-view diffraction overlay of both PbI_2 and BiI_3 on $[001]$ zone. Note that diffraction overlay is color-coded as blue, and red for PbI_2 and BiI_3 respectively and shows hexagonal array with peak double splits. b) Experimental plane-view of $(\text{PbI}_2)_{0.5}(\text{BiI}_3)_{0.5}$ on $[001]$ zone showing hexagonal array and double split of same spots. c) TEM image of thin $(\text{PbI}_2)_{0.5}(\text{BiI}_3)_{0.5}$ film prepared by Scotch tape peeling/transfer method. Please note contrast and brightness were modified to distinguish clear double split of reflections in b).

The mismatch of in-plane lattice parameters, which is 3.2 %, is the source of dislocations, stacking faults and deformation near phase boundaries to release local strain. Because these lattice defects and deformations cause local loss or loosening of iodine ions they provide paths for migration especially along the boundary walls i.e. perpendicular to the 2D layers, they are likely

at the root of the unusual conductance switching behavior. Because the observed conduction time scales point to ionic migration as a source of the conductance switching effect, we can surmise that at these phase boundaries there are a number of undercoordinated iodine terminal atoms at the ends. This is supported by the truncated layers shown in Figure 42. If sufficient bias is applied to liberate these atoms then they would be able to move along the phase boundary regions and contribute to the conductance switching behavior.

Since the nonclassical switching I-V behavior is observed in multiple compositions, we also performed TEM examination of samples in the $(\text{PbI}_2)_{1-x}(\text{BiI}_3)_x$ series where $x = 0.2$ and 0.8 to better elucidate the local nanoscale inhomogeneities and the nature of the phase boundaries. In the BiI_3 -rich sample of $x = 0.8$ (Figure 43) we observe far more and bigger Bi-rich dark regions and as a result this increases the conductivity to unmeasurable levels as noted above. In the PbI_2 -rich sample of $x = 0.2$ (Figure 50) the number of BiI_3 regions are far fewer with smaller dimensions and nearly unobservable. In these samples the I-V was linear with no observable “turn on” behavior. Please note that the viewing area of Figure 53 is bigger than in Figure 48. As the number of phase boundaries between the Pb-rich and Bi-rich domains decrease, the overall conductance switching effects are diminished and by $x = 0.8$ are quenched within our applied voltage range.

The investigation of the structure of $(\text{PbI}_2)_{1-x}(\text{BiI}_3)_x$ should be seen as a cautionary tale in directly accepting the X-ray data as true nature of any material, instead of as the average of a vast number of unit cells. At first, we observed what was thought as a single crystalline structure that demonstrated some unresolved additional order regarding the vacancies, but this was contrary to the powder diffraction data that even with slow cooling demonstrated significant diffuse scattering. It was not until we observed the local and global structure using TEM that we were able to decipher

the real construction of $(\text{PbI}_2)_{1-x}(\text{BiI}_3)_x$, a mixture of $\text{Pb}_{1-x}\text{Bi}_x\text{I}_2$ and $\text{Bi}_{1-x}\text{Pb}_x\text{I}_3$ type phases that usually present as contiguous layers but with the addition phase boundaries due to lattice mismatch.

2.4.5. Mechanism of the Conductance Switching Action

From all-scale structural characterization described above, we can construct the following model for the nature of the ionic conduction. The “turn on” contribution to the current is facilitated by ionic transport at domain boundaries between Bi rich and Pb rich regions. The “brick wall” patterns of Bi rich regions with well-defined phase boundaries harbor crystalline dislocations, bonding disorder, and stacking faults. These phase boundaries host under-coordinated iodine atoms and run perpendicular to the layers. Channels for iodine migration, or re-coordination, span the length of these boundaries (Figure 42). As shown in Figure 55, under bias these mobile iodine atoms can move within these cross-plane channels forming positively charged vacancies / defects. As current flows parallel to the c axis, vacancies can trap charge, and the dark current is established as the conduction that occurs when trap states are filled and electrons tunnel between “bricks”. When bias is reduced the removed iodine atoms and electrons remain trapped in their respective locations. As reverse bias is applied, iodine atoms can move within the phase boundaries displacing electrons hopping out of their respective trap states and followed by the establishment of the dark current flow as electrons are again trapped near vacancies / defects on the opposite end. We propose that it is these channels, iodide migration, and charge trapping/de-trapping enable the movement of charge over the course of a few tens of seconds, resulting in the sharp current peak that is seen in the I-V plots.

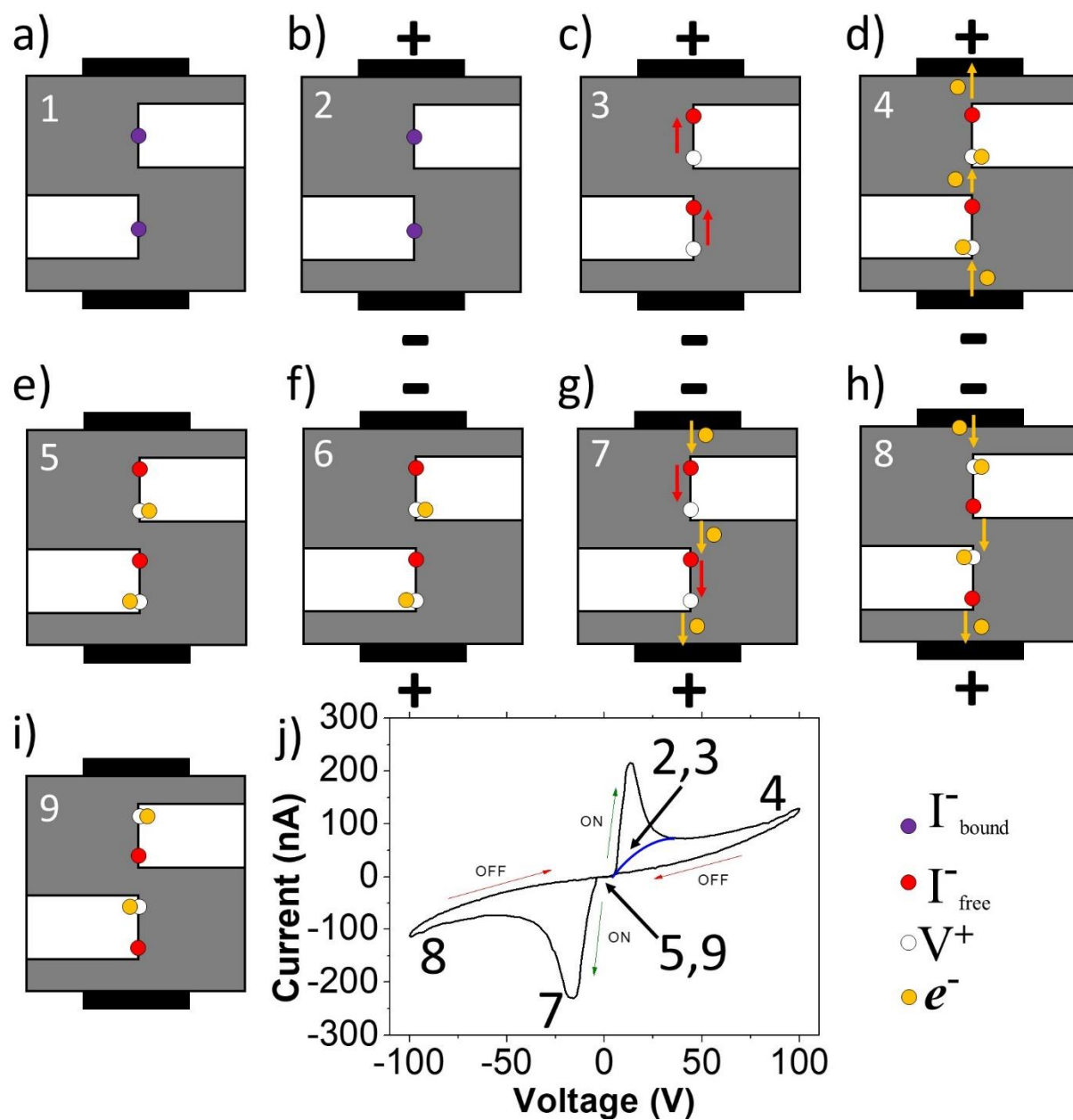


Figure 55. a) Step 1: Schematic representation of a sample of $(PbI_2)_{1-x}(BiI_3)_x$ with applied contacts that is previously unbiased. Unliberated, undercoordinated iodide atoms (depicted as colored circles) are resting at the phase boundaries between Pb and Bi rich phases. b) Step 2: Bias is applied across the crystal parallel to the c-axis, which leads to the movement and drift of iodine atoms as

shown in (c). c) Step 3: As bias is applied across the crystal the undercoordinated iodine atoms bound to metals are liberated to iodide ions, creating positive vacancies near metal sites at the phase boundary, engendering the states that are required for memristor-like behavior, but not displaying the “turn on” current yet. (see Figure 23) Step 4: As current flows through the material the leakage current increases with voltage and electrons are trapped at vacancies locally charge balancing the material. As bias is decreased the current decreases towards (e), where no bias is applied but locally trapped electrons remain. e) Step 5: The unbiased state of the $(\text{PbI}_2)_{1-x}(\text{BiI}_3)_x$ sample where iodide atoms remain in and or near their drift position and electrons remain trapped near the engendered vacancies. f) Step 6: The sample of $(\text{PbI}_2)_{1-x}(\text{BiI}_3)_x$ is biased in the opposite direction leading to the charge extraction observed shown in (g). g) Step 7: When the critical bias is achieved the iodide atoms move the opposite direction leading to electrons previously bound to the vacancies tunneling though from one “brick” to another through the material observed as charge extraction peak. h) Step 8: As the new vacancies are filled by electrons the charge extraction current is complete, leading the low resistive state that is dominated by the leakage current, analogous to the state shown in (d). i) Step 9: As the I-V sweep returns to 0 V the iodide atoms and the vacancies with bound electrons remain as in f, but charged in the opposite direction. If positive bias was swept at this time the current peak would be observed instead of steps 2 and 3, analogous to Step 7 in (g). j) Representation of the steps of the memristor-like behavior indicated on the prototypical “butterfly” I-V plot as noted by step number. Note that Steps 1, 2, and 3 will never occur again in the material as they are formative steps.

2.5. Conclusion

The 2D $(\text{PbI}_2)_{1-x}(\text{BiI}_3)_x$ system demonstrates emergent ion-migration, structural, and electronic properties that are not in the parent binaries. The $(\text{PbI}_2)_{1-x}(\text{BiI}_3)_x$ are nanostructured composites with two phases and extensive dislocation defects at the phase boundaries. The conductance switching behavior is unconventional and arises from the phase boundaries where undercoordinated iodide anions are liberated within the lattice, leading to material polarization and charge accumulation under bias. These effects remain when bias is removed and only under reverse polarization does the stored charge become apparent. Further, laterally nanoscale separated 2D systems are not known and so far $(\text{PbI}_2)_{1-x}(\text{BiI}_3)_x$ is the first well documented example.

Our results demonstrate that for similarly structured systems in the main group halides, a number of emergent properties can be unveiled pointing to similar avenues of exploration in the broader class of 2D materials

Acknowledgements

Work was supported by the U.S. Department of Energy, Office of Science (Grant No. SC0012541). We acknowledge EPIC facility of Northwestern University's *NUANCE* Center, which has received support from the Soft and Hybrid Nanotechnology Experimental (SHyNE) Resource (NSF ECCS-1542205); the MRSEC IRG2 program (NSF DMR-1720139) at the Materials Research Center; the International Institute for Nanotechnology (IIN); the Keck Foundation; and the State of Illinois, through the IIN. Work at Argonne National Laboratory was supported by the U.S. Department of Energy, Office of Science, Basic Energy Science, Materials Sciences and Engineering Division.

Chapter 3

Unconventional Below Band Gap Absorption in Nanoscale Phase Separated $(\text{PbI}_2)_{1-x}(\text{BiI}_3)_x$

3.1. Abstract

Lead and Bismuth halides have shown desirable optoelectronic properties that have impacted the realms of photovoltaics, light emission, and detector applications. Here we demonstrate that that 2D materials $(\text{PbI}_2)_{1-x}(\text{BiI}_3)_x$ exhibit absorbance properties that are nonlinear in dependence and stray far from the anticipated reaction of the binaries. The layered $(\text{PbI}_2)_{1-x}(\text{BiI}_3)_x$ demonstrates that phase integration between the two 2D binaries has a dramatic effect on the optoelectronic properties of the resultant material which can be controlled by cooling regime. We find that as ingots of $(\text{PbI}_2)_{1-x}(\text{BiI}_3)_x$ are prepared from the elements fast cooling results in a material that displays the bandgap akin to BiI_3 , whereas slow cooling yields samples that absorb closer to 0.9 eV. Employing density functional theory (DFT) calculations in conjunction with high resolution transmission electron microscopy (HRTEM) we investigated the origins of this effect from a fundamental structural standpoint. We found that the brick-in-a-way like patterns of Pb rich and Bi rich phase separation and integration yield more metal species mixing at the phase boundaries when slow cooled. This is consistent with our DFT results which demonstrate that clustering of Bi atoms in vacancy absent PbI_2 -type lattice broadens the conduction band p states for both I and Bi leading to mid-gap states that begin to optically absorb at low energy.

Portions of this chapter will appear in the upcoming publication:

G. C. B. Alexander, H. J. Jung, G. Trimarchi, Y. Xu, P. Dravid, M. G. Kanatzidis. "Unconventional Below Band Gap Absorption in Nanoscale Phase Separated $(\text{PbI}_2)_{1-x}(\text{BiI}_3)_x$ " (In preparation)

3.2 Introduction

Main group halides, both ternary and binary, are a growing field of research as their desirable structural chemistry and optoelectronic properties are probed for device applications.^{63, 79, 85, 97, 101} In particular, there is a search for alternative materials to alleviate the stability issues which plague the organic-inorganic hybrid perovskites.⁸³ Such efforts have focused on alternative M-site cations for the AMX_3 perovskites^{85, 123}, perovskite-like phases^{55, 124}, and the $A_3M'_2X_9$ defect perovskite phases where $A = Rb, Cs, Tl$; $M = Pb$; $M' = Bi, Sb$; $X = I, Br, Cl$.^{101, 125} However, prior to the expansion towards ternary systems, simple binary main group metal halides were well examined and remain materials of interest.^{6, 19, 114, 115, 126, 127} The 2D main group PbI_2 ($E_g = 2.3$ eV) and BiI_3 ($E_g = 1.7$ eV) are highly resistive semiconductors that have been exhaustively characterized for device applications^{6, 19, 114, 115} but both suffer due to their simple van der Waals structure. Structurally analogous, PbI_2 crystallizes in the CdI_2 structure type with layers of fully edge-sharing octahedral PbI_6 units whereas BiI_3 displays an analogous structure with additional ordered vacancies to compensate for Bi being trivalent (Figure 56a and 56b). We hypothesized that a combination of these related binaries would result $(PbI_2)_{1-x}(BiI_3)_x$ with new structural features and chemistry due to columbic frustration between Pb^{2+} and Bi^{3+} (Figure 56c).

$(PbI_2)_{1-x}(BiI_3)_x$ mixtures have been sparsely reported on, with brief investigation by X-ray diffraction, optical absorption, and Nuclear Quadrupole Resonance spectroscopy of powder samples.¹¹⁶⁻¹¹⁸ Here, demonstrate that in addition to Chapter 3 and the electronic characterization of $(PbI_2)_{1-x}(BiI_3)_x$ we have also discovered inducible below band gap absorption in $(PbI_2)_{1-x}(BiI_3)_x$ mixtures that is controllable by cooling rate and mixture composition. Beginning from synthesis, we demonstrate a cross-disciplinary investigation into understanding the origins of this low energy

absorption. We demonstrate that by varying the cooling regime of our samples we can control distinctive phase separation, promoting phase integration and yielding the unprecedented low CDenergy absorption.

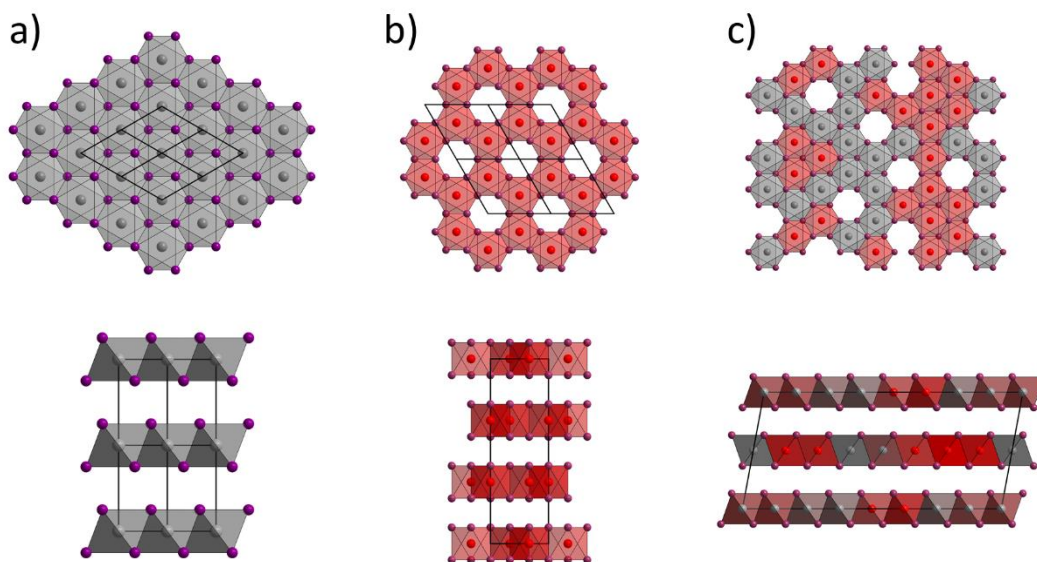


Figure 56. a) Representative supercell of PbI_2 observed along the c -axis (top) to display the a - b plane and along b (bottom) to display the 2D stacking of the van der Waals material. b) Representative supercell of BiI_3 , displayed along c -axis (top) to display the a - b plane. There are ordered vacancies that are required of the material to account for Bi being trivalent rather than divalent. The bottom diagram displays the stacking of BiI_3 sheets in a single unit cell. Due to the ordered vacancies the a and b axes in BiI_3 are doubled relative to PbI_2 and c is tripled. c) Our approximation of a mixture of PbI_2 and BiI_3 leading to a possible coulombic frustration. As shown the top projection along a theoretical c -axis displaying the a - b plane assumes a random distribution of vacancies, Pb and Bi. The bottom figure assumes that the material remains a layered van der Waals material.

3.3. Materials and Methods

3.3.1. Synthesis of Wide Gap $(\text{PbI}_2)_{1-x}(\text{BiI}_3)_x$

Pb and Bi (99.999% American Elements) were combined with I_2 (99.99% Sigma Aldrich or Alfa Aesar) in stoichiometric ratios at the 4 mmol scale of metals and sealed in 1 mm walled fused quartz ampoules at or below 3×10^{-3} mbar. Due to the thickness of the tubes and the relatively large amount of molecular iodine being employed a ramp rate of 10 C / hr was used to heat samples to 500 C. Samples were held at 500 C for 10 hours and then cooled to RT in 10 hours. Samples from the elements cooled in this relatively fast manner display only a 1.7 eV absorption edge with no low energy transitions. Yield is 95 – 100 % based on Bi.

3.3.2. Synthesis of Narrow Gap $(\text{PbI}_2)_{1-x}(\text{BiI}_3)_x$

Pb and Bi (99.999% American Elements) were combined with I_2 (99.99% Sigma Aldrich or Alfa Aesar) in stoichiometric ratios at the 4 – 20 mmol scale of metals and sealed in 1 mm walled fused quartz ampoules at or below 3×10^{-3} mbar. Due to the thickness of the tubes and the relatively large amount of molecular iodine being employed a ramp rate of 10 C / hour was used to heat samples to 500 C. Samples were held at 500 C for 10 hours, cooled to 300 C in 100 hours, and then to 30 C in 10 hours. Alternatively, we also employed a cooling regime that cooled from 500 C to 400 C, in 2 hours, followed by cooling from 400 C to 300 C in 100 hours once thermal analysis was complete. Longer cooling times yield narrow gap material from the elements. Yield 95 – 100% based on Bi.

3.3.3. Conversion of Wide Gap $(\text{PbI}_2)_{0.5}(\text{BiI}_3)_{0.5}$ to Narrow Gap $(\text{PbI}_2)_{0.5}(\text{BiI}_3)_{0.5}$

Re-melting wide gap $(\text{PbI}_2)_{0.5}(\text{BiI}_3)_{0.5}$ at 500 C followed by cooling yields narrow gap $(\text{PbI}_2)_{0.5}(\text{BiI}_3)_{0.5}$. Wide gap material was loaded into a fused quartz ampoule and sealed at or below 3×10^{-3} mbar. The sample was heated to 500 C in 6 hours, held for 6 hours, and then cooled for 24 hours. The resulting material presents low energy absorption. Once samples are narrow gap they do not convert back to the wide gap with re-melting and cooling.

3.3.4. Solid State UV-Vis Spectroscopy

A Shimadzu UV-3600 PC double-beam, double-monochromator spectrophotometer was used to collect diffuse-reflectance spectra in the range of 200–2500 nm. The instrument was equipped with an integrating sphere and controlled by a personal computer. BaSO_4 was used as a standard and set to 100% reflectance. Samples were prepared by quickly placing the ground crystalline products on a bed of BaSO_4 in air. Collected reflectance data were converted to absorbance according to the Kubelka–Munk equation $\alpha/S = (1 - R)^2 / 2R$, where α is the absorption coefficient, S is the scattering coefficient, and R is the reflectance. The initial absorption was determined by extrapolating the intercept of the fitted converted data.

3.3.5. Powder X-ray Diffraction

Samples $\text{Pb}_{0.4}\text{Bi}_{0.4}\text{I}_2$ were examined by powder diffraction using a Rigaku Miniflex power X-ray diffractometer with Ni-filtered $\text{Cu K}\alpha$ radiation operating at 30 kV and 15 mA. Scans were performed with a resolution of 0.02° and a scan rate of $10^\circ/\text{min}$

3.3.6. Thermal Analysis

Thermal properties were determined by differential thermal analysis (DTA) conducted on a Netzsch STA 449 F3 Jupiter simultaneous thermal analysis (STA) instrument. Cleaved crystals

of $(\text{PbI}_2)_{0.5}(\text{BiI}_3)_{0.5}$ were ground into a fine powder which was then loaded (approximately 50 μg) into silica ampoules and flame sealed at or below 3×10^{-3} mbar. The sample was heated to 475 °C at a rate of 10 °C/min. Heating and cooling runs were repeated to observe if the thermal behavior was replicable.

3.3.7. TEM/STEM Microscope Conditions and Sample Preparation

A Cs-corrected JEOL ARM200CF transmission electron microscope equipped with a cold field emission gun was used for STEM imaging. The microscope was operated at 200kV acceleration voltage in STEM mode. Micrographs were acquired at electron probe sizes of 8C or 9C (JEOL defined) which are measured to be 1.28 Å and 1.2 Å respectively, and a pixel dwell time of 10~15 μs with 2048x2048 pixel² area. Utilized emission current of 8~13 μA results in probe current range of 10~20 pA. A 40- μm aperture was used resulting in a beam convergence semi-angle of $\alpha=27.5$ mrad. The semi-angle measuring active area to collect the ADF signal (i.e., the inner and outer radius) is 90-370 mrad. The electron dose introduced per image varied in around 1,000 ~2,000 $\text{e}/\text{Å}^2$ depending on magnification. Micrograph was taken under spherical aberration (C3) of 0.5~1 μm results in measured phase of 27~28 mrad. ABF images are obtained with a BF aperture of 3 mm with center beam stop producing semi-collection angle ranges in 10-23 mrad. TEM Imaging conducted done with JEOL GrandARM (or ARM300CF) TEM with a Gatan® Oneview CCD detector of large viewing area (2kx2k pixels²) that allowed rapid acquisition (0.1~0.2 s) with automatic drift correction. HRTEM was taken with large beam spread to limit total dose below 10 $\text{e}/\text{Å}^2$ in order to reduce irradiation effect.

3.3.8. DFT Method and Calculations

First-principles electronic structure calculations were carried out within the density functional theory (DFT) formalism using the Projector Augmented Wave method implemented in Vienna Ab-initio Simulation Package.^{128, 129} The energy cut off for plane wave basis was set to 350 eV, and the Monkhorst–Pack k -point grid of $7 \times 7 \times 7$ was used for Brillouin zone (BZ) sampling. For the exchange-correlation function, the generalized gradient approximation (GGA) was employed within Perdew–Burke–Ernzerhof (PBE) formalism.¹³⁰ To obtain the ground states for each compound, the crystal structures, the lattice parameters, and the positions of atoms in the cells were relaxed until the atomic forces on each atom are less than 0.01 eV/Å.

3.4. Results and Discussion

3.4.1. Synthetic Approach to Narrow and Wide Gap Samples

Samples of $(\text{PbI}_2)_{1-x}(\text{BiI}_3)_x$ were directly synthesized from the elements, Pb, Bi, and I_2 sealed in quartz ampoules heated in computer controlled furnace with profiles detailed in Table 6. For the majority of experiments we focused on mixtures where $x = 0.5$. We found that samples that were cooled with the initial regime were black and presented a band gap of approximately 1.73 eV akin to BiI_3 with no trace of the PbI_2 bandgap (Figure 57). The power x-ray diffraction (PXRD) patterns (Figure 58) of these initial preparations of $(\text{PbI}_2)_{0.5}(\text{BiI}_3)_{0.5}$ demonstrate diffuse diffraction patterns that do not match either parent binary but did contain peaks consistent with basal $00l$ reflections of layered structures. However, these samples were very brittle and were difficult to use as suitable samples for single crystal diffraction experiments.

To amend the mechanical issues of the samples we cooled the reactions slowly from 500 C to 300 C between the melting points of the parent binaries, as noted in Table 6. We found that

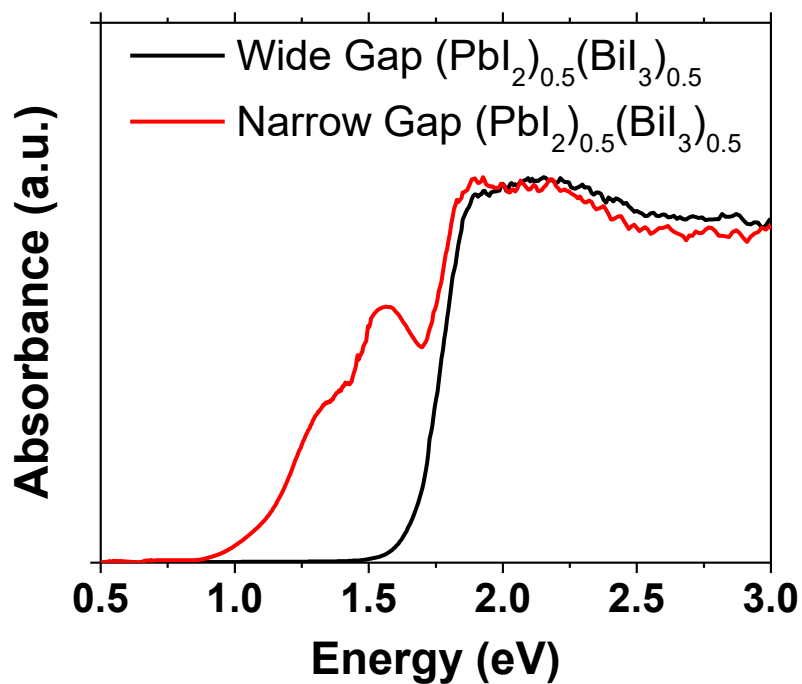


Figure 57. UV-Vis absorbance of the wide and narrow gap states of $(\text{PbI}_2)_{0.5}(\text{BiI}_3)_{0.5}$. Wide gap samples derive from quickly cooled melts of Pb, Bi and I_2 where the narrow gap behavior arises from slow cooling.

Table 6. Furnace Profiles for $(\text{PbI}_2)_x(\text{BiI}_3)_x$ Preparations

Run Type	Start T (C)	Target T (C)	Ramp Rate (C/Hr)	Hold Time (Hr)	Ramp to (C)	Rate (C/Hr)	Ramp To (C)	Rate (C/Hr)	Ramp To (C)	Rate (C/Hr)
Initial	RT	500	10	10	30	47	N/A	N/A	N/A	N/A
Slow Cool	RT	500	10	10	300	2	30	27	N/A	N/A
Standardized	RT	500	10	10	400	50	300	1	30	27

these samples displayed absorption behavior that began below that apparent band gap of BiI_3 and our fast-cooled samples (Figure 57). As such we deemed the samples that displayed the BiI_3 -type gap as “wide” gap materials and those that displayed the low energy absorption “narrow” gap samples. Narrow gap samples display a low energy absorption fraction beginning at approximately 0.9 eV, an exciton-like peak at 1.5 eV, followed by the same 1.73 eV gap as the wide gap material. These narrow gap samples also displayed similar diffuse diffraction behavior as the wide gap samples (Figure 58) but cleaved very well into independent crystalline flakes. After this revelation, we conducted Differential Thermal Analysis (DTA) on the material to determine the best cooling

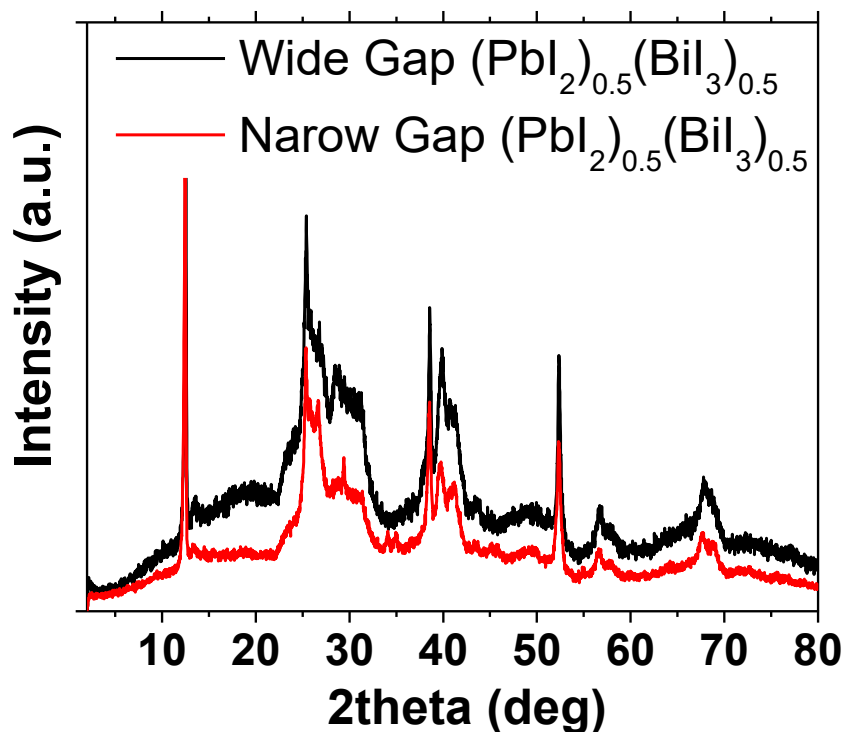


Figure 58. Wide and narrow gap powder diffraction patterns indicating that between wide and narrow gaps the sharp basal $00l$ reflections persist whereas the other reflections have become very diffuse.

regime to promote better crystallization (Figure 59) and found the melting and crystallization points to be 371 C and 381 C respectively. As such, we devised the standardized slow cooling synthetic process that cooled the reaction from 400 C to 300 C at 1 C / hour to promote crystallinity. These samples also displayed the characteristic narrow gap behavior.

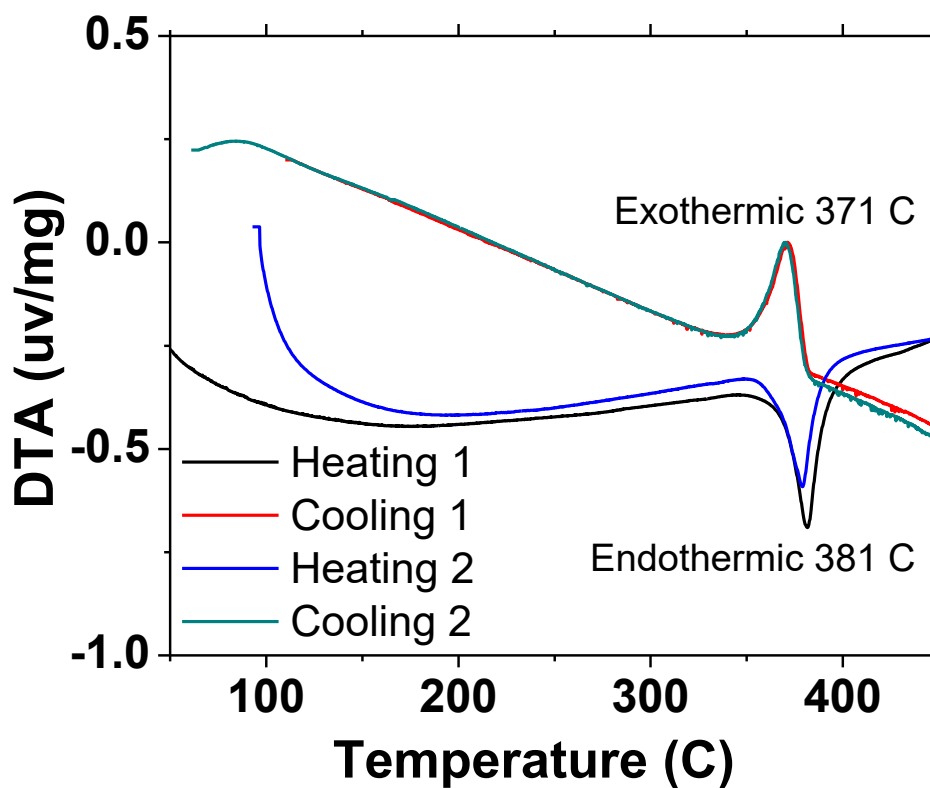


Figure 59. DTA demonstrates that the mixture $(\text{PbI}_2)_{0.5}(\text{BiI}_3)_{0.5}$ melts congruently at 381 C and crystallizes congruently at 371 C, below that of the parent binary mixtures.

With the puzzling distinction of narrow gap or wide gap $(\text{PbI}_2)_{0.5}(\text{BiI}_3)_{0.5}$ samples induced by cooling rate, we investigated the ability for interconversion between the two bandgap states. We found that if we re-melted the wide gap samples at 500 C and used slower cooling rate (24 hours) it induced narrow gap behavior (Figure 60). Additionally, annealing wide gap samples at 160 C for 24 hours did not induce interconversion (Figure 61). This negative annealing result supports our hypothesis that the origin of the narrow gap behavior is locked in upon crystallization. We also examined the stoichiometric effects of the mixtures of $(\text{PbI}_2)_{1-x}(\text{BiI}_3)_x$ on slow cooled

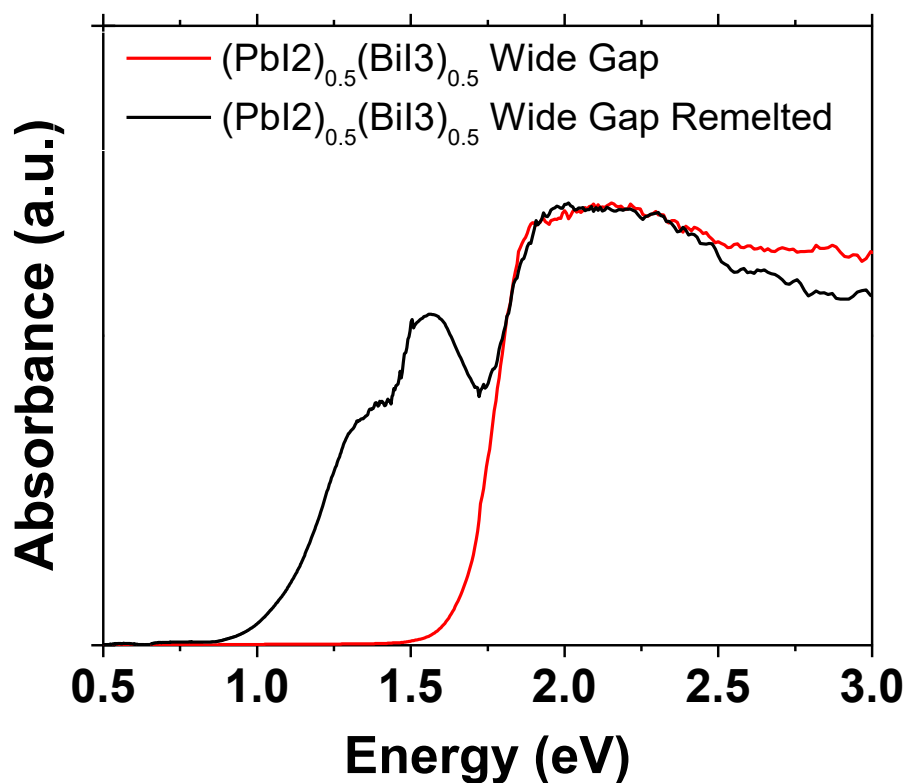


Figure 60. A wide gap sample of $(\text{PbI}_2)_{0.5}(\text{BiI}_3)_{0.5}$ was re-melted at 500 C and cooled for 24 hours, the resultant material was converted to narrow gap.

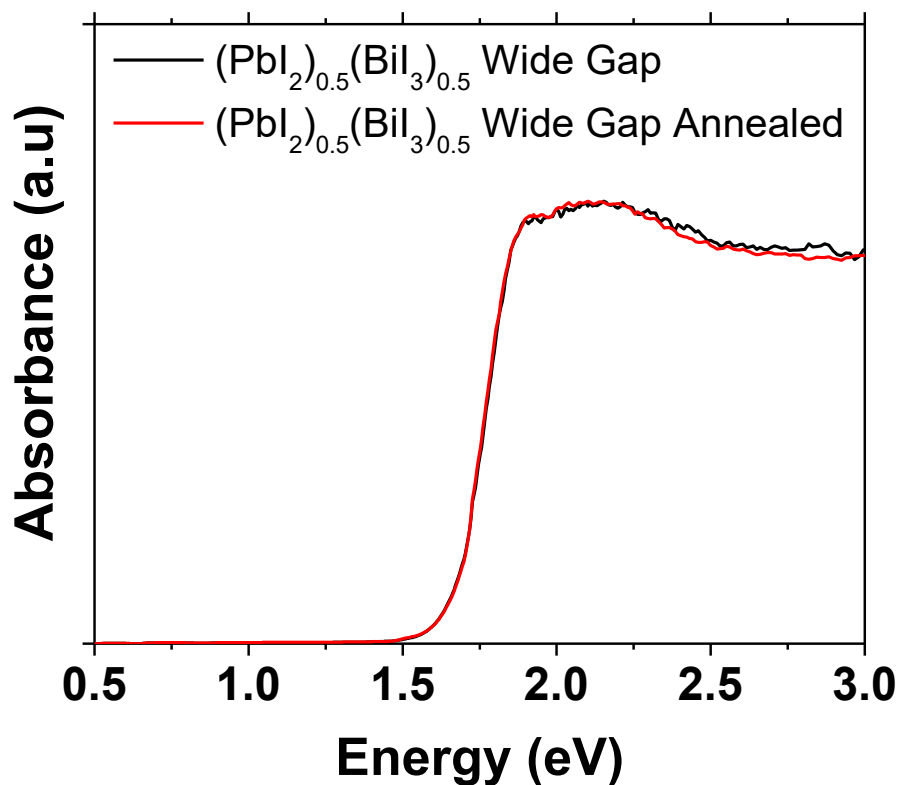


Figure 61. Wide gap material annealed at 160 C for 24 hours. No change in band gap was observed.

samples (Figure 62) which shows a dependence on BiI_3 , though no PbI_2 -like gaps are ever observed. However, this also demonstrates that as $x = 0.2$ BiI_3 in PbI_2 is enough to completely quell the gap while the low energy absorption is maximized around $x = 0.4$. This behavior is unconventional relative to other mixed metal systems where we expect anomalous trends.¹³¹⁻¹³³ Between these experiments, behavior indicative of structural features that need to be induced once by slow cooling that persist even with successive melting and cooling. As such, we needed to probe the structural features of both optically absorbing states of $(\text{PbI}_2)_{1-x}(\text{BiI}_3)_x$.

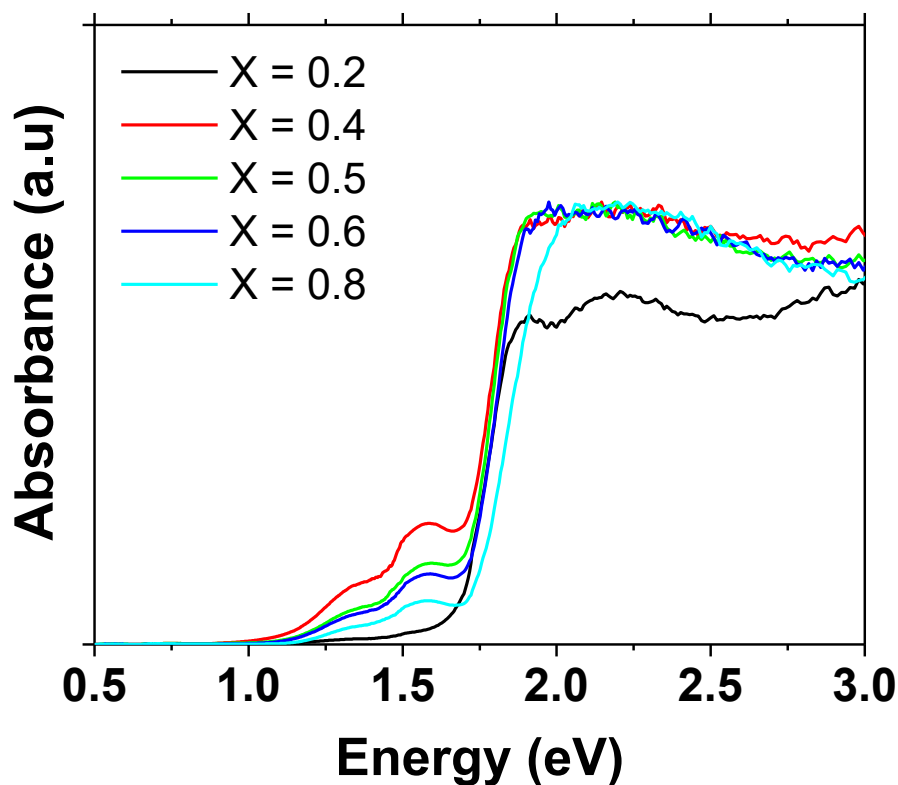


Figure 62. Compositional variation across multiple samples of $(\text{PbI}_2)_{1-x}(\text{BiI}_3)_x$ indicating that even at $x = 0.2$ the band gap is converted to that of BiI_3 and the low energy absorption is maximized at $x = 0.4$.

3.4.2. The Origin of Narrow Gap Behavior

As we discussed in our examination of the conductance switching properties of $(\text{PbI}_2)_{1-x}(\text{BiI}_3)_x$ mixtures in Chapter two, the X-ray powder diffraction patterns of wide and narrow gap samples contain both sharp Bragg reflections and diffuse scattering (Figure 58), indicating the inability of these materials to form long range, uniformly composed lattices. As we investigated these materials by Single Crystal X-ray Diffraction (SCXRD) and HRTEM we found that they were not only inhomogeneous but presented both phase integration and phase separation due to Pb

/ Bi rich domains (Figure 63). As shown in the optical spectra of Figure 57, the variable bandgap behavior between different cooling rate samples of the $(\text{PbI}_2)_{0.5}(\text{BiI}_3)_{0.5}$ could also be probed via HRTEM. The wide gap, fast cooled samples of $(\text{PbI}_2)_{0.5}(\text{BiI}_3)_{0.5}$ (Figures 63a,b), demonstrate in their HAADF images a very clear delineations between Pb-rich (brighter) and Bi-rich phases (darker) leading to well defined phase boundaries. The HAADF contrast is based on the average atomic number in the region, as such the Bi-rich regions appear darker as they contain approximately 1/3 less atoms as demonstrated in Figure 56. On the other hand, images of the narrow gap, slow cooled samples of $(\text{PbI}_2)_{0.5}(\text{BiI}_3)_{0.5}$ (Figure 63c,d) show more diffuse delineation between phase boundaries of Pb-rich (lighter) and Bi-rich (darker) phases. This diffusivity is evidence that we have greater mixing of Pb/Bi in these phase separating / integrating regions. Considering this, we sought to model these interfacial regions using Density Functional Theory (DFT) calculations to assess their impact on the observed band gaps.

We began to probe the nature of the band gaps of $(\text{PbI}_2)_{0.5}(\text{BiI}_3)_{0.5}$ using models based on the SCXRD structural study outlined in Chapter two. Taking the two-layered $\text{Pb}_{0.4}\text{Bi}_{0.4}\text{I}_2$ structure from that avenue of experimentation, we generated several supercells with random distributions of Pb, Bi, and the necessary vacancies for charge balance (examples found in Figures 56c and 64). We observed significant differences in the calculated Density of States (DOS) over the 5 configurations with band gaps ranging from 1.61 eV to 0.74 eV. To evaluate the difference in these systems, we needed to determine the level of mixing/demixing between Pb and Bi in their preferred lattices. We began by evaluating the six metal site neighbors of each vacancy in each layer of the system. From there the average number of Bi and Pb atoms to a given vacancy was calculated for each configuration as demonstrated in Figures 65, 66 and Tables 7, 8.

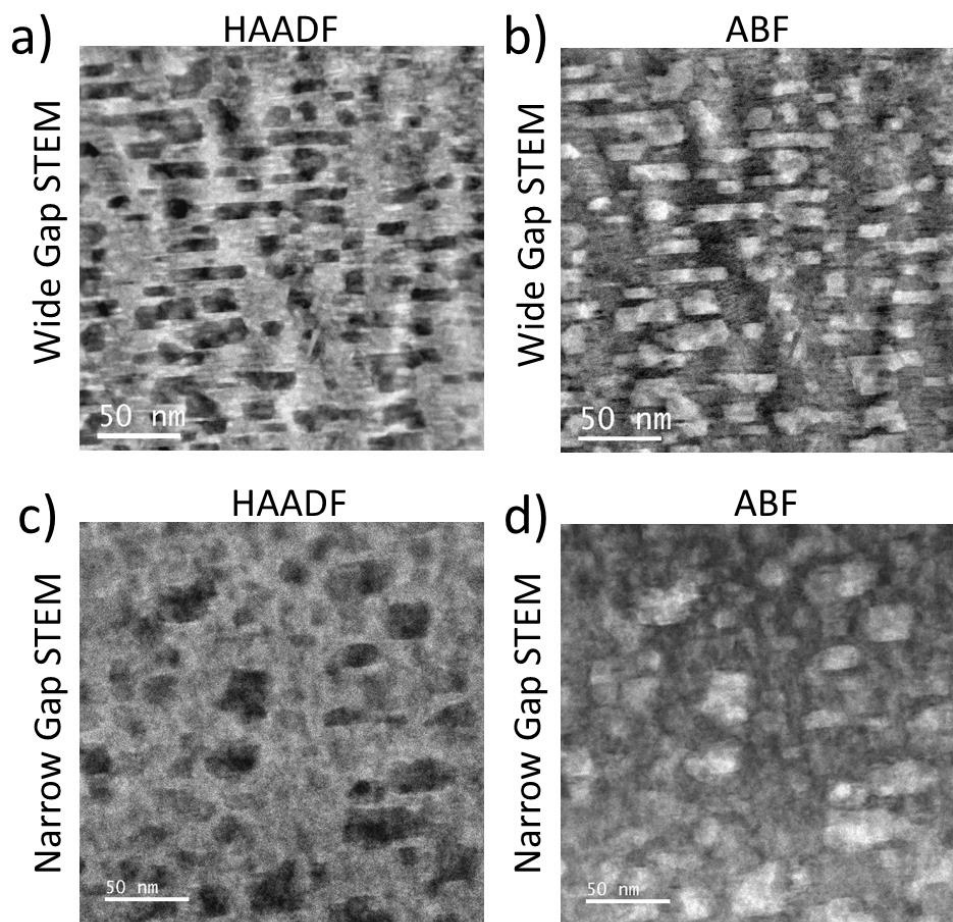


Figure 63. a, b) High angle annular dark field (HAADF) and annular bright field (ABF) images of wide gap $(\text{PbI}_2)_{0.5}(\text{BiI}_3)_{0.5}$ along the $[100]$ zone. The dark regions in the HAADF image correlate to Bi-rich regions where the overall Z is less than that of the bright Pb-rich regions due to $2/3$ of the metal atom density. This is reversed in the ABF image. The hallmark of these samples is distinct boundaries between Pb and Bi rich regions, indicative of our phase boundaries that give rise to conductance switching behavior in Chapter two. c, d) HAADF and ABF images of a narrow gap sample of $(\text{PbI}_2)_{0.5}(\text{BiI}_3)_{0.5}$, where dark regions in c again correlate to Bi-rich regions and the lighter correlate to Pb-rich regions. Here the clear phase boundaries that we observe in the wide gap samples are far more diffuse, indicating far more mixing between the Bi and Pb rich phases.

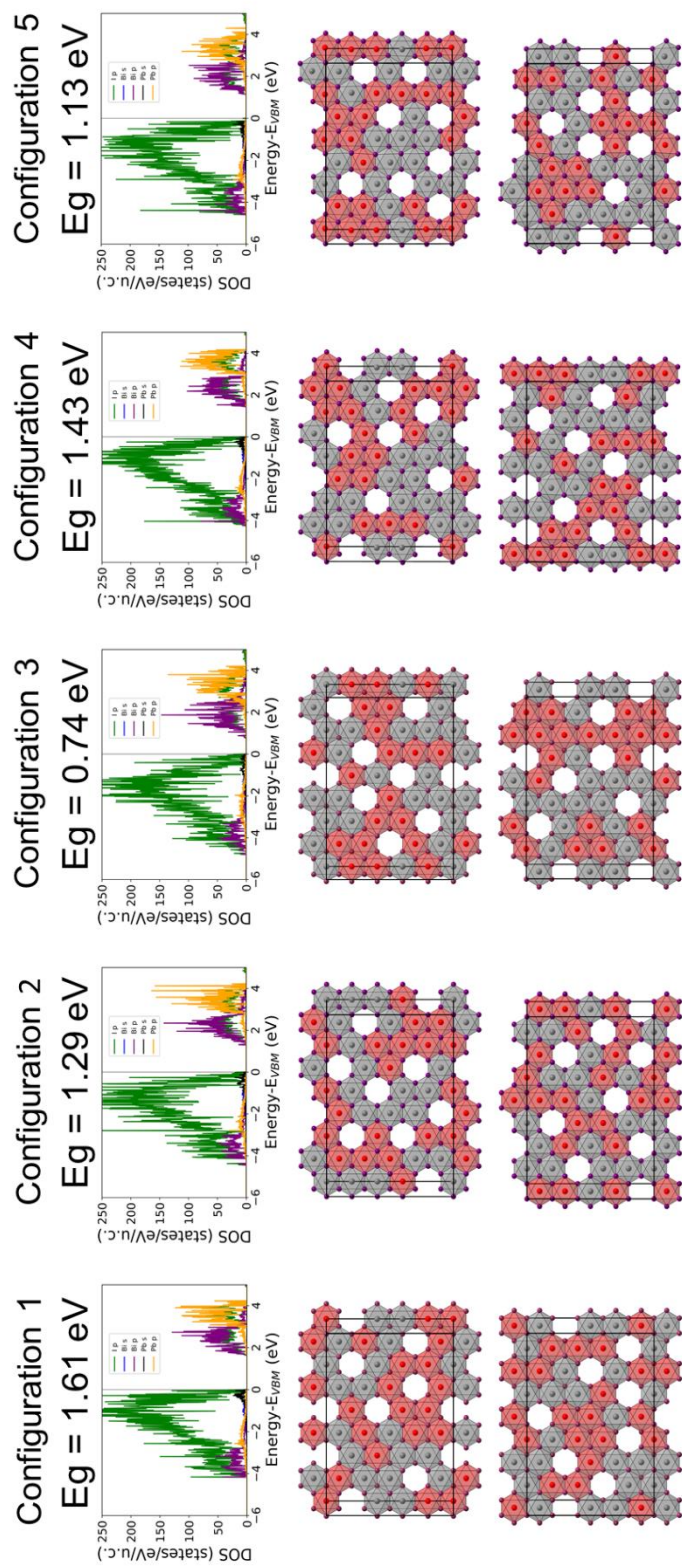
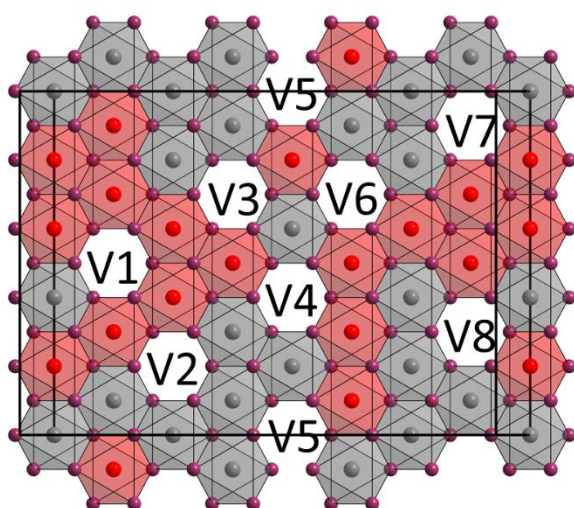


Figure 64. Configurations 1 through 5 of randomly generated supercells of $(\text{PbI}_2)_{0.5}(\text{BiI}_3)_{0.5}$. Configurations were

built via random number generation made with the assumption that no vacancies were adjacent in a supercell

model of the bilayer $\text{Pb}_{0.4}\text{Bi}_{0.4}\text{I}_2$ model described in Chapter two. Note that for configuration 3 the bandgap is the

smallest at 0.74 eV, whereas for configuration 1 the bandgap is the widest at 1.61 eV.



Vacancy Description

V1_L1: 5 Bi, 1 Pb

V2_L1: 2 Bi, 4 Pb

V3_L1: 3 Bi, 3 Pb

V4_L1: 3 Bi, 3 Pb

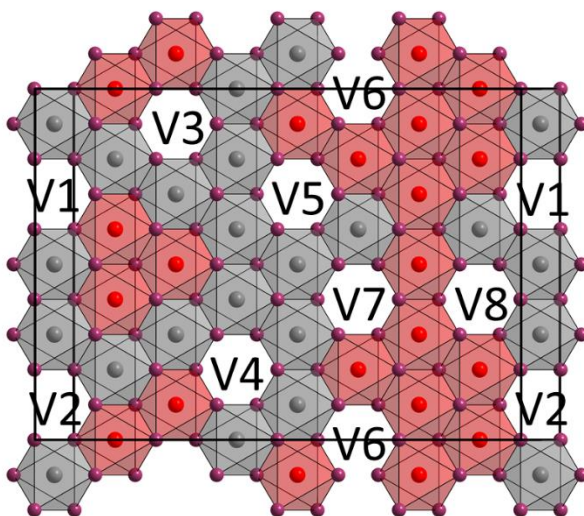
V5_L1: 2 Bi, 4 Pb

V6_L1: 3 Bi, 3 Pb

V7_L1: 2 Bi, 4 Pb

V8_L1: 2 Bi, 4 Pb

Figure 65. The top layer of configuration 3 as defined in the manuscript. Each vacancy was defined 1 – 8 and the nearest metal atoms were tabulated in Table 7. Every vacancy was defined in such a way for every configuration.



Vacancy Description

V1_L2: 2 Bi, 4 Pb

V2_L2: 3 Bi, 3 Pb

V3_L2: 2 Bi, 4 Pb

V4_L2: 1 Bi, 5 Pb

V5_L2: 2 Bi, 4 Pb

V6_L2: 5 Bi, 1 Pb

V7_L2: 3 Bi, 3 Pb

V8_L2: 3 Bi, 3 Pb

Figure 66. The bottom layer of configuration 3 as defined in the manuscript. Each vacancy was defined 1 – 8 and the nearest neighbors were tabulated in Table 7.

Table 7. Tabulated Results of the Vacancy Assessment for Configurations 1 – 5. (V = Vacancy)

Configuration	Layer 1		Layer 2		Layer 1		Layer 2		E _g (eV)
	Average	Average	Average	Overall Average Bi	Average	Average	Average	Overall Average Pb	
	Bi / V	Bi / V	Bi / V		Pb/V	Pb/V	Pb/V		
1	3.25	3.13	3.19	3.19	2.75	2.88	2.81	2.81	1.61
2	2.88	2.88	2.88	2.88	3.13	3.13	3.13	3.13	1.3
3	2.75	2.63	2.69	2.69	3.25	3.38	3.31	3.31	0.74
4	3.38	2.63	3.00	3.00	2.63	3.38	3.00	3.00	1.43
5	2.75	2.88	2.81	2.81	3.25	3.25	3.25	3.25	1.1

We hypothesized that the number of Bi neighbors to a vacancy would be more important than Pb, as vacancies are inherent to the structure of BiI₃ and not PbI₂. From the DFT calculations we were also able to extract the energy per formula unit of each configuration, which was defined from our structural model.

The clustering of Bi atoms in the layer is indicated by the decrease in the value of the average Bi neighbors at vacancies and correlates with the decrease in the observed band gap shown in Figure 64 and Table 8. In this case, we can see that for configuration **3** where $E_g = 0.74$ eV the average number of Bi neighbors at the vacancy is 2.69 Bi atoms compared than the 6 in pure BiI₃. As this average number of Bi neighbors increases to 3.18 in configuration **1**, the band gap increases to 1.61 eV akin to that of BiI₃. This supports that the clustering of Bi away from the vacancies into PbI₂-like lattices is responsible for narrowing the band gap. Electronically, the clustering of Bi aids in broadening the conduction band p states for both I and Bi, leading to mid-gap states that can begin to optically absorb at low energies. This is clearly observed by comparing DOS over the five configurations, Figure 68. Energy calculations additionally demonstrate the highest energy per formula unit (Table 8, Figure 67) correlates to the band gap, indicating the least stable is due to bismuth clustering. This is consistent with our observations by TEM, where narrow gap samples show more mixing at the apparent phase boundaries whereas wide gap samples show very clear separation between phases. These results strengthen our hypothesis that mixing/demixing in the (PbI₂)_{1-x}(BiI₃)_x at system can be controlled by the cooling rate, with fast cooling promoting clear phase delineation while slow cooling promoting additional mixing trapping Bi in more intermediate compositions with Pb.

Table 8. Configurations 1 through 5 of $(\text{PbI}_2)_{0.5}(\text{BiI}_3)_{0.5}$ listed in decreasing bandgap with the average number of Bi and Pb neighbors to each vacancy calculated between each layer. Energy per formula unit (f.u. = $\text{Pb}_{0.4}\text{Bi}_{0.4}\text{I}_2$) is calculated from each supercell of 32 formula units.

Configuration	Band Gap (eV)	Average Bi Neighbors	Average Pb Neighbors	Calculated Energy per formula unit (eV/f.u.)
1	1.61	3.18	2.82	-11.155
4	1.41	3.00	3.00	-11.135
2	1.27	2.88	3.12	-11.119
5	1.09	2.82	3.18	-11.072
3	0.74	2.69	3.31	-11.059

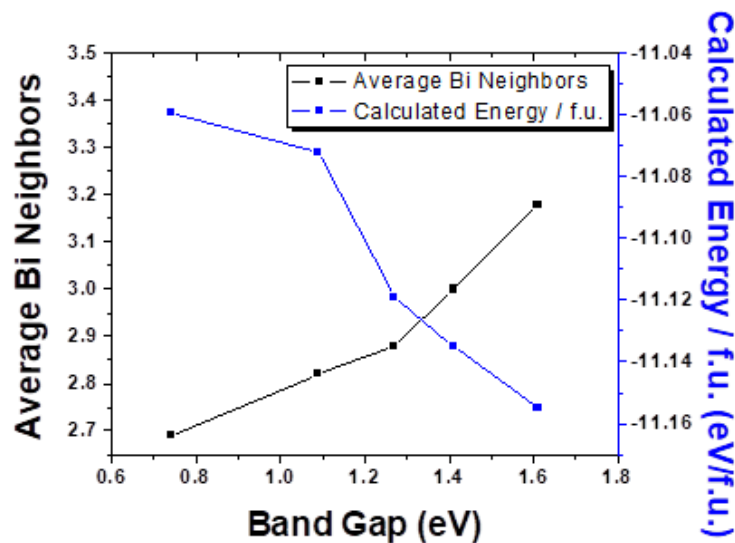


Figure 67. The band gap of Configurations 1 – 5 plotted as a function of Average Bi Neighbors per vacancy and Calculated Energy per formula unit. As the number of Bi neighbors increases at the vacancies the band gap increases and the eV/f.u. decreases.

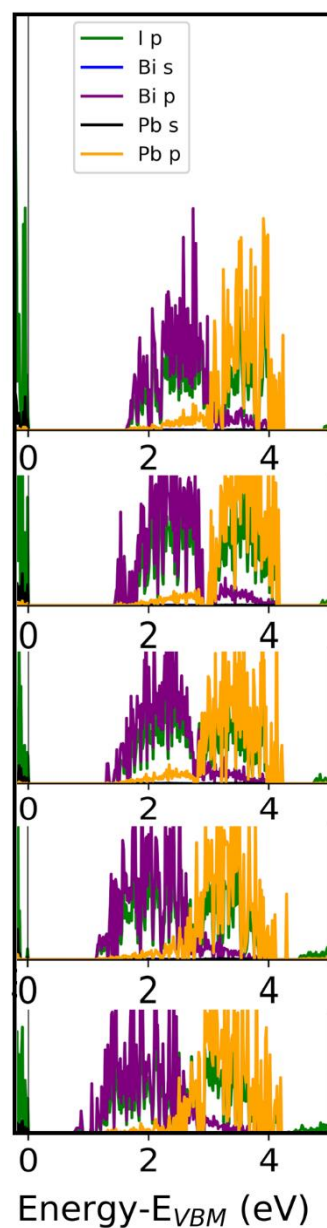


Figure 68. Expansion and Comparison of the DOS of the five supercell configurations. From top to bottom the band gap decreases from the 1.61 eV to 0.74 eV in the order defined in Table 8. Note the expansion of the Bi and I p states that leads to the decrease in the apparent band gap.

To further support our assertion that clustering of Bi atoms in the PbI_2 lattice is resultant in the narrowing of the apparent band gap, we built another model that clearly separated PbI_2 and BiI_3 phase within a monolayer (Figure 69a). DOS calculations from this model suggest that the well-defined regions have a band gap of 1.43 eV (Figure 69b). While the magnitude of the calculated band gap is still below that of the wide gap samples, this model still supports that for well-defined phase boundary systems there is no significant broadening in the Bi and I p states leading to narrow gap behavior. Considering the vast number of possible phase compositions at the boundaries of Pb-rich and Bi-rich regions, it is likely that a vast distribution of different atomic configurations exist at the phase boundaries with intermediate energies, with the most energetically unfavorable leading to the onset of the absorption edge.

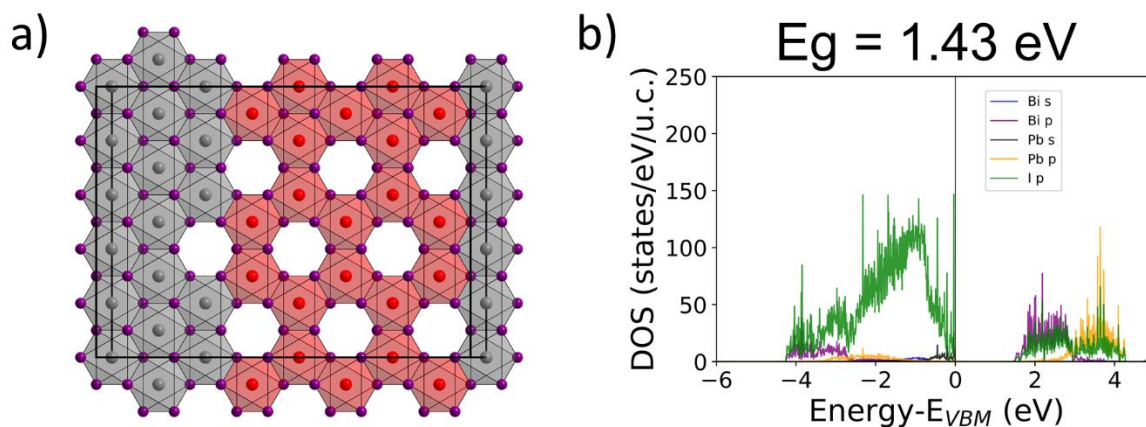


Figure 69. a) A well-defined phase boundary model built to probe the difference between it and the randomly generated configurations. b) The resulting calculated DOS from the model defined in a with a resultant gap of 1.43 eV. No significant broadening of the Bi and I p bands are observed.

3.5. Conclusion

The 2D $(\text{PbI}_2)_{1-x}(\text{BiI}_3)_x$ system displays tunable bandgap behavior driven by phase separation governed by the cooling regime of the material. As molten $(\text{PbI}_2)_{1-x}(\text{BiI}_3)_x$ is cooled, fast cooling regimes promote phase separation with clear boundaries between Pb and Bi rich regions. As the cooling rate is slowed, we promote the trapping of Bi in PbI_2 -like vacancy deficient lattices which yields material with narrow gap behavior. DFT and HRTEM experiments support this conclusion. This effect is unconventional in its manifestation, distinctly different than the anomalous band gap behavior observed in other mixed-heavy metal systems.

Our results display that for even for well documented materials, mixtures can elucidate interesting properties and effects. These results should drive not only the understanding and development of 2D materials, but also the effects of columbicly frustrated mixtures of optoelectronic materials.

Chapter 4

Rudorffite-like, Vacancy Dependent, and Copper Conducting Quaternary CuMBiI_6 ($\text{M} = \text{Cd}, \text{Pb}$) Phases

4.1. Abstract

The rudorffite-like quaternary copper containing heavy metal iodides CuMBiI_6 ($\text{M} = \text{Cd}, \text{Pb}$) are robust black materials which display completely different structural properties than their $(\text{MI}_2)_{0.5}(\text{BiI}_3)_{0.5}$ ($\text{M} = \text{Cd}, \text{Bi}$) parent compounds. CuPbBiI_6 crystallizes in the trigonal $R\bar{3}m$ space group with lattice parameters $a = 4.4125(5) \text{ \AA}$, $c = 20.815(3) \text{ \AA}$, $\gamma = 120^\circ$ where layers of octahedral edge sharing vacancy-dependent MI_6 ($\text{M} = \text{Pb}, \text{Bi}$) are bridged by diffuse copper occupancy between them to gain 3D connectivity. CuCdBiI_6 crystallizes in the cubic $Fd\bar{3}m$ space group with lattice parameter $a = 12.025(2) \text{ \AA}$ where similar octahedral edge sharing vacancy-dependent MI_6 form a defect-spinel type structure and diffuse copper occupancy is found across all tetrahedral sites. Synchrotron in situ PXRD finds that both compounds form upon heating. CuPbBiI_6 demonstrates well ordered high temperature phases upon cooling, whereas CuCdBiI_6 is found to form both a high temperature CuI phase and a hexagonal wurtzite-like phase with lattice parameters of $a = 4.3953 \text{ \AA}$ and $c = 7.1908 \text{ \AA}$ $\gamma = 120^\circ$ reminiscent of $\text{CuHg}_{0.5}\text{I}_2$. Electronic transport measurements on SPS samples of CuPbBiI_6 and CuCdBiI_6 reveal that both are relatively conductive, with hysteretic I-V curves indicative of Cu ion conductivity within the material.

Portions of this chapter will appear in the upcoming publication:

G. C. B. Alexander, M. G. Kanatzidis. "Rudorffite-like, Vacancy Dependent, and Copper Conducting Quaternary CuMBiI_6 ($\text{M} = \text{Cd}, \text{Pb}$) Phases" (In preparation)

4.2. Introduction

The development of the halide perovskites for photovoltaic^{12, 63} and detector^{66, 79} applications has been a fast growing field of study due to their desirable physical and electronic properties.^{73, 76} The result has been a dramatic development of new materials and phase based on Pb⁷³, Sn¹³⁴, and Ge^{123, 135}. While these materials have shown their promise and dramatic developments since their inception, Pb based materials suffer from environmental stability and toxicity concerns.⁸⁴ For this reason the Sn and Ge perovskites have been of interest. However, both Sn and Ge perovskites suffer from metal oxidation from 2+ to the 4+ state that hinders their air stability and requires encapsulation.^{136, 137} Consequently, materials based on non-oxidizable, non-toxic metals have been a target for optoelectronic applications. This has centered on the development of the bismuth iodide based materials due to bismuth's non-toxicity and the bismuth halides having appropriately low bandgaps for photovoltaic and detector based applications.¹¹⁴ As of now, the major materials to be investigated based on bismuth iodide have been the A₃Bi₂I₉ (A = CH₃NH₃, Rb, Cs; NH₄) compounds.^{99, 101, 138} All of these have been based around the 0D and 2D defect-perovskite crystal structure that was discussed in **1.3.4** which suffer from lower dimensionality than the 3D perovskites which limits their conductive properties. Similarly, their larger band gaps > 2 eV reduce their efficacy for solar cells while still promoting their development for hard radiation detection.¹³⁹

While these lower dimensionality bismuth iodide materials are still being investigated for optimization and applications, a class of ternary silver bismuth iodide Rudorffites has been display 3D structures that order between AgI₆ and BiI₆ octahedra (Figure 70a).¹⁴⁰ These materials have so far been targeted for development for photovoltaics.^{140, 141} AgBiI₄, AgBi₂I₇, Ag₂BiI₅, and Ag₃BiI₆

all demonstrate a crystal structure that is vacancy dependent, where alternating layers of $M''X$ and $M'X$ are composed of Ag, Bi, and vacancies, Δ . The halide sites are fully occupied. Within some compositions it is possible to find additional symmetry due to possible ordering of the metals and vacancies within the lattice which leads to monoclinic or cubic cells (Figure 70b, c).¹⁴⁰ These materials all display band gaps within the range of 1.8 eV, which is desirable for photovoltaics and within the range of band gaps for detector materials as set out in 1.2. Additionally, these materials have the applicable densities and high Z which suggested their applicability in hard radiation detector materials.

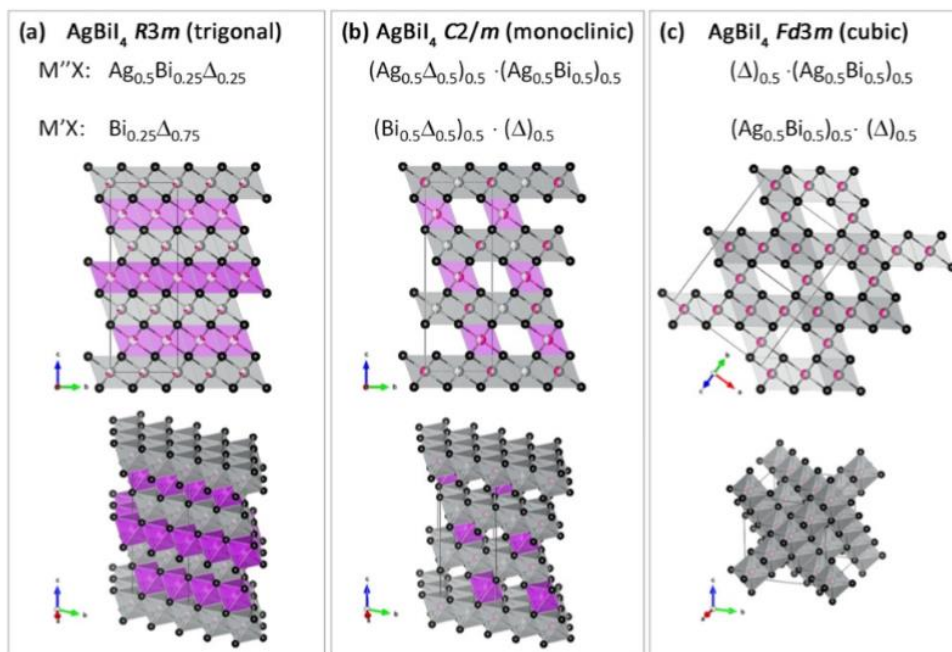


Figure 70. a) The hexagonal 3D structure of the rudorffite $AgBiI_4$ which consists of layers of Ag, Bi, Δ and Bi, Δ . The results is highly defect ridded crystal structure. b) A representation of the monoclinic structure of $AbBiI_4$ which demonstrates alternative ordering of Ag, Bi, and Δ that leads to monoclinic symmetry. c) The highly symmetric cubic crystal structure of $AgBiI_4$ which arises from equal ordering of Ag, Bi, and Δ on all sites. Adpated from Reference 140

While the silver bismuth iodide rudorffites have been well examined for solar applications we took inspiration from these phases ability to use the addition of a noble metal, not a alkali metal, to engender higher 3D dimensionality from the 2D BiI₃ structure type. With the Ag compounds being well characterized, Cu¹⁺ was selected as an alternate noble metal be investigated. While CuBiI₄ and Cu₂BiI₅ have previously been reported, they were found to be incongruently melting and are difficult to make in pure phase.¹⁴² With our understanding that the (PbI₂)_{1-x}(BiI₃)_x layered mixtures explored in Chapters two and three were congruently melting, defect ridden, and van der Waals materials, we hypothesized that the addition of CuI to these mixtures may generate additional structural features akin to the rudorffites.

Here, we demonstrate that the addition of CuI to the (MI₂)_{0.5}(BiI₃)_{0.5} (M = Cd, Pb) yields two highly disordered quaternary rudorffite type phases with impressive diffuse Cu occupancy. What we deemed CuPbBiI₆, **1**, crystallizes in the hexagonal *R-3m* space group of the typical rudorffite structure. To further expand our understanding of the system we attempted to reduce the size of the divalent cation by substituting Cd for Pb yielding CuCdBiI₆, **2**, a cubic *F-d3m* defect spinel also containing impressive diffuse copper disorder on the tetrahedral sites. Starting from a synthetic approach we examine both quaternary heavy metal halides and evaluated their structures, formation via *in situ* PXRD, and their transport properties. We demonstrate that the addition of Cu to (MI₂)_{0.5}(BiI₃)_{0.5} (M = Cd, Pb) yields not only unprecedented structural chemistry, but also robust copper ion conduction.

4.3. Materials and Methods

4.3.1. Bulk Synthesis of CuPbBiI_6 (1)

Stoichiometric amounts of CuI (Sigma Alrdich, 99.98%), PbI_2 (Sigma Aldrich 99.999%), BiI_3 (Sigma Aldrich 99.999%) stoichiometric ratios at the 4 mmol scale of metals and sealed in 1 mm walled fused quartz ampoules at or below 3×10^{-3} mbar. Samples were heated to 650 C at a rate of 100 C / hr, held at 650 C for 10 hours, and then quenched in ice water baths to limit non-stoichiometry of Cu. The resultant ingots were black, dense, and difficult to break apart. This is strikingly different than that of the layered $(\text{PbI}_2)_{0.5}(\text{BiI}_3)_{0.5}$ which are very soft. Yield is 95 – 100% based on Bi.

For larger synthesis to gain powder for spark plasma sintering (SPS) CuI (Sigma Aldrich 99.99%) was combined with Pb (American Elements 99.999%), Bi (American Elements 99.999%), and I_2 (99.99% Sigma Aldrich or Alfa Aesar) and sealed in 1 mm walled fused quartz ampoules at or below 3×10^{-3} mbar. Due to the thickness of the tubes and the relatively large amount of molecular iodine being employed a ramp rate of 10 C / hr was used to heat samples to 650 C. Samples were held at 650 C for 10 hours and then water quenched to limit non-stoichiometry of Cu within the ingot. The ingot remained black, dense, and difficult to break apart. Yield is 95 – 100 % based on Bi.

For single crystal diffraction experiments Stoichiometric amounts of CuI (Sigma Alrdich, 99.98%), PbI_2 (Sigma Aldrich 99.999%), BiI_3 (Sigma Aldrich 99.999%) stoichiometric ratios at the 4 mmol scale of metals and sealed in 1 mm walled fused quartz ampoules at or below 3×10^{-3} mbar. Samples were heated to 650 C at a rate of 100 C / hr, held at 650 C for 10 hours, and cooled

quickly to 400 C. Samples were further cooled to 300 C in 100 hr followed by furnace quenching. The resultant ingots were black, dense, and difficult to break apart. This is strikingly different than that of the layered $(\text{PbI}_2)_{0.5}(\text{BiI}_3)_{0.5}$ which are very soft. Yield is 95 – 100% based on Bi.

4.3.2. Bulk Synthesis of CuCdBiI_6 (2)

Stoichiometric amounts of CuI (Sigma Aldrich, 99.98%), CdI_2 (Sigma Aldrich 99.999%), BiI_3 (Sigma Aldrich 99.999%) stoichiometric ratios at the 4 mmol scale of metals and sealed in 1 mm walled fused quartz ampoules at or below 3×10^{-3} mbar. Samples were heated to 650 C at a rate of 100 C / hr, held at 650 C for 10 hours, and then quenched in ice water baths to limit non-stoichiometry of Cu. The resultant ingots were black, dense, and difficult to break apart. This is strikingly different than that of the layered $(\text{PbI}_2)_{0.5}(\text{BiI}_3)_{0.5}$ which are very soft. Yield is 95 – 100% based on Bi.

For larger synthesis to gain powder for spark plasma sintering (SPS) CuI (Sigma Aldrich 99.99%) was combined with Cd (American Elements 99.999%), Bi (American Elements 99.999%), and I_2 (99.99% Sigma Aldrich or Alfa Aesar) and sealed in 1 mm walled fused quartz ampoules at or below 3×10^{-3} mbar. Due to the thickness of the tubes and the relatively large amount of molecular iodine being employed a ramp rate of 10 C / hr was used to heat samples to 650 C. Samples were held at 650 C for 10 hours and then water quenched to limit non-stoichiometry of Cu within the ingot. The ingot remained black, dense, and difficult to break apart. Yield is 95 – 100 % based on Bi.

For single crystal diffraction experiments Stoichiometric amounts of CuI (Sigma Aldrich, 99.98%), CdI_2 (Sigma Aldrich 99.999%), BiI_3 (Sigma Aldrich 99.999%) stoichiometric ratios at

the 4 mmol scale of metals and sealed in 1 mm walled fused quartz ampoules at or below 3×10^{-3} mbar. Samples were heated to 650 C at a rate of 100 C / hr, held at 650 C for 10 hours, and cooled quickly to 400 C. Samples were further cooled to 300 C in 100 hr followed by furnace quenching. The resultant ingots were black, dense, and difficult to break apart. This is strikingly different than that of the layered $(\text{PbI}_2)_{0.5}(\text{BiI}_3)_{0.5}$ which are very soft. Yield is 95 – 100% based on Bi.

4.3.3. Spark Plasma Sintering (SPS)

A SPS-211LX, Fuji Electronic Industrial Co. Ltd SPS system was utilized to press pellets from powder of **1** and **2**. Powders were ground and sieved at 150 μm , loaded into 12.7 mm graphite dies and sintered at 200 C and 40 MPa for 10 minutes into ingots. Ingots were then cut via computer-controlled saw under oil to yield smaller pellets and cleaned with hexanes. Pellets were then annealed at 200 C in powdered material for 24 hours. Pellets were then polished mechanically with successively finer SiC grinding paper.

4.3.4. Structural Characterization

4.3.4.1. Powder X-ray Diffraction

Samples **1** and **2** were examined by powder diffraction using a Rigaku Miniflex power X-ray diffractometer with Ni-filtered Cu $K\alpha$ radiation operating at 30 kV and 15 mA. Scans were performed with a resolution of 0.02° and a scan rate of $10^\circ/\text{min}$. Simulated powder patterns of $(\text{PbI}_2)_{0.5}(\text{BiI}_3)_{0.5}$ were calculated using the refined room-temperature crystal structure CIF with MERCURY, part of the CSD software suite.¹¹⁹

4.3.4.2. Single Crystal X-ray Diffraction

Data collection for **1** and **2** were performed on a STOE IPDS II diffractometer using Mo K α radiation ($\lambda = 0.71073 \text{ \AA}$) operating at 50 kV and 40 mA at 293 K. Crystals of were isolated from the reaction ingot and fixed to glass fibers using super glue. Data collection was performed as 1° scans in ω at from 0 to 180° an optimized ϕ angle. Integration and numerical absorption corrections were performed on each structure using X-AREA, X-RED, and X-SHAPE.¹²⁰ The structure solved by the direct method and refined on F^2 using the SHELX14 program suite.¹²¹

4.3.4.3. In Situ Powder X-ray Diffraction at 11-BM

In situ synchrotron PXRD was taken at sector 11-BM at the Advanced Photon Source (APS) with wavelength $\lambda = 0.457658 \text{ \AA}$. The constituent binaries of **1** and **2** were ground together, sieved at $53 \mu\text{m}$, and diluted with $53 \mu\text{m}$ sieved ground fused silica 50% by weight and packed into 0.3 mm quartz capillaries. These capillaries were rotated at approximately 600 rpm and heated from room temperature to 500 C and back to room temperature in variable steps in regions of interest.

4.3.5. Thermal Analysis

Thermal properties were determined by differential thermal analysis (DTA) conducted on a Netzsch STA 449 F3 Jupiter simultaneous thermal analysis (STA) instrument. Samples of **1** and **2** were ground into a fine powder which was then loaded (approximately 50 ug) into silica ampoules and flame sealed at or below 3×10^{-3} mbar. The sample was heated to 475°C at a rate of $10^\circ\text{C}/\text{min}$. Heating and cooling runs were repeated to observe if the thermal behavior was replicable.

4.3.6. Scanning Electron Microscopy

A Hitachi S-3400 scanning electron microscope equipped with a PGT energy-dispersive X-ray analyzer was used to acquire images and semi quantitative Energy Dispersive Spectroscopy by X-ray (EDS) analyses. Spectra were collected using an accelerating voltage of 25 KeV and current of 70 uA for 60 s. No reduction of Cu was observed during the SEM experiments due to the electron beam. The reported compositions from EDS is based on multiple independent spectra.

4.3.7. Solid State UV-Vis Spectroscopy

A Shimadzu UV-3600 PC double-beam, double-monochromator spectrophotometer was used to collect diffuse-reflectance spectra in the range of 200–2500 nm. The instrument was equipped with an integrating sphere and controlled by a personal computer. BaSO₄ was used as a standard and set to 100% reflectance. Samples were prepared by quickly placing the ground crystalline products on a bed of BaSO₄ in air. Collected reflectance data were converted to absorbance according to the Kubelka–Munk equation $\alpha/S = (1 - R)^2 / 2R$, where α is the absorption coefficient, S is the scattering coefficient, and R is the reflectance.¹⁴³

4.3.8. Electronic Property Measurements

The I-V characterization curves and single bias measurements were conducted on a Keithley 6517B electrometer over multiple bias ranges. Contacts were applied to each side of pellets of **1** and **2** using graphite paint and copper wire leads and adhered to copper tape with graphite paint. Alligator clamps from the Keithley were connected to the copper tape. A Labview GUI was used to control the electrometer, which allowed for any number of seconds of delay to be added after bias applied to mitigate initial polarization. Successive sampling was averaged over the number of seconds of collection for a single point.

4.4. Results and Discussion

4.4.1. Synthesis and Thermal Behavior

The initial syntheses of **1** and **2** demonstrate that the addition of Cu into the $(MI_2)_{0.5}(BiI_3)_{0.5}$ (M = Cd, Pb) 2D materials yields compounds with much more robust mechanical properties. Once ingots were removed from the fused quartz ampoules they needed to be shattered by force in order to gather smaller samples sufficient for single crystal diffraction and to be ground for powder x-ray diffraction. This is contrary to their original van der Waals layered materials where crystals were readily cleaved from the ingots. Samples were initially quenched because we hypothesized this would increase the relative crystallinity of the samples and reduce some of the disorder observed in the powder diffraction patterns of **1**. (Figure 71) Additionally, previous syntheses of $AgBiI_4$ and Ag_3BiI_6 compounds demonstrate variable Ag compositions which can be mitigated by quenching the melt.¹⁴⁴ However, for **1** we observe that between the quenching and slow cooling there is no significant difference other than the resolution of the first Bragg reflection at 12.7° . With our understanding of the $(PbI_2)_{0.5}(BiI_3)_{0.5}$ system it is unsurprising that in the rudorffite-type structure similar degrees of disorder might occur. In the case of **2** both quenching and slow cooling do not yield significantly different results (Figure 72). Peaks are sharp and are distinctly different from that of **1**.

Thermal analysis of both **1** and **2** is shown in Figure 73 and 74. Interestingly, while the material displays much more mechanical robustness with the addition of copper, the melting points of both solids are below that of the MI_2 and BiI_3 mixtures (Figure 21 in Chapter two and Figure 75). This is curious as the synthesis of both **1** and **2** is found to be incomplete if temperatures under the melting point of CuI are used (606 C), yet the products of these reactions display melting and

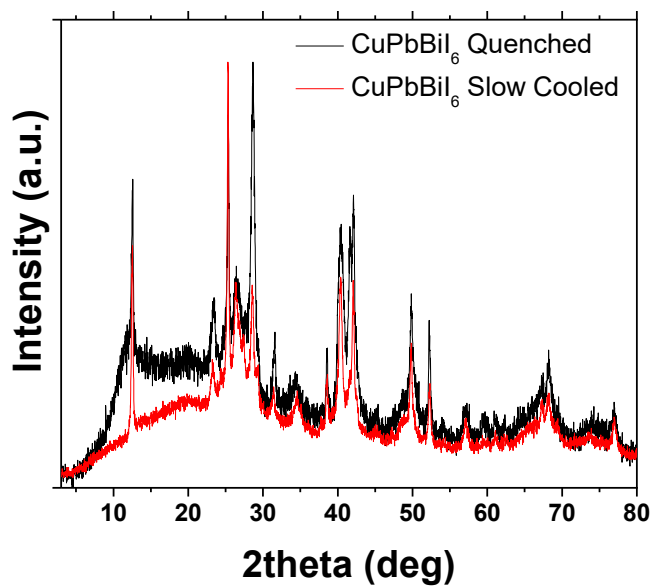


Figure 71. PXRD patterns of quenched and slow cooled samples of **1**. Note the similar, but less intense level of diffuse diffraction that was observed for the $(\text{PbI}_2)_{0.5}(\text{BiI}_3)_{0.5}$ system in chapters two and three.

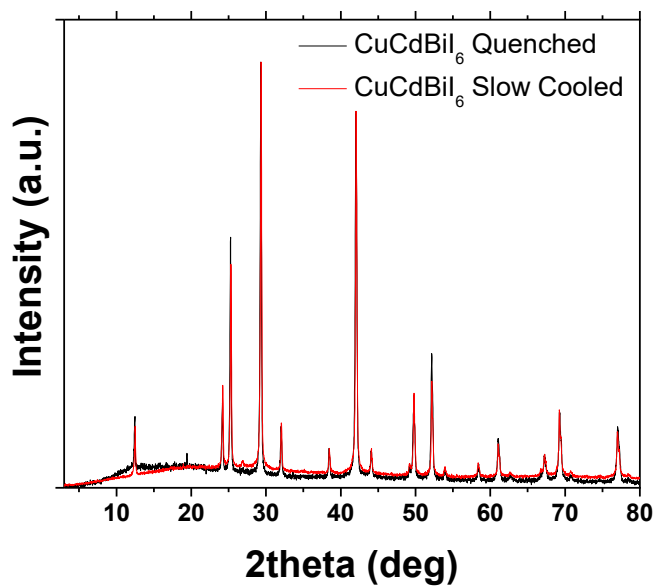


Figure 72. PXRD patterns of quenched and slow cooled samples of **2**.

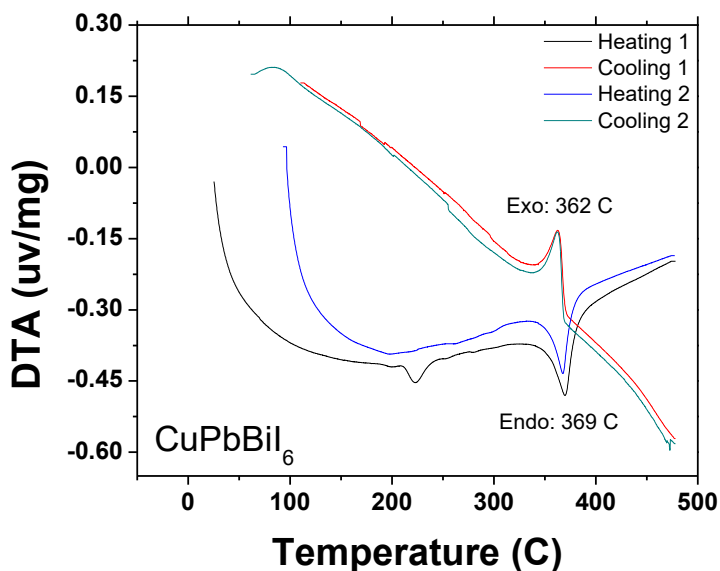


Figure 73. Differential thermal analysis of **1** showing congruent melting and crystallization at 369 C and 362 C respectively. The small peak at 220 C in the first heating cycle does not reoccur in the second cycle, indicating a possible phase transition or incomplete reaction.

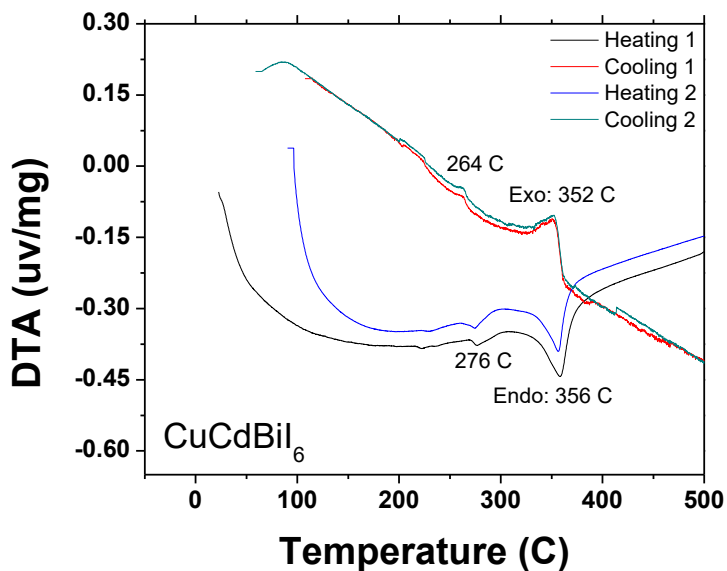


Figure 74. Differential thermal analysis of **2** showing congruent melting and crystallization at 352 C and 356 C respectively. The additional peaks at 264 C and 276 indicate the possibility of a high temperature phase.

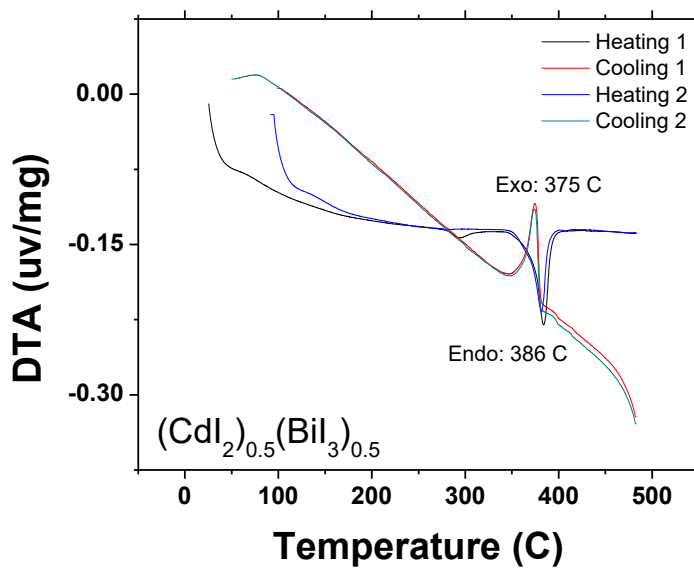


Figure 75. Differential thermal analysis of the precursor $(\text{CdI}_2)_{0.5}(\text{BiI}_3)_{0.5}$ to CuCdBiI_6 demonstrating melting of crystallization points of 375 C and 386 C respectively. The small endothermic peak in the first heating cycle can be attributed to polytype transitions in CdI₂-type van der Waals materials.

crystallization points far below that value. Contrary to other syntheses in the Cu – Bi – I system, both **1** and **2** display congruent melting and crystallization behavior.¹⁴²

4.4.2. Single Crystal X-ray Diffraction Analysis of CuPbBiI_6 (**1**)

Using the slow cooling method developed from chapter two we sufficiently cooled material of **1** to attempt to achieve better crystallinity. As noted above, this did not result in less diffuse diffraction, but did yield material that was sufficient for SCXRD. Surprisingly, despite the diffuse disorder the single crystal samples diffracted well and a solution was able to be obtained. **1** crystallizes in the trigonal space group $R\bar{3}m$ with refinement and lattice parameters given in Table 9. Additional thermal parameters and atomic coordinates are given in Tables 10 and 11.

The structure of **1** is reminiscent of the rudorffite structure, where mixed Ag, Bi, and vacancy sites, Δ , occupy one layer and the other is purely silver and vacancies with all halide sites filled (Figures 76 and 77). Here, a similar trend is found where we find mixed Pb, Bi, and Δ edge sharing octahedra occupying one layer exclusively, where metals have $2/3$ occupancy relative to $1/3$ vacancies. Like the case in chapter two, lead and bismuth are not crystallographically refinable due to being neighbors. Their relative occupancy was split in accordance with our SEM-EDS results (Figure 79, Table 12) after the occupancy of the metal on the site was freely refined to find the Δ “occupancy”. Of greater interest is that copper displays diffuse disorder over three different sites both between and nestled into the Pb, Bi layer which were able to be refined to between 4 and 6% occupancy. These copper atoms had to be fixed and refined isotopically, however after the DAMP command was removed subsequent refinements were stable and R1 did not increase. Iodine atoms were able to readily refine anisotropically and were fully occupied.

Table 9. Crystal data and structure refinement for CuPbBiI₆ at 293 K.

Empirical formula	CuPbBiI ₆
Formula weight	1241.01
Temperature	293 K
Wavelength	0.71073 Å
Crystal system	Trigonal
Space group	<i>R</i> -3 <i>m</i>
Unit cell dimensions	a = 4.4125(5) Å, α = 90° b = 4.4125(5) Å, β = 90° c = 20.815(3) Å, γ = 120°
Volume	350.97(9) Å ³
Z	1
Density (calculated)	5.872 g/cm ³
Absorption coefficient	39.109 mm ⁻¹
F(000)	512
Crystal size	0.159 x 0.072 x 0.034 mm ³
θ range for data collection	2.936 to 24.999°
Index ranges	-5 ≤ h ≤ 5, -5 ≤ k ≤ 5, -24 ≤ l ≤ 24
Reflections collected	1965
Independent reflections	103 [R _{int} = 0.0838]
Completeness to θ = 24.999°	100%
Refinement method	Full-matrix least-squares on F ²
Data / restraints / parameters	103 / 0 / 12
Goodness-of-fit	1.348
Final R indices [I > 2σ(I)]	R _{obs} = 0.0649, wR _{obs} = 0.1379
R indices [all data]	R _{all} = 0.0649, wR _{all} = 0.1379
Extinction coefficient	0.013(4)
Largest diff. peak and hole	3.969 and -7.984 e·Å ⁻³

$R = \frac{\sum ||F_o| - |F_c||}{\sum |F_o|}$, $wR = \frac{(\sum [w(|F_o|^2 - |F_c|^2)^2])^{1/2}}{\sum [w(|F_o|^4)]^{1/2}}$ and $w = 1/[\sigma^2(F_o^2) + (0.1056P)^2]$ where $P = (F_o^2 + 2F_c^2)/3$

Table 10. Atomic coordinates ($\times 10^4$) and equivalent isotropic displacement parameters ($\text{\AA}^2 \times 10^3$) for CuPbBiI_6 at 293 K with estimated standard deviations in parentheses.

Label	x	y	z	Occupancy	U_{eq}^*
Bi(1)	3333	6667	6667	0.3334	20(2)
Pb(1)	3333	6667	6667	0.3334	20(2)
I(02)	6667	3333	5796(1)	1	15(2)
Cu(3)	6667	3333	7080(30)	0.05(2)	10(30)
Cu(2)	10000	0	5260(40)	0.0459	12(4)
Cu(1)	6667	3333	4540(20)	0.06	12(4)

* U_{eq} is defined as one third of the trace of the orthogonalized U_{ij} tensor.

Table 11. Anisotropic displacement parameters ($\text{\AA}^2 \times 10^3$) for CuPbBiI_6 at 293 K with estimated standard deviations in parentheses.

Label	U_{11}	U_{22}	U_{33}	U_{12}	U_{13}	U_{23}
Bi(1)	21(2)	21(2)	18(2)	10(1)	0	0
Pb(1)	21(2)	21(2)	18(2)	10(1)	0	0
I(02)	18(2)	18(2)	10(2)	9(1)	0	0

The anisotropic displacement factor exponent takes the form: $-2\pi^2[h^2a^{*2}U_{11} + \dots + 2hka^*b^*U_{12}]$.

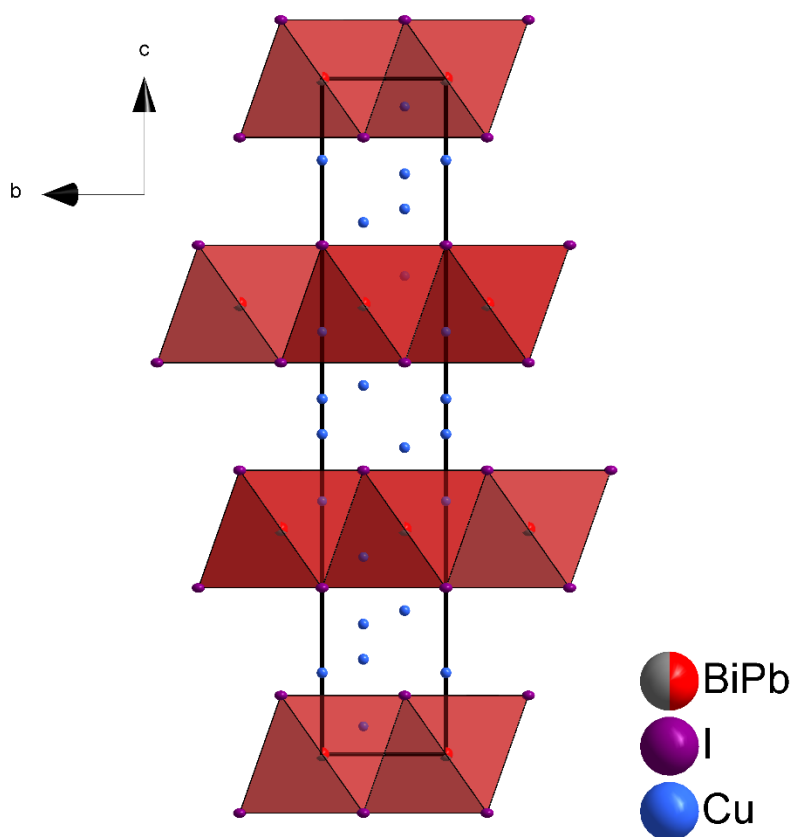


Figure 77. The rudorffite-like unit cell of **1** where Cu sites and Pb, Bi, and Δ sites occupy one layer dominated by edge sharing octahedra. Diffuse Cu disorder leads to the generation of the second layer as better shown in Figure 78. The metal site contains $2/3$ metal and $1/3$ vacancies and metal composition is set to equal amounts of Pb and Bi. Anisotropic parameters are shown for the heavy metal site and I.

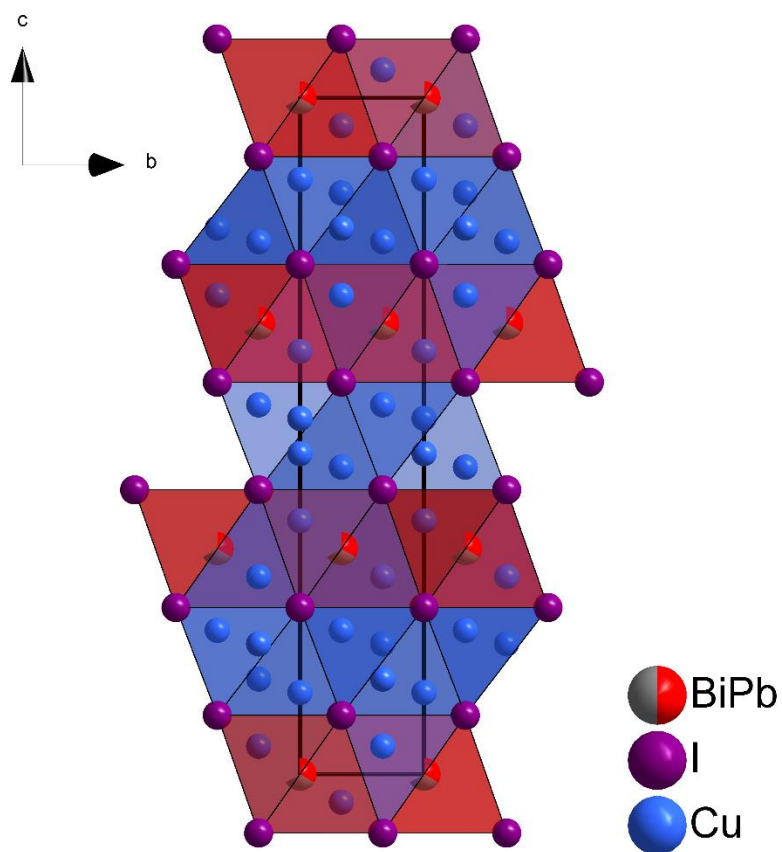


Figure 78. The rudorffite-like unit cell of **1** where Cu sites and Pb, Bi, and Δ sites occupy one layer and diffuse Cu disorder leads to the generation of the second layer. There the coordination polyhedra have been added to the Cu atoms to further explore the rudorffite behavior.

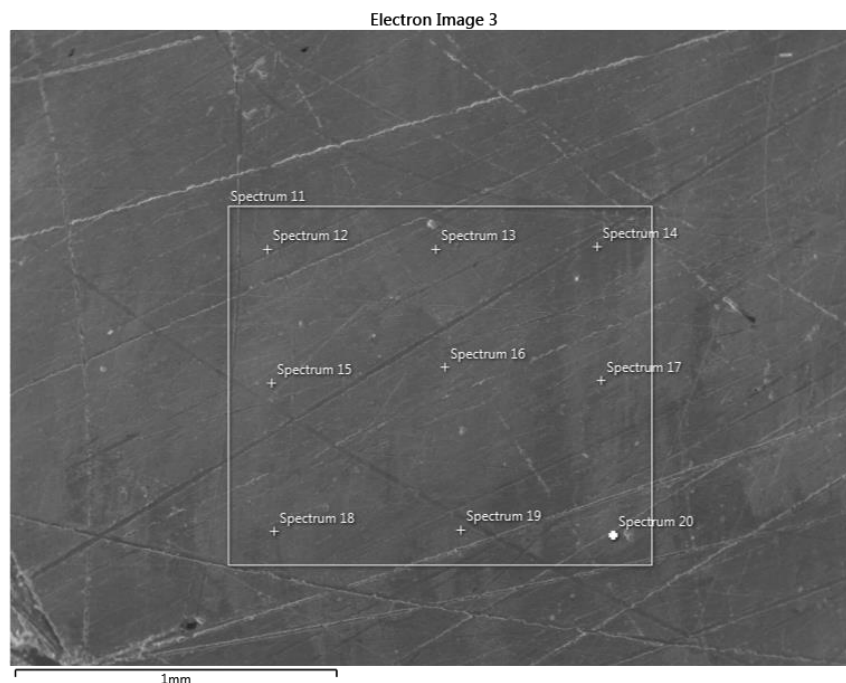


Figure 79. SEM image of the surface of a sample of **1**. Multiple spectra have been averaged to find a composition of $\text{Cu}_{1.13}\text{Pb}_{1.07}\text{BiI}_{5.99}$. Given the inherent error in EDS signal this agrees well with our crystallographic model.

Table 12. SEM-EDS Results for **1**. Some variance is seen across the material.

RESULT TYPE	ATOMIC %			
	Cu	I	Pb	Bi
ATOM				
MAX	18.15	67.21	13.35	12.29
MIN	8.34	61.55	9.06	9.4
AVERAGE	12.29	65.19	11.65	10.87
STANDARD DEVIATION	3.33	1.71	1.3	0.89

Within the crystal structure of **1**, the octahedral metal site is very symmetric within the layer as shown in Figure 80. Bond distances range from 3.1259 to 3.1260 Å and bond angles of I – Pb/Bi – I remain very close to 90°. These are very similar to the rudorffite bond distances of 3.0762 Å as reported in the literature as well as reported bond angles.¹⁴⁴ The hallmark difference between the Ag₃BiI₆ rudorffite and **1** is the addition of Cu instead of Ag, which results in far more diffuse copper occupancy on within the material. Within **1** we can observe three different copper sites, the first for Cu1 found sitting in a tetrahedral site between the layers coordinated to four iodine atoms (Figures 81) The tetrahedron is slightly distorted as shown in Figure 82 left. Cu2 sits on an octahedral site and is significantly distorted as the Cu atom attempts to gain tetrahedral geometry which is reflected in the minimum and maximum bond distances as shown in Figure 82 middle. Interestingly, the last copper site, Cu3, lies within the metal layer as shown in Figure 82 right. Due to the overall disorder and vacancies, Cu can bond in these tetrahedral sites which remain relatively symmetric with only one reduced bond length of 2.672 Å.

Using this single crystal solution, the calculated powder pattern can be generated and compared to the experimental patterns in Figure 83. Here we see that as compared to calculated model, the experimental results match very well apart from the broad peak at 35° which can be attributed to some degree of PbI₂ and BiI₃ type layers within the system. Additionally, the comparison of the calculated pattern of **1** to that of Ag₃BiI₆ further demonstrates the validity of the trigonal *R-3m* unit cell and the rudorffite structure type.

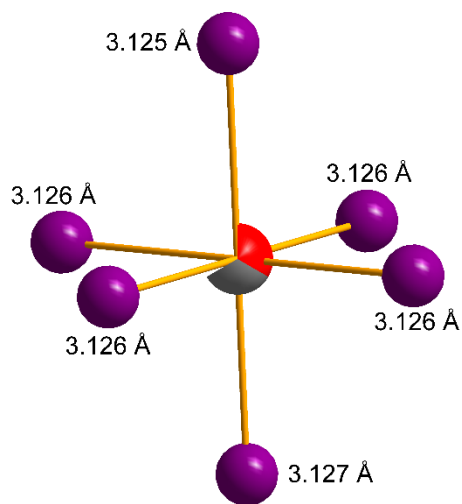


Figure 80. The octahedral coordination of the Pb, Bi, Δ site which generates the heavy metal containing layers in **1**.

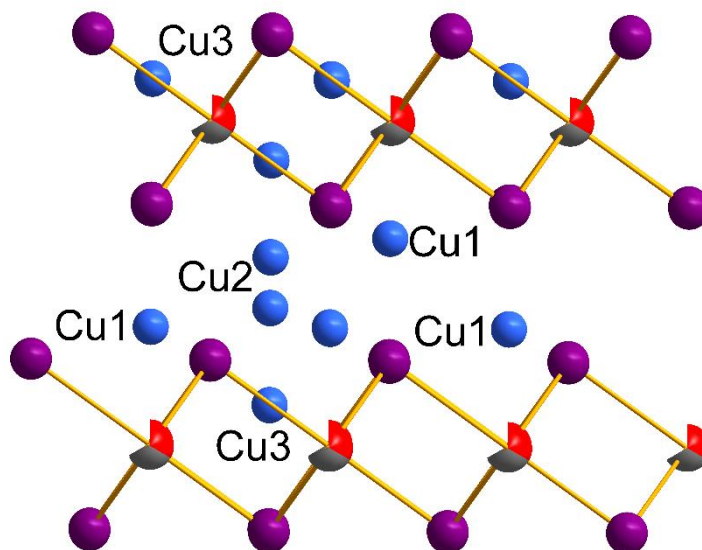


Figure 81. The three different copper sites that are found within the structure of **1**. Note that Cu1 sits near the edge of the heavy metal layer, Cu2 sits on a distorted site between the two layers, and Cu3 is found between the layers.

4.4.3. Single Crystal X-ray Diffraction Analysis of CuCdBiI_6 (**2**)

As with **1**, we used the slow cooling method to acquire crystals of **2**. These crystals diffracted very well and did not demonstrate any diffuse scattering, consistent with the powder diffraction pattern. **2** crystallizes in the cubic $Fd-3m$ space group with lattice parameters and refinement details given in Table 13. Additional thermal parameters and atomic coordinates are given in Tables 14 and 15. Due to the nature of the refinement, the resultant stoichiometry is shown as $\text{Cu}_{0.67}\text{Bi}_{0.67}\text{Cd}_{0.67}\text{I}_4$ which is a simple 1/3 reduction in the calculated formula from CuCdBiI_6

The structure of **2** is that of a AgBiI_4 -type defect spinel where Cd, Bi, and Δ occupy the octahedral metal sites (Figures 84 and 85). As with the **1**, metal sites are occupied 2/3 by Cd or Bi and 1/3 by Δ generating corner sharing heavy metal octahedra in three dimensions rather than two. The result being a defect ridden structure which allows for diffuse Cu occupancy on the tetrahedral sites between iodine atoms. The non-layered nature of this material additionally leads the well-ordered tetrahedral sites and no split positions are found for Cu. Similar to **1**, the occupancy of the metal sites was refined freely to arrive at the 1/3 value for Δ . The subsequent distribution of Cd and Bi could theoretically be refined, but due to the complexity of the system it was set by SEM-EDS results as a 50% distribution over the remaining occupancy (Figures 86, Table 16). Both the metals and the iodine were refined anisotropically. Free refinement of occupancy on I also retains the fully occupied state expected for the defect spinel structure. Copper atoms were all refined isotropically and needed to be fixed due to significant disorder. Occupancies were adjusted and refined freely with the use of the DAMP command to arrive at the correct stoichiometry. Further refinement without the DAMP command did not raise R1 or yield an unstable model. The occupancy of Cu ranges from 6 – 16% over the three sites as shown in Table 14.

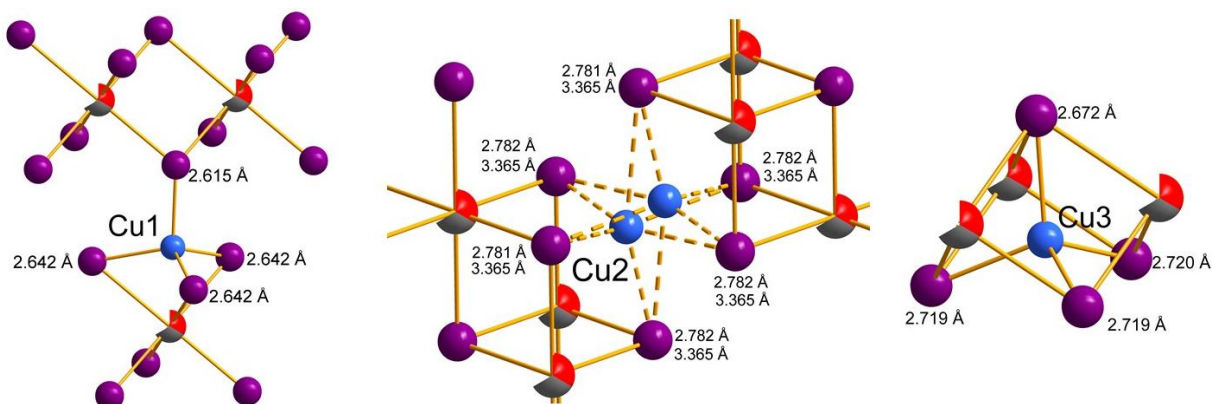


Figure 82. Left: the coordination environment of Cu1, which sits on a tetrahedral site between the two heavy metal layers. Bond distances to the four iodine atoms are given next to the respective atom. Middle: The coordination environment of Cu2, which resides within a distorted octahedral site. The bond distances are given as the maximum and minimum values for a given distorted Cu octahedron. Right: The tetrahedral coordination of Cu3 within the rudorffite-like heavy metal layer. Due to the density of Δ on the metal site, some copper can be found in these sites.

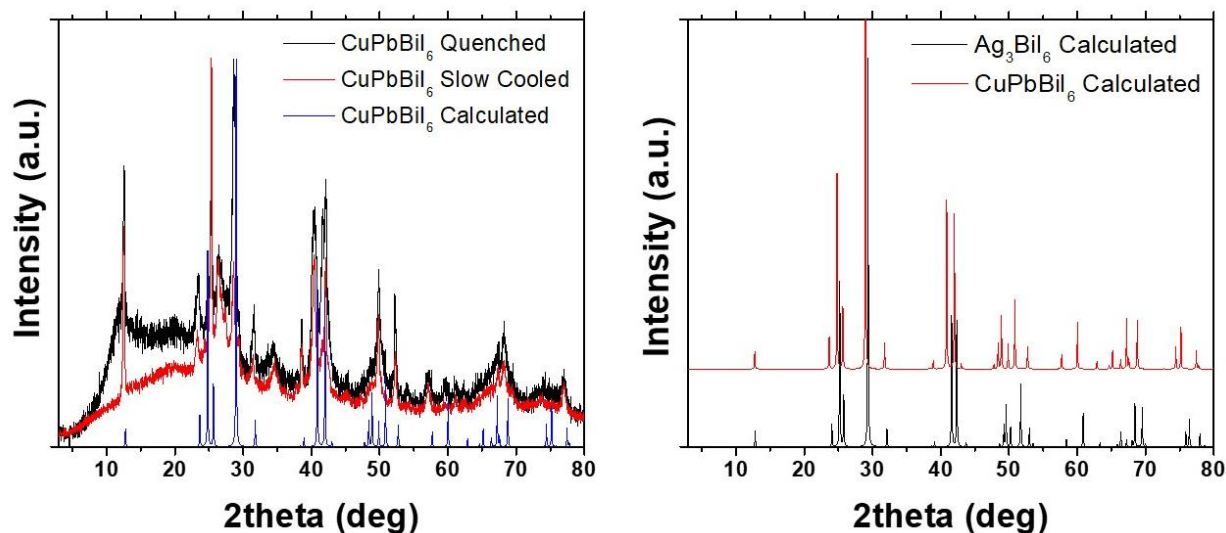


Figure 83. Comparison of the calculated pattern of **1** with experimental and to the Ag_3BiI_6 rudorffite. The additional peaks can be attributed to PbI_2 and BiI_3 -type layers as no other traces of the binary are apparent. The theoretical patterns of **1** and Ag_3BiI_6 agree well.

Table 13. Crystal data and structure refinement for $\text{Cu}_{0.67}\text{Bi}_{0.67}\text{Cd}_{0.67}\text{I}_4$ at 293 K.

Empirical formula	$\text{Cu}_{0.67}\text{Bi}_{0.67}\text{Cd}_{0.67}\text{I}_4$
Formula weight	764.47
Temperature	293 K
Wavelength	0.71073 Å
Crystal system	Cubic
Space group	<i>Fd-3m</i>
Unit cell dimensions	a = 12.025(2) Å, $\alpha = 90^\circ$ b = 12.025(2) Å, $\beta = 90^\circ$ c = 12.025(2) Å, $\gamma = 90^\circ$
Volume	1739.0(9) Å ³
Z	8
Density (calculated)	5.840 g/cm ³
Absorption coefficient	30.855 mm ⁻¹
F(000)	2550
Crystal size	0.089 x 0.051 x 0.029 mm ³
θ range for data collection	2.934 to 24.966°
Index ranges	-14 ≤ h ≤ 14, -14 ≤ k ≤ 14, -14 ≤ l ≤ 14
Reflections collected	6534
Independent reflections	98 [$R_{\text{int}} = 0.0219$]
Completeness to $\theta = 24.966^\circ$	100%
Refinement method	Full-matrix least-squares on F^2
Data / restraints / parameters	98 / 0 / 11
Goodness-of-fit	1.426
Final R indices [$I > 2\sigma(I)$]	$R_{\text{obs}} = 0.0405$, $wR_{\text{obs}} = 0.1036$
R indices [all data]	$R_{\text{all}} = 0.0439$, $wR_{\text{all}} = 0.1088$
Extinction coefficient	0.00005(3)
Largest diff. peak and hole	2.184 and -6.558 e·Å ⁻³

$$R = \frac{\sum ||F_o| - |F_c||}{\sum |F_o|}, wR = \frac{(\sum [w(|F_o|^2 - |F_c|^2)^2])^{1/2}}{\sum [w(|F_o|^4)]^{1/2}} \text{ and } w = 1/[\sigma^2(F_o^2) + (0.0613P)^2 + 28.1404P] \text{ where } P = (F_o^2 + 2F_c^2)/3$$

Table 14. Atomic coordinates ($\times 10^4$) and equivalent isotropic displacement parameters ($\text{\AA}^2 \times 10^3$) for $\text{Cu}_{0.67}\text{Bi}_{0.67}\text{Cd}_{0.67}\text{I}_4$ at 293 K with estimated standard deviations in parentheses.

Label	x	y	z	Occupancy	U_{eq}^*
Bi(02)	2500	5000	7500	0.3336	14(1)
Cd(02)	2500	5000	7500	0.3336	14(1)
I(00)	5015(1)	5015(1)	7485(1)	1	8(1)
Cu(2)	6250(20)	3750	3750	0.0593	12(16)
Cu(0A)	6250	6250	6250	0.1627	90(20)
Cu(1A)	1250	6250	6250	0.1485	72(18)

* U_{eq} is defined as one third of the trace of the orthogonalized U_{ij} tensor.

Table 15. Anisotropic displacement parameters ($\text{\AA}^2 \times 10^3$) for $\text{Cu}_{0.67}\text{Bi}_{0.67}\text{Cd}_{0.67}\text{I}_4$ at 293 K with estimated standard deviations in parentheses.

Label	U_{11}	U_{22}	U_{33}	U_{12}	U_{13}	U_{23}
Bi(02)	14(1)	14(1)	14(1)	0(1)	0(1)	0(1)
Cd(02)	14(1)	14(1)	14(1)	0(1)	0(1)	0(1)
I(00)	8(1)	8(1)	8(1)	1(1)	-1(1)	-1(1)

The anisotropic displacement factor exponent takes the form: $-2\pi^2[h^2a^{*2}U_{11} + \dots + 2hka^*b^*U_{12}]$.

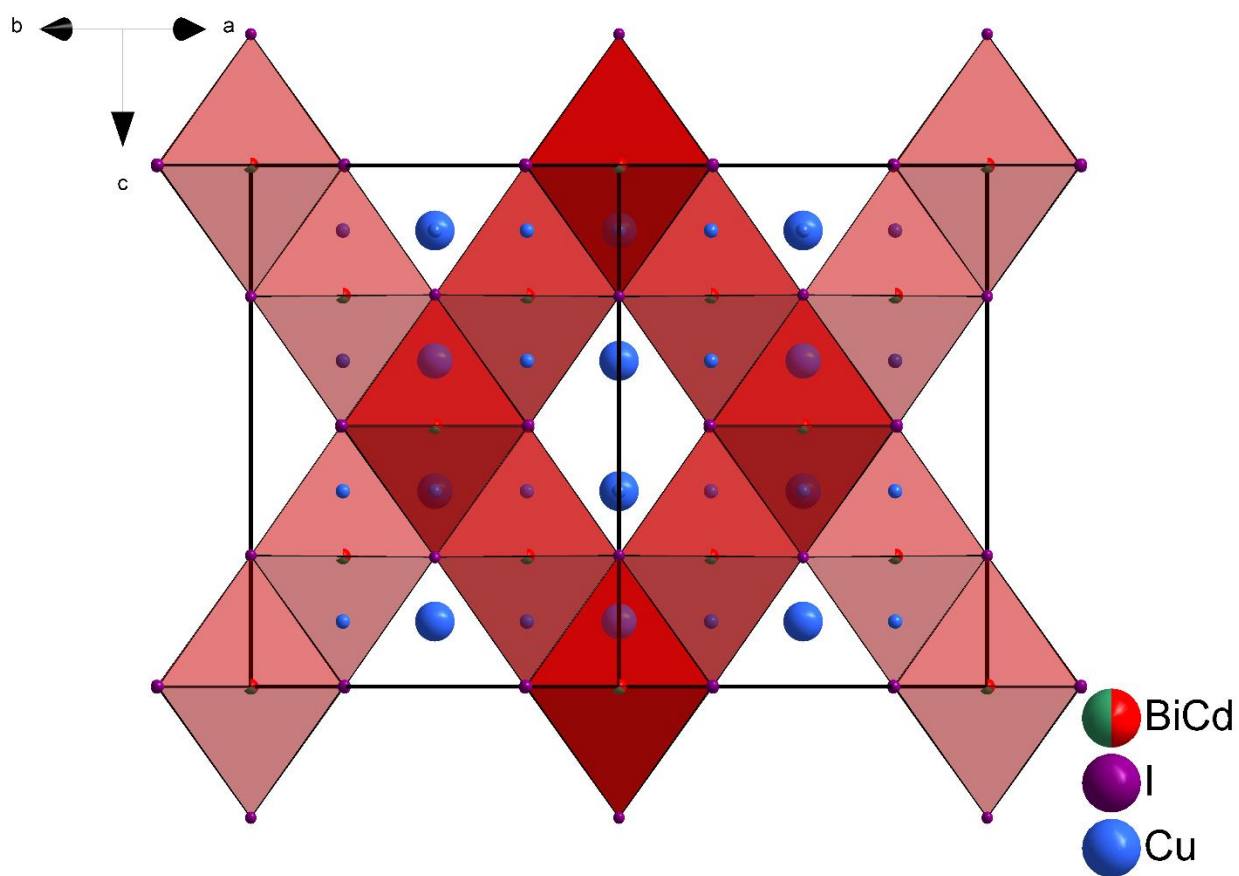


Figure 84. A [110] projection of the unit cell of **2** demonstrating the 3D nature of the defect-spinel as corner sharing heavy metal octahedra generate channels for Cu coordination. Anisotropic thermal parameters are shown for the heavy metal site and I, while Cu remains isotropic. The larger isotropic parameters on the Cu atoms reflect greater occupancy, where tetrahedral copper is more likely to fall channel tetrahedral sites rather than within the heavy metal lakes akin to Cu₃ in **1**.

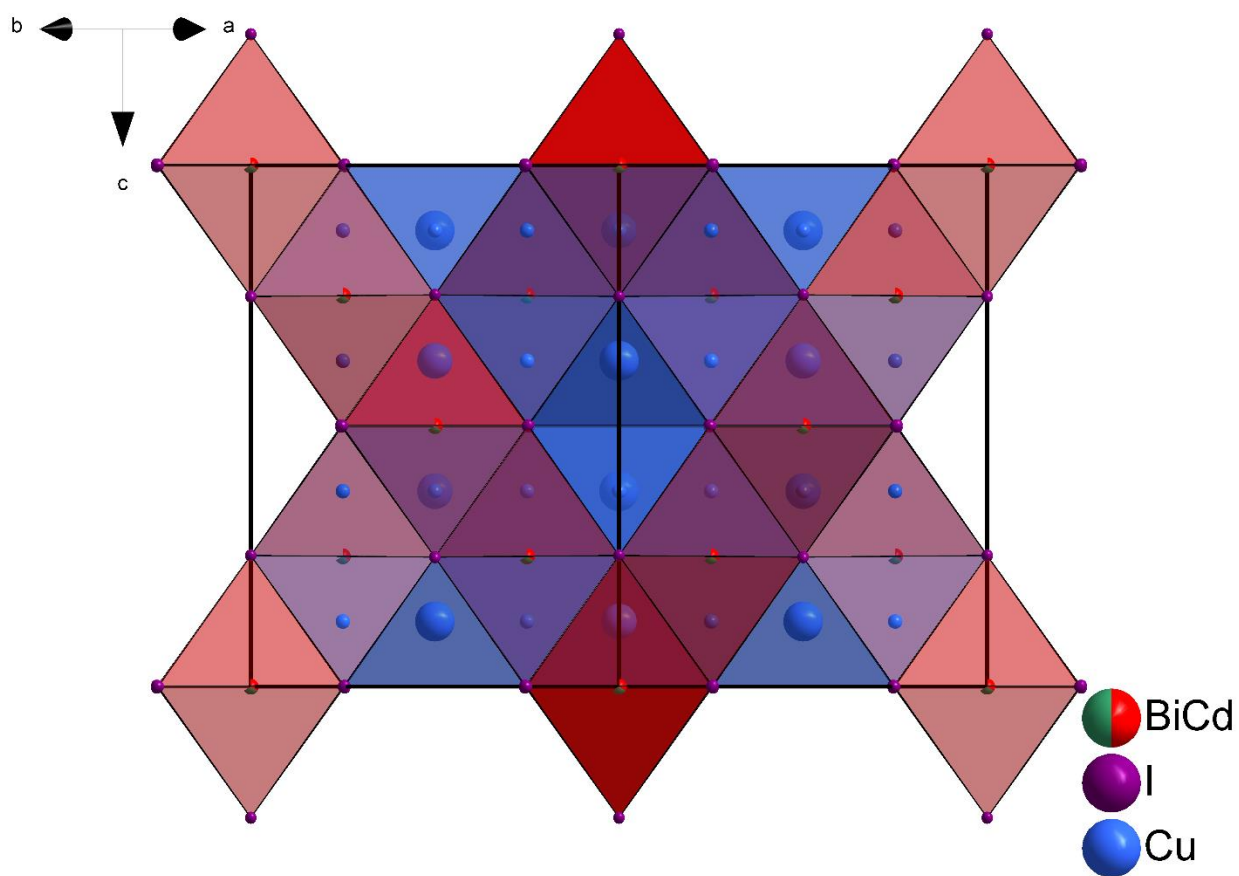


Figure 85. A [110] projection of the unit cell of **2** demonstrating the 3D nature of the defect-spinel as corner sharing heavy metal octahedra generate channels for Cu coordination as shown in Figure 84, however the addition of the CuI_4 polyhedra demonstrates that opposed to the AgBiI_4 defect spinel, the inclusion of tetrahedral copper generates far more space filling sites that would otherwise be empty.

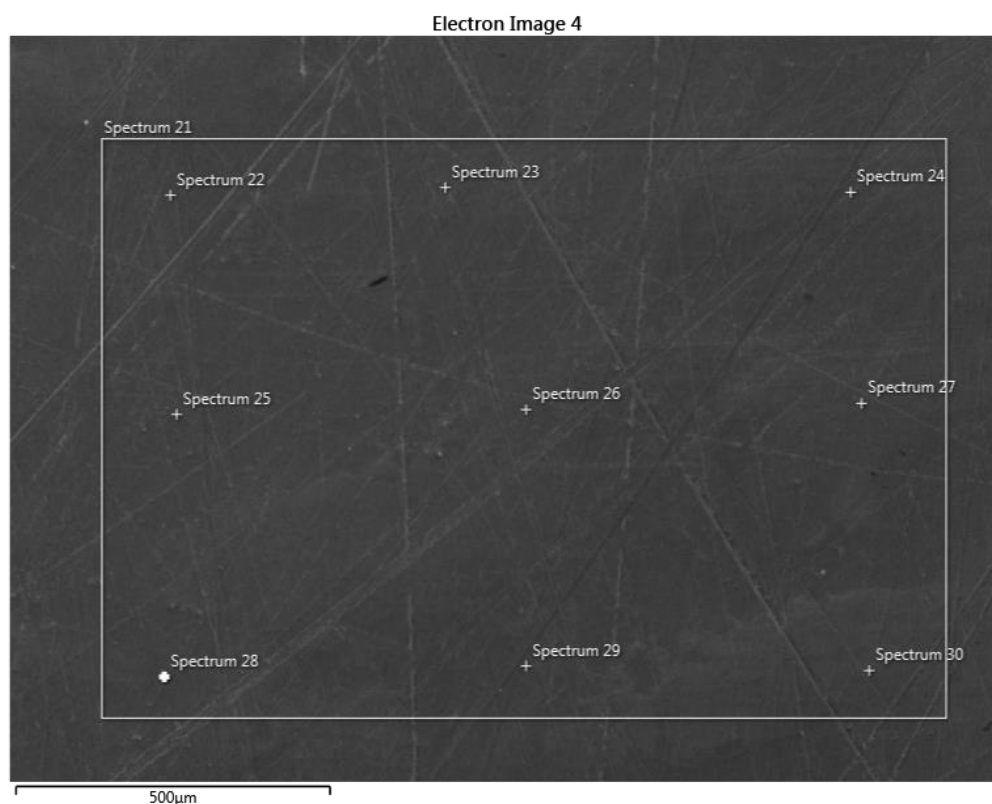


Figure 86. SEM image of the surface of a sample of **2**. Multiple spectra have been averaged to find a composition of $\text{Cu}_{1.13}\text{Pb}_{0.94}\text{BiI}_{5.99}$. Given the inherent error in EDS signal this agrees well with our crystallographic model.

Table 16. SEM-EDS Results for **2**. Some variance is seen across the material.

RESULT TYPE	ATOMIC %			
	Cu	Cd	I	Bi
STATISTICS				
MAX	19.69	12.86	67.2	13.19
MIN	6.76	8.43	61.06	9.85
AVERAGE	13.03	10.77	64.73	11.47
STANDARD DEVIATION	4.07	1.33	1.94	0.95

Akin to the trigonal R-3m rudoiffite structural phase of **1**, **2** demonstrates the a similarly highly symmetric octahedral Cd, Bi and Δ site (Figure 87) with symmetric bond lengths of 3.025(1) Å. These bond distances are smaller than the AgBiI₄ octahedral bond distances of 3.0722 Å, which is likely due to the smaller size of Cd than Ag on the octahedral site. Very little octahedral distortion is observed, with the greatest deviance from a I – Cd/Bi/ Δ – I angle being 89.301(13)° and the corresponding 90.699(14)°. Again, like in **1** we observe three different Cu sites, however in the case of **2** all of them are tetrahedral (Figure 88). Another significant difference is the clear preference of Cu to occupy two sites opposed to the very small variance in copper occupancy reflected in **1**.

The first copper site Cu1, has a refined occupancy of 14.9% and is found in a tetrahedral site between four edge sharing (Cd/Bi/ Δ)I₆ octahedra (Figure 89 (left)). The site is fully symmetric with bond lengths of 2.636(1) Å, a contrast to the partially distorted tetrahedra in **1**. Despite having the option to be completely encased, this site still demonstrates the second highest refined occupancy. The second tetrahedral site is found in one of the channels of the defect spinel, Cu2, and has symmetrical bond lengths of 2.571(1) Å (Figure 88 (middle) Copper shows the most preference for this site with the greatest refined occupancy of 16.3%. This is unsurprising as this site is relatively less hindered. Finally, the last Cu site, Cu3, lies in the tetrahedral site within the (Cd/Bi/ Δ)I₆ octahedra that is nearly analogous to Cu3 in **1** (Figure 89 (right)). Here copper only displays 5.9% occupancy with the only distorted tetrahedron, with Cu3 pushed out away from the (Cd/Bi/ Δ)I₆ octahedra it may lie between with bond lengths of 2.593(14) Å and 2.613(14) Å.

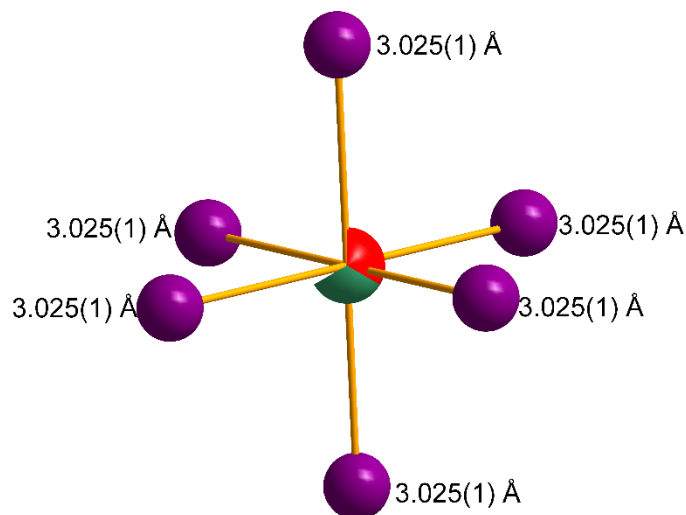


Figure 87. The octahedral coordination of the Cd, Bi, and Δ site which generates the 3D edge sharing $(\text{Cd}/\text{Bi}/\Delta)\text{I}_6$ octahedra network in **2**.

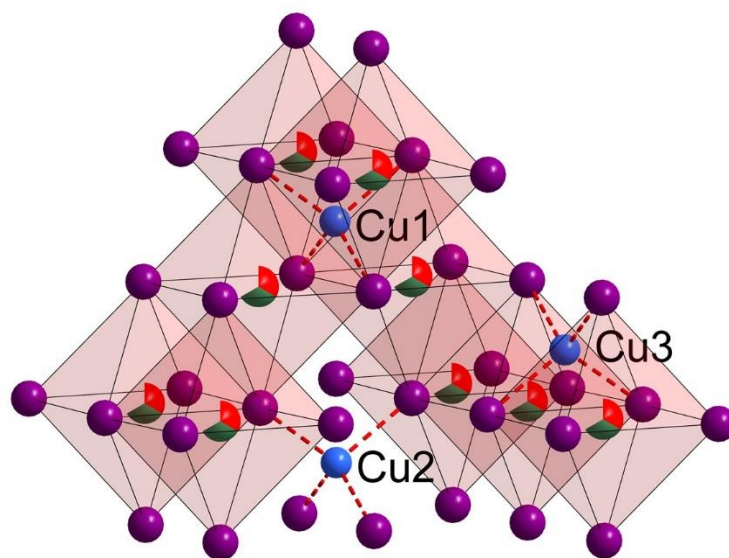


Figure 88. The three different copper sites that are found within the structure of **2**. Note that Cu1 sits between four possible $(\text{Cd}/\text{Bi}/\Delta)\text{I}_6$ octahedra, whereas Cu2 sits in a tetrahedral channel site, and Cu3 sits between $(\text{Cd}/\text{Bi}/\Delta)\text{I}_6$ octahedra akin to Cu3 in **1**.

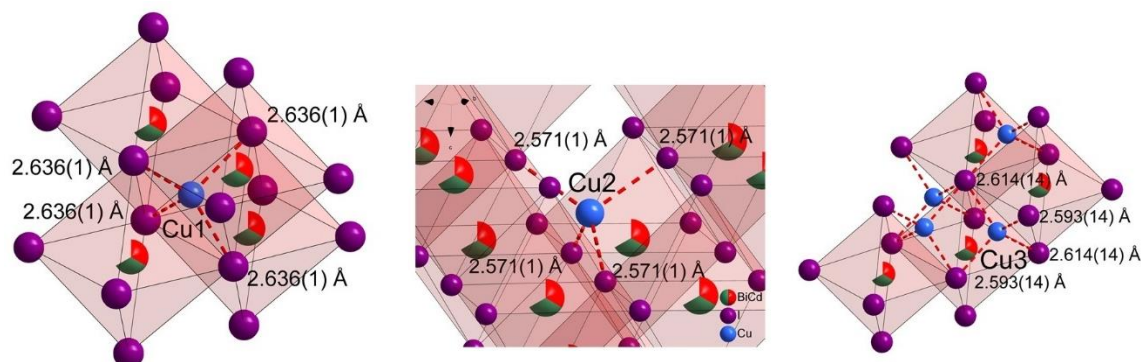


Figure 89. Right: The coordination environment of Cu1, which is found between four edge sharing (Cd/Bi/ Δ) I_6 octahedra. Despite this, the occupancy of this site is still refined to have 14.9% occupancy. Middle: The coordination environment of Cu2 which resides in a tetrahedral site in the channels of the defect-spinel with 16.9% occupancy. Right: The Cu3 sites which reside between two (Cd/Bi/ Δ) I_6 octahedra within the 3D structure and features the lowest occupancy of 5.9%. It features the only tetrahedral distortion with Cu pushed from the shared edge of the octahedra.

As with **1**, using the single crystal model the calculated PXRD pattern was used to verify the consistency of our single crystal model with our experimental powder diffraction profiles (Figure 90). Compared to the experimental, the calculated agrees well for **2** indicating that our quenching and slow cooling runs produce the same 3D defect spinel structure. In comparison to the known spinel-type phase of the AgBi I_4 rudorffite, we see similar agreement when taking into account their difference in lattice parameters. While in some cases it has been found that the difference between these structure types can be difficult to discern, here it is very clear that the **1** is a trigonal system whereas **2** relates well to the cubic.¹⁴⁵ Interestingly, despite the significant

amount of CuI_4 tetrahedral coordination within both structures the resultant calculated patterns are nearly identical to those of the Ag – Bi – I rudorffites.

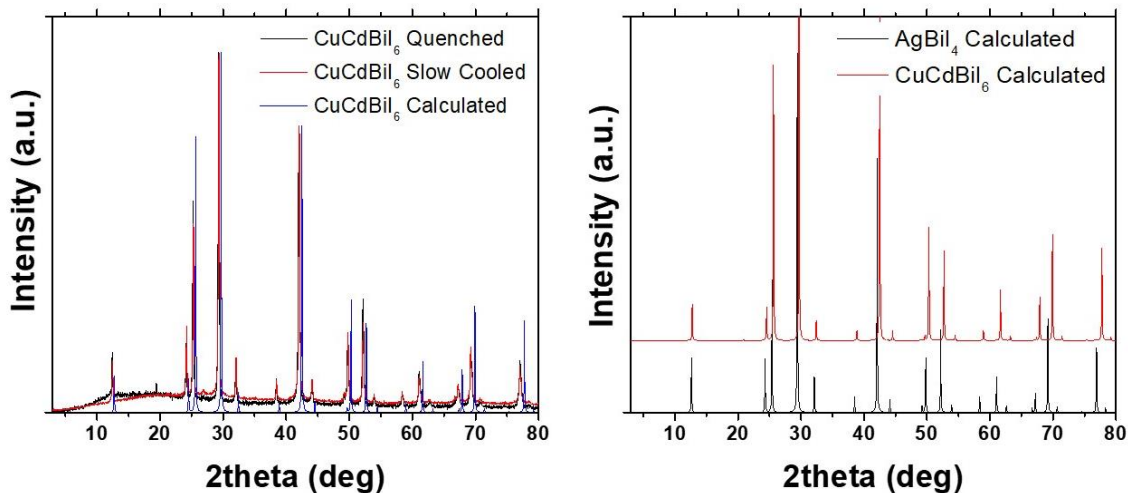


Figure 90. Comparison of the calculated pattern of **2** with experimental and to the AgBiI_4 rudorffite. The theoretical patterns of **2** and AgBiI_4 agree well.

4.4.4. Probing the limits of Cu addition to $(\text{MI}_2)_{0.5}(\text{BiI}_3)_{0.5}$ Layers

As Oldag et al. demonstrate in their syntheses of AgBiI_4 rudorffites there is some tolerance for noble metal deficiency.¹⁴⁴ Similarly, we investigated the tolerance at CuPbBiI_6 (**1**) and CuCdBiI_6 (**2**) revert to their layered forms as Cu Content is reduced. While not completely analogous to the rudorffites as Ag and Bi occupy the same crystallographic site, it is clear that the addition of Cu I to these mixtures induces their transition from 2D $(\text{MI}_2)_{0.5}(\text{BiI}_3)_{0.5}$ van der Waals materials to the 3D structures. To accomplish this we synthesized $\text{Cu}_{1-x}\text{M}\text{BiI}_{6-x}$ ($\text{M} = \text{Cd}, \text{Pb}$) mixtures in $x = 0.1$ increments by the standard 4 mmol routine and examined the resultant PXRD patterns for each mixture. For **1**, the resultant materials show that for the $\text{M} = \text{Pb}$ containing system the transition from 2D to 3D can be achieved between $x = 0.2$ and 0.3 (Figure 91). This indicates

only a small fraction of CuI, which yields the addition of the CuI_4 tetrahedral units, is required to transform the layered 2D van der Waals material into the Ag_3BiI_6 ruderffite type phase. Interestingly, the diffuse disorder also increases as the fraction of CuI is increased which can be readily seen in the peaks near 40° . Interestingly, there is no significant change in the peak locations once additional CuI is added, which suggests that once the 3D structure is manifested the lattice parameters remain nearly constant.

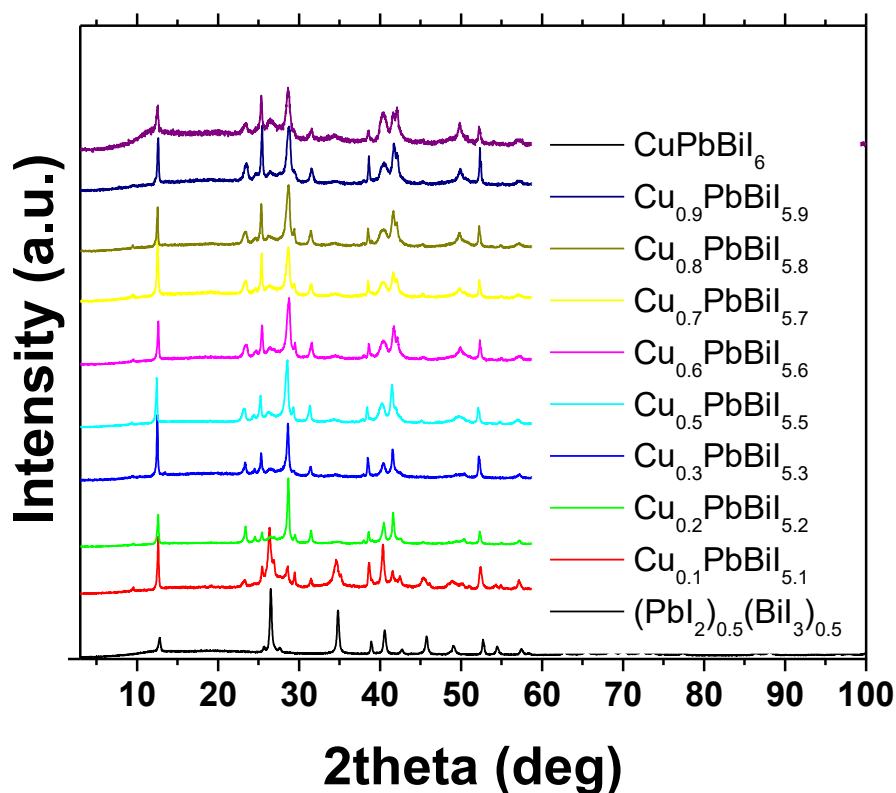


Figure 91. Powder diffraction patterns of $\text{Cu}_{1-x}\text{PbBiI}_{6-x}$ compositions. By $x = 0.2$ the 3D phase is the dominant phase in the powder diffraction pattern and by $x = 0.3$ there is no observation of the 2D parent mixtures. Note that $x = 0.4$ is missing as the ampoule broke during quenching.

For **2**, the addition of CuI to $(\text{CdI}_2)_{0.5}(\text{BiI}_3)_{0.5}$ mixtures requires at $x = 0.6$ to yield an apparent pure 3D defect spinel phase, with intermediate phases similar to that of **1** and the $(\text{CdI}_2)_{0.5}(\text{BiI}_3)_{0.5}$ mixtures. (Figure 92). These results suggest that while CuI addition to **1**, readily induces the rudorffite phases, when the system contains a slightly smaller divalent cation Cd the requisite amount of CuI is greater to induce the 3D transformation. Of note, the pure $(\text{CdI}_2)_{0.5}(\text{BiI}_3)_{0.5}$ mixture that was quenched strikingly resembles the quaternary phase of **2** despite having no CuI addition indicating a field of future investigation.

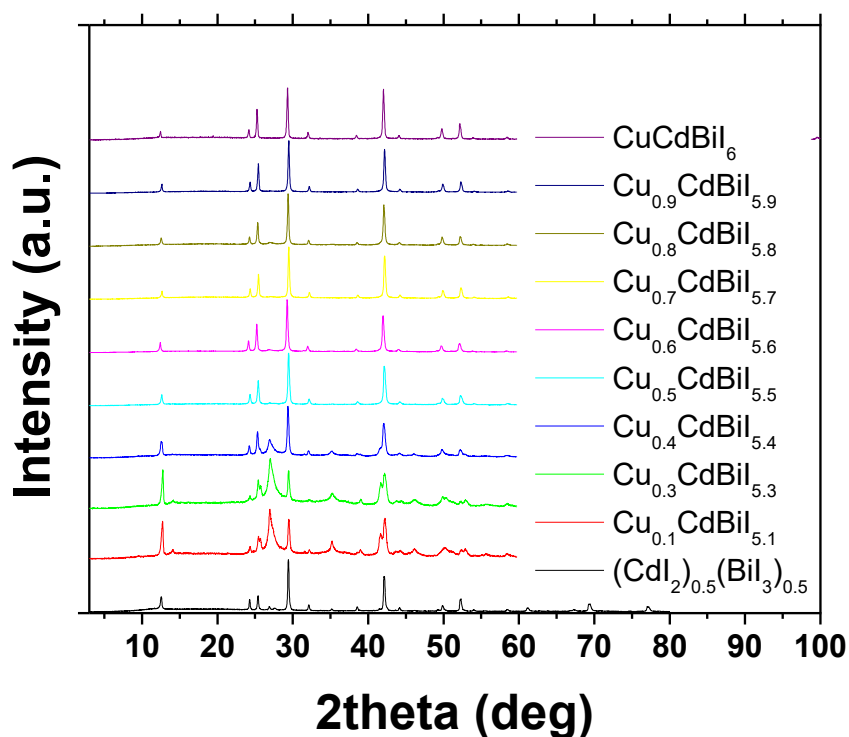


Figure 92. Powder diffraction patterns of $\text{Cu}_{1-x}\text{CdBi}_{6-x}$ compositions. Only at $x = 0.6$ does the 3D defect spinel phase become apparently phase pure. Note that the $x = 0.2$ sample is missing due the ampoule breaking during the quenching process.

4.4.5. High Temperature In Situ Powder Diffraction of CuPbBiI_6 (**1**)

Using the 11-BM beamline at APS we examined the formation of both **1** and **2** and the possibility of high temperature phases as informed by DTA. For the in situ reaction of **1**, we observe that upon heating the binaries CuI , PbI_2 , and BiI_3 reach the melt by 349 C, slightly below the recorded melting temperature by DTA (Figure 93). Formation of the rudorffite phase can also be observed in the 249 C and 299 C profiles. Upon cooling, crystallization begins near 326 C where we see the growth of the 003 reflection within the melt at 3.74° . Between 267 C and 223 C the trigonal rudorffite cell of **1** can be observed, however upon cooling below 201 C the disorder is induced that is observed in the bulk PXRD patterns (Figure 94).

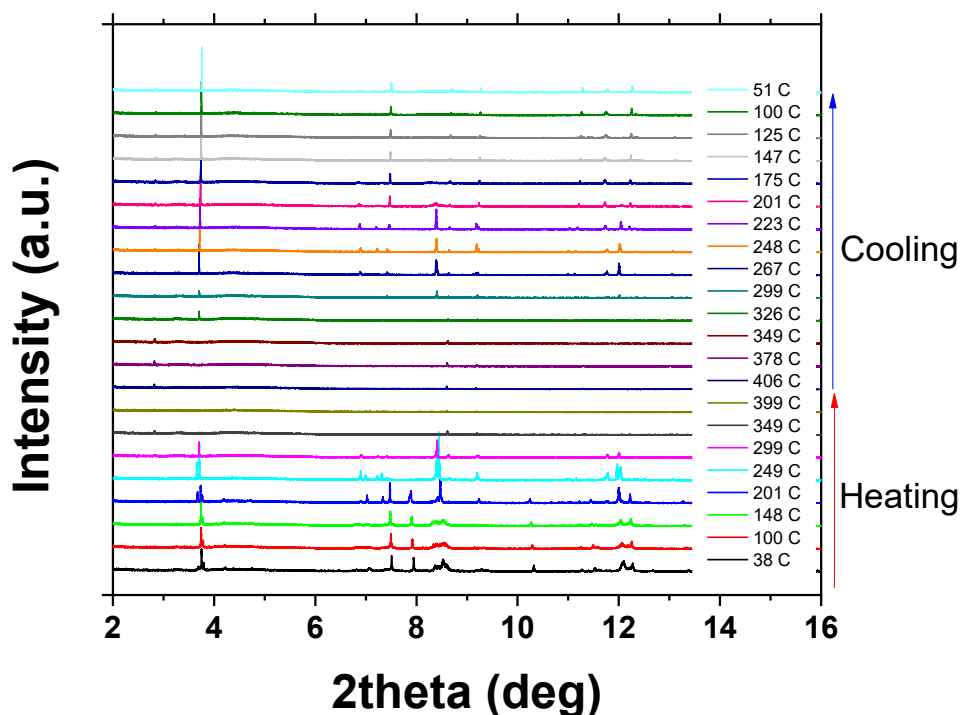


Figure 93. In Situ powder diffraction of **1**, where upon heating the binaries react by 299 C to yield the 3D rudorffite phase. Upon cooling crystallization is observed near 326 C which yields a well ordered rudorffite phase at high temperature. Further cooling promotes disorder below 201 C.

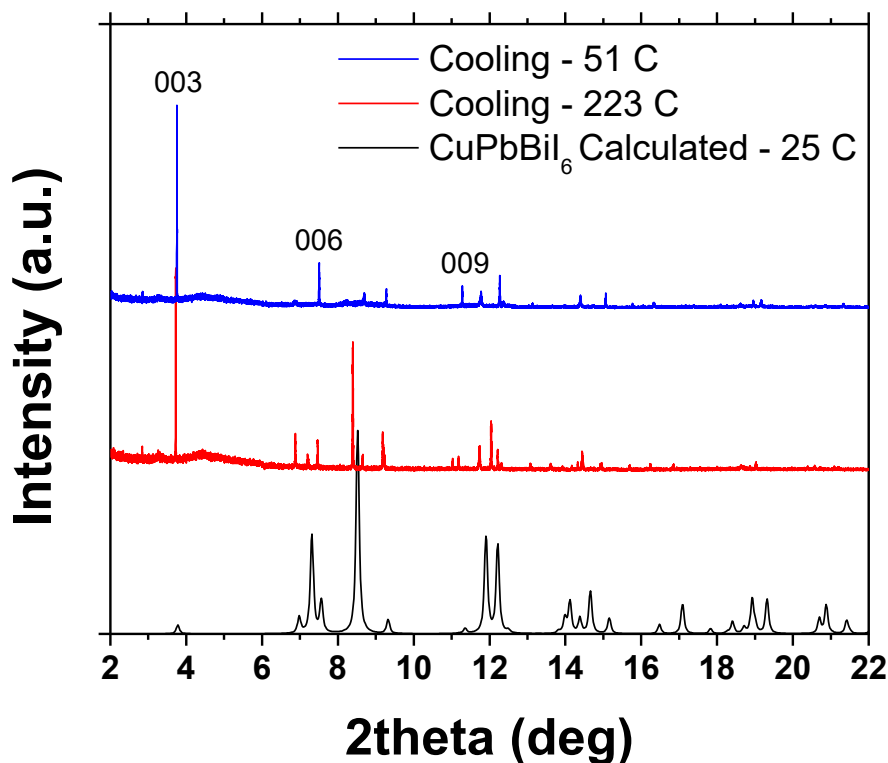


Figure 94. Comparison of the PXRD pattern on cooling for **1**. As noted, upon cooling between 267 C and 223 C the rudorffite phase is observed demonstrated in Figure 95 . Cooling below 201 C demonstrates the ability of the mixed Pb/Bi systems to induce disorder with the clear reflections corresponding to basal $00l$ peaks similar to the $(\text{PbI}_2)_{1-x}(\text{BiI}_3)_x$ system in chapter two.

To further demonstrate the assertion that the rudorffite phase we fit the powder pattern of the 223 C as shown in Figure 95 yielding trigonal unit cell parameters of $a = 4.476 \text{ \AA}$, $c = 21.101 \text{ \AA}$ and $\beta = 120^\circ$. Due to the relatively low intensity of the peaks and their irregular shape due to particle size full Rietveld refinement was unable to be completed. What we observe is that for the elevated temperature cell the parameters and reflections for the trigonal $R\text{-}3m$ unit cell agree well with the reported room temperature structure considering the elevated temperature.

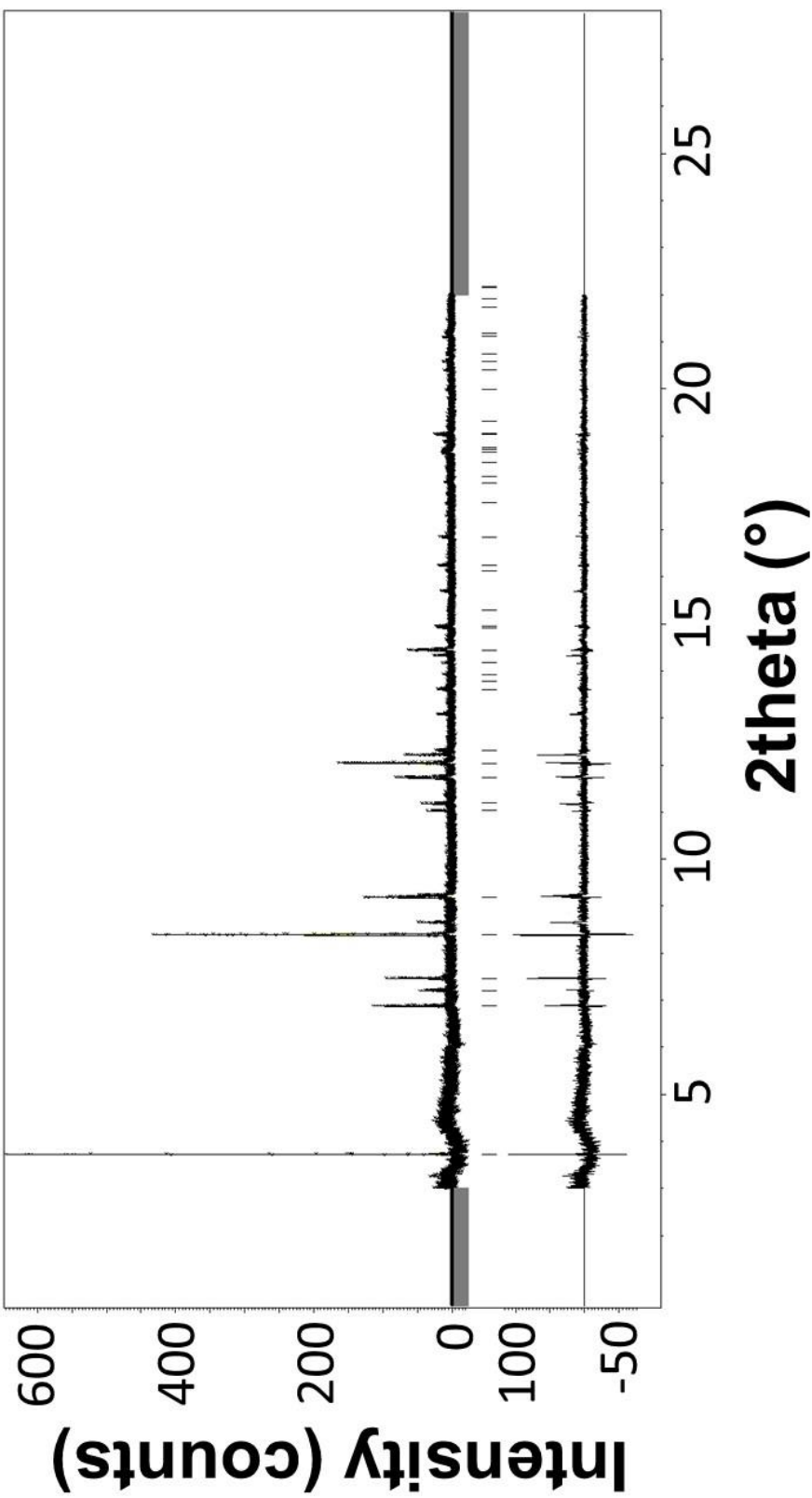


Figure 95. Fitted PXRD profile for the 223 C cooling of **1**. The fitted pattern agrees well with the experimental with regard to the predicted peak locations for the trigonal $R\text{-}3m$ unit cell. Peak shapes were irregular due to particle sizes and relatively low intensities due to heavy absorbing elements. The excluded regions did not contain useful data for profile matching only the reflection from the Kapton windows of the apparatus.

4.4.6. High Temperature In Situ Powder Diffraction of CuCdBiI_6 (**2**)

For the in situ investigation of **2** we again observe that upon heating the quaternary compound forms. In this case by the time the reaction has reached 241 C (Figure 96). Larger steps were taken in this trial as it was conducted before that of **1** at the beamline (as such we increased the number of steps). We achieve melt by 350 C which is below what DTA data suggested, but this may be due to placement of the thermocouple. Interestingly, we observe a high temperature phase on cooling between 299 C and 198 C that does not contain any low angle reflections of the

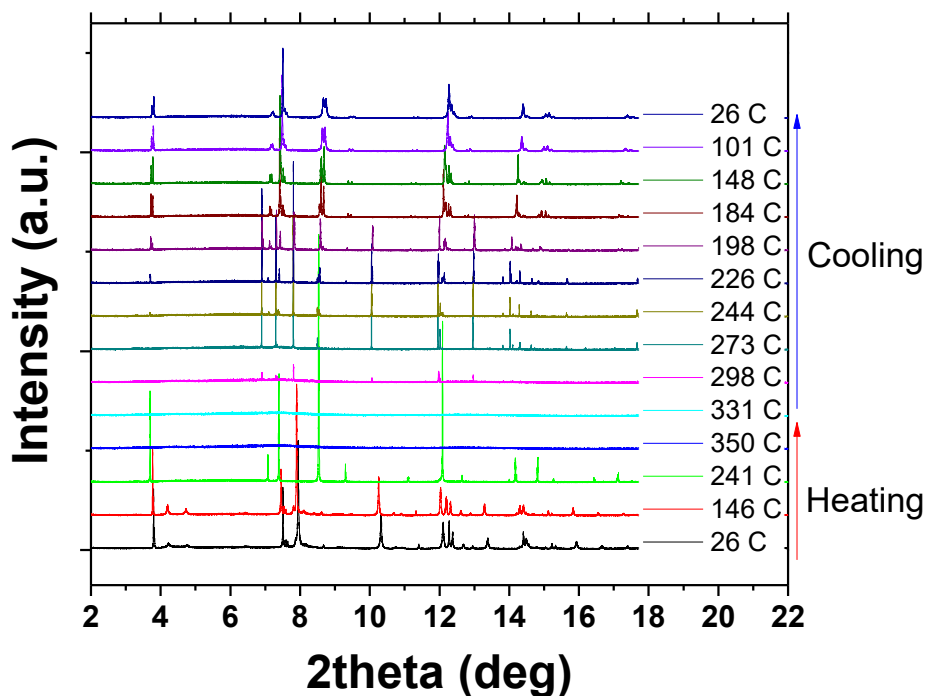


Figure 96. In Situ powder diffraction of **2**, where upon heating the binaries react by 241 C to yield the defect-spinel phase. An CuI and $\text{Cu}_{1-x}\text{CdBiI}_6$ high temperature phases begin to appear near 298 C. Upon cooling, crystallization of the defect-spinel begins at 244 C. Further cooling promotes disorder below 198 C from multiple phase compositions arising from Cu inhomogeneity.

defect-spinel (Figure 97). Phase matching for this pattern strongly suggests a mixture of a CuI-type structure and suggested hexagonal $\text{CuHg}_{0.5}\text{I}_2$ for the remaining peaks.¹⁴⁶ Considering the starting materials, CuI has a high temperature sphalerite phase that could co-exist with the a CuI deficient $\text{Cu}_{1-x}\text{CdBiI}_{6-x}$ phase.¹⁴⁷ From profile fitting alone, the rock salt phase and hexagonal phase at 273 C were successfully fit to demonstrate the presence of both (Figure 98). Lattice parameters for the CuI cubic sphalerite $F-43m$ phase are found to be $a = 6.1843\text{\AA}$ while the hexagonal $P6_3/mmc$ phase $a = 4.3953\text{\AA}$ and $c = 7.1908\text{\AA}$. Preliminary Reitveld refinement of just the hexagonal peaks suggest the same structure as $\text{CuHg}_{0.5}\text{I}_2$, but proves hard to refine due to the metal site having Cu, Cd, and Bi occupancy. (Figure 99)

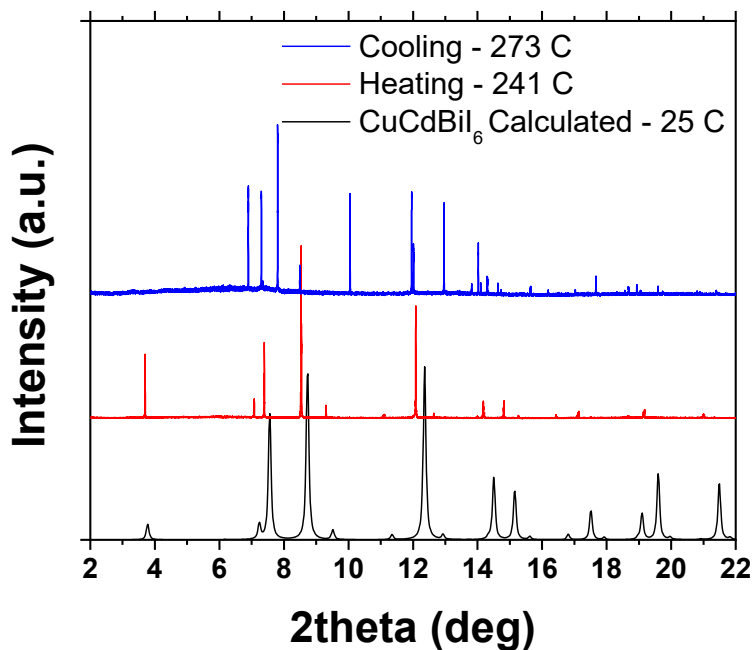


Figure 97. Comparison of the calculated PXRD pattern of **2** to the formation of **2** observed at 241 C. Additionally, the pattern of the combined hexagonal phase and cubic sphalerite CuI phase mixture at 273 C upon cooling demonstrate no low angle reflections.

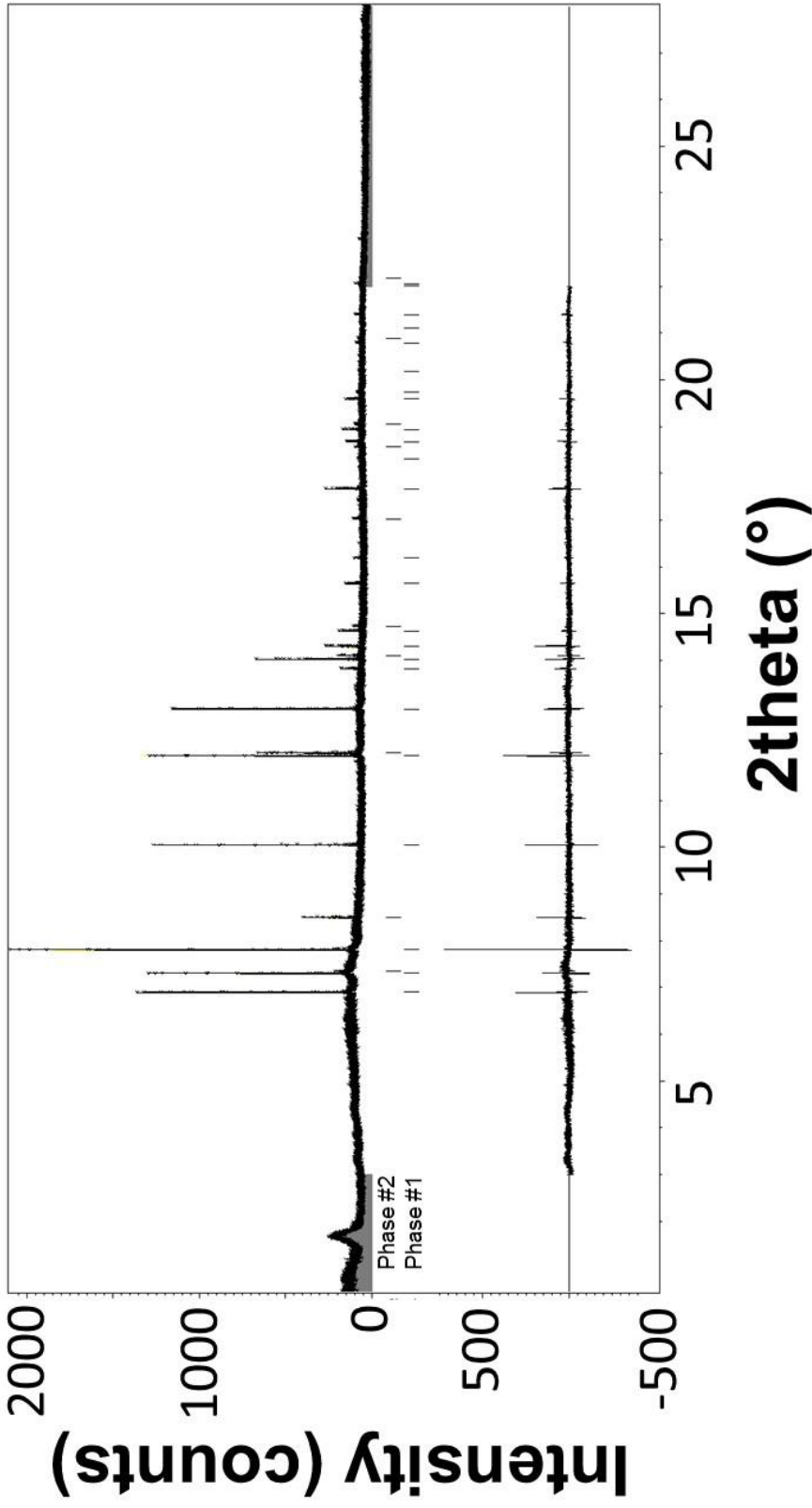


Figure 98. Fitted PXR profile for the 273 C cooling of 2. The fitted pattern agrees well with the experimental data with regard to the predicted peak locations for both the cubic sphalerite CuI (Phase #2) and the hexagonal $\text{CuHg}_{0.5}\text{I}_2$ -type phase (Phase #1). The excluded regions did not contain useful data for profile matching only the reflection from the Kapton windows of the apparatus.

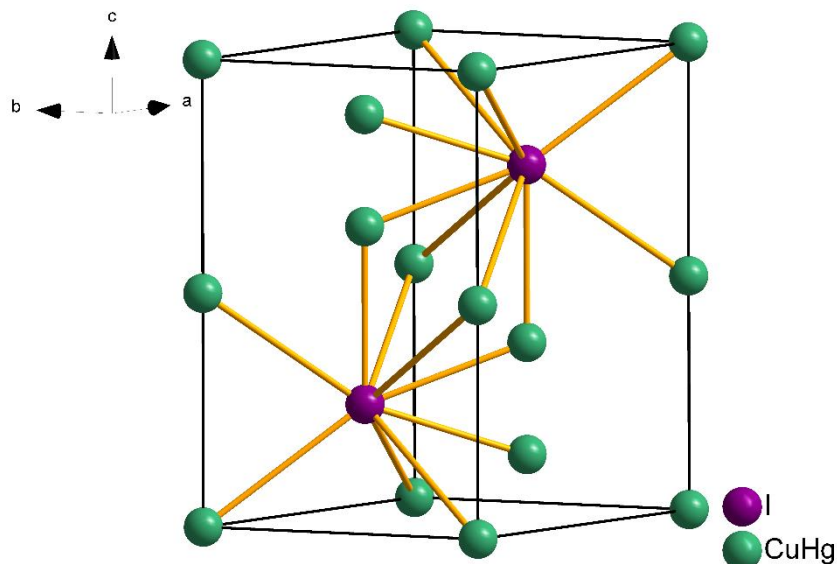


Figure 99. The $P6_3/mmc$ Unit cell of $\text{CuHg}_{0.5}\text{I}_2$ which reflects the same symmetry and analogous unit cell parameters as the high temperature hexagonal phase. The metal sites have no more than 30% occupancy between the Cu and Hg. For $\text{Cu}_{1-x}\text{CdBiI}_{6-x}$ the metal sites would have Cu, Cd, and Bi occupancy.

Contrary to our bulk syntheses, cooling of the in situ sample also displays peak separation and some diffuse scattering. This arises from multiple Cu compositions being within the beam path, which can be distinguished due to the resolution of the instrument. This compositional inhomogeneity stems from the preparation of the sample with fused quartz as a diluent which can physically separate the reactants once they melt. In fact, when further examining the 241 C heating pattern that reflects the defect-spinel formation we observe that two phases are already present. Similar to our difficulties fitting the pattern in **1**, the peak shape and presence of two nearly identical compositions makes Rietveld refinement inapplicable. However, profile matching refinements for two phases show good agreement with the cubic $Fd-3m$ unit cells where $a = 12.565$ Å or 12.349 Å. (Figure 100).

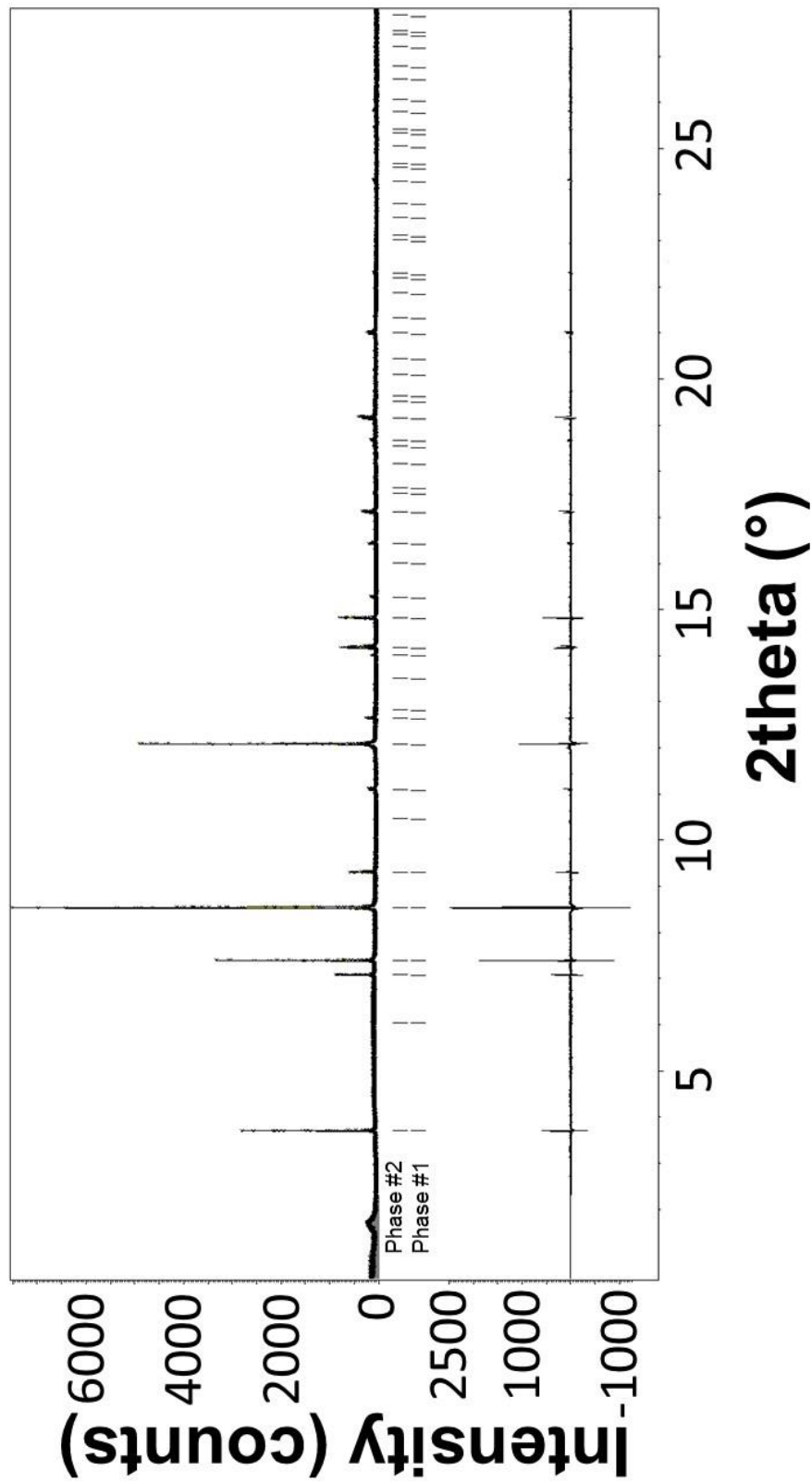


Figure 100. Fitted PXRD profile for the 241 C cooling of **2**. Due to Cu inhomogeneity in the sample two very similar cubic defect-spinel phases need to be accounted for, giving similar lattice parameters of $a = 12.565 \text{ \AA}$ or 12.349 \AA . The excluded regions did not contain useful data for profile matching only the reflection from the Kapton windows of the apparatus.

4.4.7. Optical properties of CuPbBiI_6 (1) and CuCdBiI_6 (2)

From samples of **1** and **2** solid states UV-Vis spectroscopy was used to measure the bandgaps of the samples (Figure 101). As shown, both materials display low energy absorption

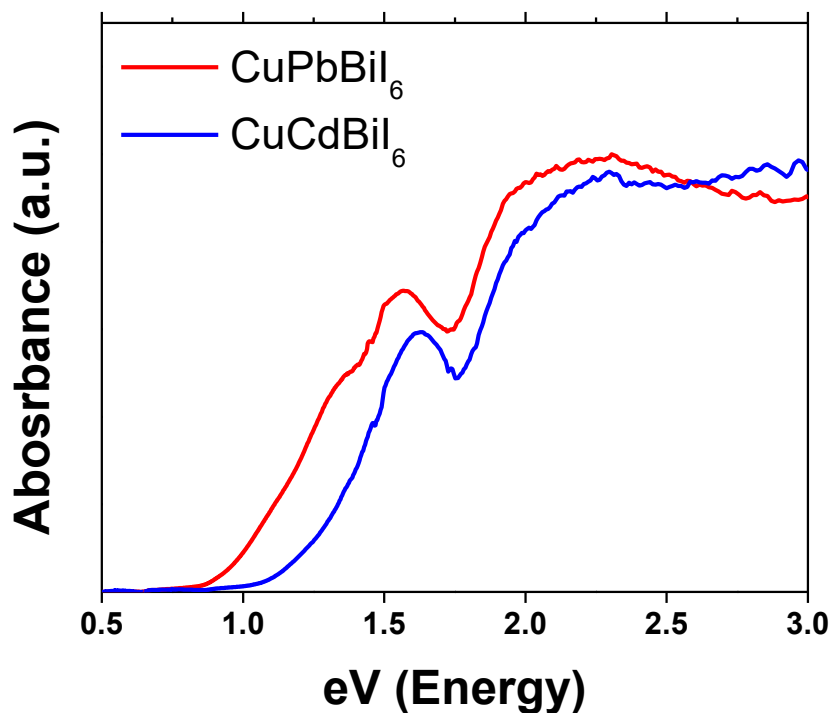


Figure 101. The optical absorbance of quenched samples of **1** and **2**. Both materials display band gaps like those seen in chapter three where the mixture of the $(\text{MI}_2)_{0.5}(\text{BiI}_3)_{0.5}$ ($\text{M} = \text{Cd}, \text{Pb}$) leads to low energy absorption. The addition of Cu does not make a significant effect on the band gap, indicating the BiI_3 -type absorption and clustering is still in effect in these quaternary materials.

akin to their $(\text{PbI}_2)_{0.5}(\text{BiI}_3)_{0.5}$ inspiration, with **1** beginning to absorb at approximately 0.9 eV followed by the exciton-like peak at 1.55 eV and the BiI_3 -type band gap at 1.7 eV. For **2**, the onset of absorption begins closer to 1.1 eV with a similar exciton-like peak at ~ 1.6 eV followed by the

same BiI_3 -type band gap. Considering the relative structure of these materials which is related to the parent CdI_2 structure type binaries (including CdI_2), we can explain the nature of the band gap to be almost identical to that in chapter three, **3.4.1**.

In **1**, similar layers of $(\text{MI}_2)_{0.5}(\text{BiI}_3)_{0.5}$ are seen between the layers of Cu occupancy. In these layers the same clustering of Bi can occur, but in this case the fast cooling of the melt does not promote wide gap behavior. Slow cooled samples for SCXRD also displayed the narrow gap behavior as expected from systems based on $(\text{MI}_2)_{0.5}(\text{BiI}_3)_{0.5}$. If we consider the role of Cu, it may aid in clustering of Bi by adding additional dimensionality to the structure. For **2**, we also can find regions where Bi could be clustered due to the overall metal disorder in the material. While **3D**, there are still sites for this to be able to occur in the defect-spinel structure. Slow cooled samples of **2** were also found to display the characteristic narrow gap behavior. Interestingly, for these Cd containing sample the binary CdI_2 is white and the resultant materials black. This further demonstrates the significant role that Bi plays on the optical character within these quaternary compounds. The persistent low energy absorption in the samples of **2** also helps support our position that Bi clustering as they hint that the divalent metal plays little role in the nature of the band gap.

Unfortunately, DFT calculations were not able to be conducted on these systems to further validate these claims. The nature of the disorder on the metal sites and the diffuse copper occupancy lead to unstable relaxation of the structures.

4.4.8. Electronic Transport Measurements

As mentioned, ingots of **1** and **2** are hard and brittle when removed from the furnace. Initial attempts at machining and polishing samples broken from the ingot for electrical transport measurements were met with crumbling, unreliable material. Attempts at pressing pellets mechanically from powders also yielded very soft, flexible pellets which were unsuitable for substantive measurements. Instead we employed spark plasma sintering (SPS) to apply pressure, heat, and current to powders to generate hard pellets. Due to the possibility of BiI₃ sublimation from the mixtures, we selected 200 C as a safe temperature to sinter our material. Powders SPS samples were measured before and after sintering to verify that significant phase separation had not occurred.

In the case of **1**, we can observe that before and after SPS we conserve the overall disordered structure of the quaternary compound, with some PbI₂/BiI₃ reflection character seen around 26° and 35°. However, these reflections are also seen in the pre-SPS quenched material and not display any phase separation by optical analysis which supports that the material remains single phase (Figure 102). For **2**, we do not observe any second phase peaks that do not pertain to the calculated PXRD pattern, indicating that the material can survive SPS treatment (Figure 103).

From the pressed ingots samples of **1** and **2** were cut with a computer controlled saw, polished, and contacts applied. Samples were all between 1.2 mm and 1.4 mm thick for a given sample (Figure 104). Some samples were saved to investigate whether or not annealing might demonstrate different electrical properties, however after 24 hours at 200 C in their own powder pellets of both **1** and **2** were found to degrade instead (Figure 105).

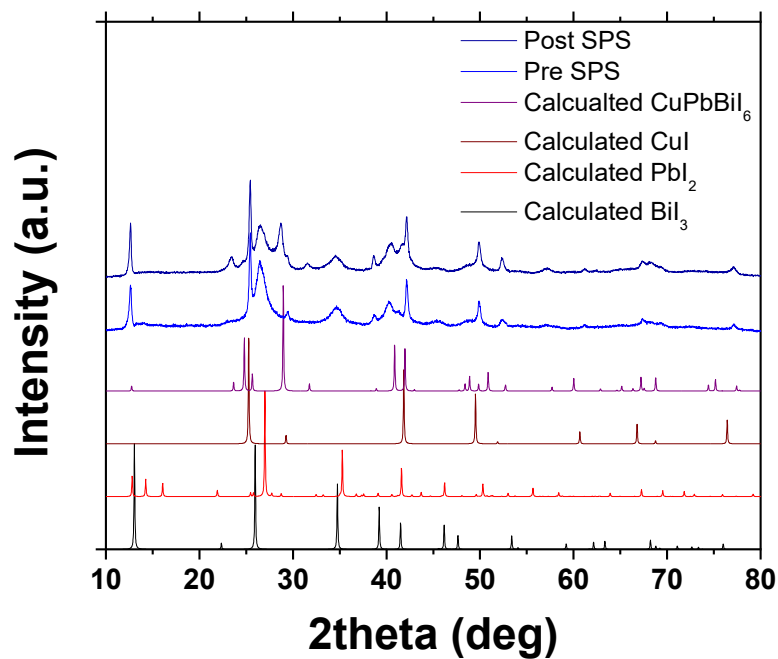


Figure 102. Comparison of pre and post-SPS samples of **1** compared to the constituent binaries and the calculated powder diffraction pattern from single crystal refinement.

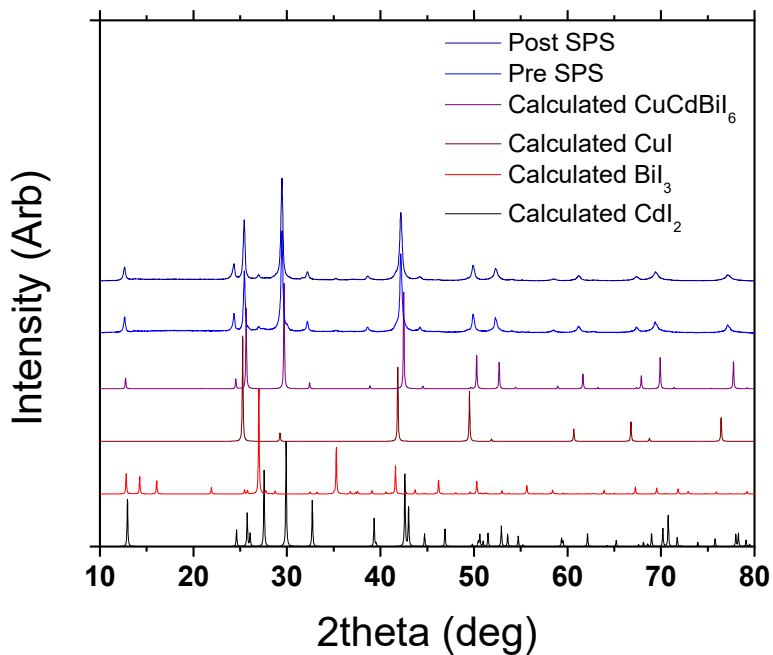


Figure 103. Comparison of pre and post-SPS samples of **2** compared to the constituent binaries and the calculated powder diffraction pattern from single crystal refinement.

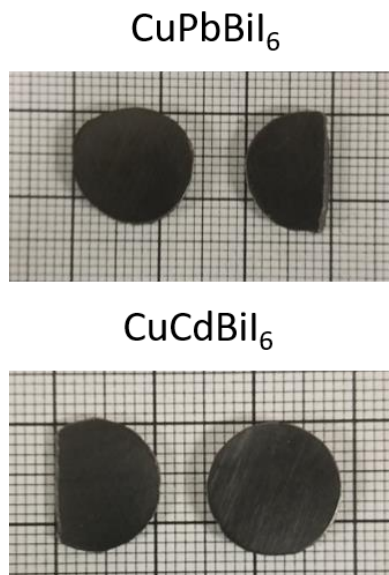


Figure 104. Polished post-SPS samples of **1** and **2**. Contacts were applied to the faces of the pellets on both sides.

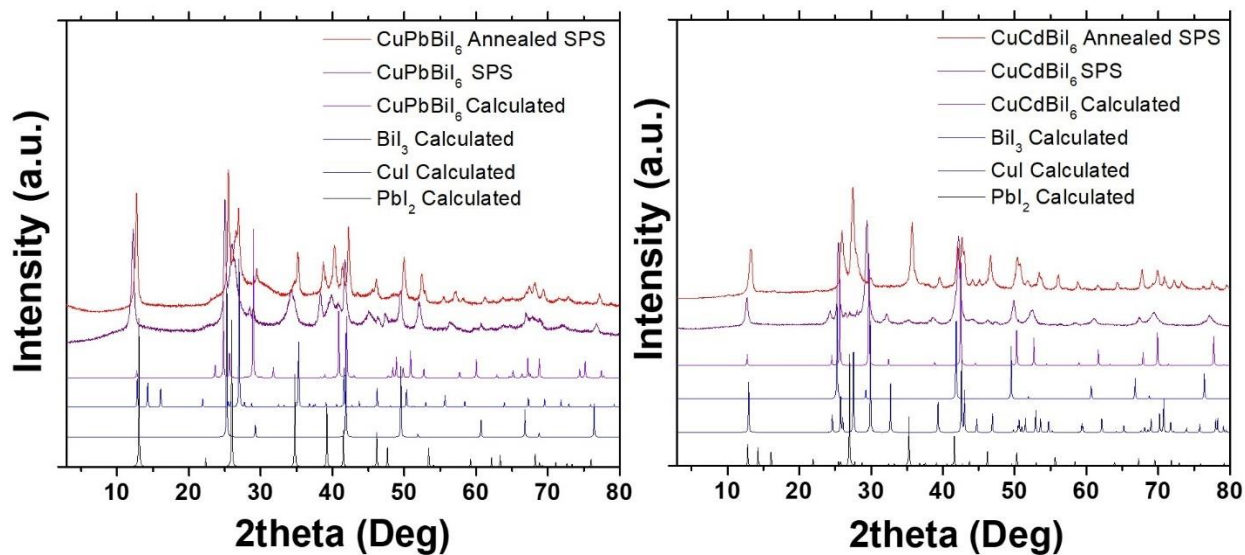


Figure 105. PXRD patterns of samples of **1** and **2** that were annealed for 24 hours at 200 C. After annealing both samples had degraded with additional binary peaks observed in both. Annealed samples were not used in transport measurements.

Applying bias across SPS samples of **1** yield an interesting hysteresis effect. Opposed to the highly resistive samples of $(\text{PbI}_2)_{0.5}(\text{BiI}_3)_{0.5}$ the addition of copper significantly reduces the apparent resistance and does not yield the same sort of conduction switching that the $(\text{Pb}_2)_{0.5}(\text{BiI}_3)_{0.5}$ material readily demonstrated. Instead samples of **1** show that over successive runs at lower bias ($< 30 \text{ V}$) the conductivity of the material increases as successive sweeps are conducted, which nearly reaches the maximum current allowed by the instrument ($1 \times 10^{-3} \text{ A}$) (Figure 106). Slower initial I-V sweep begins with an inherently resistive material, which then begins to show exponential increase in current. Once the maximum bias has been reached, the return to low bias reveals that current continues to increase until bias is sufficiently reduced whereupon the measured current “discharges”. This effect occurs in both positive and negative bias. Sweeps were conducted a faster rate to further investigate the behavior of the material, and as such the relative hysteresis is not as pronounced with faster runs (Figure 107). For this sample the dependence on the contact size on each side was made clear as one direction was able to achieve very high conductivity, when sweep direction and contacts were applied in reverse the same effects was observed.

Applied bias across samples of **2** show an analogous I-V behavior to that of samples of **1**. Sweeps on the same sample show increased overall resistance to the electronic and possible ionic conduction (Figure 108). Opposed to the layered 3D type rudorffite structure of **1**, **2** demonstrates increased resistance that may arise from the defect-spinel structure that hinders conduction. In either case, both **1** and **2** have such disordered, defect ridden structures that there is a significant the possibility ionic conduction.

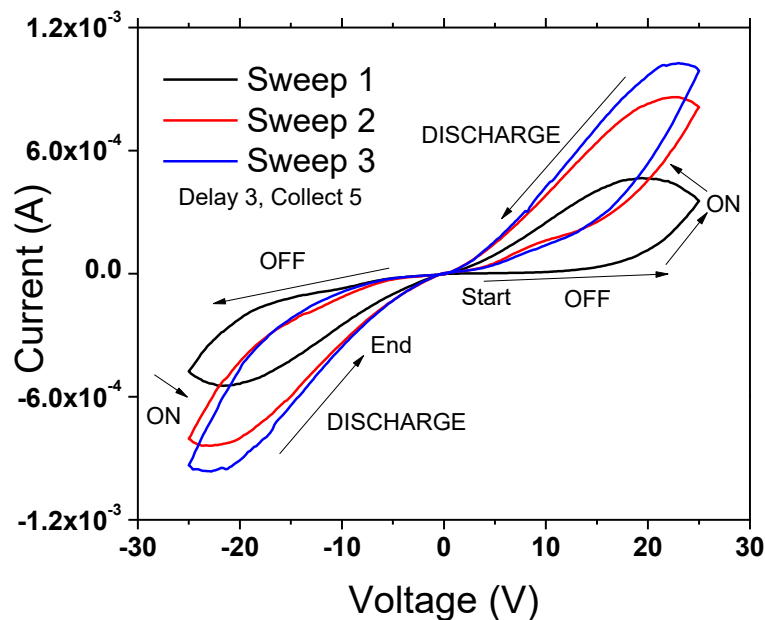


Figure 106. Successive sweeps of ± 25 V on a sample of **1**. Successive sweeps demonstrate that the OFF, ON, and DISCHARGE cycle are dependent on the number of bias applications.

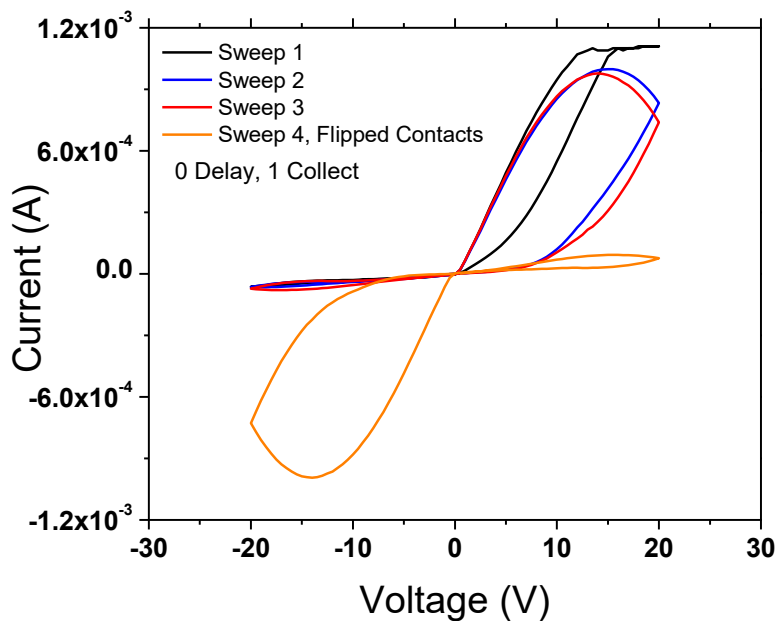


Figure 107. Successive sweeps of ± 20 V on a sample of **1**. Successive sweep show that for a given sample the intrinsic conductivity varies. Sweep 1 resulted hitting the maximum current for the electrometer. Successive sweeps were conducted and current was within measurable limits.

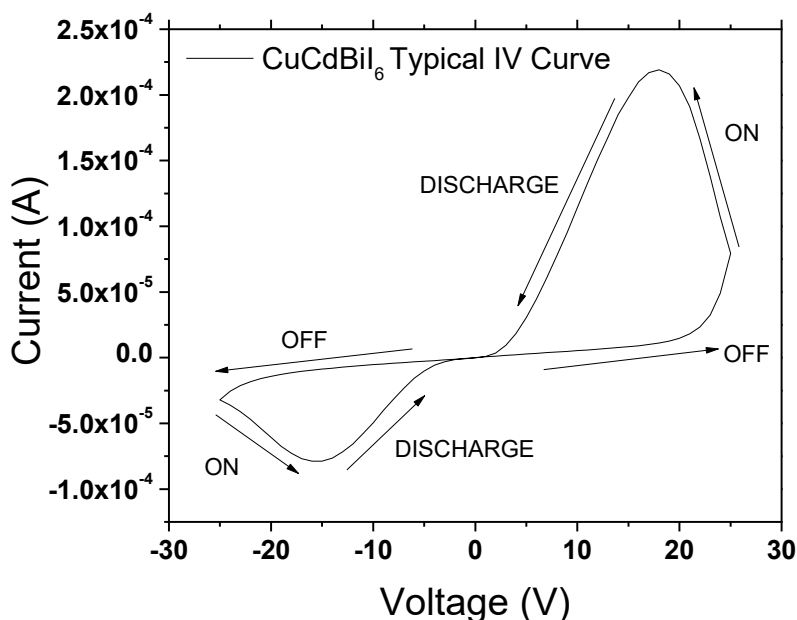


Figure 108. Representative I-V sweep of samples of **2**. Similar increasing current is observed over subsequent sweeps with the magnitude of the current peak dependent on the contact site for the given side of a device as demonstrated in Figure 107.

To additionally probe the nature of the I-V sweeps in **1** and **2** single point bias measurements were conducted with regard to time of applied bias. The results for samples of both **1** and **2** demonstrate that even under low but sufficient constant bias the electrical conductivity increases within the samples (Figures 109 and 110). This serves to indicate that under bias both **1** and **2** increase their ability to conduct electrons and ions, and as such we observed to contact regions of both under SEM after the single point bias measurements. Both **1** and **2** exhibited Cu metal buildup at the contact sites (Figure 111 and 112). This indicates the mobility and ionic conductivity of Cu within the crystalline matrixes of **1** and **2**.

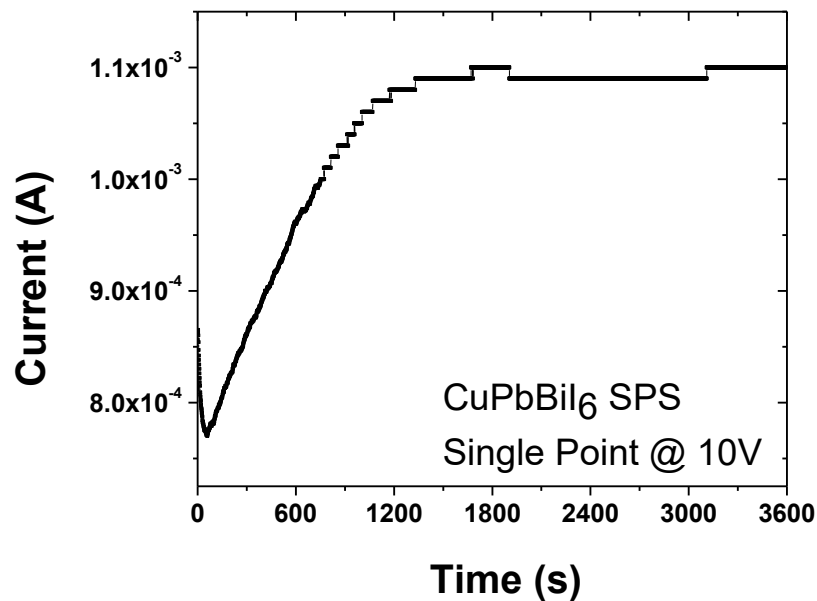


Figure 109. Single point measurement of **1** under constant 1 V bias for hour. The material hit the conductivity limit of the instrument within the first 20 minutes.

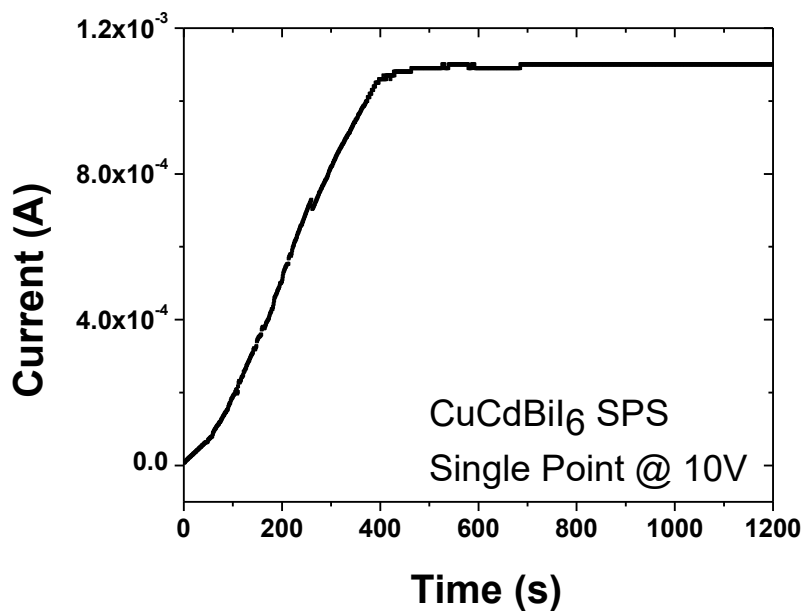


Figure 110. Single point measurement of **2** under constant 1 V bias for 20 minutes. The material hit the conductivity limit of the instrument within the first 7 minutes

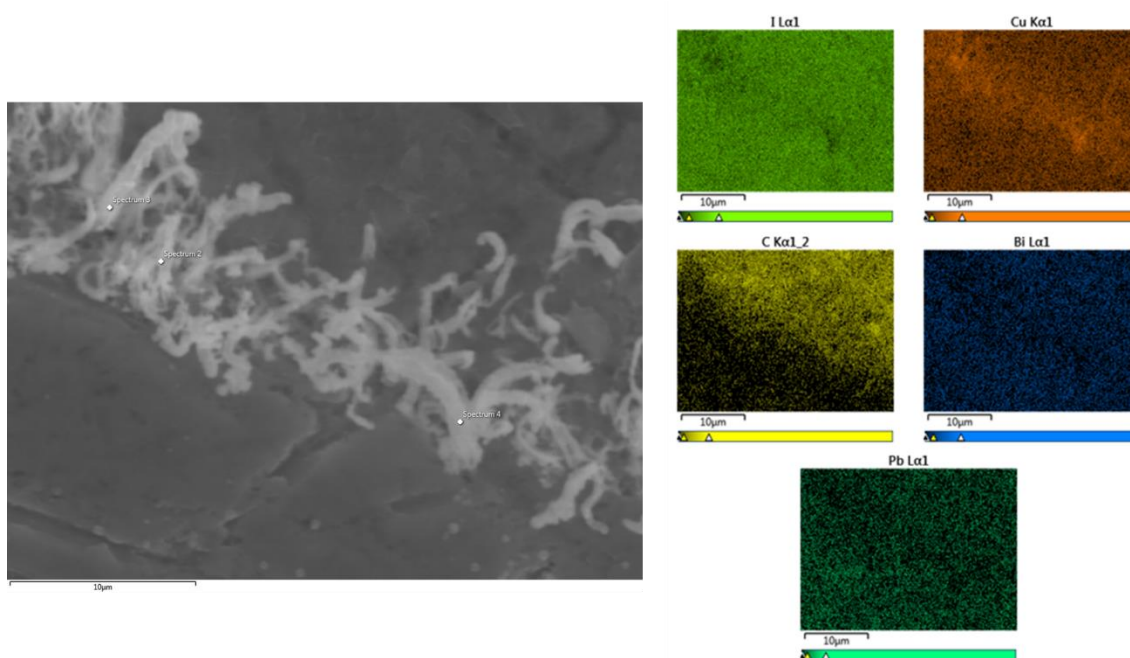


Figure 111. Evidence of Cu buildup for **1** at the carbon contact site after long term single point measurements bias measurements.

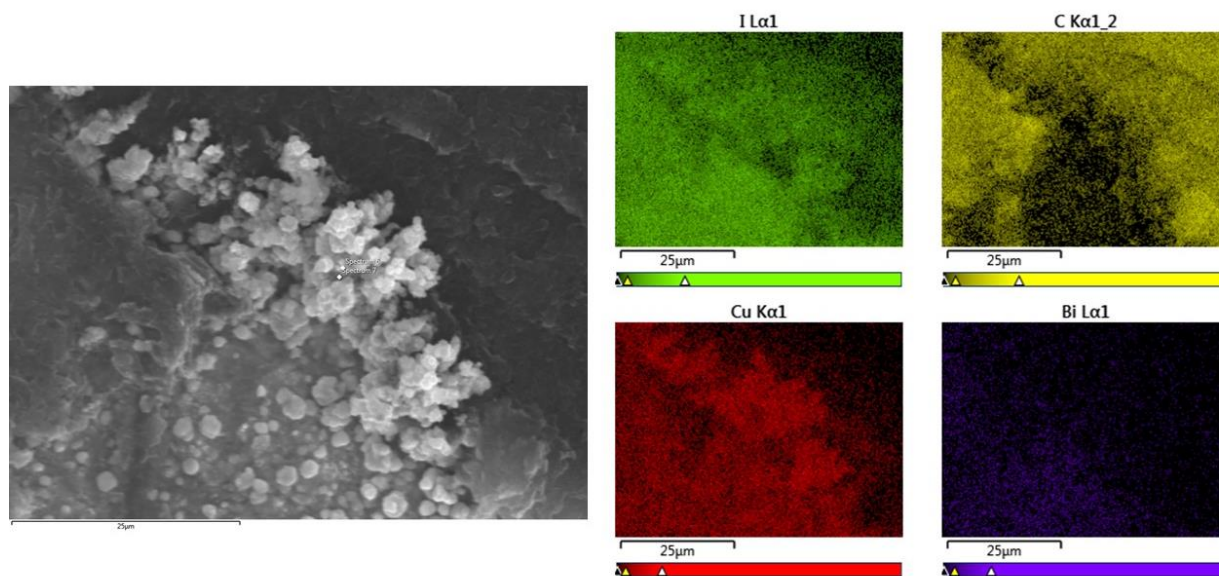


Figure 112. Evidence of Cu buildup for **2** at the carbon contact site after long term single point measurements bias measurements.

The evidence for Cu ion conductivity in **1** and **2** is made clear not only by their I-V sweep behavior, but additional supported by the single point bias measurements and the observation reduced Cu being expelled at the contact sites post induced bias. These observations support the notion of Cu ion conduction within the material, however these need to be further affirmed through more rigorous electronic characterization as evidenced in chapter two.

4.5. Conclusion

The 3D quaternary copper containing heavy metal halides demonstrate robust mechanical stability relative to their parent 2D $(MI_2)_{0.5}(BiI_3)_{0.5}$ ($M = Cd, Bi$) van der Waals materials. The inclusion of copper within the crystal structure not only yields the mechanical stability, but also increased dimensionality from 2D van der Waals materials to 3D quaternary ruderfite-type structures. The crystal structures of **1** and **2** demonstrate that mixed Cu/Bi/ Δ dominate the overarching structure of the solids and Cu prefers the inherent tetrahedral sites in $(MI_2)_{0.5}(BiI_3)_{0.5}$ system. Copper occupancy is diffuse throughout the applicable tetrahedra sites. Optical properties of both **1** and **2** follow in suite with the optical properties of 2D $(PbI_2)_{0.5}(BiI_3)_{0.5}$ as discussed in chapter three. The electrical properties demonstrate that for these highly defect containing structures the addition of Cu increases the overall conductivity, and SEM-EDS affirms the ionic conductivity of Cu within these materials.

The results in this chapter demonstrate the for a ternary system such as 2D $(MI_2)_{0.5}(BiI_3)_{0.5}$ the addition of a monovalent preferably tetrahedral cation not only lead to greater dimensionality, but robust mechanical properties and increases ionic conduction. Future work should focus on the nature of the probable ionic conduction and the development of other possible ionic conductors base on the $CuCdBiI_6$ structural features.

Chapter 5

AuPb₂I₇: A Narrow Bandgap Au³⁺ Iodide Semiconductor

5.1. Abstract

The unusual Au³⁺ ternary halide AuPb₂I₇ has been isolated from reactions of AuI, PbI₂, and I₂. AuPb₂I₇ crystallizes in the triclinic *P*-1 space group as micron-scale needles with cell dimensions $a = 4.5170(3)$ Å, $b = 7.3847(4)$ Å, $c = 12.2970(7)$ Å, $\alpha = 76.374(4)^\circ$, $\beta = 83.711(4)^\circ$, $\gamma = 72.987(3)^\circ$ at room temperature with $\rho = 6.538$ g/cm³ and has no structural phase transition down to 100 K. The title compound has a unique three-dimensional structure composed of [Pb₂I₇]³⁻ pseudo-layers extending in [010] bridged by square planar Au³⁺ at an oblique angle in the [001] direction. The pseudo-layers are composed of $1/\infty$ [Pb₂I₂]²⁺ chains propagating down [100] linked by square planar I⁻ ions through [010]. AuPb₂I₇ has a band gap of 1.17 eV and is stable in air for a several days, before degrading to PbI₂, Au⁰, and I₂. Density Functional Theory calculations show that AuPb₂I₇ is an indirect bandgap semiconductor where the band gap stems predominantly from Au – I metal ligand charge transfer.

The material in this chapter has been published previously:

G. C. B. Alexander, D. H. Fabini, R. Seshadri, M. G. Kanatzidis, “AuPb₂I₇: A Narrow Bandgap Au³⁺ Semiconductor” *Inorg. Chem.*, **2018**, 57, 804 – 810.

5.2. Introduction

The class of heavy-metal halide semiconductors without organic cations has sparked a quickly growing interest in understanding their structural chemistry and optoelectronic properties for potential uses in various electronic devices including hard and soft radiation detection.^{85, 97, 101, 131, 148} In particular, there is a search for alternative materials to alleviate the stability issues which plague the organic-inorganic hybrid perovskites.⁸³ Such efforts have focused on alternative B-site cations for the AMX_3 perovskites^{85, 123}, perovskite-like phases^{55, 124}, and the $A_3M'_2X_9$ defect perovskite phases where $A = Rb, Cs, Tl$; $M = Pb$; $M' = Bi, Sb$; $X = I, Br, Cl$.^{101, 125} Very little perovskite chemistry has been reported when the A site is not an alkali ion but a group 11 ion. Literature reveals that no report of $CuPbI_3$, and the $AgI - PbI_2$ system is shown only to have ordered mixtures at elevated temperatures.¹⁴⁹ Thus, Au remains the last system to investigate.

In the case of ternary Au halides, few have been isolated as purely inorganic phases¹⁵⁰⁻¹⁵², and even fewer with iodine as a direct ligand to Au.¹⁵²⁻¹⁵⁵ First are the monoclinic phases of an alkali metal ion with Au in the 3+ oxidation state, such as $LiAuI_4$ and $KAuI_4$, having molecular square planar $[AuI_4]^-$ units charge balanced by the alkali metal cation, Figure 113a. Rb and Cs stabilize the formation of tetragonal perovskite-like $Rb_2[AuI_4][AuI_2]$ and $Cs_2[AuI_4][Au^I I_2]$, Figure 113b.^{153, 155} In these phases gold is found in two different valence states (1+ and 3+), alternating in square planar and linear coordination to form the pseudo-perovskite lattice encapsulating the cation. There are no current reports of Au being substituted on the A site of AMI_3 phases. Au^{1+} is much smaller than Rb or Cs, and if it could be incorporated it would surely destabilize the perovskite-type lattice but it could be expected to form other structure types similar to $TlPbI_3$ which is two dimensional.¹⁵⁶

Here we report that our attempts to produce “AuPbI₃” led to the isolation of the surprising compound AuPb₂I₇ which does not contain Au⁺ but is composed of anisotropic pseudo-layers of a 3D structure of extended [Pb₂I₇]³⁻ pseudo-layers bridged by square planar Au³⁺. AuPb₂I₇ is the first reported gold heavy metal halide to be structurally characterized. AuPb₂I₇ grows on the surface of recrystallized PbI₂ from the off-stoichiometric reactions of AuI and PbI₂ as well as direct synthetic methods with I₂. The compound is black with an experimental band gap of 1.17 eV. Density Functional Theory calculations demonstrate an indirect bandgap semiconductor.

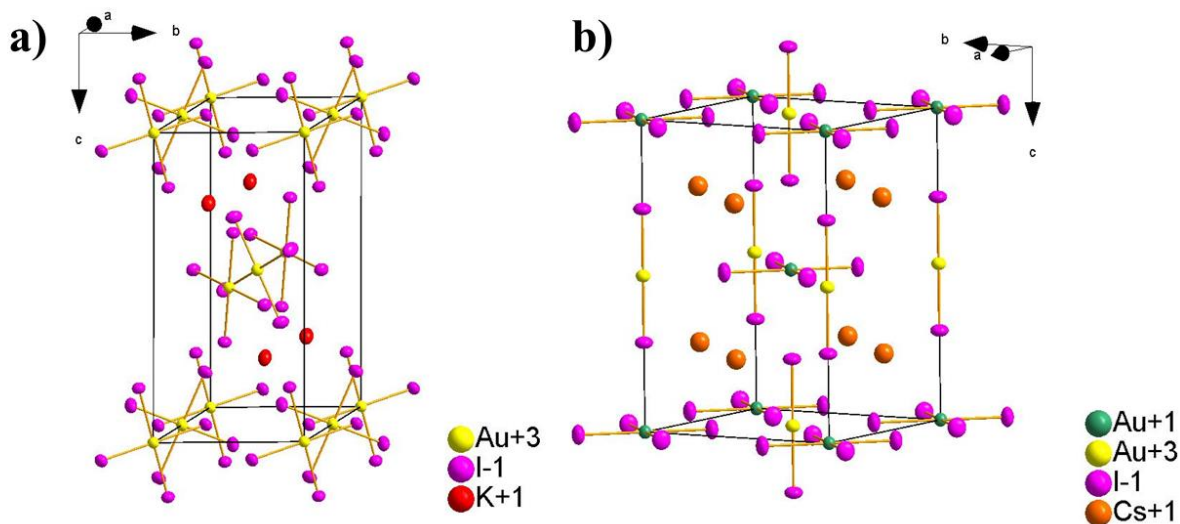


Figure 113. a) The structure of KAu₃I₄ where [AuI₄]⁻ units extend down [010] charge balanced by K⁺, a direct analog of LiAuI₄ as drawn from reference 16. b) The perovskite-like structure of Cs₂Au¹⁺Au³⁺I₆ where alternating [AuI₂]⁻ and [AuI₄]⁻ form pseudo-octahedra around charge balancing Cs cations, as drawn from reference 15. Rb₂ Au¹⁺Au³⁺I₆ forms the same structure.

5.3. Experimental Details

5.3.1 Synthesis and Isolation

All chemicals were used as obtained from the supplier: AuI, PbI₂, and I₂ (99.999%, Sigma-Aldrich, St. Louis, MO). 1 to 1 and 1 to 2 ratios of AuI and PbI₂ were used for initial off stoichiometry syntheses at the 1 mmol (323.8 mg AuI and 461.0 or 921.0 mg PbI₂) or 2 mmol (627.6 mg AuI and 921 mg or 1842 mg PbI₂). For direct syntheses 1 mmol scale stoichiometric ratios of AuI (323.8 mg), PbI₂ (921 mg), and I₂ (253.8 mg) were used. All materials were weighed, mixed, and transferred into 13 mm fused quartz tubes on the benchtop. Tubes were sealed at or below 3×10^{-3} mbar and heated to 600 C in 48 hours, held for 48 hours, and cooled to 30 C in 24 hours. Minute quantities of micron-scale black crystals of the title compound grow on surfaces of recrystallized PbI₂. Due to crystallization on the surface of PbI₂, AuPb₂I₇ proves difficult to mechanically isolate as a pure phase (Yield: 0.1g, Less than 10% based on Au).

A vapor transport experiment was also conducted; 1 mmol AuI (323.8 mg), 2 mmol of PbI₂ (921 mg), and 1.2 mmol of I₂ (304.6 mg) were combined on the bench and sealed in a fused quartz tube at or below 3×10^{-3} mbar. A slight excess of I₂ was added to help function as a transport agent. The tube measured approximately 230 mm, and was centered in a horizontal two zone furnace with the hot zone set to 450 C and cold zone set to 200 C. Reagents were set in the hot zone. For both zones temperature controllers were set to ramp to the target temperature in 10 hours, hold for 72 hours, and cool to room temperature in 15 hours. No transport of the title compound was achieved, but unreacted PbI₂ was transported away from the product yielding slightly easier isolation. Micron scale crystals can be isolated in small quantities for optical and single crystal diffraction experiments (Yield: 0.1g, Less than 10% based on Au).

5.3.2. Single Crystal X-Ray Diffraction

Single Crystals of AuPb_2I_7 were isolated from the reaction mixture under Paratone N oil to shield samples from oxygen. Samples of sufficient size were isolated off the surface of PbI_2 for X-ray diffraction. Once selected the small needles were mounted on a MiTeGenTM mounts using Paratone N oil. Diffraction was conducted at 298 K and 100 K on a Bruker KAPPA APEX diffractometer with a $\text{MoK}\alpha$ microsource and QuazarTM optics monochromator. Using the COSMO program provided in the APEX 3 software, data collection strategy with a series of 0.5° scans in ω and ϕ was determined.¹⁵⁷ The exposure time was 10 s/frame, and the crystal-to-detector distance was 60 mm. SADABS or TWINABS was used for face-indexed absorption, incident beam, and decay corrections.^{158, 159} The structure solved by the direct method and refined on F^2 using the SHELX14 program suite.¹²¹ All atoms were refined anisotropically.

5.3.3. Powder X-ray diffraction

The presence of AuPb_2I_7 was verified by powder diffraction using a Rigaku Miniflex power X-ray diffractometer with Ni-filtered $\text{Cu K}\alpha$ radiation operating at 30 kV and 15 mA. Scans were performed with a resolution of 0.02° and a scan rate of $10^\circ/\text{min}$. Simulated powder patterns of AuPb_2I_7 were calculated using the refined room-temperature crystal structure CIF with MERCURY, part of the CSD software suite.¹¹⁹

5.3.4. Scanning Electron Microscopy

A Hitachi S-3400 scanning electron microscope equipped with a PGT energy-dispersive X-ray analyzer was used to acquire images and semi quantitative EDS analyses. Spectra were collected using an accelerating voltage of 25 KeV and current of 70 uA for 60 s. No reduction of

Au was observed during the SEM experiments due to the electron beam. The reported composition from EDS is based on multiple independent spectra, see supporting information.

5.3.5. Solid State UV-Vis Spectroscopy

A Shimadzu UV-3600 PC double-beam, double-monochromator spectrophotometer was used to collect diffuse-reflectance spectra in the range of 200–2500 nm. The instrument was equipped with an integrating sphere and controlled by a personal computer. BaSO₄ was used as a standard and set to 100% reflectance. Samples were prepared by quickly placing the ground crystalline products on a bed of BaSO₄ in air. Collected reflectance data were converted to absorbance according to the Kubelka–Munk equation $\alpha/S = (1 - R)^2 / 2R$, where α is the absorption coefficient, S is the scattering coefficient, and R is the reflectance.¹⁴³ The band gap was determined by extrapolating the intercept of the fitted converted data.

5.3.6. Density Functional Theory (DFT) Calculations

Calculations of the electronic structure were performed with the Vienna Ab initio Simulation Package (VASP)^{129, 160-162} which implements the Kohn–Sham formulation of density functional theory (DFT) using a plane wave basis set and the projector augmented wave formalism.^{163, 164} The generalized gradient approximation was employed using the exchange and correlation functional of Perdew, Burke, and Ernzerhof (GGA–PBE), with and without the inclusion of spin-orbit coupling (SOC).¹³⁰ Hybrid functional calculations which incorporate exact exchange were prohibitively expensive due to the low symmetry and heavy atoms. Electrons were included in the valence as follows: Au, 6s²5d⁹; Pb, 6s²5d¹⁰6p²; I, 5s²5p⁵. The plane wave basis set cutoff energy (500 eV) and k-point mesh density (9×5×3 for total energy and band calculations, 15×9×5 for density of states, all Monkhorst–Pack sampling¹⁶⁵) were chosen based on convergence

of the total energy. The Brillouin zone path for band structure calculations was taken from Setyawan and Curtarolo.¹⁶⁶ Ground-state DFT structure relaxations poorly reproduced the experimental structures, in a manner similar to other soft metal halides. However, unlike higher symmetry crystals (where the differences between DFT and experiment are more isotropic), the highly anisotropic connectivity of AuPb₂I₇ leads to significant shearing of the unit cell (such that the lattice angle α becomes more acute). As such, the experimental crystal structure was employed for electronic structure calculations. The net forces on the ions in the experimental structure were highest for the iodine labeled “I1” in Tables 20 and 23.

5.4. Results and Discussion

5.4.1. Synthesis and Isolation

All reactions performed between AuI and PbI₂ aimed at obtaining a AuPbI₃ or AuPb₂I₅ compositions failed to do so. No evidence for the existence of such phases was present, however, we were able to obtain black needle-like crystals of the ternary compound AuPb₂I₇ as evidenced by SEM-EDS (Figure 114, Tables 17 and 18). Despite many attempts at synthesizing a pure phase of AuPb₂I₇, the compound grows directly on the surface of PbI₂ crystals (Figures 114 and 115) and forms regardless of the ratio of AuI and PbI₂ combined. To balance charge in this phase, the Au must be in the 3+ oxidation state. Because the starting Au source is AuI, to form AuPb₂I₇ Au^I must undergo the oxidation *in situ* to Au³⁺. However, this oxidation must be a disproportionation reaction of Au⁺ to Au⁰ and Au³⁺, and therefore removes gold metal from the reaction, which can be observed in Figure 116.

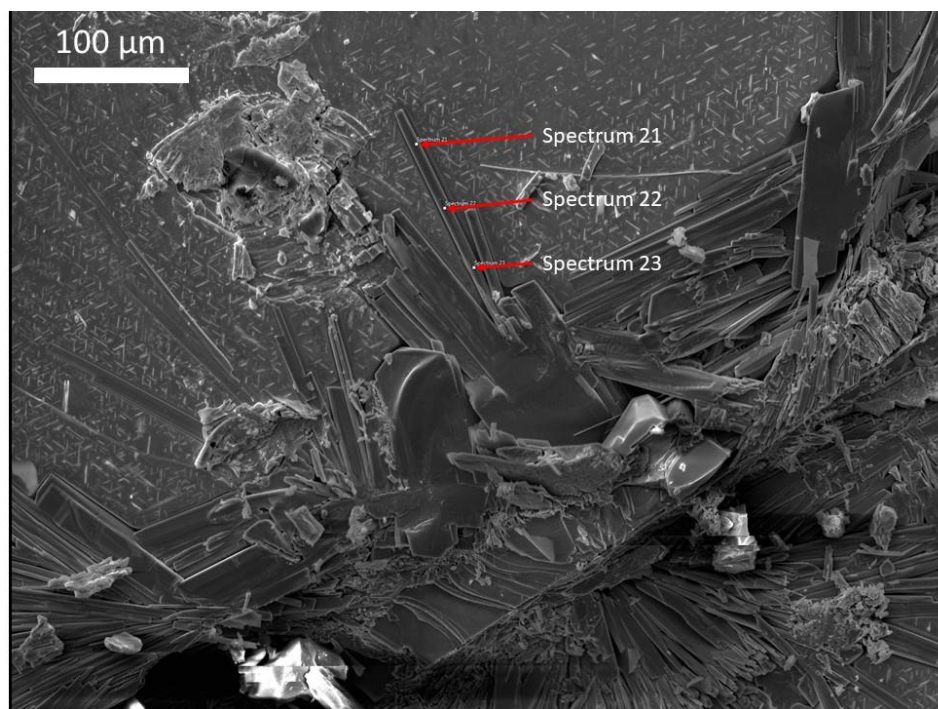


Figure 114. SEM image of the regions chosen to gather EDS data from AuPb₂I₇. Due to growth on the surface of PbI₂, often the penetration depth of the electron beam will be greater than the thickness of the crystal resulting in overrepresented Pb and I atomic %.

Table 17. SEM-EDS Spectra Results of AuPb₂I₇ as assessed from the regions in Figure 114 in Atomic %.

Spectrum Label	Spectrum 21	Spectrum 22	Spectrum 23
I	68.35	67.08	67.84
Au	10.14	10.12	10.35
Pb	21.51	22.79	21.81
Total	100	100	100

Table 18. Average Values and Standard Deviation of SEM-EDS Results from Table 17.

Atom Type	I	Au	Pb
Max	68.4	10.4	22.8
Min	67.1	10.1	21.5
Average	67.8	10.2	22.0
Standard Deviation	0.64	0.12	0.67
Relative Ratio (Based on Au)	6.6	1	2.2

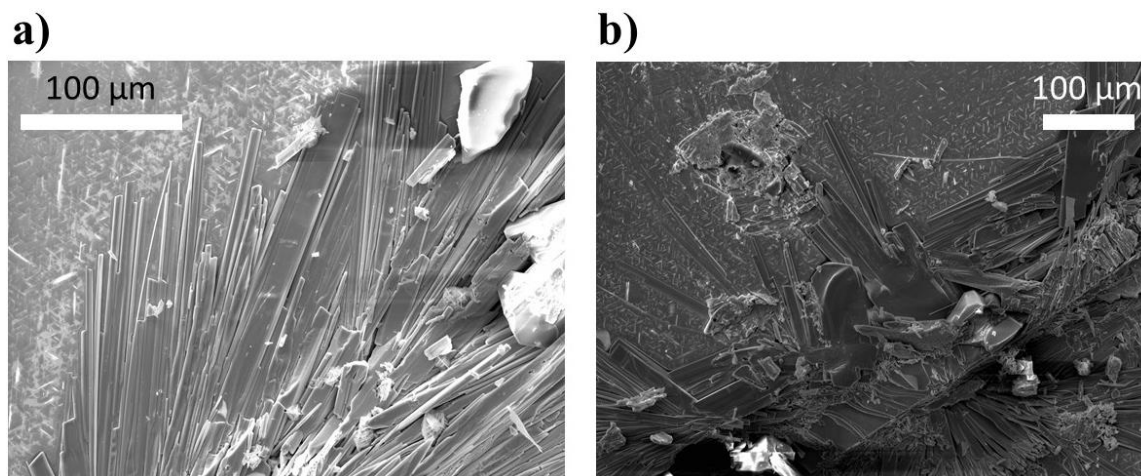


Figure 115. SEM Images of single crystals of AuPb_2I_7 growing on the surface of recrystallized PbI_2 . Crystals tend to grow near edges where nucleation begins to occur.

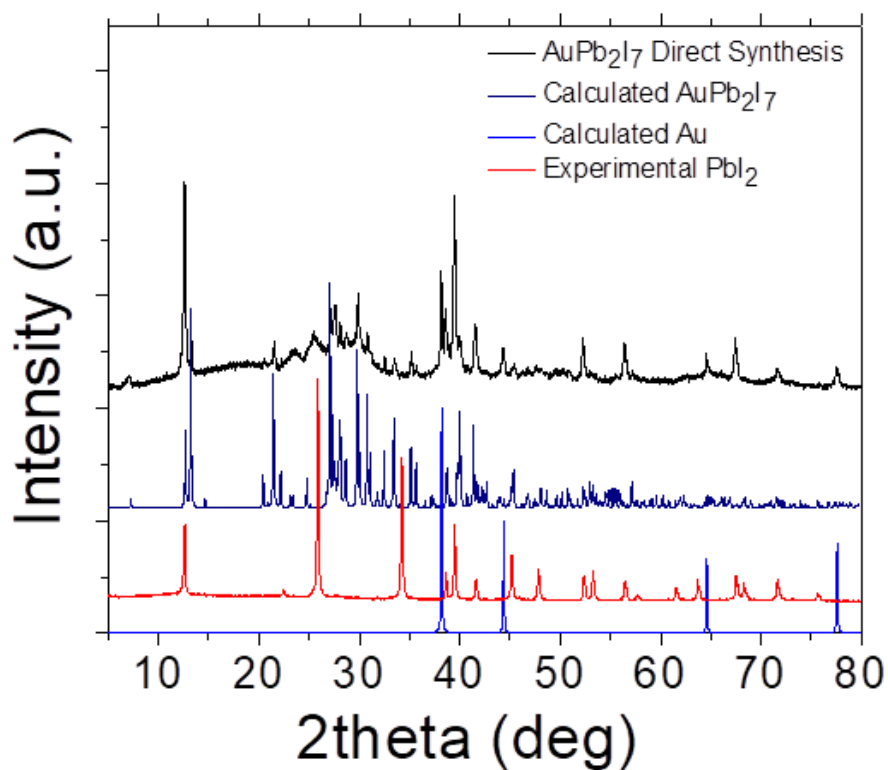


Figure 116. A typical powder diffraction pattern for the reaction mixture of AuPb_2I_7 . Au and PbI_2 are clearly represented in the pattern, but peaks of the calculated pattern from single crystal data confirms the presence of the title compound.

To mitigate Au loss to disproportionation, iodine was added to the reaction mixture to act as an oxidant. The direct method of synthesis with I_2 yields slightly more product, but the reaction products remain a mixture of $AuPb_2I_7$, PbI_2 , I_2 , and Au^0 , Figure 115. Varying the reaction heating rate, soak time, and cooling rate from 6 to 48 hours did not show any significant effect on the formation fraction of $AuPb_2I_7$. Attempting vapor transport did not yield significant improvement in isolating the $AuPb_2I_7$, however due to the temperature gradient PbI_2 was transported away from the product, localizing most of the growth of the title compound on the non-transported PbI_2 (Figures 117 and 118). This can be seen in the larger patches of growth, but underneath remains the PbI_2 substrate, Figure 119a. $AuPb_2I_7$ decomposes slowly in air to yield Au^0 , PbI_2 and I_2 , which is unsurprising as the previously discussed Au iodide compounds all undergo the same reduction. This is evident in Figure 119b, where Au has physically expelled itself from the crystal matrix.

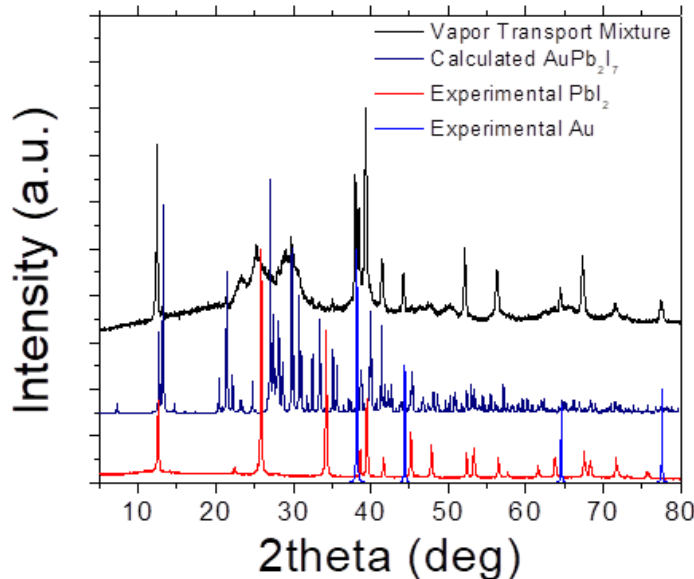
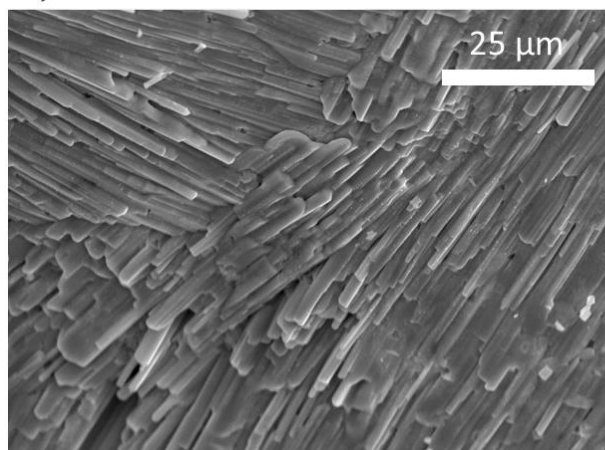


Figure 117. Powder diffraction from the vapor transport mixture shows little evidence of the title compound despite having the most observed by electron microscopy. Due to transport of unreacted PbI_2 away from the melt the mixture that remained in the hot end of the tube was far more gold rich as further described in Figure 118.



Figure 118. Vapor Transport tube after the transport experiment shows the transported PbI_2 on the right side of the image. The black solid on the left hand side is the remaining AuPb_2I_7 grown on PbI_2 , with a dominant amount of metallic gold. This was in the hot zone.

a)



b)

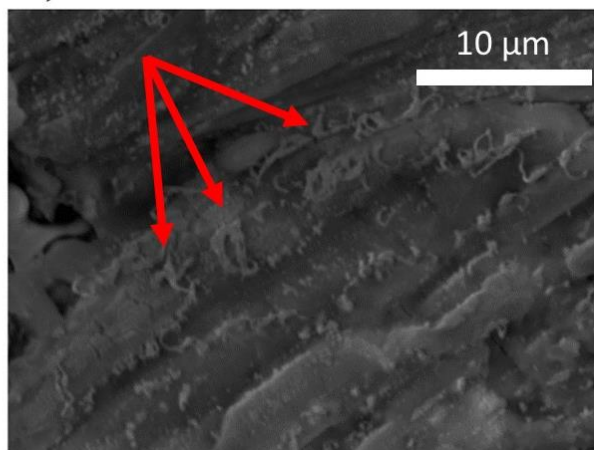


Figure 119. a) A larger forest of needles found after vapor transport. These crystals still grow as layers on top of PbI_2 substrate. b) Au metal expelling from needles of AuPb_2I_7 one month after preparation.

5.4.2. Crystal Structure Description

AuPb₂I₇ crystallizes in the triclinic *P*-1 space group (No. 2) and presents a 3D structure of extended [Pb₂I₇]³⁻ pseudo-layers extending in [010] bridged by square planar Au³⁺ at an oblique angle in the [001] direction. See Tables 19 – 25 for crystallographic data pertaining to refinement details, atom coordinates, anisotropic parameters, and selected bond distances and angles. The [Pb₂I₇]³⁻ layers can be better described as $1/\infty$ [Pb₂I₂]²⁺ backbone-like chains propagating down [100] linked by square planar I along [010], Figure 120 A full view of the ball and stick representation of the structure is shown in Figure 121. The Au atom must be 3+ to charge balance the stoichiometry.

Table 19. Crystal data and structure refinement for AuPb₂I₇ at 100 and 298 K.

Formula weight	1499.65	1499.65
Temperature	100 K	298 K
Wavelength	0.71073 Å	0.71073 Å
Crystal system	Triclinic	Triclinic
Space group	<i>P</i> -1	<i>P</i> -1
Unit cell dimensions	a = 4.4803(9) Å, α = 76.29(3)° b = 7.3443(15) Å, β = 84.00(3)° c = 12.226(3) Å, γ = 73.06(3)°	a = 4.5170(3) Å, α = 76.374(4)° b = 7.3847(4) Å, β = 83.711(4)° c = 12.2970(7) Å, γ = 72.987(3)°
Volume	373.60(15) Å ³	380.83(4) Å ³
Z	1	1
Density (calculated)	6.665 g/cm ³	6.539 g/cm ³
Absorption coefficient	46.683 mm ⁻¹	45.797 mm ⁻¹
F(000)	614	614
Crystal size	0.129 x 0.041 x 0.02 mm ³	0.027 x 0.042 x 0.067 mm ³
θ range for data collection	1.716 to 24.999°	1.706 to 24.999°
Index ranges	-5<=h<=5, -8<=k<=8, 0<=l<=14	-5<=h<=5, -8<=k<=8, - 14<=l<=14
Reflections collected	5840	6032
Independent reflections	1279 [R _{int} = 0.0363]	1346 [R _{int} = 0.0437]
Completeness to θ = 26.000°	97.8%	99.8%
Refinement method	Full-matrix least- squares on F ²	Full-matrix least- squares on F ²
Data / restraints / parameters	1279 / 0 / 50	1346 / 0 / 49
Goodness-of-fit	1.235	1.067
Final R indices [I > 2σ(I)]	R _{obs} = 0.0365, wR _{obs} = 0.1201	R _{obs} = 0.0335, wR _{obs} = 0.0804
R indices [all data]	R _{all} = 0.0376, wR _{all} = 0.1235	R _{all} = 0.0406, wR _{all} = 0.0880
Largest diff. peak and hole	2.848 and -3.664 e·Å ⁻³	2.929 and -1.602 e·Å ⁻³

$R = \sum ||F_o| - |F_c|| / \sum |F_o|$, $wR = (\sum [w(|F_o|^2 - |F_c|^2)^2] / \sum [w(|F_o|^4)])^{1/2}$ and $w = 1/[\sigma^2(F_o^2) + (0.0155P)^2 + 4.1752P]$
where $P = (F_o^2 + 2F_c^2)/3$

Table 20. Atomic coordinates ($\times 10^4$) and equivalent isotropic displacement parameters ($\text{\AA}^2 \times 10^3$) for AuPb_2I_7 at 298 K with estimated standard deviations in parentheses.

Label	x	y	z	Occupancy	U_{eq}^*
Au	5000	5000	5000	1	24(1)
Pb	1641(2)	2749(1)	8594(1)	1	37(1)
I1	7315(2)	7904(2)	4043(1)	1	26(1)
I2	4704(2)	6069(2)	6916(1)	1	26(1)
I3	-1961(2)	-349(2)	8621(1)	1	30(1)
I4	5000	5000	0000	1	33(1)

* U_{eq} is defined as one third of the trace of the orthogonalized U_{ij} tensor.

Table 21. Anisotropic displacement parameters ($\text{\AA}^2 \times 10^3$) for AuPb_2I_7 at 298 K with estimated standard deviations in parentheses.

Label	U_{11}	U_{22}	U_{33}	U_{12}	U_{13}	U_{23}
Au	27(1)	29(1)	16(1)	-11(1)	3(1)	-3(1)
Pb	29(1)	40(1)	43(1)	-14(1)	4(1)	-10(1)
I1	36(1)	32(1)	23(1)	-17(1)	3(1)	-2(1)
I2	46(1)	38(1)	20(1)	-20(1)	8(1)	-9(1)
I3	22(1)	30(1)	25(1)	-10(1)	1(1)	-2(1)
I4	24(1)	32(1)	24(1)	-10(1)	0(1)	-9(1)

The anisotropic displacement factor exponent takes the form: $-2\pi^2[h^2a^{*2}U_{11} + \dots + 2hka^*b^*U_{12}]$.

Table 22. Selected Bond lengths [\AA] and Bond angles [$^\circ$] for AuPb_2I_7 Pb_2 at 298 K with estimated standard deviations in parentheses.

Label	Distances	Label	Angles
Au – I1 x 2	2.6330(9)	I1 – Au – I1	180.0
Au – I2 x 2	2.6344(9)	I1 – Au – I2	88.37(3)
Pb – I3	3.1149(10)	I2 – Au – I1	91.63(3)
Pb – I3	3.1644(10)	I2 – Au – I2	180.0
Pb – I2	3.3407(11)	I3 – Pb – I3	92.00(3)
Pb – I1	3.3529(11)	I3 – Pb – I1	76.56(3)
Pb – I4	3.3849(6)	I3 – Pb – I1	76.97(3)
Pb – I3	3.4617(11)	I3 – Pb – I2	90.28(3)
Pb – I4	3.4714(6)	I3 – Pb – I2	143.69(3)
Pb – I2	3.8247(12)	I2 – Pb – I1	68.71(2)
		Pb – I2 – Pb	77.83(2)
		Au – I1 – Pb	99.69(3)
		Au – I2 – Pb	99.97(3)

Symmetry transformations used to generate equivalent atoms:

(1) $-x+1, -y+1, -z+1$ (2) $x+1, y, z$ (3) $x-1, y, z$

Table 23. Atomic coordinates ($\times 10^4$) and equivalent isotropic displacement parameters ($\text{\AA}^2 \times 10^3$) for AuPb_2I_7 at 100 K with estimated standard deviations in parentheses.

Label	x	y	z	Occupancy	U_{eq}^*
Au	5000	5000	5000	1	9(1)
Pb	8374(2)	3660(1)	8591(1)	1	13(1)
I4	5000	0	0	1	9(1)
I3	1961(3)	6750(2)	8626(1)	1	10(1)
I1	2668(3)	3038(2)	4039(1)	1	10(1)
I2	5226(3)	2018(2)	6927(1)	1	11(1)

* U_{eq} is defined as one third of the trace of the orthogonalized U_{ij} tensor.

Table 24. Anisotropic displacement parameters ($\text{\AA}^2 \times 10^3$) for AuPb_2I_7 at 100 K with estimated standard deviations in parentheses.

Label	U_{11}	U_{22}	U_{33}	U_{12}	U_{13}	U_{23}
Au	10(1)	12(1)	6(1)	-4(1)	2(1)	-5(1)
Pb	11(1)	14(1)	15(1)	-4(1)	1(1)	-7(1)
I4	9(1)	10(1)	8(1)	-4(1)	2(1)	-4(1)
I3	9(1)	13(1)	9(1)	-4(1)	3(1)	-7(1)
I1	13(1)	13(1)	8(1)	-5(1)	2(1)	-6(1)
I2	15(1)	12(1)	8(1)	-5(1)	0(1)	-4(1)

The anisotropic displacement factor exponent takes the form: $-2\pi^2[h^2 a^{*2} U_{11} + \dots + 2hka^* b^* U_{12}]$.

Table 25. Selected Bond lengths [\AA] for AuPb₂I₇ Pb₂ at 298 K and 100 K with estimated standard deviations in parentheses.

	298 K	100 K
Label	Distances	Distance
Au – I1 x 2	2.6330(9)	2.5464(12)
Au – I2 x 2	2.6344(9)	2.7986(15)
Pb – I3	3.1149(10)	3.1029(17)
Pb – I3	3.1644(10)	3.1493(15)
Pb – I2	3.3407(11)	3.2144(15)
Pb – I1	3.3529(11)	3.5209(18)
Pb – I4	3.3849(6)	3.4794(13)
Pb – I3	3.4617(11)	3.3355(16)
Pb – I4	3.4714(6)	3.6371(17)
Pb – I2	3.8247(12)	3.5658(18)

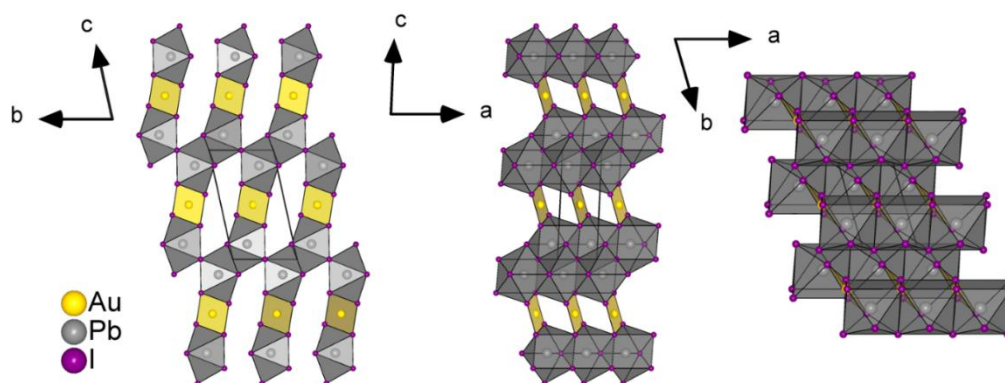


Figure 120. Left) A projection of along $[100]$ of the pseudo-layers in a $3 \times 3 \times 3$ supercell of $\text{AuPb}_2\text{I}_7 \cdot \frac{1}{\infty}[\text{Pb}_2\text{I}_2]^{2+}$ can be seen propagating down $[100]$ and bridged by Au^{3+} . Middle) A projection down $[010]$ further demonstrates the pseudo-layered nature of the system. Right) The projection down $[001]$ which shows the corrugated nature of the pseudo-layers.

Au^{3+} sits in a square planar site bridging the layers together such that a three-dimensional structure is attained. The plane of the $[\text{AuI}_4]^-$ unit does not correspond to any cardinal coordinate and is oblique to $[001]$. Bond distances for the $[\text{AuI}_4]^-$ are within 2.6330(9) to 2.6344(9) Å, which agrees with other square planar Au^{3+} in⁹⁸ $\text{A}_2\text{Au}^{\text{I}}\text{Au}^{\text{III}}\text{I}_6$ compounds that report 2.644 Å or 2.645 Å for $\text{A} = \text{Rb}, \text{Cs}$ respectively, Figure 122.⁵⁵

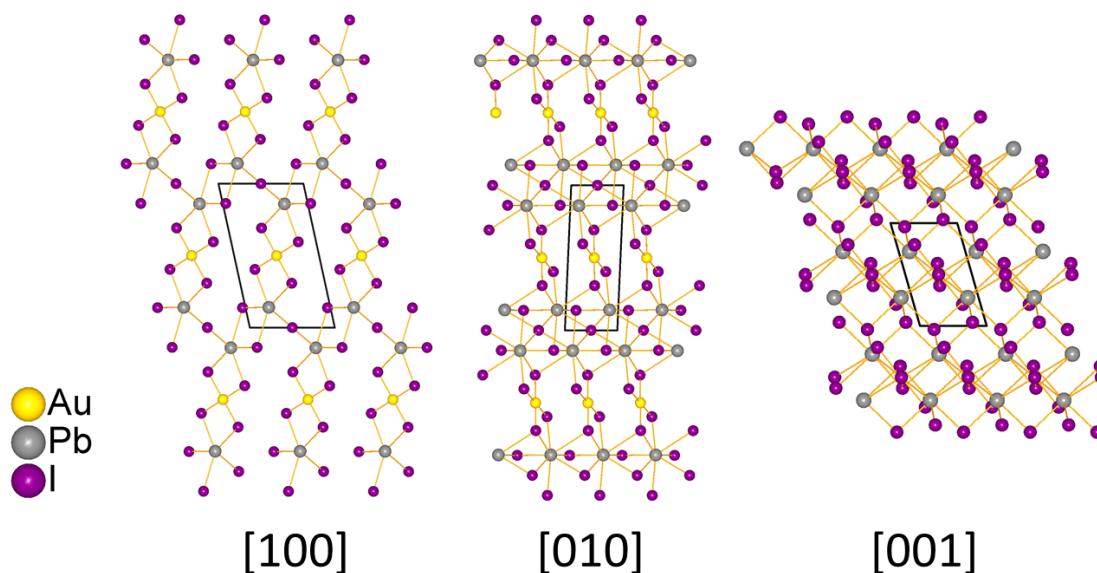


Figure 121. Stick and ball model of the structure of AuPb_2I_7 viewed down the three different crystallographic directions. In the view down the $[001]$ direction the Au are totally eclipsed.

The Pb^{2+} atom is eight coordinate, Figure 123a,b, and forms distorted hendecahedra that are face-sharing in the $[001]$ direction and edges at an angle oblique to $[010]$ to other Pb hendecahedrons, Figure 123c. When $[\text{AuI}_4]^-$ and square planar I are considered discrete units, this suggests the $^{1/\infty}[\text{Pb}_2\text{I}_2]^{2+}$ backbone that propagates down $[100]$, Figure 123c. The 8 Pb – I bonds range from 3.1149(10) to 3.8247(12) Å, Figure 121b. Seven of the eight bonds agree with the hendecahedral bonds seen in InPb_2I_5 where they range from 3.123 to 3.573 Å.¹⁶⁷ The final coordination of Pb to I in the hendecahedra extends to 3.8247(12) Å, which is unprecedentedly long and occurs due to the stereo active lone pair that resides on the Pb atom, which pushes the I atom further away from the coordination sphere.

Within the structure, the iodine atoms occupy four sites and exhibit three different coordination environments. First, two iodine atoms act as a both part of the hendecahedral

geometry of Pb and the square planar geometry of Au which can readily be observed in Figure 120. They coordinate in a distorted half trigonal prismatic geometry between two Pb atoms and Au, with the longest 'bond' being 3.8247(12) Å for the distant Pb. The $1/\infty[\text{Pb}_2\text{I}_2]^{2+}$ backbone contains another distorted half trigonal prismatic coordinated iodine between three Pb atoms mimicking the coordination in PbI_2 in the [100] direction, Figure 123c. The final iodine sits in a unique square planar geometry between 4 Pb atoms and links the $1/\infty[\text{Pb}_2\text{I}_2]^{2+}$ backbones together to form the pseudo-layered structure, Figure 120d.

The overarching structure of AuPb_2I_7 does not undergo a phase transition at low temperature with lattice parameters shrinking predictably. However, at 100 K the $[\text{AuI}_4]^-$ unit distorts and Au – I bonds elongate and shorten from 2.6340(11) and 2.6328(10) Å to 2.7986(15) and 2.5464(12) Å respectively. Additional bond shortening in the Pb hendecahedron allows the unit cell to be drawn differently, Figure 124, due to the reduction in the distance between square planar iodide atoms from 12.7657(8) to 12.226(3) Å.

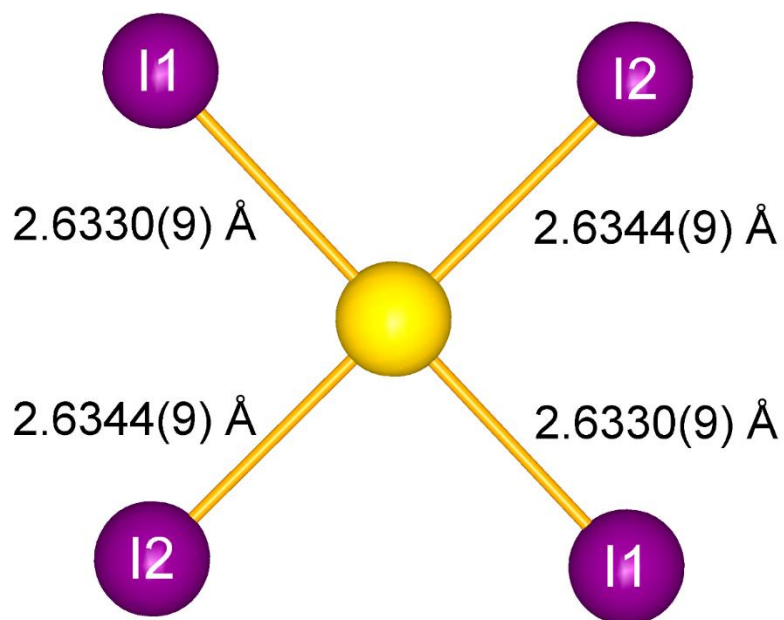


Figure 122. Au³⁺ center in a square planar site of I atoms with bond lengths of 2.6330(9) and 2.6344(9) Å.

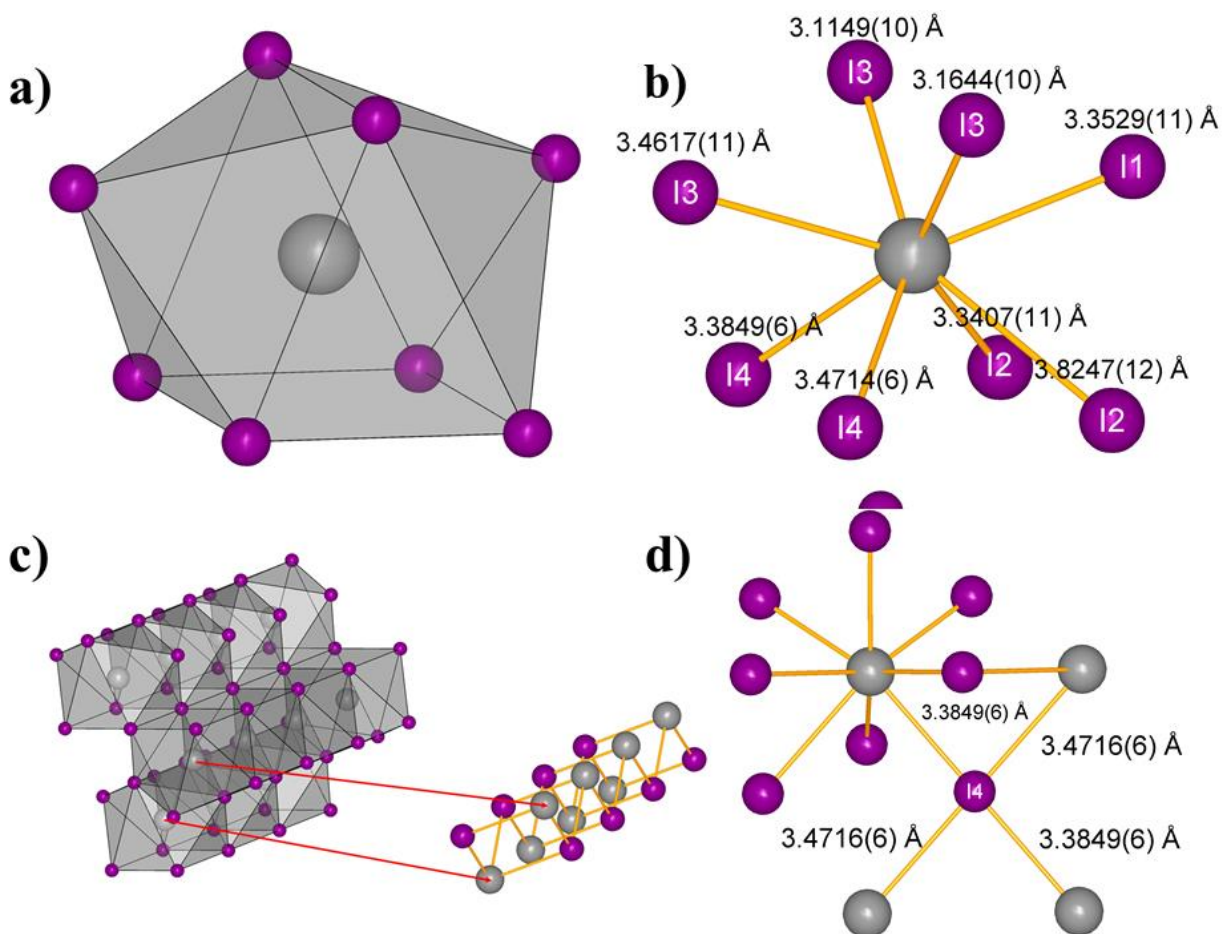


Figure 123. a) The distorted hendecahedron that Pb forms when fully coordinated to neighboring I atoms. b) Atoms labels and bond distances for the Pb hendecahedron in the same relative representation as given in a. c) The greater packing of the Pb polyhedra that extend form the pseudo-layers that are bridged by Au³⁺ with a representation of the $1/\infty[\text{Pb}_2\text{I}_2]^{2+}$ backbone in the same orientation. d) The square planar orientation of I bridging the $1/\infty[\text{Pb}_2\text{I}_2]^{2+}$ units to facilitate coordination down [010].

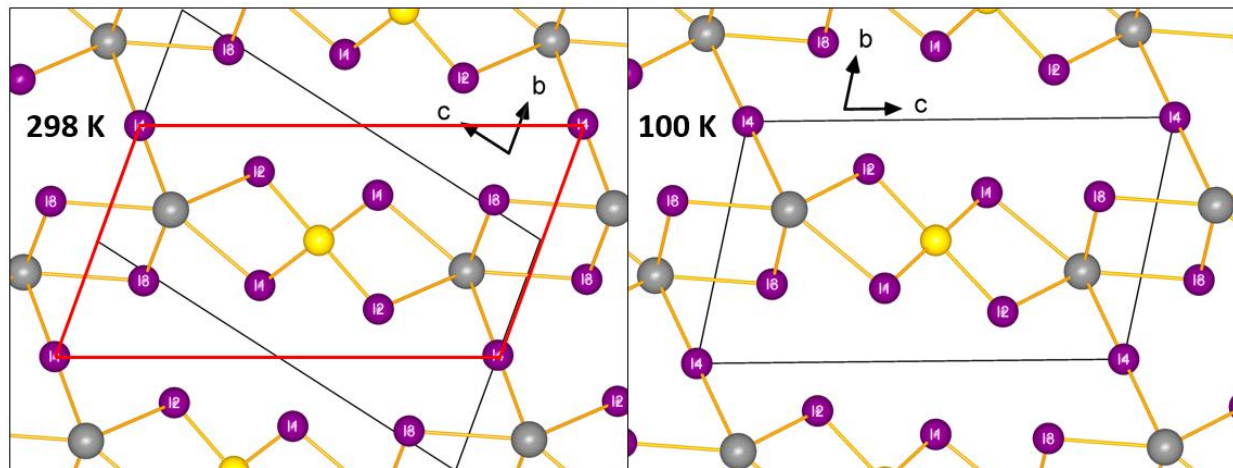


Figure 124. Unit cells of AuPb_2I_7 at 298 K and 100 K with the low temperature cell superimposed in red. Due to the change in Au – I bond lengths at low temperature and the general decrease of Pb – I bond distances the I4 – I4 distance decreases and becomes the c axis of the low temperature unit cell.

5.4.3. Optical Absorption and Electronic Structure

The band gap of black AuPb_2I_7 was determined to be 1.17 eV by UV-vis diffuse reflectance spectroscopy measurements, Figure 125. Here optical absorption is dominated by metal-ligand charge transfer transitions within the $[\text{AuI}_4]^-$ unit, thus acting as strong chromophore. This interpretation is supported by the DFT calculations below.

The calculated electronic band structure and density of states (DOS) for AuPb_2I_7 (Figure 126) indicates a small bandgap (0.35 eV) between valence bands derived primarily from I *p* orbitals and a single conduction band derived primarily from an empty Au *d* orbital, consistent with a square planar crystal field for d^8 Au^{3+} . Relatively weak mixing of the filled Pb *s* states with the iodine orbitals (due to the distorted hendecahedral coordination) leads to rather localized, slightly

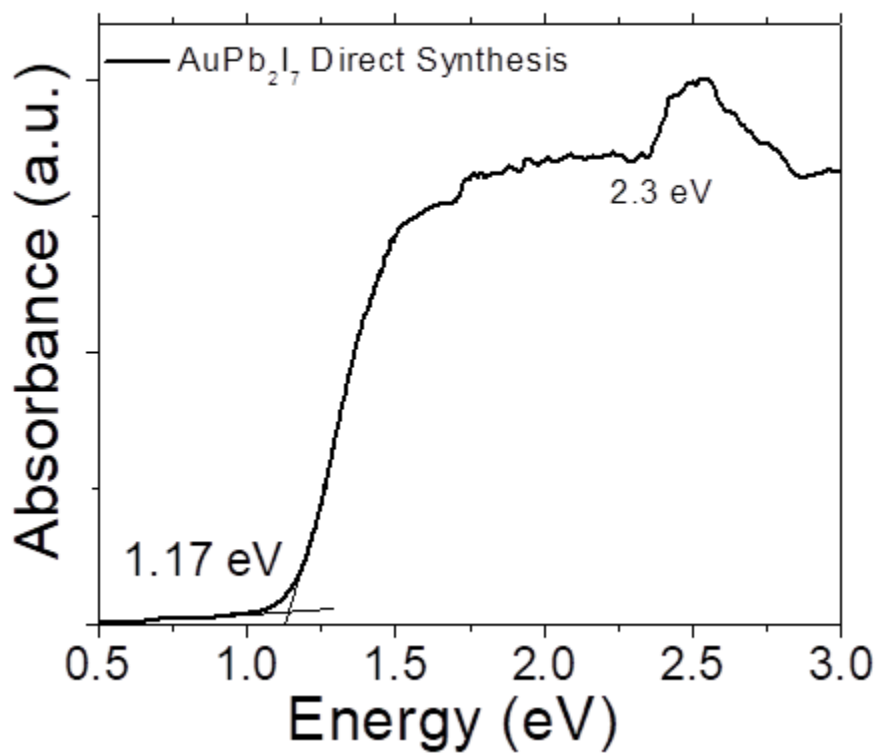


Figure 125. The optical absorbance of a mixture of AuPb₂I₇ with some contaminant PbI₂ that can be observed at 2.3 eV. The band gap for the title compound was determined to be 1.17 eV and a direct function of the [AuI₄]⁻ unit in the structure.

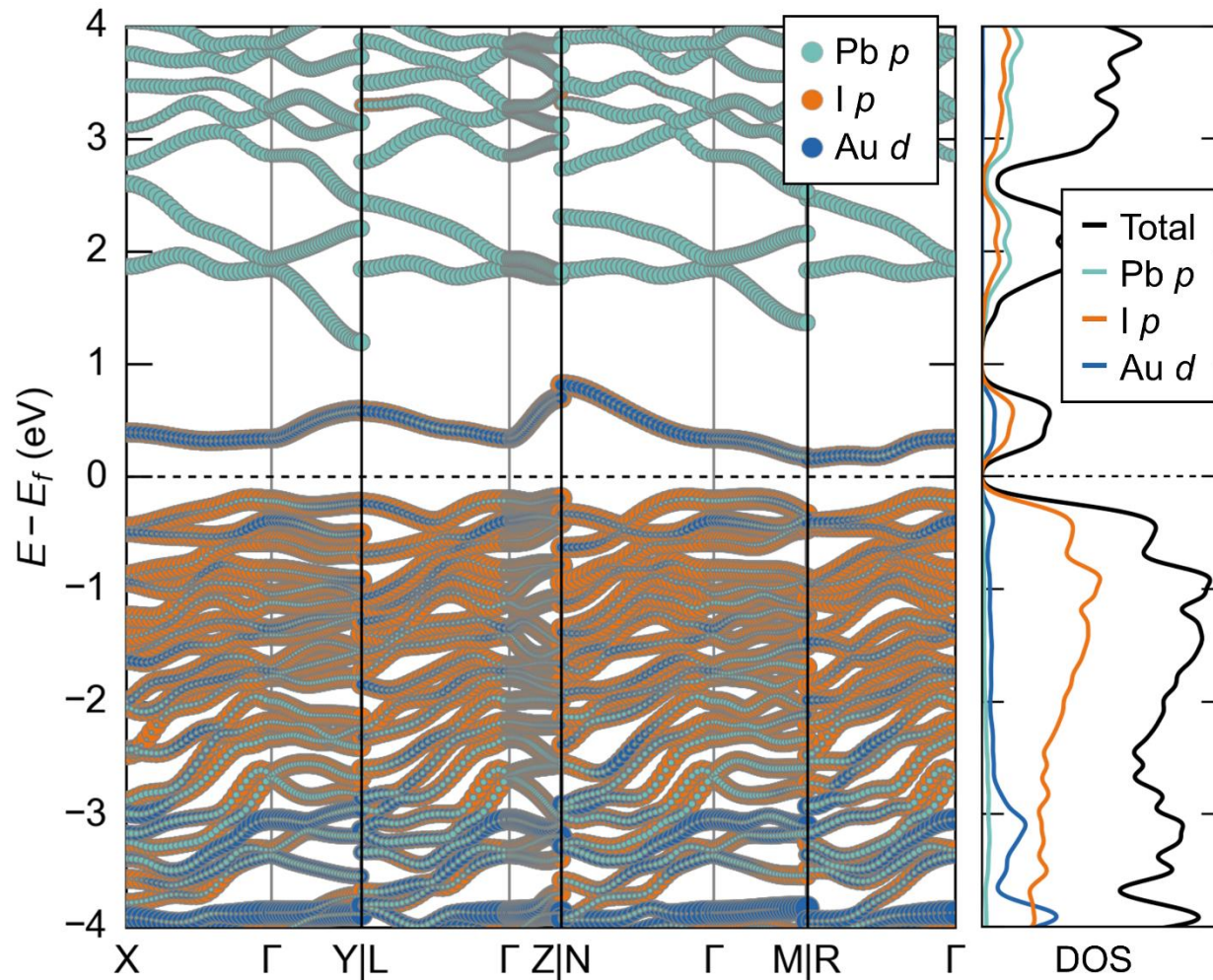


Figure 126. Electronic band structure and density of states (DOS) for AuPb_2I_7 from density functional theory, calculated using the generalized gradient approximation (GGA–PBE, with spin-orbit coupling). Orbital projections indicate the bandgap is dominated by filled $\text{I } p$ states and empty $\text{Au } d$ states (consistent with the square planar environment for Au^{3+}), while the empty $\text{Pb } p$ orbitals lie higher in energy.

bonding Pb *s* states nearly 8 eV below the Fermi level, and weak, slightly antibonding Pb *s* contributions to the valence bands within ~2 eV of the Fermi level. The unoccupied Pb *p* states are substantially higher in energy than the lowest conduction band, and are unlikely to be responsible for optical absorption near the absorption onset. The magnitude of the underestimate of the observed bandgap is typical of calculations employing the generalized gradient approximation. Spin-orbit coupling has a significant impact only on the higher-lying excited states derived from Pb *p* orbitals (Figure 127).

The calculated bandgap is indirect, between the valence band maximum along R– Γ and the conduction band minimum at R. Given the narrow bandwidths, there are multiple local extrema within a few 10s of meV of the band edges, and the details of the electronic structure may change with a more sophisticated treatment of exchange and correlation. The effective masses of holes and electrons along the R– Γ direction are calculated as $1.3m_e$ and $2.3m_e$, respectively. Wavevectors near the band edges correspond to traveling waves at a slightly oblique angle to the pseudo-layers that stack along [010], suggesting the bridging iodine atoms participate in charge transport. Thus, despite the rather heavy carriers, the material is best thought of as 3D in an electronic sense, rather than layered. This is consistent with the absence of obvious excitonic features in the optical absorption, in contrast to layered halides with significant dielectric confinement and correspondingly large exciton binding energies.¹⁶⁸

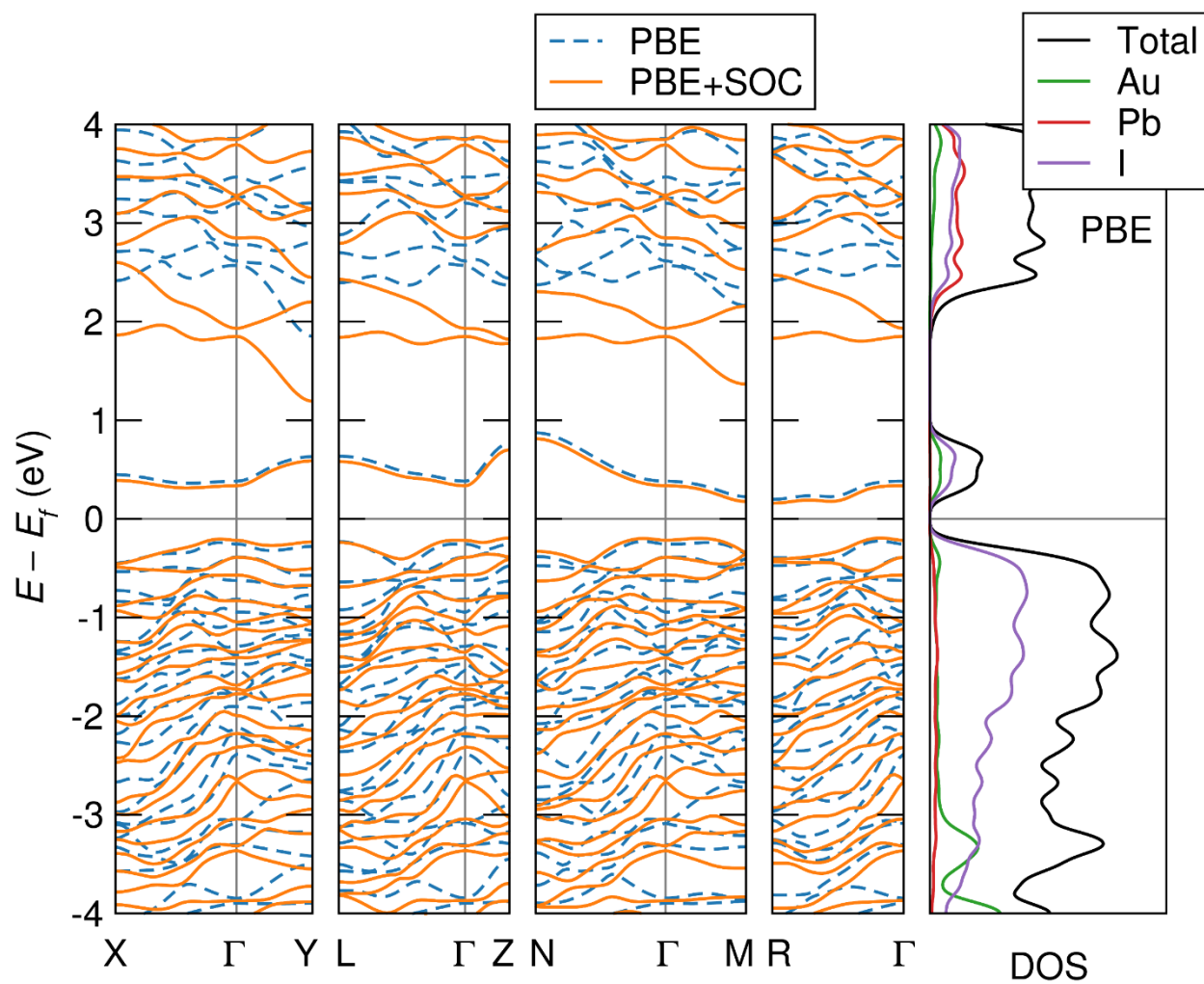


Figure 127. Electronic band structure and density of states (DOS) for AuPb₂I₇ from density functional theory, calculated using the generalized gradient approximation (GGA–PBE). The band structure is shown with and without the inclusion of spin-orbit coupling (SOC), which most strongly affects states with Pb character.

5.5. Conclusion

Here we reported the synthesis and subsequent characterization of the novel Au^{3+} semiconductor AuPb_2I_7 . The structure presents the modification of the PbI_2 sublattice, causing the formation of a three-dimensional anisotropic network of $1/\infty[\text{Pb}_2\text{I}_2]^{2+}$ chains bridged by $[\text{AuI}_4]^-$ and square planar I . The experimental band gap was found to be approximately 1.17 eV. Ab initio calculations indicate the lowest energy excited states derive from the empty d orbital of the square planar $d^8 \text{Au}^{\text{III}}$. AuPb_2I_7 demonstrates the versatility of the PbI_2 lattice to incorporate Au^{3+} and suggests that further investigation of lattice modifications in PbI_2 , as new interesting structures are surely undiscovered.

Concluding Remarks

While the aim of the research in this dissertation was to generate new semiconductor materials for radiation detection, results have not generated any suitable material. However, what has been uncovered is a host of new chemical, structural, electronic, and optical features that were previously unknown. From the development of PbI_2 and BiI_3 mixtures we observe a new conductance switching phenomenon which arises from unprecedented phases separation and integration found by HRTEM. Further, the optical properties of both $(\text{PbI}_2)_{1-x}(\text{BiI}_3)_x$ mixtures were determined to arise from the trapping and clustering of Bi atoms as found by asking “What happens in randomly generated unit cells?” These results directly translate in to explaining the optical properties of the quaternary rudorffite type phases which not only display similar low energy absorption, but the transition from 2D to 3D order from the addition of the small, tetrahedral Cu^+ cation. Further, the attempted A site substitution in APbI_3 compounds with Au^+ gave rise the unpredicted triclinic $\text{Au}^{3+}\text{Pb}_2\text{I}_7$, where the $[\text{AuI}_4]^-$ units act as a chromophore turning the material black. These results show that even acting within the design parameters of heavy metal semiconductors for detection applications new chemistry and new materials are waiting to be found.

References

1. Guarnieri, M., More Light on Information [Historical]. *IEEE Industrial Electronics Magazine* **2015**, 9 (4), 58-61.
2. Owens, A.; Peacock, A., Compound semiconductor radiation detectors. *Nuclear Instruments and Methods in Physics Research Section A: Accelerators, Spectrometers, Detectors and Associated Equipment* **2004**, 531 (1–2), 18-37.
3. Sellin, P. J., Recent advances in compound semiconductor radiation detectors. *Nuclear Instruments and Methods in Physics Research Section A: Accelerators, Spectrometers, Detectors and Associated Equipment* **2003**, 513 (1–2), 332-339.
4. Knoll, G. F., *Radiation detection and measurement*. John Wiley & Sons: 2010.
5. Johns, P. M.; Nino, J. C., Room temperature semiconductor detectors for nuclear security. *J. Appl. Phys.* **2019**, 126 (4), 040902.
6. Milbrath, B. D.; Peurrung, A. J.; Bliss, M.; Weber, W. J., Radiation detector materials: An overview. *J. Mater. Res.* **2008**, 23 (10), 2561-2581.
7. Stoumpos, C. C.; Kanatzidis, M. G., Halide Perovskites: Poor Man's High-Performance Semiconductors. *Adv. Mater.* **2016**, 28 (28), 5778-5793.
8. Mariette, H., In *CdTe and Related Compounds; Physics, Defects, Hetero- and Nano-structures, Crystal Growth, Surfaces and Applications*, Triboulet, R.; Siffert, P., Eds. Elsevier: Amsterdam, 2010; pp 99-132.
9. Terterian, S.; Chu, M.; Ting, D., Distribution of the high resistivity region in CdZnTe and its effects on gamma-ray detector performance. *J. Electron. Mater.* **2004**, 33 (6), 640-644.
10. Szeles, C., Advances in the crystal growth and device fabrication technology of CdZnTe room temperature radiation detectors. *IEEE Trans. Nucl. Sci.* **2004**, 51 (3), 1242-1249.
11. Bolotnikov, A. E.; Babalola, S. O.; Camarda, G. S.; Chen, H.; Awadalla, S.; Cui, Y.; Egarevwe, S. U.; Fochuk, P. M.; Hawrami, R.; Hossain, A.; James, J. R.; Nakonechnyj, I. J.; Mackenzie, J.; Yang, G.; Xu, C.; James, R. B., Extended Defects in CdZnTe Radiation Detectors. *IEEE Trans. Nucl. Sci.* **2009**, 56 (4), 1775-1783.x

12. Candelise, C.; Winkler, M.; Gross, R., Implications for CdTe and CIGS technologies production costs of indium and tellurium scarcity. *Progress in Photovoltaics: Research and Applications* **2012**, *20* (6), 816-831.
13. Ugucioni, J. C.; Ferreira, M.; Fajardo, F.; Mulato, M., Growth of Mercuric Iodide Crystals. *Braz. Jour. Phys.* **2006**, *36*, 274-277.
14. Hermon, H.; Schieber, M.; Roth, M., Study of trapping levels in doped HgI₂ radiation detectors. *Nuclear Instruments and Methods in Physics Research Section A: Accelerators, Spectrometers, Detectors and Associated Equipment* **1996**, *380* (1-2), 10-13.
15. Zhang, Z.; Zheng, W.; Chen, A.; Ding, K.; Huang, F., Crystal Growth of α -HgI₂ by the Temperature Difference Method for High Sensitivity X-ray Detection. *Cryst. Growth Des.* **2015**, *15* (7), 3383-3387.
16. Shah, K. S.; Bennett, P.; Klugerman, M.; Moy, L.; Cirignano, L.; Dmitriyev, Y.; Squillante, M. R.; Olschner, F.; Moses, W. W., Lead iodide optical detectors for gamma ray spectroscopy. *IEEE Trans. Nucl. Sci.* **1997**, *44* (3), 448-450.
17. Deich, V.; Roth, M., Improved performance lead iodide nuclear radiation detectors. *Nuclear Instruments and Methods in Physics Research Section A: Accelerators, Spectrometers, Detectors and Associated Equipment* **1996**, *380* (1-2), 169-172.
18. Lintereur, A. T.; Qiu, W.; Nino, J. C.; Baciak, J., Characterization of bismuth tri-iodide single crystals for wide band-gap semiconductor radiation detectors. *Nuclear Instruments and Methods in Physics Research Section A: Accelerators, Spectrometers, Detectors and Associated Equipment* **2011**, *652* (1), 166-169.
19. Han, H.; Hong, M.; Gokhale, S. S.; Sinnott, S. B.; Jordan, K.; Baciak, J. E.; Nino, J. C., Defect Engineering of BiI₃ Single Crystals: Enhanced Electrical and Radiation Performance for Room Temperature Gamma-Ray Detection. *J. of Phys. Chem. C* **2014**, *118* (6), 3244-3250.
20. Matsumoto, M.; Hitomi, K.; Shoji, T.; Hiratate, Y., Bismuth tri-iodide crystal for nuclear radiation detectors. *IEEE Trans. Nucl. Sci.* **2002**, *49* (5), 2517-2520.
21. Onodera, T.; Hitomi, K.; Shoji, T., Fabrication of Indium Iodide X- and Gamma-Ray Detectors. *IEEE Trans. Nucl. Sci.* **2006**, *53* (5), 3055-3059.
22. Squillante, M. R.; Zhou, C.; Zhang, J.; Moy, L. P.; Shah, K. S., InI nuclear radiation detectors. *IEEE Trans. on Nucl. Sci.* **1993**, *40* (4), 364-366.

23. Owens, A.; Bavdaz, M.; Lisjutin, I.; Peacock, A.; Sipila, H.; Zatoloka, S., On the development of compound semiconductor thallium bromide detectors for astrophysics. *Nuclear Instruments and Methods in Physics Research Section A: Accelerators, Spectrometers, Detectors and Associated Equipment* **2001**, 458 (1–2), 413-417.
24. Hitomi, K.; Tada, T.; Kim, S. Y.; Wu, Y.; Tanaka, T.; Shoji, T.; Yamazaki, H.; Ishii, K., Recent Development of TlBr Gamma-Ray Detectors. *IEEE Trans. Nucl. Sci.* **2011**, 58 (4), 1987-1991.
25. Jeffrey, G. A.; Vlasse, M., Crystal structures of the red, yellow, and orange forms of mercuric iodide. *Inorg. Chem.* **1967**, 6 (2), 396-399.
26. Hermon, H.; Roth, M.; Schieber, M., Improved technique for HgI₂ crystal growth. *Nuclear Instruments and Methods in Physics Research Section A: Accelerators, Spectrometers, Detectors and Associated Equipment* **1992**, 322 (3), 432-434.
27. Piechotka, M., Mechanism of vapour growth and defect formation in large mercuric iodide crystals. *J. Cryst. Growth* **1995**, 146 (1-4), 1-8.
28. McGregor, D. S.; Ariesanti, E., Platelet growth of mercuric iodide. *J. Cryst. Growth* **2013**, 379, 7-15.
29. Ugucioni, J.; Netto, T. G.; Mulato, M., Mercuric iodide crystals obtained by solvent evaporation using ethanol. *Nuclear Instruments and Methods in Physics Research Section A: Accelerators, Spectrometers, Detectors and Associated Equipment* **2010**, 615 (3), 259-266.
30. Rao, M. R.; Verma, J.; Patro, A., Solution grown mercuric iodide crystals as low-energy gamma-ray conduction type detectors. *J. Phys. D: Appl. Phys.* **1980**, 13 (8), 1545.
31. Alexander, W. B.; Sandoval, J.; van den Berg, L. In *Characterization of strain and crystallographic defects in HgI₂ single crystals*, Hard X-Ray and Gamma-Ray Detector Physics VI, International Society for Optics and Photonics: 2004; pp 106-115.
32. Owens, A., *Compound semiconductor radiation detectors*. CRC Press: 2016.
33. Martins, J. F. T.; Santos, R. A. d.; Ferraz, C. d. M.; Oliveira, R. R.; Fiederle, M.; Amadeu, R. d. A.; Santos, R. S. d.; Silva, T. L. B. d.; Hamada, M. M., Optimization of the HgI₂ Crystal Preparation for Application as a Radiation Semiconductor Detector. *Studies in Engineering and Technology; Vol 5, No 1 (2018)DO - 10.11114/set.v5i1.3149* **2018**.

34. Palosz, B., The structure of PbI_2 polytypes 2H and 4H: a study of the 2H-4H transition. *J. Phys. Condens. Matter* **1990**, 2 (24), 5285.
35. Wei, Q.; Shen, B.; Chen, Y.; Xu, B.; Xia, Y.; Yin, J.; Liu, Z., Large-sized PbI_2 single crystal grown by co-solvent method for visible-light photo-detector application. *Mater. Lett.* **2017**, 193, 101-104.
36. Hui, S.; Xinghua, Z.; Dingyu, Y.; Zhiyu, H.; Shifu, Z.; Beijun, Z., Electrical and γ -ray energy spectrum response properties of PbI_2 crystal grown by physical vapor transport. *J. Semicon.* **2012**, 33 (5), 053002.
37. Zhu, X.; Wei, Z.; Jin, Y.; Xiang, A., Growth and characterization of a PbI_2 single crystal used for gamma ray detectors. *Crystal Research and Technology: Journal of Experimental and Industrial Crystallography* **2007**, 42 (5), 456-459.
38. He, Y.; Zhu, S.; Zhao, B.; Jin, Y.; He, Z.; Chen, B., Improved growth of PbI_2 single crystals. *J. Cryst. Growth* **2007**, 300 (2), 448-451.
39. Shah, K.; Bennett, P.; Klugerman, M.; Moy, L.; Cirignano, L.; Dmitriyev, Y.; Squillante, M.; Olschner, F.; Moses, W., Lead iodide optical detectors for gamma ray spectroscopy. *IEEE Trans. on Nucl. Sci.* **1997**, 44 (3), 448-450.
40. Shah, K.; Olschner, F.; Moy, L.; Bennett, P.; Misra, M.; Zhang, J.; Squillante, M.; Lund, J., Lead iodide X-ray detection systems. *Nuclear Instruments and Methods in Physics Research Section A: Accelerators, Spectrometers, Detectors and Associated Equipment* **1996**, 380 (1-2), 266-270.
41. Podraza, N. J.; Qiu, W.; Hinojosa, B. B.; Xu, H.; Motyka, M. A.; Phillipot, S. R.; Baciak, J. E.; Trolier-McKinstry, S.; Nino, J. C., Band gap and structure of single crystal BiI_3 : Resolving discrepancies in literature. *J. Appl. Phys.* **2013**, 114 (3), 033110.
42. Trotter, J.; Zobel, T., The crystal structure of SbI_3 and BiI_3 . In *Zeitschrift für Kristallographie - Crystalline Materials*, 1966; Vol. 123, p 67.
43. Nason, D.; Keller, L., The growth and crystallography of bismuth tri-iodide crystals grown by vapor transport. *J. Cryst. Growth* **1995**, 156 (3), 221-226.
44. Johns, P. M.; Baciak, J. E.; Nino, J. C., Enhanced gamma ray sensitivity in bismuth triiodide sensors through volumetric defect control. *Appl. Phys. Lett.* **2016**, 109 (9), 092105.

45. Johns, P. M.; Sulekar, S.; Yeo, S.; Baciak, J. E.; Bliss, M.; Nino, J. C., Superheating suppresses structural disorder in layered BiI₃ semiconductors grown by the Bridgman method. *J. Cryst. Growth* **2016**, *433*, 153-159.
46. Bhattacharya, P.; Groza, M.; Cui, Y.; Caudel, D.; Wrenn, T.; Nwankwo, A.; Burger, A.; Slack, G.; Ostrogorsky, A., Growth of InI single crystals for nuclear detection applications. *J. Cryst. Growth* **2010**, *312* (8), 1228-1232.
47. Jones, R. E.; Templeton, D. H., The crystal structure of indium (I) iodide. *Acta Crystallogr.* **1955**, *8* (12), 847-847.
48. Smakula, A.; Kalnajs, J., Precision determination of lattice constants with a Geiger-counter x-ray diffractometer. *Phys. Rev.* **1955**, *99* (6), 1737.
49. Kim, H.; Cirignano, L.; Churilov, A.; Ciampi, G.; Higgins, W.; Olschner, F.; Shah, K., Developing Larger TlBr Detectors—Detector Performance. *IEEE Trans. Nucl. Sci.* **2009**, *56* (3), 819-823.
50. Hitomi, K.; Tada, T.; Kim, S.; Wu, Y.; Tanaka, T.; Shoji, T.; Yamazaki, H.; Ishii, K., Recent Development of TlBr Gamma-Ray Detectors. *IEEE Trans. Nucl. Sci.* **2011**, *58* (4), 1987-1991.
51. Wang, S.; Liu, Z.; Peters, J. A.; Sebastian, M.; Nguyen, S. L.; Malliakas, C. D.; Stoumpos, C. C.; Im, J.; Freeman, A. J.; Wessels, B. W., Crystal growth of Tl₄CdI₆: a wide band gap semiconductor for hard radiation detection. *Cryst. Growth Des.* **2014**, *14* (5), 2401-2410.
52. Franiv, A.; Kushnir, O.; Girnyk, I.; Franiv, V.; Kityk, I.; Piasecki, M.; Plucinski, K., Growth, crystal structure, thermal properties, optical anisotropy of Tl₄CdI₆ single crystals. *Ukr. J. Phys. Opt.* **2013**, (14, № 1), 6-14.
53. Kahler, D.; Singh, N.; Knuteson, D.; Wagner, B.; Berghmans, A.; McLaughlin, S.; King, M.; Schwartz, K.; Suhre, D.; Gotlieb, M., Performance of novel materials for radiation detection: Tl₃AsSe₃, TlGaSe₂, and Tl₄HgI₆. *Nuclear Instruments and Methods in Physics Research Section A: Accelerators, Spectrometers, Detectors and Associated Equipment* **2011**, *652* (1), 183-185.
54. Parasyuk, O.; Khyzhun, O.; Piasecki, M.; Kityk, I.; Lakshminarayana, G.; Luzhnyi, I.; Fochuk, P.; Fedorchuk, A.; Levkovets, S.; Yurchenko, O., Synthesis, structural, X-ray

photoelectron spectroscopy (XPS) studies and IR induced anisotropy of Tl_4HgI_6 single crystals. *Mater. Chem. Phys.* **2017**, *187*, 156-163.

55. Lin, W.; Stoumpos, C. C.; Liu, Z.; Das, S.; Kontsevoi, O. Y.; He, Y.; Malliakas, C. D.; Chen, H.; Wessels, B. W.; Kanatzidis, M. G., TlSn_2I_5 , a Robust Halide Antiperovskite Semiconductor for γ -Ray Detection at Room Temperature. *ACS Photonics* **2017**, *4* (7), 1805-1813.

56. Wibowo, A. C.; Malliakas, C. D.; Li, H.; Stoumpos, C. C.; Chung, D. Y.; Wessels, B. W.; Freeman, A. J.; Kanatzidis, M. G., An Unusual Crystal Growth Method of the Chalcohalide Semiconductor, $\beta\text{-Hg}_3\text{S}_2\text{Cl}_2$: A New Candidate for Hard Radiation Detection. *Cryst. Growth Des.* **2016**, *16* (5), 2678-2684.

57. Li, H.; Meng, F.; Malliakas, C. D.; Liu, Z.; Chung, D. Y.; Wessels, B.; Kanatzidis, M. G., Mercury Chalcohalide Semiconductor $\text{Hg}_3\text{Se}_2\text{Br}_2$ for Hard Radiation Detection. *Cryst. Growth Des.* **2016**, *16* (11), 6446-6453.

58. He, Y.; Kontsevoi, O. Y.; Stoumpos, C. C.; Trimarchi, G. G.; Islam, S. M.; Liu, Z.; Kostina, S. S.; Das, S.; Kim, J.-I.; Lin, W.; Wessels, B. W.; Kanatzidis, M. G., Defect Antiperovskite Compounds $\text{Hg}_3\text{Q}_2\text{I}_2$ (Q = S, Se, and Te) for Room-Temperature Hard Radiation Detection. *J. Am. Chem. Soc.* **2017**, *139* (23), 7939-7951.

59. Johnsen, S.; Liu, Z.; Peters, J. A.; Song, J.-H.; Nguyen, S.; Malliakas, C. D.; Jin, H.; Freeman, A. J.; Wessels, B. W.; Kanatzidis, M. G., Thallium Chalcohalides for X-ray and γ -ray Detection. *J. Am. Chem. Soc.* **2011**, *133* (26), 10030-10033.

60. Nguyen, S. L.; Malliakas, C. D.; Peters, J. A.; Liu, Z.; Im, J.; Zhao, L.-D.; Sebastian, M.; Jin, H.; Li, H.; Johnsen, S.; Wessels, B. W.; Freeman, A. J.; Kanatzidis, M. G., Photoconductivity in Tl_6SI_4 : A Novel Semiconductor for Hard Radiation Detection. *Chem. Mater.* **2013**, *25* (14), 2868-2877.

61. Wibowo, A. C.; Malliakas, C. D.; Liu, Z.; Peters, J. A.; Sebastian, M.; Chung, D. Y.; Wessels, B. W.; Kanatzidis, M. G., Photoconductivity in the Chalcohalide Semiconductor, SbSeI : a New Candidate for Hard Radiation Detection. *Inorg. Chem.* **2013**, *52* (12), 7045-7050.

62. Lin, W.; Stoumpos, C. C.; Kontsevoi, O. Y.; Liu, Z.; He, Y.; Das, S.; Xu, Y.; McCall, K. M.; Wessels, B. W.; Kanatzidis, M. G., $\text{Cu}_2\text{I}_2\text{Se}_6$: A Metal-Inorganic Framework Wide-Bandgap Semiconductor for Photon Detection at Room Temperature. *J. Am. Chem. Soc.* **2018**, *140* (5), 1894-1899.

63. Stoumpos, C. C.; Kanatzidis, M. G., The Renaissance of Halide Perovskites and Their Evolution as Emerging Semiconductors. *Acc. Chem. Res.* **2015**, *48* (10), 2791-2802.
64. Xiang, W.; Tress, W., Review on Recent Progress of All-Inorganic Metal Halide Perovskites and Solar Cells. *Adv. Mater.* **2019**, *31* (44), 1902851.
65. Wei, H.; Fang, Y.; Mulligan, P.; Chuirazzi, W.; Fang, H.-H.; Wang, C.; Ecker, B. R.; Gao, Y.; Loi, M. A.; Cao, L.; Huang, J., Sensitive X-ray detectors made of methylammonium lead tribromide perovskite single crystals. *Nature Photonics* **2016**, *10* (5), 333-339.
66. He, Y.; Ke, W.; Alexander, G. C. B.; McCall, K. M.; Chica, D. G.; Liu, Z.; Hadar, I.; Stoumpos, C. C.; Wessels, B. W.; Kanatzidis, M. G., Resolving the Energy of γ -Ray Photons with MAPbI₃ Single Crystals. *ACS Photonics* **2018**, *5* (10), 4132-4138.
67. Yakunin, S.; Dirin, D. N.; Shynkarenko, Y.; Morad, V.; Cherniukh, I.; Nazarenko, O.; Kreil, D.; Nauser, T.; Kovalenko, M. V., Detection of gamma photons using solution-grown single crystals of hybrid lead halide perovskites. *Nat. Photonics* **2016**, *10* (9), 585-589.
68. Wei, H.; Huang, J., Halide lead perovskites for ionizing radiation detection. *Nat. Commun.* **2019**, *10* (1), 1066.
69. Goldschmidt, V. M., Die gesetze der krystallochemie. *Naturwissenschaften* **1926**, *14* (21), 477-485.
70. Sani, F.; Shafie, S.; Lim, H. N.; Musa, A. O., Advancement on Lead-Free Organic-Inorganic Halide Perovskite Solar Cells: A Review. *Materials* **2018**, *11* (6), 1008.
71. Li, C.; Lu, X.; Ding, W.; Feng, L.; Gao, Y.; Guo, Z., Formability of ABX₃ (X= F, Cl, Br, I) Halide Perovskites. *Acta Crystallogr. Sect. B: Struct. Sci.* **2008**, *64* (6), 702-707.
72. Travis, W.; Glover, E.; Bronstein, H.; Scanlon, D.; Palgrave, R., On the application of the tolerance factor to inorganic and hybrid halide perovskites: a revised system. *Chem. Sci.* **2016**, *7* (7), 4548-4556.
73. Stoumpos, C. C.; Malliakas, C. D.; Kanatzidis, M. G., Semiconducting Tin and Lead Iodide Perovskites with Organic Cations: Phase Transitions, High Mobilities, and Near-Infrared Photoluminescent Properties. *Inorg. Chem.* **2013**, *52* (15), 9019-9038.
74. Wang, L.; Yuan, G.; Duan, R.; Huang, F.; Wei, T.; Liu, Z.; Wang, J.; Li, J., Tunable bandgap in hybrid perovskite CH₃NH₃Pb(Br_{3-y}X_y) single crystals and photodetector applications. *AIP Adv.* **2016**, *6* (4), 045115.

75. Adjokatse, S.; Fang, H.-H.; Loi, M. A., Broadly tunable metal halide perovskites for solid-state light-emission applications. *Mater. Today* **2017**, *20* (8), 413-424.
76. Shi, D.; Adinolfi, V.; Comin, R.; Yuan, M.; Alarousu, E.; Buin, A.; Chen, Y.; Hoogland, S.; Rothenberger, A.; Katsiev, K.; Losovyj, Y.; Zhang, X.; Dowben, P. A.; Mohammed, O. F.; Sargent, E. H.; Bakr, O. M., Low trap-state density and long carrier diffusion in organolead trihalide perovskite single crystals. *Science* **2015**, *347* (6221), 519-522.
77. Zhumekenov, A. A.; Saidaminov, M. I.; Haque, M. A.; Alarousu, E.; Sarmah, S. P.; Murali, B.; Dursun, I.; Miao, X.-H.; Abdelhady, A. L.; Wu, T.; Mohammed, O. F.; Bakr, O. M., Formamidinium Lead Halide Perovskite Crystals with Unprecedented Long Carrier Dynamics and Diffusion Length. *ACS Energy Lett.* **2016**, *1* (1), 32-37.
78. Steirer, K. X.; Schulz, P.; Teeter, G.; Stevanovic, V.; Yang, M.; Zhu, K.; Berry, J. J., Defect Tolerance in Methylammonium Lead Triiodide Perovskite. *ACS Energy Lett.* **2016**, *1* (2), 360-366.
79. He, Y.; Matei, L.; Jung, H. J.; McCall, K. M.; Chen, M.; Stoumpos, C. C.; Liu, Z.; Peters, J. A.; Chung, D. Y.; Wessels, B. W.; Wasielewski, M. R.; Dravid, V. P.; Burger, A.; Kanatzidis, M. G., High spectral resolution of gamma-rays at room temperature by perovskite CsPbBr₃ single crystals. *Nat. Commun.* **2018**, *9* (1), 1609.
80. Nazarenko, O.; Yakunin, S.; Morad, V.; Cherniukh, I.; Kovalenko, M. V., Single crystals of caesium formamidinium lead halide perovskites: solution growth and gamma dosimetry. *NPG Asia Mater.* **2017**, *9* (4), e373-e373.
81. Han, Q.; Bae, S.-H.; Sun, P.; Hsieh, Y.-T.; Yang, Y.; Rim, Y. S.; Zhao, H.; Chen, Q.; Shi, W.; Li, G.; Yang, Y., Single Crystal Formamidinium Lead Iodide (FAPbI₃): Insight into the Structural, Optical, and Electrical Properties. *Adv. Mater.* **2016**, *28* (11), 2253-2258.
82. Dang, Y.; Liu, Y.; Sun, Y.; Yuan, D.; Liu, X.; Lu, W.; Liu, G.; Xia, H.; Tao, X., Bulk crystal growth of hybrid perovskite material CH₃NH₃PbI₃. *CrystEngComm* **2015**, *17* (3), 665-670.
83. Niu, G.; Guo, X.; Wang, L., Review of recent progress in chemical stability of perovskite solar cells. *J. Mater. Chem. A* **2015**, *3* (17), 8970-8980.
84. Fabini, D., Quantifying the potential for lead pollution from halide perovskite photovoltaics. *J. Phys. Chem. Lett.* **2015**, *6* (18), 3546-3548.

85. Stoumpos, C. C.; Malliakas, C. D.; Peters, J. A.; Liu, Z.; Sebastian, M.; Im, J.; Chasapis, T. C.; Wibowo, A. C.; Chung, D. Y.; Freeman, A. J.; Wessels, B. W.; Kanatzidis, M. G., Crystal Growth of the Perovskite Semiconductor CsPbBr₃: A New Material for High-Energy Radiation Detection. *Cryst. Growth Des.* **2013**, *13* (7), 2722-2727.
86. Sutton, R. J.; Eperon, G. E.; Miranda, L.; Parrott, E. S.; Kamino, B. A.; Patel, J. B.; Hörantner, M. T.; Johnston, M. B.; Haghighirad, A. A.; Moore, D. T.; Snaith, H. J., Bandgap-Tunable Cesium Lead Halide Perovskites with High Thermal Stability for Efficient Solar Cells. *Adv. Energy Mater.* **2016**, *6* (8), 1502458.
87. Kang, J.; Wang, L.-W., High defect tolerance in lead halide perovskite CsPbBr₃. *J. Phys. Chem. Lett.* **2017**, *8* (2), 489-493.
88. Yuan, Y.; Huang, J., Ion migration in organometal trihalide perovskite and its impact on photovoltaic efficiency and stability. *Acc. Chem. Res.* **2016**, *49* (2), 286-293.
89. Dirin, D. N.; Cherniukh, I.; Yakunin, S.; Shynkarenko, Y.; Kovalenko, M. V., Solution-grown CsPbBr₃ perovskite single crystals for photon detection. *Chem. Mater.* **2016**, *28* (23), 8470-8474.
90. Ding, J.; Du, S.; Zuo, Z.; Zhao, Y.; Cui, H.; Zhan, X., High detectivity and rapid response in perovskite CsPbBr₃ single-crystal photodetector. *J. of Phys. Chem. C* **2017**, *121* (9), 4917-4923.
91. Volonakis, G.; Filip, M. R.; Haghighirad, A. A.; Sakai, N.; Wenger, B.; Snaith, H. J.; Giustino, F., Lead-Free Halide Double Perovskites via Heterovalent Substitution of Noble Metals. *J. Phys. Chem. Lett.* **2016**, *7* (7), 1254-1259.
92. Theofylaktos, L.; Kosmatos, O.-K.; Giannakaki, E.; Kourti, E.; Deligiannis, D.; Konstantakou, M.; Stergiopoulos, T., Perovskites with d-block metals for solar energy applications. *Dalton Trans.* **2019**.
93. Schade, L.; Wright, A. D.; Johnson, R. D.; Dollmann, M.; Wenger, B.; Nayak, P. K.; Prabhakaran, D.; Herz, L. M.; Nicholas, R.; Snaith, H. J.; Radaelli, P. G., Structural and Optical Properties of Cs₂AgBiBr₆ Double Perovskite. *ACS Energy Lett.* **2019**, *4* (1), 299-305.
94. Yuan, W.; Niu, G.; Xian, Y.; Wu, H.; Wang, H.; Yin, H.; Liu, P.; Li, W.; Fan, J., In Situ Regulating the Order–Disorder Phase Transition in Cs₂AgBiBr₆ Single Crystal toward the Application in an X-Ray Detector. *Adv. Funct. Mater.* **2019**, *29* (20), 1900234.

95. Yin, L.; Wu, H.; Pan, W.; Yang, B.; Li, P.; Luo, J.; Niu, G.; Tang, J., Controlled Cooling for Synthesis of Cs₂AgBiBr₆ Single Crystals and Its Application for X-Ray Detection. *Adv. Opt. Mater.* **2019**, 1900491.
96. Chang, J.-H.; Doert, T.; Ruck, M., Structural Variety of Defect Perovskite Variants M₃E₂X₉ (M = Rb, Tl, E = Bi, Sb, X = Br, I). *Z. Anorg. Allg. Chem.* **2016**, 642 (13), 736-748.
97. Saparov, B.; Hong, F.; Sun, J.-P.; Duan, H.-S.; Meng, W.; Cameron, S.; Hill, I. G.; Yan, Y.; Mitzi, D. B., Thin-Film Preparation and Characterization of Cs₃Sb₂I₉: A Lead-Free Layered Perovskite Semiconductor. *Chem. Mater.* **2015**, 27 (16), 5622-5632.
98. Lehner, A. J.; Fabini, D. H.; Evans, H. A.; Hébert, C.-A.; Smock, S. R.; Hu, J.; Wang, H.; Zwanziger, J. W.; Chabynyc, M. L.; Seshadri, R., Crystal and Electronic Structures of Complex Bismuth Iodides A₃Bi₂I₉ (A= K, Rb, Cs) Related to Perovskite: Aiding the Rational Design of Photovoltaics. *Chem. Mater.* **2015**, 27 (20), 7137-7148.
99. Hoye, R. L.; Brandt, R. E.; Osherov, A.; Stevanović, V.; Stranks, S. D.; Wilson, M. W.; Kim, H.; Akey, A. J.; Perkins, J. D.; Kurchin, R. C., Methylammonium bismuth iodide as a lead-free, stable hybrid organic–inorganic solar absorber. *Chem. - Eur. J.* **2016**, 22 (8), 2605-2610.
100. Hebig, J.-C.; Kühn, I.; Flohre, J.; Kirchartz, T., Optoelectronic properties of (CH₃NH₃)₃Sb₂I₉ thin films for photovoltaic applications. *ACS Energy Lett.* **2016**, 1 (1), 309-314.
101. McCall, K. M.; Stoumpos, C. C.; Kostina, S. S.; Kanatzidis, M. G.; Wessels, B. W., Strong Electron–Phonon Coupling and Self-Trapped Excitons in the Defect Halide Perovskites A₃M₂I₉ (A = Cs, Rb; M = Bi, Sb). *Chem. Mater.* **2017**, 29 (9), 4129-4145.
102. Hu, Y.; Zhang, S.; Miao, X.; Su, L.; Bai, F.; Qiu, T.; Liu, J.; Yuan, G., Ultrathin Cs₃Bi₂I₉ Nanosheets as an Electronic Memory Material for Flexible Memristors. *Adv. Mater. Interfaces* **2017**, 4 (14), 1700131.
103. Yang, T.-Y.; Gregori, G.; Pellet, N.; Grätzel, M.; Maier, J., The Significance of Ion Conduction in a Hybrid Organic–Inorganic Lead-Iodide-Based Perovskite Photosensitizer. *Angew. Chem. Int. Ed.* **2015**, 54 (27), 7905-7910.
104. Mizusaki, J.; Arai, K.; Fueki, K., Ionic conduction of the perovskite-type halides. *Solid State Ionics* **1983**, 11 (3), 203-211.
105. Eames, C.; Frost, J. M.; Barnes, P. R. F.; O'Regan, B. C.; Walsh, A.; Islam, M. S., Ionic transport in hybrid lead iodide perovskite solar cells. *Nat. Commun.* **2015**, 6, 7497.

106. Yu, H.; Lu, H.; Xie, F.; Zhou, S.; Zhao, N., Native Defect-Induced Hysteresis Behavior in Organolead Iodide Perovskite Solar Cells. *Adv. Funct. Mater.* **2016**, *26* (9), 1411-1419.
107. Game, O. S.; Buchsbaum, G. J.; Zhou, Y.; Padture, N. P.; Kington, A. I., Ions Matter: Description of the Anomalous Electronic Behavior in Methylammonium Lead Halide Perovskite Devices. *Adv. Funct. Mater.* **2017**, *27* (16), 1606584.
108. Tsai, H.; Asadpour, R.; Blancon, J.-C.; Stoumpos, C. C.; Durand, O.; Strzalka, J. W.; Chen, B.; Verduzco, R.; Ajayan, P. M.; Tretiak, S.; Even, J.; Alam, M. A.; Kanatzidis, M. G.; Nie, W.; Mohite, A. D., Light-induced lattice expansion leads to high-efficiency perovskite solar cells. *Science* **2018**, *360* (6384), 67-70.
109. Kim, G. Y.; Senocrate, A.; Yang, T.-Y.; Gregori, G.; Grätzel, M.; Maier, J., Large tunable photoeffect on ion conduction in halide perovskites and implications for photodecomposition. *Nat. Mater.* **2018**, *17* (5), 445-449.
110. Bag, M.; Renna, L. A.; Adhikari, R. Y.; Karak, S.; Liu, F.; Lahti, P. M.; Russell, T. P.; Tuominen, M. T.; Venkataraman, D., Kinetics of Ion Transport in Perovskite Active Layers and Its Implications for Active Layer Stability. *J. Am. Chem. Soc.* **2015**, *137* (40), 13130-13137.
111. Leijtens, T.; Eperon, G. E.; Noel, N. K.; Habisreutinger, S. N.; Petrozza, A.; Snaith, H. J., Stability of Metal Halide Perovskite Solar Cells. *Adv. Energy Mater.* **2015**, *5* (20), 1500963.
112. Brennan, M. C.; Draguta, S.; Kamat, P. V.; Kuno, M., Light-Induced Anion Phase Segregation in Mixed Halide Perovskites. *ACS Energy Lett.* **2018**, *3* (1), 204-213.
113. Draguta, S.; Sharia, O.; Yoon, S. J.; Brennan, M. C.; Morozov, Y. V.; Manser, J. S.; Kamat, P. V.; Schneider, W. F.; Kuno, M., Rationalizing the light-induced phase separation of mixed halide organic-inorganic perovskites. *Nat. Commun.* **2017**, *8* (1), 200.
114. Brandt, R. E.; Kurchin, R. C.; Hoye, R. L. Z.; Poindexter, J. R.; Wilson, M. W. B.; Sulekar, S.; Lenahan, F.; Yen, P. X. T.; Stevanović, V.; Nino, J. C.; Bawendi, M. G.; Buonassisi, T., Investigation of Bismuth Triiodide (BiI₃) for Photovoltaic Applications. *J. Phys. Chem. Lett.* **2015**, *6* (21), 4297-4302.
115. Zhu, X. H.; Wei, Z. R.; Jin, Y. R.; Xiang, A. P., Growth and characterization of a PbI₂ single crystal used for gamma ray detectors. *Cryst. Res. Technol.* **2007**, *42* (5), 456-459.
116. Gorban, I. S., Optical Properties of (PbJ₂)_x(BiJ₃)_{1-x} Crystals. *Ukrainskil Fizicheskil Zhurnal* **1981**, *3* (26), 495-496.

117. Dmitriev, Y. N.; Bennett, P. R.; Cirignano, L. J.; Gupta, T. K.; Klugerman, M.; Shah, K. S., Solid Solutions $(\text{PbI}_2)_x-(\text{BiI}_3)_{1-x}$. *MRS Proceedings* **1999**, 580, 99.
118. Gnatenko, Y. P.; Barabash, A. I.; Vertegel, I. G.; Chesnokov, E. D.; Ovcharenko, A. I.; Pogrebnyak, S. V., Investigation of I^{127} NQR spectra of the mixed $(\text{BiI}_3)_n(\text{PbI}_2)_{1-n}$ semiconducting layered crystals. *Funct. Mater.* **2010**, 17 (1).
119. Macrae, C. F.; Edgington, P. R.; McCabe, P.; Pidcock, E.; Shields, G. P.; Taylor, R.; Towler, M.; Streek, J. v. d., Mercury: visualization and analysis of crystal structures. *J. Appl. Crystallogr.* **2006**, 39 (3), 453-457.
120. Cie, S., X-area (version 1.18) and X-Red 32 (Version 1.04). **2002**.
121. Sheldrick, G. M., Crystal structure refinement with SHELXL. *Acta Crystallogr., Sect. C: Struct. Chem.* **2015**, 71 (1), 3-8.
122. Williams, D. B.; Carter, C. B., Other Imaging Techniques. In *Transmission Electron Microscopy*, Springer: 2009; pp 511-532.
123. Stoumpos, C. C.; Frazer, L.; Clark, D. J.; Kim, Y. S.; Rhim, S. H.; Freeman, A. J.; Ketterson, J. B.; Jang, J. I.; Kanatzidis, M. G., Hybrid Germanium Iodide Perovskite Semiconductors: Active Lone Pairs, Structural Distortions, Direct and Indirect Energy Gaps, and Strong Nonlinear Optical Properties. *J. Am. Chem. Soc.* **2015**, 137 (21), 6804-6819.
124. Qiu, X.; Cao, B.; Yuan, S.; Chen, X.; Qiu, Z.; Jiang, Y.; Ye, Q.; Wang, H.; Zeng, H.; Liu, J.; Kanatzidis, M. G., From unstable CsSnI_3 to air-stable Cs_2SnI_6 : A lead-free perovskite solar cell light absorber with bandgap of 1.48 eV and high absorption coefficient. *Sol. Energy Mater. Sol. Cells* **2017**, 159, 227-234.
125. Lehner, A. J.; Fabini, D. H.; Evans, H. A.; Hébert, C.-A.; Smock, S. R.; Hu, J.; Wang, H.; Zwanziger, J. W.; Chabinyk, M. L.; Seshadri, R., Crystal and Electronic Structures of Complex Bismuth Iodides $\text{A}_3\text{Bi}_2\text{I}_9$ (A = K, Rb, Cs) Related to Perovskite: Aiding the Rational Design of Photovoltaics. *Chem. Mater.* **2015**, 27 (20), 7137-7148.
126. Hermon, H.; Schieber, M.; Roth, M., Study of trapping levels in doped HgI_2 radiation detectors. *Nuclear Instruments and Methods in Physics Research Section A: Accelerators, Spectrometers, Detectors and Associated Equipment* **1996**, 380 (1), 10-13.
127. Schieber, M.; Hermon, H.; Zuck, A.; Vilensky, A.; Melekhov, L.; Shatunovsky, R.; Meerson, E.; Saado, H., Theoretical and experimental sensitivity to X-rays of single and

polycrystalline HgI₂ compared with different single-crystal detectors. *Nuclear Instruments and Methods in Physics Research Section A: Accelerators, Spectrometers, Detectors and Associated Equipment* **2001**, 458 (1), 41-46.

128. Kresse, G.; Hafner, J., Ab initio molecular-dynamics simulation of the liquid-metal--amorphous-semiconductor transition in germanium. *Phys. Rev. B* **1994**, 49 (20), 14251-14269.

129. Kresse, G.; Furthmüller, J., Efficient iterative schemes for ab initio total-energy calculations using a plane-wave basis set. *Phys. Rev. B* **1996**, 54 (16), 11169-11186.

130. Perdew, J. P.; Burke, K.; Ernzerhof, M., Generalized Gradient Approximation Made Simple. *Phys. Rev. Lett.* **1996**, 77 (18), 3865-3868.

131. Im, J.; Stoumpos, C. C.; Jin, H.; Freeman, A. J.; Kanatzidis, M. G., Antagonism between Spin–Orbit Coupling and Steric Effects Causes Anomalous Band Gap Evolution in the Perovskite Photovoltaic Materials CH₃NH₃Sn_{1-x}Pb_xI₃. *J. Phys. Chem. Lett.* **2015**, 6 (17), 3503-3509.

132. Arachchige, I. U.; Kanatzidis, M. G., Anomalous Band Gap Evolution from Band Inversion in Pb_{1-x}Sn_xTe Nanocrystals. *Nano Lett.* **2009**, 9 (4), 1583-1587.

133. Kyratsi, T.; Dyck, J. S.; Chen, W.; Chung, D.-Y.; Uher, C.; Paraskevopoulos, K. M.; Kanatzidis, M. G., Highly anisotropic crystal growth and thermoelectric properties of K₂Bi_{8-x}Sb_xSe₁₃ solid solutions: Band gap anomaly at low x. *J. Appl. Phys.* **2002**, 92 (2), 965-975.

134. Konstantakou, M.; Stergiopoulos, T., A critical review on tin halide perovskite solar cells. *J. Mater. Chem. A* **2017**, 5 (23), 11518-11549.

135. Krishnamoorthy, T.; Ding, H.; Yan, C.; Leong, W. L.; Baikie, T.; Zhang, Z.; Sherburne, M.; Li, S.; Asta, M.; Mathews, N., Lead-free germanium iodide perovskite materials for photovoltaic applications. *J. Mater. Chem. A* **2015**, 3 (47), 23829-23832.

136. Noel, N. K.; Stranks, S. D.; Abate, A.; Wehrenfennig, C.; Guarnera, S.; Haghghirad, A.-A.; Sadhanala, A.; Eperon, G. E.; Pathak, S. K.; Johnston, M. B., Lead-free organic–inorganic tin halide perovskites for photovoltaic applications. *Energy Environ. Sci.* **2014**, 7 (9), 3061-3068.

137. Abate, A., Perovskite solar cells go lead free. *Joule* **2017**, 1 (4), 659-664.

138. Sun, S.; Tominaka, S.; Lee, J.-H.; Xie, F.; Bristowe, P. D.; Cheetham, A. K., Synthesis, crystal structure, and properties of a perovskite-related bismuth phase, (NH₄)₃Bi₂I₉. *APL Mater.* **2016**, 4 (3), 031101.

139. Lu, C.; Zhang, J.; Sun, H.; Hou, D.; Gan, X.; Shang, M.-h.; Li, Y.; Hu, Z.; Zhu, Y.; Han, L., Inorganic and Lead-Free AgBiI_4 Rudorffite for Stable Solar Cell Applications. *ACS Appl. Energy Mater.* **2018**, *1* (9), 4485-4492.
140. Turkevych, I.; Kazaoui, S.; Ito, E.; Urano, T.; Yamada, K.; Tomiyasu, H.; Yamagishi, H.; Kondo, M.; Aramaki, S., Photovoltaic Rudorffites: Lead-Free Silver Bismuth Halides Alternative to Hybrid Lead Halide Perovskites. *ChemSusChem* **2017**, *10* (19), 3754-3759.
141. Zhu, H.; Pan, M.; Johansson, M. B.; Johansson, E. M. J., High Photon-to-Current Conversion in Solar Cells Based on Light-Absorbing Silver Bismuth Iodide. *ChemSusChem* **2017**, *10* (12), 2592-2596.
142. Bahari, Z.; Thévet, F.; Rivet, J.; Dugué, J., Contribution à l'étude expérimentale du système ternaire Bi-Cu-I : Description du triangle CuI-BiI₃-I. *JEEP – Journées d'Etude des Equilibres entre Phases* **2009**, 00020.
143. Kortüm, G.; Braun, W.; Herzog, G., Prinzip und Meßmethodik der diffusen Reflexionsspektroskopie. *Angew. Chem.* **1963**, *75* (14), 653-661.
144. Oldag, T.; Aussieker, T.; Keller, H.-L.; Preitschaft, C.; Pfitzner, A., Solvothermale Synthese und Bestimmung der Kristallstrukturen von AgBiI_4 und Ag_3BiI_6 . *Z. Anorg. Allg. Chem.* **2005**, *631* (4), 677-682.
145. Sansom, H. C.; Whitehead, G. F. S.; Dyer, M. S.; Zanella, M.; Manning, T. D.; Pitcher, M. J.; Whittles, T. J.; Dhanak, V. R.; Alaria, J.; Claridge, J. B.; Rosseinsky, M. J., AgBiI_4 as a Lead-Free Solar Absorber with Potential Application in Photovoltaics. *Chem. Mater.* **2017**, *29* (4), 1538-1549.
146. Hull, S.; Keen, D. A., Structural characterization of further high temperature superionic phases of Ag_2HgI_4 and Cu_2HgI_4 . *J. Phys.: Condens. Matter* **2001**, *13* (24), 5597-5610.
147. Yude, Y.; Boysen, H.; Schulz, H., Neutron powder investigation of CuI. *Zeitschrift für Kristallographie-Crystalline Materials* **1990**, *191* (1-4), 79-92.
148. Hu, Y.; Zhang, S.; Miao, X.; Su, L.; Bai, F.; Qiu, T.; Liu, J.; Yuan, G., Ultrathin $\text{Cs}_3\text{Bi}_2\text{I}_9$ Nanosheets as an Electronic Memory Material for Flexible Memristors. *Adv. Mater. Interfaces* **2017**, *4* (14), 1700131-n/a.
149. Brightwell, J. W.; Buckley, C. N.; Ray, B., Electrical and phase behaviour of the system AgI-PbI_2 . *Solid State Commun.* **1982**, *42* (10), 715-716.

150. Strähle, J.; Bärnighausen, H., Kristallchemischer Vergleich der Strukturen von RbAuCl_4 und RbAuBr_4 . *Z. Kristallogr* **1971**, *134*, 471.
151. Eijndhoven, J. C. M. T.-v.; Verschoor, G. C., Redetermination of the crystal structure of $\text{Cs}_2\text{AuAuCl}_6$. *Mater. Res. Bull.* **1974**, *9* (12), 1667-1670.
152. Strähle, J.; Gelinek, J.; Kölmel, M.; Nemecek, A.-M., Die Kristallstruktur der Salze $\text{K}_2\text{Au}_2\text{I}_6$ und $\text{Cs}_2\text{Ag}_x\text{Au}^{I}_{1-x}\text{Au}^{III}\text{Br}_6$. Ein Beitrag zur Kristallchemie der Alkalihexahalogenaurate(I,III) / Crystal Structure of the Salts $\text{K}_2\text{Au}_2\text{I}_6$ and $\text{Cs}_2\text{Ag}_x\text{Au}^{I}_{1-x}\text{Au}^{III}\text{Br}_6$. A Contribution to the Crystal Chemistry of the Alkali Hexahalogeno Aurates(I,III). In *Zeitschrift für Naturforschung B*, 1979; Vol. 34, p 1047.
153. Matsushita, N.; Kitagawa, H.; Kojima, N., A Three-Dimensional Iodo-Bridged Mixed-Valence Gold(I, III) Compound, $\text{Cs}_2\text{Au}_1\text{Au}^{III}\text{I}_6$. *Acta Crystallogr., Sect. C: Struct. Chem.* **1997**, *53* (6), 663-666.
154. Schulz Lang, E.; Abram, U.; Strähle, J., Synthese, Eigenschaften und Struktur von LiAuI_4 und KAuI_4 mit einer Diskussion der kristallchemischen Verwandtschaft zwischen den Halogenauraten RbAuCl_4 , AgAuCl_4 , RbAuBr_4 und LiAuI_4 . *Z. Anorg. Allg. Chem.* **1997**, *623* (11), 1791-1795.
155. Matsushita, N.; Tanaka, A.; Kojima, N., A three-dimensional iodo-bridged mixed-valence gold(I,III) compound, $\text{Rb}_2[\text{Au}^I\text{I}_2][\text{Au}^{III}\text{I}_4]$. *Acta Crystallogr., Sect. E: Crystallogr. Commun.* **2005**, *61* (9), i201-i203.
156. Khyzhun, O.; Fochuk, P.; Kityk, I.; Piasecki, M.; Levkovets, S.; Fedorchuk, A.; Parasyuk, O., Single crystal growth and electronic structure of TlPbI_3 . *Mater. Chem. Phys.* **2016**, *172*, 165-172.
157. Bruker-AXS, APEX3 (version 2016.1-0) **2016**, Madison, WI, 2016.
158. Krause, L.; Herbst-Irmer, R.; Sheldrick, G. M.; Stalke, D., Comparison of silver and molybdenum microfocus X-ray sources for single-crystal structure determination. *J. Appl. Crystallogr.* **2015**, *48* (1), 3-10.
159. Sheldrick, G. M. *TWINABS*, University of Göttingen, Germany., 2012.
160. Kresse, G.; Hafner, J., Ab initio. *Phys. Rev. B* **1993**, *47* (1), 558-561.
161. Kresse, G.; Hafner, J., Ab initio. *Phys. Rev. B* **1994**, *49* (20), 14251-14269.

162. Kresse, G.; Furthmüller, J., Efficiency of ab-initio total energy calculations for metals and semiconductors using a plane-wave basis set. *Comput. Mater. Sci.* **1996**, *6* (1), 15-50.
163. Blöchl, P. E., Projector augmented-wave method. *Phys. Rev. B* **1994**, *50* (24), 17953-17979.
164. Kresse, G.; Joubert, D., From ultrasoft pseudopotentials to the projector augmented-wave method. *Phys. Rev. B* **1999**, *59* (3), 1758-1775.
165. Monkhorst, H. J.; Pack, J. D., Special points for Brillouin-zone integrations. *Phys. Rev. B* **1976**, *13* (12), 5188-5192.
166. Setyawan, W.; Curtarolo, S., High-throughput electronic band structure calculations: Challenges and tools. *Comput. Mater. Sci.* **2010**, *49* (2), 299-312.
167. Becker, D.; Beck, H. P., High Pressure Study of NH₄Pb₂Br₅ Type Compounds. I structural parameters and their evolution under high pressure. *Z. Anorg. Allg. Chem.* **2004**, *630* (12), 1924-1932.
168. Cao, D. H.; Stoumpos, C. C.; Farha, O. K.; Hupp, J. T.; Kanatzidis, M. G., 2D Homologous Perovskites as Light-Absorbing Materials for Solar Cell Applications. *J. Am. Chem. Soc.* **2015**, *137* (24), 7843-7850.

Grant C. B. Alexander

720A Hinman Ave Apt 1N ◦ Evanston, IL 60202 ◦ (608) 772 – 0056 ◦ grantcbalexander@gmail.com

EDUCATION

Northwestern University Evanston IL

Ph.D. Candidate in Materials Chemistry, December 2019

Lake Forest College, Lake Forest, IL

B. A. in Chemistry, May 2014

Magna cum Laude, Phi Beta Kappa

PROFICIENCY AND SKILLS

Synthetic methods: air-free preparations, solid state, solvothermal, crystal growth

X-ray Diffraction: single crystal, powder, Rietdvelt refinement

Optical spectroscopy: reflectance, absorbance, photoluminescence

Electrical: device preparation, I-V characterization, time-delay measurements

Electron Microscopy: SEM-EDS, SEM-WDS

Software: Adobe Photoshop, Microsoft Office Suite, Origin 8 Pro, Apex 3, X-Area, CMPR, Jana2006, Inca, Aztec

RESEARCH EXPERIENCE

Ph.D Candidate, Northwestern University, Evanston, IL

September 2014 – Present

Materials Chemistry

- Conceptualize and design experiments probing the unexplored regions of main group metal halide chemistry yielding more than ten new materials and leading to peer-reviewed publications
- Characterize materials exhaustively by diffraction, optical, electrical, thermal analysis, and microscopy experiments to build and develop structure-property relationships
- Establish a knowledge base on materials by integrating experimental and literature observations with chemical trends to predict future results and direct project development
- Develop and implement new methods and procedures to probe the nature of material properties
- Problem solve and reconcile experimental data to theoretical calculations to aid the explanation of physical and chemical properties
- Actively manage and facilitate collaboration between research groups in the departments of Chemistry, Materials Science, and Physics to drive project success
- Aid colleagues to fulfil their crystal growth, SEM, and crystallographic needs
- Train and supervise graduate student and post-doctoral researchers' use two STOE single crystal diffractometers

Undergraduate Research Assistant, Lake Forest College, Lake Forest, IL

May 2011 – May 2014

Inorganic Synthesis & Computational Chemistry

- Conducted exploratory synthesis of new compounds in ionic liquids, uncovering new dynamics in the chemistry of metal thiophosphates via wet chemical and computational routes
- Developed and adapted new procedures with existing instrumentation to increase lab productivity and reduce necessity of travel to other institutions for analysis

- Results directly aided in the publication and co-authorship of two journal articles during my working period and once since my departure
- Trained and mentored younger undergraduate researchers in wet chemical techniques and safe lab practices

TEACHING EXPERIENCE

Graduate Assistant, Northwestern University Dept. of Chemistry, Evanston IL
September 2016 – December 2018

- Supported and substituted for the professor teaching Principles of Inorganic Chemistry to incoming graduate students and upper level undergraduate students
- Helped students develop and understanding of inorganic chemistry concepts when students were coming from non-chemistry backgrounds
- Created keys, graded exams and homework, and monitored student progress through the quarter
- Revised and updated coursework and course content

Teaching Assistant, Northwestern University Dept. of Chemistry, Evanston IL
September 2014 – August 2015

- Taught laboratory sections of undergraduate inorganic chemistry,
- Prepared short pre-laboratory lectures to instruct students on the intricates and pitfalls of given weekly experiments
- Graded laboratory reports and held office hours to assist in student success

SELECTED PUBLICATIONS AND PRESENTATIONS

G. C. B. Alexander, H. J. Jung, P. W. Krantz, § G. Trimarchi, K. M. McCall, S. Davis, Y. Xu, B. W. Wessels, V. P. Dravid, V. Chandrasekhar, M. G. Kanatzidis. “Controllable Nonclassical Conductance Switching in Nanoscale Phase Separated $(\text{PbI}_2)_{1-x}(\text{BiI}_3)_x$ Layered Crystals” (In preparation)

G. C. B. Alexander, H. J. Jung, P. W. Krantz, § G. Trimarchi, K. M. McCall, S. Davis, Y. Xu, B. W. Wessels, V. P. Dravid, V. Chandrasekhar, M. G. Kanatzidis. “Memristor Behavior and Novel Structural Properties in $(\text{PbI}_2)_{1-x}(\text{BiI}_3)_x$ Mixtures” 2018 Fall Meeting of the Materials Research Society, November 29, 2018

G. C. B. Alexander, D. H. Fabini, R. Seshadri, M. G. Kanatzidis, “ AuPb_2I_7 : A Narrow Bandgap Au^{3+} Semiconductor” *Inorganic Chemistry*, **2018**, 57, 804 – 810.

Y. He, W. Ke, **G. C. B. Alexander**, K. M. McCall, D. G. Chica, Z. Liu, I. Hadar, C. C. Stoumpos, B. W. Wessels, M. G. Kanatzidis. “Resolving the Energy of γ -ray Photons with MAPbI_3 Single Crystals” *ACS Photonics*, **2018**, 5, 4132 – 4138.

J. M. Hodges, Y. Xia, C. D. Malliakas, **G. C. B. Alexander**, M. K. Y. Chan, M. G. Kanatzidis. “Two Dimensional $\text{CsAg}_5\text{Te}_3\text{-xS}_x$ Semiconductors, Multi-anion Chalcogenides with Dynamic Disorder and Ultralow Thermal Conductivity” *Chemistry of Materials*, **2018**, 30, 7245 – 7254.

J. A. Cody, K. B. Finch; G. Reynders, **G. C. B. Alexander**, H. G. Lim, C. Nather, W. Bensch, “Ionothermal Synthesis of Four New Nickel Thiophosphate Anions: $[\text{Ni}(\text{P}_2\text{S}_8)_2]^{2-}$, $[\text{Ni}(\text{P}_3\text{S}_9)(\text{P}_2\text{S}_8)]^{3-}$, $[\text{Ni}(\text{P}_3\text{S}_9)_2]^{4-}$, and $[(\text{NiP}_3\text{S}_8)_4(\text{PS}_4)]^{7-}$ ” *Inorganic Chemistry*, **2012**, 51, 13357 – 13362.